

VON KARMAN INSTITUTE FOR FLUID DYNAMICS
AERONAUTICS & AEROSPACE DEPARTMENT

UNIVERSITÉ CATHOLIQUE DE LOUVAIN
ÉCOLE POLYTECHNIQUE DE LOUVAIN

Thermal ablation and radiation modeling of meteor phenomena

September 2020

Thesis presented by Bruno Dias in order to obtain the degree of "Doctor in Engineering",
Université catholique de Louvain, 4th of September 2020.

Supervisors:

Prof. Philippe Chatelain (Université catholique de Louvain) and
Prof. Thierry Magin (von Karman Institute for Fluid Dynamics)

Doctoral Committee:

Prof. Laurent Delannay (Université catholique de Louvain), President of the Jury
Prof. Juray De Wilde (Université catholique de Louvain), Secretary of the Jury
Prof. Joris Proost (Université catholique de Louvain), Examiner
Adj. Prof. Maria Gritsevich (University of Helsinki), External examiner
Dr. Christopher Johnston (NASA Langley Research Center), External examiner
Dr. Johan De Keyser (Royal Belgian Institute for Space Aeronomy), External examiner

*There is no “answer”.
But Tânia & Mimouche are the answer.*

Abstract

Meteoroids provide Earth’s primary source of extraterrestrial materials from the various nebular and planetary environments of the Solar System and beyond. These naturally delivered samples bring 50 to 100 tons of material daily. A community of researchers devotes themselves to study meteors. Their interest lies in a quest for answers in aeronomy, astronomy, geophysics, and planetology. The understanding of meteor phenomena usually derives from the correlation between observations and simplified models. However, these models lump most of the physics, incapacitating an in-depth comprehension. For instance, the Chelyabinsk event in 2013 raised awareness within the scientific community and urged them to improve the legacy models.

Meteor phenomena are complex since they involve many physical aspects, such as multi-phase and non-equilibrium flows. Up to date, the most detailed simulations are incapable of coping with all these physical features. This thesis aims to build models that accurately describe a meteoroid entry and compare the results obtained with observations. We leverage engineering models developed for reentry space vehicles and extend them to meteoroid applications. We focus first on the flow analysis – high-temperature effects and radiation – and then on the material – evaporation and shear ablation. These models are valid within the continuum regime, meaning that they can be employed to derive flow characteristics of fireballs and to study bolide ablation.

Chapter 2 presents state-of-the-art physico-chemical models relevant to meteoroid entry conditions. We review the necessary data to compute the metallic species thermochemical properties. These data are essential to understand the flow features and strengthen the accuracy of the meteor ablation description. We integrate the required metals data into the open-source MUTATION⁺⁺ library, which is coupled to a Computational Fluid Dynamics solver to provide thermochemical closure to the governing equations.

In Chapter 3, we improve the engineering-based models to study meteoroid degradation and develop kinetic-based evaporation models. The former models consider chemical equilibrium at the gas/liquid interface, whereas the latter account for chemical non-equilibrium and rarefied gas effects due to the presence of the Knudsen layer. We observe a significant deviation between both models under strong evaporation conditions and a considerable temperature jump at the interface due to rarefied effects.

The high heating load on the meteoroid during entry leads to a phase-change of the material. As the material melts, the aerodynamic forces drive the removal of the molten layer. This behavior was observed on several ground experiments based on real meteorite samples. In Chapter 4, we apply an enthalpy method and solve the material thermal behavior to study the phase-transition phenomenon. We extend a shear ablation model developed for glass materials

to meteoroids. We make a comparison between the results obtained with our models and the experiments carried out at NASA Ames Research Center on a Tamdakht H5 ordinary chondrite. For those conditions, our results show that evaporation is negligible compared to the molten layer removal.

The presence of alkali metals in the flow, due to the evaporation, causes the bright light that is observed during a meteor entry. This light is owed to the radiation of the chemical species within the flow. Coupling the flow field with thermal radiation is a complicated task due to the inherent high computational cost. In this work, we employ the Hybrid Statistical Narrow-Band model, which is accurate and efficient in previous studies for the reentry of space vehicles. In Chapter 5, we compare the spectral measurements carried out in the VKI Plasmatron with the numerical results and observe a good agreement between the spectral measurements and the simulated spectra regarding the emission of Fe and K. Unfortunately, it is not possible to analyze the Na intensity due to a spectral saturation from the experiment.

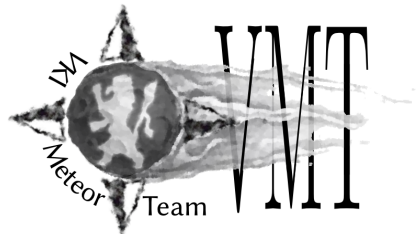
Chapter 6 combines all the models developed in the previous chapters to study the Lost City bolide event. We couple radiation, flow, and evaporation to reproduce the luminosity at different altitudes. The numerical outcome is compared with the observations; a good agreement is found. The simulated spectra lack the presence of refractory element Ca, which is usually detected during meteor entry. We suspect that the presence of Ca results from droplet evaporation sheared away from the main body. The coupling between the flow and material suggests that the primary source of material degradation is due to the removal of the molten layer, for most of the trajectory. Below a certain altitude, radiative heating increases substantially, leading to more substantial evaporation. This analysis is made only in a small segment of the trajectory due to the complexity inherent to the coupling.

In this work, we could shift from the 0D correlations or legacy models to predictive engineering models, allowing us to describe meteor phenomena in fair agreement with the observations. The outcome of this thesis can also be applied to study man-made space debris degradation in Earth's atmosphere, in particular, to detect their radiative signature during reentry phase.

Acknowledgements

I first came to VKI in 2012 to do an internship. Looking back, I realize the fantastic journey that I have gone through. I was lucky since the first day I set foot at the VKI, and I met my longtime supervisor, Prof. Thierry Magin. He gave me the book *Introduction to physical gas dynamics* from Vicenti & Kruger, and he told me that later they would have the famous VKI BBQ for the Research Master graduation. Without knowing anybody, I decided to join the BBQ when the most fantastic thing happened . . . they had free beers. From that moment on, I fell in love with VKI. In retrospect, I was very fortunate to have the most friendly and understanding supervisor. I believe that if our paths hadn't crossed, I wouldn't have chosen research . . . so in a way, you are my inspiration. I cannot thank you enough for believing and allowing me to do something that I really enjoy.

My supervisor wasn't the only person inspiring me along the way. None of this work would be possible without the VKI Meteor Team's support, more specifically Federico and Stefano. To my scientific soulmate, Federico, I thank you for the constant words of encouragement and how you made my life better with



your wisdom and patience. Your ability to calm me down and caring made this thesis possible. With great affection, I will always remember our great adventures to all the conferences, our trip to the USA, and all those hotel rooms we shared (especially the love pension in Strasbourg). To Stefano, you are one of the most intelligent and passionate researchers I ever met; your love for science is a source of inspiration. You made me a better researcher.

I will never forget the great time spent with Georgios. I will always remember all our discussions, such as the meaning of meteor in Greek, to more essential life arguments such as stoicism. I miss our passionate discussions on science and messing around with you. On a technical and personal level, you JB have been one of the most influential people during my Ph.D. You have always cared for my success and always been there to listen to my problems. Even in times when you complained that I asked too many questions, I was training you to become a professor (I am sure you will be a great one). I will never forget what you have done for me. To all my colleagues that helped me explore the space and to come back to Earth, I thank you for all the support you gave throughout these years: Anabel, Bernd, Alessandro Turchi, Alessandro Munafò, David, Erik, Aurélie, Alex, Guillaume, Fran, Andrea, and Michele. All these years in

Brussels have many stories to tell, and Clara, Jorge, Ben, Fabri, and Alessia are present in many of them. I genuinely appreciate your friendship and the support you gave in the bad and good moments. I wish you the best; that our friendship continues for many years and that we can have many more stories to tell. Finally, I thank my VKI colleagues that in a way or another have shared this path with me: Bogdan, Elissavet, Maria, Miguel, Orkun, Nicolas, Adriana, Ludovico, Sophia, and so many others.

During this journey, I had the opportunity to work and learn from so many people. A piece of this thesis belongs to you . . . I was lucky to meet Aldo, who taught me so much, not only about evaporation but also about dedication. You are one of the most passionate teachers I have met, and I am proud to have learned from you. I want to thank Laurent Soucasse, Anouar Soufiani, and Philippe Rivière from the Laboratoire EM2C-CentraleSupélec for all the support and time you have spent with me. My short time at NASA ARC was terrific! I have to thank Eric Stern for inviting and allowing me to enjoy a month of sunny California and to be able to work with a fantastic group. My stay at NASA wouldn't be possible without the support of Francesco Panerai; you were a fantastic guide in showing the best that California has to offer. I hope one day I can give back all the help you gave me. I want to thank all the support from Cenaero, more specifically Jean-Sébastien Cagnone and Koen Hillewaert. A special thanks goes to Pierre Schrooyen for all the valuable discussions and everything you did for me. I acknowledge Hervé Lamy, Johan De Keyser, and all the BIRA group for introducing me to this beautiful meteor world. This thesis started thanks to yours and Thierry's vision to approximate to the meteor community to the engineering world. I want to thank everybody from UCLouvain, particularly my promoter Philippe Chatelain, for accepting me as his student and always welcoming me with open arms the times I went to Louvain-la-Neuve. I want to acknowledge all jury members for their critical feedback and suggestions to improve this thesis. This thesis wouldn't be possible without the financial support of Fonds de la Recherche Scientifique (FRS-FNRS). I sincerely admire their effort in financing young researchers.



To all VKI Green Office members, I thank you for making our institute a better and enjoyable workplace. Your tenacity and willingness to turn VKI into a greener and eco-friendly institute are uplifting. Even if sometimes your efforts are

not recognized, never stop and keep up the excellent work!

To Marco, Fernando, and Cansev, I really had a lot of fun with you guys! You are one of the best people I have met, and it was a pleasure to share so many adventures with you. To my dearest friends, Barbs and Joey, a huge thanks! You have always been there for me and helped me to disconnect from the engineering world. I am thankful for all the time we have spent together. Also, I want to thank Thibault for the fantastic illustration you did for the

thesis. I love your work as an illustrator and wish you the best for the future.

Aos meus queridos amigos Toca, Rui e Jonas, aos meus primos, Joana, Marco e ao meu tio Lipes, vocês têm sido os meus companheiros ao longo destes anos. Com o número de histórias que temos podíamos escrever um livro. O vosso apoio e palavras de encorajamento foram das mais importantes para esta tese. Esta tese também é para vocês e pelo tempo todo que não passamos juntos. Um abraço a vocês e obrigado por estarem sempre lá. Nada disto seria possível sem o eterno apoio dos meus pais, Adolfo e Amélia. Vocês sempre me apoiaram e deram-me toda a liberdade do mundo para eu crescer e tornar-me melhor. Obrigado por todos os conselhos e lições de vida que me deram ao longo dos anos.

Finalmente, os últimos agradecimentos vão para pessoa mais importante que apareceu na minha vida durante o doutoramento. À minha querida namorada Tânia, sem ti nada disto seria possível. Obrigado por seres a pessoa mais paciente e encorajadora do mundo. Tu fazes-me ser uma pessoa melhor. Estes últimos anos têm sido os mais felizes por tudo que construímos juntos... Incluindo o gato mais fofo do mundo, Mimouche. Tu és verdadeiramente a melhor pessoa que eu conheço por todo o carinho e amizade que dás aos outros. Por todas as nossas aventuras e por tudo aquilo que já passámos juntos eu sou a pessoa mais sortuda do mundo por te ter ao meu lado. Obrigado por tudo!



*Bruno Dias
Brussels, 2020*

Contents

List of Publications	xiii
List of Figures	xviii
List of Tables	xix
Nomenclature	xxi
Constants	xxi
Roman Symbols	xxi
Greek Symbols	xxiv
Acronyms	xxv
1. Introduction	1
1.1. Meteoroids and the meteor phenomenon	1
1.2. Detection and observation of meteoroids	3
1.3. State-of-the-art of the meteor physics	7
1.3.1. Meteor modeling	9
1.3.2. Ground experiments of meteorites	12
1.4. Objectives and outline of the thesis	13
2. Gas-phase modeling	19
2.1. Introduction	19
2.2. Governing equation for hypersonic flows	20
2.3. Physico-chemical models for gas phase	24
2.3.1. Thermodynamic properties	24
2.3.2. Transport properties	30
2.3.3. Chemical kinetic	37
2.3.4. Energy transfer mechanisms	39
2.4. Numerical methods	41
2.4.1. Stagnation-line discretization	41
2.4.2. Flux splitting methods	44
2.5. Results	46
2.6. Conclusion	48
3. Surface evaporation	51
3.1. Introduction	51
3.2. Flux balances at the surface	53
3.2.1. Surface mass balance	53
3.2.2. Surface energy balance	54
3.2.3. Equilibrium vapor pressure	55

3.3.	Equilibrium evaporation models	58
3.4.	Kinetic-based evaporation models	62
3.4.1.	The Knudsen layer	63
3.4.2.	Multicomponent non-equilibrium model	65
3.4.3.	The Hertz-Knudsen model	68
3.4.4.	The Schrage model	69
3.5.	Numerical methods	70
3.5.1.	The Direct Simulation Monte Carlo (DSMC) method	70
3.5.2.	Comparison with non-equilibrium evaporation models	70
3.6.	Results	76
3.6.1.	Navier-Stokes solution for evaporation	77
3.6.2.	Comparison with the equilibrium and non-equilibrium evaporation model	81
3.6.3.	Comparison with the Navier-Stokes and Boltzmann solution	81
3.7.	Conclusion	82
4.	Material melting	85
4.1.	Introduction	85
4.2.	Multi-phase model	87
4.2.1.	Material phase-transition	87
4.2.2.	Removal of the molten material	89
4.2.3.	Finite-differences method	92
4.3.	Arc Jet validation experiment	93
4.4.	Results	95
4.4.1.	Flow results	96
4.4.2.	Multi-phase results	100
4.5.	Conclusion	108
5.	Flow radiation	111
5.1.	Introduction	111
5.2.	Flow radiation modeling	112
5.2.1.	Radiative transfer in participating media	112
5.2.2.	The Hybrid Statistical Narrow-Band method	119
5.2.3.	Radiative source terms and HSNB tangent-slab	128
5.3.	H5 Chondrite Plasmatron experiment	131
5.3.1.	Plasmatron facility description	131
5.3.2.	Test sample and holder	132
5.3.3.	Experimental results	134
5.4.	Comparison with Plasmatron experiments	141
5.4.1.	Numerical set-up	142
5.4.2.	6 seconds	146
5.4.3.	14 seconds	152
5.5.	Conclusion	152

6. Lost City case study	157
6.1. Introduction	157
6.2. Coupling between solvers	158
6.3. Methodology to compute luminosity and heat transfer coefficient	161
6.3.1. Heat transfer coefficient and luminous efficiency	161
6.3.2. Application of the methodology	163
6.3.3. Luminosity of the Lost City bolide	175
6.4. Lost City radiation/flow/material coupling	182
6.5. Conclusion	183
7. Conclusions and Perspectives	189
7.1. Contribution of this work	189
7.2. Future work and perspectives	195
Appendices	197
A. Physico-chemical properties	199
A.1. Chemical reactions	199
A.2. Transport properties	201
A.3. Equilibrium vapor pressure	202
A.4. Modified Steger-Warming scheme	203
B. Melting properties	205
B.1. Verification of the material solver	205
B.2. Stagnation-point formulation	206
B.3. Average surface formulation	208
C. Radiation Properties	211
C.1. HTGR database	211
C.2. Line broadening mechanisms	213
C.2.1. Doppler broadening	213
C.2.2. Collision broadening	214
C.3. Comparison with Plasmatron for higher nitridation and oxidation probability	217
C.3.1. Flow field	217
C.3.2. Radiative field	217
C.4. Filter	218
Bibliography	223

List of Publications

Journal articles

1. B. Dias, A. Turchi, E. Stern, and T. E. Magin, A model for meteoroid ablation including melting and vaporization, *Icarus*, 345(2020) 113710.
2. B. Dias, J.B. Scoggins, and T. E. Magin, Luminosity calculation of meteor entry based on detailed flow simulations in the continuum regime, *Astronomy & Astrophysics* 635, A184, 2020.
3. B. Helber, B. Dias, F. Bariselli, L. F. Zavalan, L. Pittarello, S. Goderis, B. Soens, S. J. McKibbin, P. Claeys, and T. E. Magin, Analysis of meteoroid ablation based on plasma wind-tunnel experiments, surface characterization, and numerical simulations, *The Astrophysical Journal*, 876(2):120-134, 2019
4. L. Pittarello, S. Goderis, B. Soens, S. J. McKibbin, G. Giuli, F. Bariselli, B. Dias, B. Helber, G. O. Lepore, F. Vanhaecke, C. Koeberl, T. E. Magin, and P. Claeys, Meteoroid atmospheric entry investigated with plasma flow experiments: Petrography and geochemistry of the recovered material, *Icarus*, 331:170-178, 2019
5. S. Boccelli, F. Bariselli, B. Dias and T. E. Magin, Lagrangian diffusive reactor for detailed thermochemical computations of plasma flows, *Plasma Sources Science and Technology*, 28(6):065002, 2019
6. G. Grossir, B. Dias, O.Chazot, and T. E. Magin, High temperature and thermal non-equilibrium effects on the determination of free-stream flow properties in hypersonic wind tunnels, *Physics of Fluids*, 30(12):126102, 2018
7. F. Bariselli, S. Boccelli, B. Dias, A. Hubin, T. E. Magin, A self-consistent method for the simulation of meteor trails with application to radio observations, (accepted in *Astronomy & Astrophysics*)
8. J. B. Scoggins, V. Leroy, G. Bellas-Chatzigeorgis, B. Dias and T. E. Magin, Mutation++: MULTicomponent Thermodynamic And Transport properties for IONized gases in C++, *SoftwareX*, 12:100575, 2020

Book chapters

1. G. Grossir and B. Dias, Flow characterization of the VKI Longshot wind tunnel, *Flow Characterization and Modeling of Hypersonic Wind Tunnels*, STO-AVT-325

Conference proceedings

1. B. Dias, A. Turchi and T. E. Magin, Stagnation-Line Simulations of Meteor Ablation, *2015 Joint Thermophysics and Heat Transfer Conference*, Dallas, Texas, USA, AIAA 2015-2349, 2015
2. B. Dias, F. Bariselli, A. Turchi, A. Frezzotti, P. Chatelain, T. E. Magin, Development of a melting model for meteors, *30th International Symposium on Rarefied Gas Dynamics*, Victoria, British Columbia, Canada, 1786(1):160004, 2016
3. D. Henneaux, P. Schrooyen, B. Dias, A. Turchi, P. Chatelain, and T. E. Magin, Towards a High-Fidelity Multiphase Solver with Application to Space Debris Aerothermal Ablation Modeling, *2019 Joint Thermophysics and Heat Transfer Conference*, Dallas, Texas, USA, AIAA 2019-2876, 2019
4. D. Henneaux, P. Schrooyen, B. Dias, A. Turchi, P. Chatelain, and T. E. Magin, Extended Discontinuous Galerkin Method for Solving Gas-Liquid Compressible Flows with Phase Transition, *Virtual Event*, AIAA 2020-2971, 2020

List of Figures

1.1.	Illustration of meteoroids and their shape during entry.	3
1.2.	Excerpt original report on space exploration.	4
1.3.	Fireballs reported by USA government sensors.	5
1.4.	Meteoroid trajectory estimated with the meteor physics equations.	7
1.5.	Illustration of the thesis structure.	16
2.1.	Spherical body of radius subjected to a hypersonic flow.	21
2.2.	Na partition function for different amounts of energy levels.	27
2.3.	Energy levels for Na.	28
2.4.	Energy-level reduction of Na.	29
2.5.	Equilibrium composition for $\{\text{NaO}, \text{Na}, \text{O}, \text{Na}^+, \text{O}^+, \text{e}^-\}$	30
2.6.	Illustration of an elastic collision.	32
2.7.	Comparison of the thermodynamic properties between Roe and AUSM ⁺ -up2 scheme.	47
2.8.	Composition along the stagnation streamline computed with AUSM ⁺ -up2 scheme.	48
2.9.	Energy transfer source terms computed with AUSM ⁺ -up2 scheme.	49
3.1.	Illustration of the mass balances on the surface.	53
3.2.	Illustration of the energy balances on the surface.	54
3.3.	Saturation vapor pressure of Na.	56
3.4.	Saturation vapor pressure computed by MAGMA.	58
3.5.	Multiphase equilibrium composition for pure Na, Mg and N.	60
3.6.	Multiphase constrained equilibrium composition for pure Na, Mg and N.	61
3.7.	B' comparison between unconstrained and constrained multiphase-equilibrium solutions.	63
3.8.	Illustration of the Knudsen layer jump conditions on the surface.	63
3.9.	Illustration of the Maxwellian distribution function in the Knudsen layer.	64
3.10.	Velocity ratio vs. pressure jump.	69
3.11.	Temperature for $\mu=1$	72
3.12.	Normalized density profile in the Knudsen layer for different M_∞	72
3.13.	Comparison of the evaporation rate between Direct Simulation Monte Carlo (DSMC) and non-equilibrium models for $\mu=1$	73
3.14.	Normalized temperature profile in the Knudsen layer for different edge Mach number, for $\mu=2$	74
3.15.	Temperature components of the light and heavy species in the Knudsen layer.	74

3.16. Species mole fraction downstream of the Knudsen layer for different M_∞	75
3.17. Comparison of the evaporation rate between DSMC and non-equilibrium models for $\mu=2$	75
3.18. Comparison of the evaporation rate between DSMC and non-equilibrium models for $\mu=10$	76
3.19. Physical properties along the stagnation streamline due to the evaporation of Na and Mg into N for $T_w = 1125$	77
3.20. Composition along the stagnation streamline due to the evaporation of Na and Mg into N for $T_w = 1125$	78
3.21. Physical properties along the stagnation streamline due to the evaporation of Na and Fe into N for $T_w = 1067$	79
3.22. Composition along the stagnation streamline due to the evaporation of Na and Fe into N for $T_w = 1067$	79
3.23. Physical properties along the stagnation streamline due to the evaporation of Na, K and Fe into N for $T_w = 1040$	80
3.24. Composition along the stagnation streamline due to the evaporation of Na, K and Fe into N for $T_w = 1040$	80
3.25. Evaporation rate of Na and Mg into N for different surface temperatures.	81
3.26. Comparison of the evaporation properties between DSMC and multicomponent non-equilibrium model for $\mu=1$	82
3.27. Comparison of the evaporation properties between DSMC and multicomponent non-equilibrium model for binary and ternary surface composition.	83
4.1. Enthalpy method.	88
4.2. Thermal conductivity as a function of temperature.	89
4.3. Viscosity of the material as a function of temperature.	90
4.4. Illustration of a half-sphere.	91
4.5. Model assembly for Arc Jet experiment.	94
4.6. Frame from high-speed video captured at 1.49 seconds from model insertion.	94
4.7. Sample shape pre and post test.	95
4.8. Stagnation-streamline temperature profile at different times.	97
4.9. Stagnation point heat flux in time taking into account the evaporation of the molten layer.	97
4.10. Gradient of the aerodynamic forces in time around the sphere.	98
4.11. Plasma composition along the stagnation streamline at 0 seconds.	98
4.12. Evaporation species at the beginning and at the end of the test.	99
4.13. Decrease of the evaporation mass blowing rate in time.	100
4.14. Parametric study on the thermal conductivity of the material.	102
4.15. Study on the empirical viscosity models.	103
4.16. Parametric study on the mushy temperature range.	104
4.17. In-depth material temperature along the centerline.	105

4.18. Surface and core temperature for the heating and cooling period of the experiment.	106
4.19. Heat of ablation at the stagnation point in time.	107
4.20. Average aerodynamic forces in time around the sphere.	108
4.21. Comparison of two mass removal models.	109
5.1. Radiative processes in participating media.	113
5.2. Doppler, Lorentz and Voigt line shape.	115
5.3. Energy balance in an infinitesimal pencil of rays.	117
5.4. Molecular and continuum processes in the Statistical Narrow-Band (SNB) database.	122
5.5. Illustration of the tangent-slab approximation.	130
5.6. Schematic of experimental setup (not to scale) with diagnostics for meteoroid ablation analysis.	133
5.7. Schematic of the sample and its cork holder.	134
5.8. Snap shots during ordinary chondrite test.	135
5.9. Ordinary chondrite samples for the plasmatron experiment.	136
5.10. Samples after plasma exposure.	136
5.11. Surface Temperature of the H5 sample measured by the two-color pyrometer.	137
5.12. Emission spectra overview of air plasma and cork holder.	138
5.13. Duplication of the Plasmatron test conditions to flight conditions.	141
5.14. Projection of stagnation streamline field using spherical caps with constant properties.	144
5.15. Energy profile along the plasma jet radius.	144
5.16. Contour of the temperature field.	145
5.17. Swelling of the cork holder.	146
5.18. Flow field properties along the stagnation streamline at 6s.	148
5.19. Comparison of the integrated intensity at different locations with the data recorded by the three spectrometers.	149
5.20. Comparison of the simulated intensity with the spectrometer data at a certain location.	150
5.21. Spectral intensity of the individual mechanisms compared with the data recorded by the middle spectrometer at 6s.	151
5.22. Flow field properties along the stagnation streamline at 14s.	153
5.23. Comparison of the integrated intensity at different locations with the data recorded by the three spectrometers.	154
5.24. Comparison of the intensity simulated.	155
5.25. Spectral intensity of the individual mechanisms.	156
6.1. Procedure of the radiation/flow coupling.	160
6.2. Procedure of the radiation/flow/material coupling.	161
6.3. Flow field results along the stagnation streamline of the H5 chondrite.	165
6.4. Flow field results along the stagnation streamline of the iron meteoroid.	169

6.5. Radiative heat flux along the stagnation streamline.	171
6.6. Narrowband spectral intensity of the 1.0 m radius of the H5 chondrite at 50 km altitude.	173
6.7. Narrowband spectral intensity of the 1.0 m radius of the iron meteoroid at 50 km altitude.	174
6.8. Absolute magnitude luminosity of the Lost City bolide.	177
6.9. Flow field results along the stagnation streamline of the Lost City.	178
6.10. Narrowband spectral intensity of the Lost City at 50 km altitude.	179
6.11. Variation of the Lost City mass along the trajectory.	182
6.12. Mass removal rate along the trajectory of the Lost City.	183
6.13. Boundary conditions from the flow to the material solver along the trajectory of the Lost City bolide.	184
6.14. Material molten thickness of the Lost City along the trajectory.	185
6.15. Material temperature of the Lost City.	186
A.1. Comparison of the thermodynamic properties between Roe and Modified Steger-Warming scheme.	204
B.1. Comparison of the analytical and numerical solution for the mesh movement due to surface recession.	206
B.2. Comparison of the analytical and numerical solution for the Stefan problem.	207
C.1. Flow field properties along the stagnation streamline at 6 s.	218
C.2. Comparison of the integrated intensity at different locations with the data recorded by the three spectrometers.	219
C.3. Comparison of the simulated intensity with the spectrometer data at a certain location.	220
C.4. Verification of the narrowband properties of the filtered spectral intensity.	221

List of Tables

1.1. Worldwide observation networks	8
1.2. Comparison of recent meteorite ablation test campaigns in different high-enthalpy facilities	13
1.3. Description of the research milestone, general assumptions and input/output the models in each chapter.	17
2.1. Gaseous species used in Chapter 2	46
3.1. Major oxides present in an H5 chondrite in weight percentage.	57
3.2. Evaporation parameters	68
4.1. Gaseous species used in Chapter 4.	96
5.1. Black equivalent line widths for non-uniform paths using the Lindquist-Simmons approximation.	124
5.2. Characteristics of the El Hammami H5 ordinary chondrite . . .	134
5.3. Major species chemical composition before the experiments . .	135
5.4. Overview of Plasmatron results for condition (1)	135
5.5. Plasmatron test conditions	140
5.6. Gaseous species used to simulate the plasmatron experiment . .	146
6.1. Gaseous species used in Chapter 6.	159
6.2. Parameters concerning the SEB and SMB on the H5 chondrite.	167
6.3. Parameters concerning the SEB and SMB from the iron meteoroid.	170
6.4. Total intensity and absolute light magnitude obtained from the H5 chondrite.	172
6.5. Total intensity and absolute light magnitude obtained from the iron meteoroid.	175
6.6. Luminous and heat transfer coefficient obtained from the H5 chondrite and the iron meteoroid.	176
6.7. Parameters concerning the SEB and SMB on the Lost City. . .	181
A.1. Arrhenius parameters for the gas-phase chemical reactions. . .	199
A.2. Parameters of the Lennard-Jones potential for neutral-neutral interaction.	201
A.3. Equilibrium vapor pressure fit.	202
C.1. Radiative mechanisms in the High Temperature Gas Radiation (HTGR) database.	211

Nomenclature

Symbols with multiple definitions should be clear from the context in which they are used.

Constants

c	Speed of light	$299\,792\,458\text{ m s}^{-1}$
h	Planck's constant	$6.626\,070\,04 \times 10^{-34}\text{ J s}$
k_B	Boltzmann constant	$1.380\,649 \times 10^{-23}\text{ J K}^{-1}$
N_A	Avogadro number	$6.022\,140\,76 \times 10^{23}\text{ mol}^{-1}$
\mathcal{R}	universal gas constant, $\mathcal{R} = k_B N_A$	$8.314\text{ J K}^{-1}\text{ mol}^{-1}$
σ	Stefan-Boltzmann constant	$5.670\,374\,419 \times 10^{-8}\text{ W m}^{-2}\text{ K}^{-4}$
ϵ_0	Vacuum permittivity	$8.854\,187\,812\,8 \times 10^{-12}\text{ F m}^{-1}$

Roman Symbols

a	speed of sound	m s^{-1}
a	degeneracy of a particular energy state	—
A_{ul}^{bb}	spontaneous emission Einstein coefficient of bound-bound transition ul	s^{-1}
B_{lu}^{bb}	absorption Einstein coefficient of bound-bound transition ul	$\text{m}^2\text{ J}^{-1}\text{ s}^{-1}$
B_{ul}^{bb}	induced emission Einstein coefficient of bound-bound transition ul	$\text{m}^2\text{ J}^{-1}\text{ s}^{-1}$
A_{jk}^{bf}	spontaneous emission rate of bound-free transition	s^{-1}
B_i^{bf}	absorption rate of bound-free transition	$\text{m}^2\text{ J}^{-1}\text{ s}^{-1}$
B_{jk}^{bf}	induced emission rate of bound-free transition	$\text{m}^2\text{ J}^{-1}\text{ s}^{-1}$
c_p	specific heat at constant pressure	$\text{J kg}^{-1}\text{ K}^{-1}$

c_v	specific heat at constant volume	$\text{J kg}^{-1} \text{K}^{-1}$
\mathcal{D}	binary diffusion coefficient	$\text{m}^2 \text{s}^{-1}$
E	energy of a particle or energy level	J or cm^{-1}
\mathbf{E}	electric field	V m^{-1}
f^{ab}	absorption spectral line profile	cm
f^{ie}	induced emission spectral line profile	cm
f^{se}	spontaneous emission spectral line profile	cm
u_σ	radiative energy density	J cm m^{-3}
f	oscillator strength	—
g	relative velocity between two particles	m s^{-1}
h	enthalpy	J kg^{-1}
\mathcal{H}	set of heavy species	—
\mathcal{A}	set of atoms	—
\mathcal{M}	set of molecules	—
\mathcal{G}	set of gas species	—
\mathcal{S}	set of all species	—
\mathcal{C}	set of condensed species	—
$\bar{\mathbf{I}}$	identity matrix	—
I	radiant intensity	$\text{W cm m}^{-2} \text{sr}^{-1}$
I^b	Planck function	$\text{W cm m}^{-2} \text{sr}^{-1}$
\bar{k}	mean absorption coefficient per partial pressure of absorbing species	$\text{m}^{-1} \text{Pa}^{-1}$
M	molecular weight	kg mol^{-1}
m	particle mass	kg
n	number density	m^{-3}
p	pressure	Pa
\mathcal{P}^{rad}	radiative power	W m^{-3}
$\mathcal{P}^{\text{rad,ve}}$	radiative power	W m^{-3}

q	charge	C
\mathbf{q}^{rad}	radiative heat flux	W m^{-2}
Q	partition function	—
\bar{Q}	reduced collision integral	m^2
R	specific gas constant, $R_j = \mathcal{R}/M_j$	$\text{J kg}^{-1} \text{K}^{-1}$
T	temperature	K
\mathbf{u}	hydrodynamic velocity	m s^{-1}
\mathbf{V}	diffusion velocity	m s^{-1}
\bar{W}	mean black equivalent line width	cm^{-1}
x	mole fraction	—
y	mass fraction	—
$\hat{\mathbf{s}}$	unit direction vector	—
$P(S)$	Probability distribution of line intensities	—
M	Mach number	—
L_{heat}	latent heat evaporation	J kg^{-1}
p_{vap}	vapor pressure	Pa
\dot{m}	mass blowing rate	$\text{kg m}^{-2} \text{s}^{-1}$
\mathbf{u}_w	gases blowing velocity	m s^{-1}
\mathbf{u}_Γ	surface recession velocity	m s^{-1}
B'	non-dimensional mass blowing rate	—
f	one particle velocity distribution function	$\text{m}^6 \text{s}^{-3}$
$S_{\infty,i}$	Speed Ratio	—
\mathcal{L}	pressure jump ratio	—
\mathcal{R}	temperature jump ratio	—
\dot{m}_{ablat}	thermochemical ablation source term	$\text{kg m}^{-2} \text{s}^{-1}$
\dot{m}_{vap}	evaporation source term	$\text{kg m}^{-2} \text{s}^{-1}$
T_{solidus}	solidus temperature	K
T_{liquidus}	liquidus temperature	K

T_m	melting temperature	K
k_{solid}	solid thermal conductivity	$\text{W K}^{-1} \text{m}^{-1}$
k_{liquidus}	liquid thermal conductivity	$\text{W K}^{-1} \text{m}^{-1}$
L_m	latent heat fusion	J kg^{-1}
$c_{p,\text{liquid}}$	liquid specific heat at constant pressure	$\text{J kg}^{-1} \text{K}^{-1}$
α_{liquid}	liquid diffusivity	$\text{m}^2 \text{s}^{-1}$
α_{solid}	solid diffusivity	$\text{m}^2 \text{s}^{-1}$
h_{eff}	effective heat of ablation	J kg^{-1}

Greek Symbols

$\bar{\beta}$	line overlap parameter for narrow band	—
χ^{neq}	non-equilibrium coefficient used for bound-free processes	—
ϵ	emittance or emissivity	—
η	emission coefficient	$\text{W cm m}^{-3} \text{sr}^{-1}$
μ	shear viscosity	$\text{kg m}^{-1} \text{s}^{-1}$
κ	absorption coefficient	m^{-1}
λ	thermal conductivity	$\text{W K}^{-1} \text{m}^{-1}$
μ	reduced mass of two particles	kg
$\bar{\tau}$	viscous stress tensor	Pa
$\dot{\omega}^{\text{chem}}$	mass production rate due to chemical reactions	$\text{kg m}^{-3} \text{s}^{-1}$
$\dot{\omega}^{\text{rad}}$	mass production rate due to photochemistry	$\text{kg m}^{-3} \text{s}^{-1}$
Ω^{CV}	chemical-vibrational energy coupling term	W m^{-3}
Ω^{CE}	chemical-electronic-electron energy coupling term	W m^{-3}
Ω^{ET}	heavy-electron translational energy relaxation rate	W m^{-3}
Ω^{I}	thermal energy lost provided by electrons during electron impact reactions	W m^{-3}
Ω^{VT}	vibrational-translational energy relaxation rate	W m^{-3}
ρ	mass density	kg m^{-3}

σ	wavenumber	cm^{-1}
τ	transmissivity	—
θ^B	non-Boltzmann equilibrium parameter	—
θ^V	characteristic vibrational temperature	K
θ^R	characteristic rotational temperature	K
τ	radiative lifetime	s
λ_D	Debye length	m
$\dot{\Omega}_{\text{surf}}$	surface source term	$\text{kg m}^{-2} \text{s}^{-1}$
ξ	particle velocity vector	m s^{-1}
Ω	solid angle	sr
α_{evap}	evaporation coefficient	—
α_{cond}	condensation coefficient	—

Acronyms

CFD	Computational Fluid Dynamics
CFL	Courant-Friedrichs-Lewy
FV	Finite Volume
GSI	Gas-Surface Interaction
HSNB	Hybrid Statistical Narrow-Band
HTGR	High Temperature Gas Radiation
LBL	Line-By-Line
LHTS	Local Heat Transfer Simulation
LTE	Local Thermodynamic Equilibrium
MUSCL	Monotone Upstream Centered Schemes for Conservation Laws
ODE	Ordinary Differential Equation
QSS	Quasi-Steady-State
CCD	Charge-Coupled Device
OES	Optical Emission Spectroscopy

IMCC	Ideal Mixing of Complex Components
PDE	Partial Differential Equation
MOL	Method-Of-Lines
BE	Backward-Euler
FDS	Flux Difference Splitting
NEO	Near-Earth Object
UQ	Uncertainty Quantification
ML	Machine Learning
RRHO	Rigid-Rotor Harmonic-Oscillator
RTE	Radiative Transport Equation
SNB	Statistical Narrow-Band
STS	State-To-State
TOPBASE	The Opacity Project atomic database
TPS	Thermal Protection System
VDF	Velocity Distrution Function
PATO	Porous-material Analysis Toolbox based on OpenFOAM
ATAP	Asteroid Threat Assessment Project
FRIPON	Fireball Recovery and Planetary InterPlanetary Observation Network
BRAMS	Belgian RAdio Meteor Stations
SEB	Surface Energy Balance
SMB	Surface Mass Balance
ESMB	Elemental Surface Mass Balance
DSMC	Direct Simulation Monte Carlo
VKI	von Karman Institute for fluid dynamics
IRS	Institut für Raumfahrtsysteme
UV	UltraViolet
VIS	Visible

IR	InfraRed
VUV	Vacuum-Ultraviolet
MD	Molecular Dynamics
KT	Kinetic Theory

CHAPTER 1

Introduction

I would rather be ashes than dust! I would rather that my spark should burn out in a brilliant blaze than it should be stifled by dry-rot. I would rather be a superb meteor, every atom of me in magnificent glow, than a sleepy and permanent planet. The function of man is to live, not to exist. I shall not waste my days trying to prolong them. I shall use my time.

— Jack London

1.1. Meteoroids and the meteor phenomenon

Fun fact 1

In 1956, Patterson [203] determined Earth's age (4.55 ± 0.07 billion years) with a high-degree of accuracy through isotopic analysis ($\text{Pb}^{207}/\text{Pb}^{206}$) of several meteorites, including the Canyon Diablo meteorite.

Carl Sagan once said, “...because the cosmos is also within us. We’re made of star-stuff”. What does he mean by that? In his television show, *Cosmos*, he explains that the necessary components for the existence of life can also be found in stars or any other cosmic body.

The desire to understand the origin of life has motivated generations of researchers from different fields. A community of passionate astrophysics, astronomers, planetary scientists, geochemists, and more recently, engineers devote themselves to study the meteor phenomenon in a quest for answers. Meteoroids provide our primary source of extraterrestrial materials from the various nebular and planetary environments of the Solar System and beyond. These naturally delivered samples, bring 50 to 100 tons of material every day [83]. In the early stages of our planet, the meteor influx was 100 times higher than today [124]. The presence of organic components (highly polymerized carbon) in asteroids and comets is well known from meteorite laboratory analyses. Exciting research aims to comprehend the delivery of these carbonates compounds

from meteoroid entry [152] and how they react with the atmosphere during the harsh entry conditions [153].

The interest in meteoroid entry goes beyond the origin of life. A better understanding of such phenomena is essential in a variety of fields such as aeronomy, astronomy, geophysics, and planetology. Space agencies launched sample-return missions to asteroids such as Hayabusa II [261], and to comets such as 67P/Churyumov-Gerasimenko [249] to collect relevant data to their formation and composition. The complexity and operational costs of these missions motivate scientist to pursue the study of the meteor phenomenon. Tracing a large number of meteoroid orbits in the Solar System allows clarifying the association of meteoroids with asteroids, comets, or the zodiacal cloud.

Most meteor showers are remnants of comets traveling the solar system [124, 258]. A comet can be seen as a rubble pile bonded by an ice matrix. As the comet travels closer to the sun, the ice matrix sublimates, leading to a trail of gaseous water and solid particles. When Earth's orbit crosses this stream of particles, they create a fantastic show if the weather allows for it. The most famous showers are the Perseids and the Leonids; the former occurs every year between July and August whereas the latter takes place around November.

The meteor showers pose no threat since most of the delivered material ablates in the atmosphere. On the other hand, fireballs and bolides are larger bodies that might survive the entry and can become potential hazards [253]. These bodies mostly derive from the asteroid belt between Mars and Jupiter. The collision between asteroids within this belt leads to smaller fragments escaping the initial orbit, and if they get closer to Earth, they are designated as a Near-Earth Object (NEO). When these large meteoroids enter Earth's atmosphere, they undergo melting and evaporation. Their motion and rotation in the atmosphere is somehow random and depends on how they entered in the first place. Figure (1.1) exemplifies possible orientations that the meteoroids might undergo during entry, based on shape of the meteorites. For instance, in Fig. (1.1) the Dhofar 182 meteorite was discovered with a cone shape showing flow structures due to the material melting. Another case is an iron meteorite with a shield shape found in Chile.

Meteorites are one of the reasons re-entry capsules have a sphere-cone shape. Robert H. Goddard was a pioneer in aerospace engineering, who envisioned space exploration and the space vehicle design. Figure (1.2) shows an excerpt from the original report, written by Goddard [95] disclosing his ideas on the different steps for a successful space mission. The vision of this pioneer is an excellent example of how nature inspires engineers.

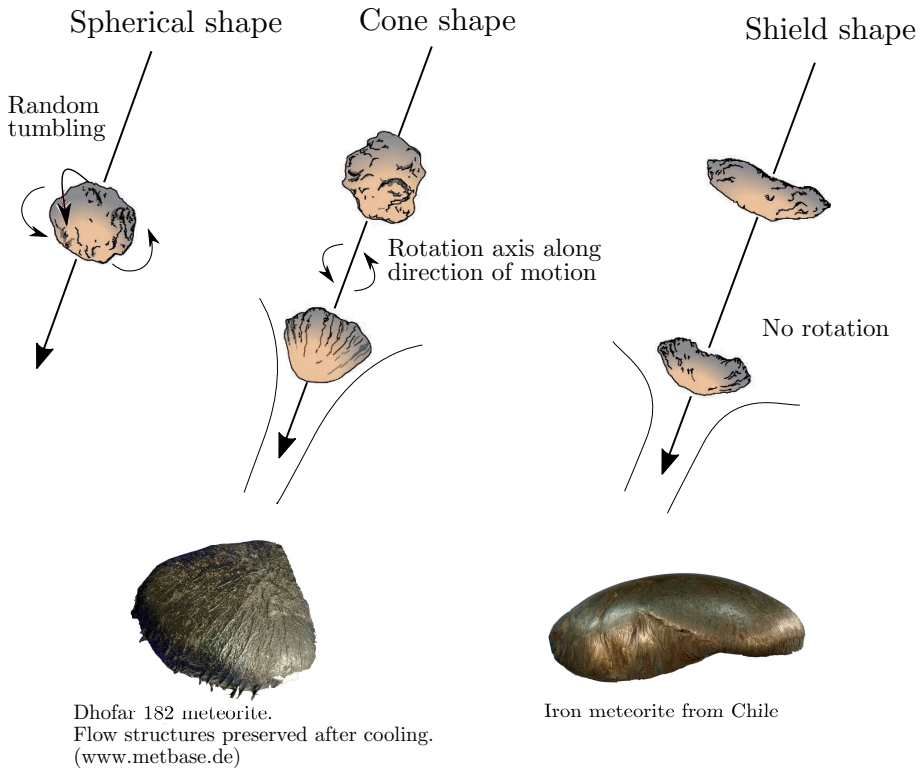


Figure 1.1.: Illustration of meteoroids and their shape during entry. This figure has been reproduced from Norton and Chitwood [185].

1.2. Detection and observation of meteoroids

Fun fact 2

In Australia, the Yarrabubba impact structure was established by Erickson et al. [78] as the oldest asteroid impact on Earth. With almost 2.2 billion years, the impact occurred during the ice age, and the study highlights that it produced enough H_2O vapor to modify Earth's climate.

Humankind has been witnessing meteor showers for centuries, and for a long time, mythological stories were attributed to explain these events. The Leonid shower in 1833¹ was so magnificent that it drove the scientific interest towards meteors and encouraged systematic observations. Since then, amateur and professional astronomers have joined forces to build a worldwide network, enabling

¹<https://blog.nationalgeographic.org/2014/08/30/1833-meteor-storm-started-citizen-science/>

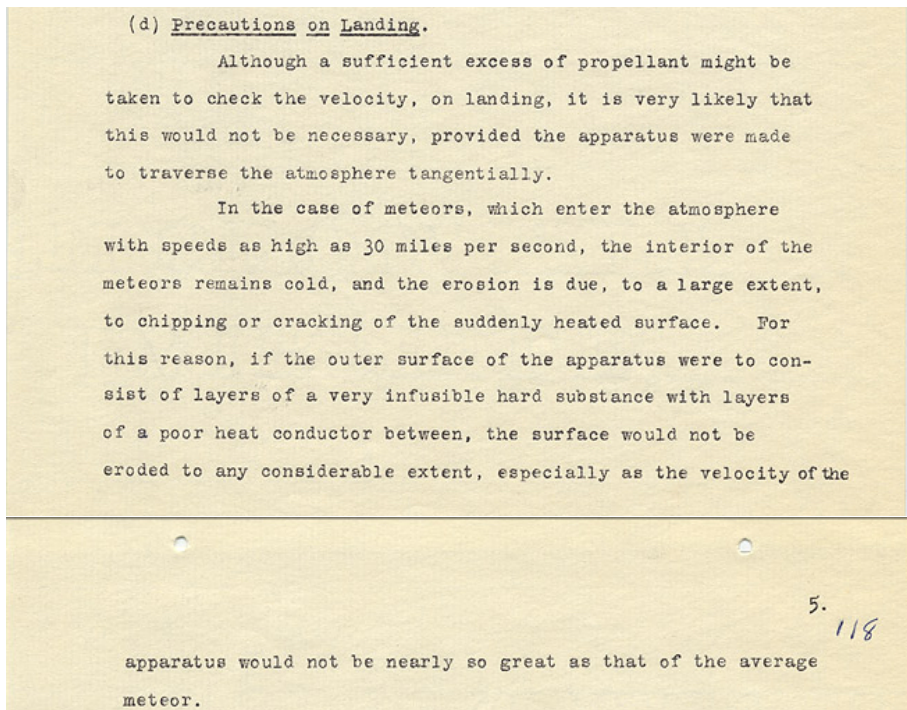


Figure 1.2.: Excerpt of Goddard [95] original report on space exploration. In this excerpt, he points out that the spacecraft heat shield should be inspired on meteoroids since they can survive entry conditions.

a share of knowledge. Table (1.1) shows some of these networks among dozens more.

Meteors are fast objects that make them hard to observe *in situ* with spaceborne instruments or remote sensing techniques. Astronomers employ detection techniques such as video/photographic/spectral or radar/radio observations to track them, allowing them to estimate the meteoroid influx [34, 119, 269]. The former type of observations is used to measure the light magnitude and spectral features, while the latter is sensitive to the ionization of evaporated particles forming the meteor.

We recall that occasionally more considerable objects (bolides and superbolides) enter the Earth's atmosphere, sometimes posing a threat to human populations [35, 43]. Among the daily material delivered into our planet, the Chelyabinsk event (15 February 2013) [43] renewed awareness of potential hazards. This event motivated the planning of incoming asteroids deflection and mitigation strategies [211]. Shortly after the incident, NASA's planetary defense coordination office created the Asteroid Threat Assessment Project (ATAP) to provide to policy and decision makers accurate predictions of impact effects in the event of a significant asteroid encounter. Figure (1.3) shows

the detected fireballs/bolides since 1988 and their respective impact energy.

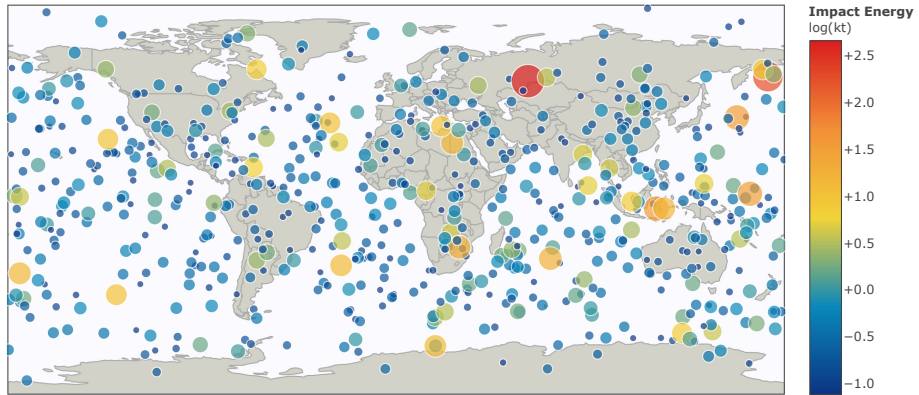


Figure 1.3.: Fireballs reported by USA government sensors from Apr 1988 – Mar 2020. The large impact in Russia represents the Chelyabinsk superbolide event on 15 February 2013. This figure was taken from Chamberlain [58].

Within the several worldwide networks, only three will be mentioned herein, more specifically as examples:

- **Belgian Radio Meteor Stations (BRAMS):** Recent efforts have been made by the Belgian Institute for Space Aeronomy (BIRA-IASB) to predict the velocity and trajectory of meteoroids. The meteor detection is done employing an innovative technique based on the radio waves reflection due to the electron concentration [166]. The Belgian Radio Meteor Stations [18] experiment consists of a series of receivers spread all over Belgium to collect and standardize the meteor observations. One of the main objectives of these projects is the computation of the meteoroid flux densities. However, this quantity is hardly quantifiable from the lone radio observation, and it is necessary to rely on comparison with numerical models to estimate it. From a modeling perspective, BRAMS requires an accurate description of the electrons in the trail, which can only be modeled with a high-fidelity flow field calculation.
- **Fireball Recovery and Planetary InterPlanetary Observation Network (FRIPON):** The European project Fireball Recovery and Planetary InterPlanetary Observation Network [90] detects more significant objects with a set of high-definition cameras and spectrometers distributed all over France. One of the objectives is to recover meteorites. The network of cameras enables them to reconstruct the trajectory, and from the spectrometer results, they are capable of quantifying the luminosity produced during a bolide entry. The latter can be linked to the radiation emitted from the ablation of the meteor. Therefore, FRIPON needs accurate radiation models, which can be further related to the luminosity measurements.

- **Asteroid Threat Assessment Project (ATAP):** Since 2014, there has been a growing interest from ATAP to better understand the meteor phenomenon for planetary defense purposes. More specifically, the program's main scope is to understand and quantify the risk of airburst/impact of potentially hazardous asteroids smaller than 0.5 km. More accurate ablation models will aid in understanding whether a bolide with a specific trajectory and size presents a potential hazard to the community. ATAP demands accurate ablation modes (evaporation, melt removal, fragmentation) to assess whether the bolide is a potential threat.

The conventional meteor physics equations (single-body theory), rely on a zero-dimensional method and lack a precise treatment of the particle interaction with the atmosphere from the fluid dynamics point of view. Moreover, the study of the material response (melting and possible material removal) is often neglected. The single-body theory includes the following system of Ordinary Differential Equation (ODE)'s [265],

$$\frac{dV}{dt} = -\Gamma V^2 \frac{3\rho_a}{4\rho_m R}, \quad (1.1a)$$

$$\frac{dm}{dt} = \alpha_{\text{evap}} p_{\text{vap}} S \sqrt{\frac{M}{2\pi k_B T_w}}, \quad (1.1b)$$

$$\frac{dH}{dt} = -V \cos \gamma, \quad (1.1c)$$

$$\frac{1}{2}\pi R^2 V^3 \rho_a C_h = 4\pi R^2 \epsilon \sigma (T_w^4 - T_{\text{env}}^4) + \frac{4}{3}\pi R^3 \rho_m c_p \frac{dT_w}{dt} + L_{\text{heat}} \frac{dm}{dt} \quad (1.1d)$$

$$I = -\tau \left(\frac{V^2}{2} \frac{dm}{dt} + mV \frac{dV}{dt} \right). \quad (1.1e)$$

The first equation corresponds to the deceleration of the object where V is the velocity, t the time, Γ the drag coefficient, R the body radius, ρ_a and ρ_m are the density of the atmosphere and material, respectively. The second equation corresponds to the mass loss derived from the Knudsen-Langmuir law. Quantity m is the mass of the object, α_{evap} the evaporation coefficient, p_{vap} the equilibrium vapor pressure, S the particle surface area, M the molecular weight of the gaseous vapor, k_B the Boltzmann constant, and T_w the surface temperature. The third equation allows us to compute the trajectory altitude H in function of time, where γ is the entry angle to the zenith. The fourth equation is a surface energy balance to estimate T_w . Quantity C_h is the heat transfer coefficient, T_{env} the temperature of the surrounding environment, c_p the bulk material specific heat, and L_{heat} the latent heat of vaporization. The final equation corresponds to the luminosity I , where τ is the luminous efficiency. The meteoroid mass along the trajectory can be derived by Eq. (1.1a) or Eq. (1.1e) since the deceleration and the luminosity result from observations. The former derivation is called dynamic mass, while the latter is known as photographic mass.

As a simple example, we use Eqs. (1.1a) to (1.1d) to estimate the trajectory

of three meteoroids with an initial radius of 0.1, 1 and 10 cm. Figure (1.4) shows the trajectory with the corresponding Knudsen number Kn contour and the above detection networks. The Knudsen number is defined as the ratio of the mean-free path based on the free-stream conditions and the body radius. One can see that the objects observed by BRAMS are close to the free-molecular regime ($Kn > 10$). The meteoroids relevant for the FRIPON and ATAP projects are in the transition and continuum regimes.

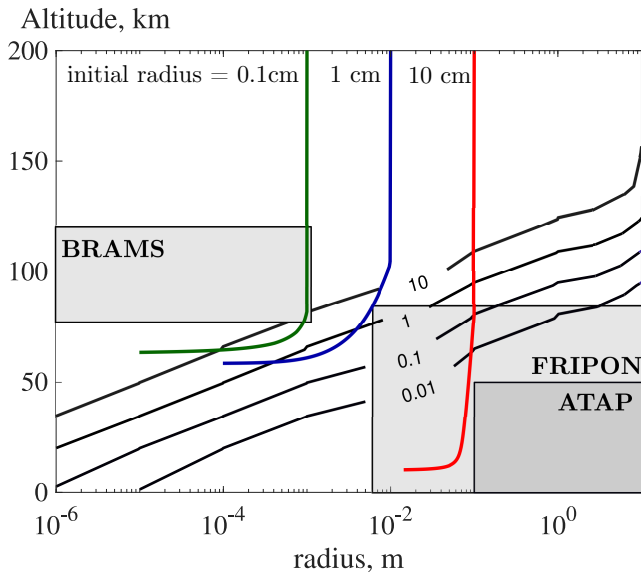


Figure 1.4.: Meteoroid trajectory estimated with the meteor physics equations. The contour represents the Knudsen number ($Kn = 0.01, 0.1, 1, 10$) based on the free-stream conditions. The initial velocity is $V_\infty = 12 \text{ km s}^{-1}$ for all trajectories.

1.3. State-of-the-art of the meteor physics

Fun fact 3

Furukawa et al. [91] found the presence of extraterrestrial ribose and other sugars on meteorites. Ribose is an essential building block of RNA, thus, the formation of life. This study strengthens the theory that meteoroids might have contributed to the origin of life on Earth. That is what we call a sweet meteorite!

Table 1.1.: Worldwide observation networks

Network	Country	link
<i>video/photographic/spectral observations</i>		
ASGARD All-Sky Camera Network	Canada	1
European Fireball Network	Czech Republic	2
Fireball Recovery and InterPlanetary Observation Network (FRIPON)	France	3
Croatian Meteor Network (CMN)	Croatia	4
Desert Fireball Network	Australia	5
Canary Islands Long-Baseline Observatory (CILBO)	Spain (ESA)	6
Cameras for Allsky Meteor Surveillance (CAMS)	U.S.A./BeNeLux	7
NASA All Sky Fireball Network	U.S.A.	8
Polish Fireball Network (PFN)	Poland	9
SPANish Meteor Network (SPMN)	Spain	10
IMO Video Meteor Network	Germany	11
SonotaCo	Japan	12
BRAZilian Meteor Observation Network (BRAMON)	Brazil	13
Finnish Fireball Network	Finland	
<i>radar/radio observations</i>		
The Canadian Meteor Orbit Radar (CMOR)	Canada	14
Belgian RADio Meteor Stations (BRAMS)	Belgium	15
Multi-static Multi-frequency Agile Radar for Investigation of the Atmosphere (MMARIA)	Germany	

References. (1) <http://aquarid.physics.uwo.ca/research/allsky/overview.html>, (2) https://en.wikipedia.org/wiki/European_Fireball_Network, (3) <https://www.fripon.org/?lang=en>, (4) <http://zbornik.rgn.hr>, (5) <https://dfn.gfo.rocks>, (6) <https://www.cosmos.esa.int/web/meteor/cilbo>, (7) <http://cams.seti.org>, (8) <https://fireballs.ndc.nasa.gov>, (9) <https://www.pkim.org>, (10) <http://www.spmn.uji.es/ENG/presentation.html>, (11) <https://www.imonet.org>, (12) <https://sonotaco.jp>, (13) <http://www.bramonmeteor.org/bramon/en/>, (14) http://aquarid.physics.uwo.ca/research/radar/cmor_intro.html (15) <https://brams.aeronomie.be>

1.3.1. Meteor modeling

Because even large meteoroids typically lose a significant part of their mass due to ablation during the atmospheric passage, accurate physical models for these phenomena are requisite to predictions of the ensuing consequences on the ground due to the arrival of the remaining object.

The current models of meteoroid ablation often rely on the single body theory [169] and recently have been extended to include fragmentation [45, 103, 271]. These models seek to draw improved inference about the size of the meteoroids from observations and to assess the ground risk of the bolide fragmentation [270]. The major drawback of the single body theory is that all the physics is lumped into the coefficients. As mentioned above, this theory relies on a system of ODE's that cannot simulate in detail the hypersonic flow field formed during meteor entry. An accurate description of this field allows us to gain insight into chemical species produced during the event, its impact on the luminosity produced by flow radiation, and a better description of the thermal ablation of the meteoroid.

Another approach involves detailed computational simulations of the phenomena. Although these simulations are computationally expensive, they provide the flow's physical features, that the single body theory cannot.

Single-body theory

Although there exists a worldwide effort to detect meteors [34, 119, 143, 269], the meteoroid mass entering planet Earth is not certain. This uncertainty is greatly affected by the inaccuracy of the meteor physics equations used to derive composition, mass, and trajectory parameters of each incoming object. The system of ODE's in Eq. (1.1) go back to the work of Öpik [280] from a time during which the computational resources to solve such a phenomenon were limited; today, this remains a colossal task. The heuristic coefficients, such as the heat-transfer and luminous efficiency (part of the kinetic energy which is transformed into light), are often correlated to meteor observations [169].

Many authors have previously integrated photographic observations with an extension of the single body theory, including fragmentation [10], to derive the mass and the trajectory of meteoroids by obtaining the best fit for heuristic coefficients. For example, Gritsevich and Koschny [101] combined photometric with dynamic measurements from several observations to constrain the luminous efficiency. Gritsevich [100], Gritsevich et al. [102], Sansom et al. [222] constrained all the unknown coefficients shown in Eq. (1.1) into two parameters α (ballistic coefficient) and β (mass loss) retrieved by a best fit with observations using a least-squares method. The α - β method categorize the meteor events into unlikely, possible, and likely falls without additional assumptions on coefficients present in Eq. (1.1). Sansom et al. [220] employed an Extended Kalman Filter (EKF) to determine trajectory parameters from observations, permitting the derivation of the initial and final mass of the objects in an automated manner. Sansom et al. [221] improved their previous methodology using an Unscented Kalman Filter (U FK) and an Interacting Multiple Model

(IMM), enabling then to consider nonlinearity of the meteor physics equations due to fragmentation.

Among several observations, the Lost City bolide [170] is one of the first well-documented events, whereby light magnitude and trajectory were measured. This bolide serves as a reference to infer heuristic coefficients, and ReVelle and Rajan [214] sought the opportunity to deduce the luminous efficiency and photographic mass from these observations, disregarding fragmentation. Years later, Ceplecha [53] used the same observations and improved the inference of the luminous efficiency and the photographic mass by including a gross-fragmentation model. Ceplecha and ReVelle [54] generalized the meaning of luminous efficiency as a function of mass, velocity, and normalized air density. These authors obtained this intrinsic luminous efficiency by calibrating their fragmentation model with the Lost City bolide's best observational fit. This work represented a breakthrough in the definition of the luminous efficiency because it is typically assumed that this parameter depends only on the velocity [259]. More recently, Subasinghe and Campbell-Brown [243] inferred the luminous efficiency from 15 meteoroids and showed that this parameter does not depend only on the velocity.

The meteoroid composition dramatically affects the intensity of the meteor luminosity. Due to spectral measurements of several meteors [37, 158, 159], astronomers can now catalog the composition of different meteor showers and infer their origin [263]. Moreover, Borovička and Betlem [32] derived the luminous efficiency from the classical luminosity equation by analyzing the spectra of two meteors from the Perseid shower. From the spectra, Borovička and Betlem [32] and Borovička and Berezhnoy [31] could identify the temperature of each chemical species assuming radiative equilibrium conditions, distinguishing two regions; a vapor layer region including species with a temperature below 5000 K (mostly evaporation components also recognized as the main spectrum), and the shock layer region where the species have temperatures above 10000 K (known as the second spectrum containing mainly N and O from the shock layer).

One significant drawback of the meteor physics equations are the lack of detailed physico-chemical modeling, which is fundamental to simulate hypersonic entries. For example, these equations do not account for the thermodynamic and chemical non-equilibrium across the shock and boundary layer [94]. Moreover, the radiative effects on the shock layer are neither considered. Ceplecha et al. [56] mentions this lack of fidelity by showing some trajectories that cannot be explained with these equations alone. Furthermore, [54] suggest that the meteor physics equations may require improvements. The entry of meteoroids is complex and challenging to model because it involves numerous physical phenomena in the shock layer and the multiphase physics that the material endures, involving melting and evaporation. Moreover, during the flight, the meteoroid spans a wide range of flow conditions, from free-molecular and rarefied effects to the continuum regime. For smaller meteoroids at high altitude, the Kn number is high, and the flow is under rarefied conditions. At these conditions, the Navier-Stokes equations are no longer valid and one can solve

the Boltzmann equation with numerical methods such as Direct Simulation Monte Carlo (DSMC). The interested reader is directed to the works of Boyd [40], Jenniskens [123]. Recently, Bariselli [16], Bariselli et al. [17] developed an ablation model for rarefied flows with application to meteoroid entry.

Computational simulations of meteors

In the last twenty years, several authors have been engaged in developing models to include detailed flow, radiation, and ablation coupling effects in the continuum regime. These models encompass two types of approaches: The first concerns inviscid simulations that are fast and relatively easy to solve, but the dissipation terms in the boundary layer are neglected, which influences the evaporation boundary condition. The second involves viscous simulations that resolve the boundary layer but, in turn, are harder to solve and are computationally expensive for multidimensional cases. Park [199, 200, 201] performed coupled ablation radiation simulations assuming an inviscid flow field in thermal-equilibrium conditions. The incoming air layer and ablation layer divide the shock layer into two flow regions, and approximated methods are used to simulate them. Moreover, Park [199, 200, 201] modeled the radiative transfer with the Rosseland approximation, which is only valid for optically thick systems. Golub et al. [96] derived heat-transfer and luminous efficiency, assuming an inviscid flow including thermal non-equilibrium effects. These authors modeled the ablation products as a 1D cylindrical piston plunging into a quasi-stationary hypersonic flow, assuming no mixing between the two layers. Snettsov et al. [246] computed the radiative field of Chelyabinsk using the Rosseland approximation. The body was treated as a liquid-like strengthless object [235] due to a lack of solidity at low altitude. Shuvalov and Artemieva [235] computed the effects of radiation felt on Earth's surface by solving the radiative transfer equation assuming an inviscid, thermal-equilibrium flow around the body.

Silber et al. [236] solved the Navier-Stokes equations for the flow field via Computational Fluid Dynamics method. These authors studied the chemical kinetics effect on the trail of a nonablative small meteoroid at high altitude. Although the objective of their work was to study reaction rates during a meteoroid entry, it lacks fundamental thermodynamic and transport properties at high temperatures, which might result in an erroneous interpretation of the chemical kinetics. To date, Johnston et al. [130] showed one of the highest-fidelity models for flow, ablation, and radiation coupling for meteoroid entries. In that work, the authors derived heat-transfer coefficients for Chelyabinsk-type bolides; even though they use state-of-the-art physico-chemical models to treat hypersonic flows, the surface evaporation is in equilibrium. The equilibrium boundary condition might be a strong assumption for these flow conditions because non-equilibrium effects become more predominant for massive ablation rates. Moreover, with their boundary condition, it is impossible to solve the evaporation of volatiles. The extraction of the meteoroid physical parameters from observations requires strong assumptions on the flow physics, such as

local thermo-chemical equilibrium conditions. A more systematic approach is to compare the observations with 3D computational fluid dynamic (CFD) simulations, but these are computationally expensive for the flow in question.

1.3.2. Ground experiments of meteorites

Ground experiments provide the opportunity to look at the meteor phenomenon in detail, allowing us to focus on the gas-surface interaction for well-defined flight conditions and material properties, which remain poorly understood.

The first experiments in an Arcjet facility at NASA Ames were performed by Shepard et al. [233], who compared the luminous intensity of meteorite analogs such as gabbro and basalt with stony meteorites. The authors observed similar intensities from artificial and natural meteorites proposing the use of artificial samples to understand the ablation of asteroidal meteors better. Bronshten [42] conducted experiments on samples of stony and iron meteorites in an inductively-coupled plasma facility. After an initial stage during which the sample warms up, softens, and liquefies, the sample started to ablate. From the observations, it was possible to infer that melting and mechanical disintegration were probably dominant at altitudes lower than 100 km, with the direct vaporization of material dominating only above 120 km. As the author admitted, however, it is questionable that the mentioned experiments had been able to replicate the extreme environment taking place during hypervelocity atmospheric entry, with realistic surface temperatures and heat fluxes.

More recently, three series of experiments were performed, making use of improved measurement and inspection techniques. Loehle et al. [151] tested an H4 chondrite and analog samples at the Institut für Raumfahrtsysteme (IRS) with the objective of gaining a better understanding of the ablation process and associated spectral features. Cylindrical shape samples were exposed to high heat flux until complete disintegration. The spectra measured by Echelle spectroscopy gave a good comparison with flight data.

Helber et al. [113] tested a sample of the El Hammami H5 ordinary chondrite at the von Karman Institute for fluid dynamics (VKI) in the Plasmatron facility to better understand the gas-surface interaction processes occurring during a meteoroid entry. The outcome of this experiment allowed for the development of thermochemical ablation models and understanding of the chemical processes at the surface, as shown in Pittarello et al. [206]. More details regarding this experiment are given in Section 5.3.

In the work of Agrawal et al. [2], the extreme entry conditions experienced by the Chelyabinsk meteorite during its entry were reproduced. Two samples of the H5 Tamdakht chondrite and one iron meteorite, all carved into a spherical cone shape, were exposed for few seconds to a plasma flow in the Arcjet Interaction Heating Facility of NASA Ames Research Center. The chondrite resisted for 2s while the iron meteorite was destroyed after 2.5s. For all samples, substantial removal of the melt by shearing effects was observed, and values for the effective heat of ablation were derived, leading to an improvement of the current models. Table (1.2) shows the test conditions of the latest test

campaigns done on meteorites in high-enthalpy facilities.

Table 1.2.: Comparison of recent meteorite ablation test campaigns in different high-enthalpy facilities. The experimental quantities p_s , \dot{q}_{cw} and h_e are the stagnation pressure and heat flux and boundary-layer edge enthalpy, respectively.

Facility	p_s hPa	\dot{q}_{cw} MW m ⁻²	h_e MJ kg ⁻¹	Configuration	Reference
VKI Plasmatron	15-200	1-3	24-54	Stagnation point	[113]
IRSArcjet	24	16	70	Cylindrical sample	[151]
Ames Arcjet	14	40	20	Full axisymmetric body	[2]

In parallel to the experiments in high-enthalpy facilities, intensive evaporation has been studied by directing a high-power laser beam towards the surface of meteorite test samples. This experiment reproduces the strong heating rate on the surface upon the entry of a bolide at high velocities. Milley et al. [175] investigated the production of light during meteoroid ablation to better estimate the luminosity efficiency. The expanding vapor was observed by CCD detectors used for meteor observations. The spectral features contained mainly neutral atoms, and light production from the vapor was observed even without high-speed collisions with air constituents. The same technique was used to study the material's thermo-chemical behavior when subjected to high heat fluxes [272]. Ferus et al. [81] developed a methodology to analyze and interpret real-time plasma spectra from meteor detections using a calibration-free method. The method was validated by comparison with laboratory experiments in which measurements, performed by using laser-induced breakdown spectroscopic (LIBS), allowed quantitative determination of elemental compositions and temperatures in Perseid and Leonid events.

In the work of Bones et al. [29], a new facility (The Meteoric Ablation Simulator) was presented to study differential evaporation in interplanetary dust particles ($< 50 \mu\text{m}$) in free-molecular flow. The authors could produce a controlled heating rate to represent entry conditions and to measure impact ionization coefficients for the interpretation of radio and radar observations. Martín et al. [167] observed differential ablation effects showing that sodium is the major contributor for radio observation due to its high volatility and low ionization energy.

1.4. Objectives and outline of the thesis

Fun fact 4

For several years, researchers have been debating if the dinosaurs' extinction was owed to the impact of an asteroid or climate change caused

by volcanic emissions. Hull et al. [120] shows that the cause of the end-Cretaceous mass extinction was due to a massive impact. Not so fun for dinosaurs in the end.

From the state-of-the-art review, the inadequacy of the models employed nowadays to understand the flow field details of the meteor phenomenon is evident. These models are commonly employed to access the atmosphere's energy deposition, estimate the electron concentration, study the luminosity of meteors, and many other purposes. The coefficients of the single-body theory are hard to generalize due to a broad spectrum of entry conditions, e.g., velocity, altitude, size, and composition. Besides, the interest in detailed simulations is new, and the models still require significant development to cope with the multi-physics associated with the meteor phenomenon.

This thesis aims to develop models able to describe the multi-physics phenomena of a meteoroid entry. We focus on the different flow aspects – high-temperature effects and radiation – and material analysis – evaporation and shear ablation – within the continuum regime. These models can be applied to derive flow features of fireballs and to study bolide ablation. The underlying objective is to develop comprehensive models that can be applied to interpret meteor observations and assess the incoming object's risk. Only a single body is studied here, and fragmentation is beyond the scope of this work.

The specific objectives of this thesis are:

Obj.1 Development of the models to study the meteoroid thermal ablation in the continuum regime:

- a) Derivation of **evaporation** and **melting models** to study the material ablation,
- b) Application of a **radiation model** which is computationally inexpensive and accurate for hypersonic flows.

Obj.2 Design of a methodology to relate the models with meteor observations:

- a) Comparison of the models with **luminosity** and **dynamic mass** observations,
- b) **Derivation of the single-body theory coefficients** from detailed simulations.

We leverage engineering models developed for re-entry space vehicles, and we extend them to meteoroid applications. With this thesis, we intend to build a bridge between aerospace engineers and the meteor community, opening possible collaborations for future research.

To address the stated objectives, the thesis is framed such that all phenomena can be tackled. This structure can be best depicted in Fig. (1.5). Chapters 2 to 5 describes separately phenomena concerning the modeling of the gas-phase, surface evaporation, material melting, and flow radiation, respectively. The modeling chapters are organized similarly, i.e., starting by the model's description, moving to the numerical methods, and ending with results. The results

are either experimental comparison or verification with other methods. In Chapter 6, we combine these models in an overarching application of a fireball entry, and we can compare our results with the observations.

The thesis is divided into seven chapters, including the introduction and detailed description of each chapter follow.

Chapter 2 presents the gas-phase models relevant to hypersonic flows. We show the governing equations in a quasi 1-D form and their closure using state-of-the-art physico-chemical models. We present the discretized version of the governing equations, with the Finite Volume method, and detail the in-house Computational Fluid Dynamics solver responsible for solving them. Finally, we employ the gas-phase models to the hypersonic simulation of a non-ablating meteor, describing the flow field features.

Chapter 3 starts with an overview of surface balances to account for gas-surface interaction. Afterward, we introduce engineering and kinetic-based evaporation models. We analyze both models under strong evaporation conditions in a hypersonic flow. Lastly, we compare the kinetic-based evaporation model with the Direct Simulation Monte Carlo method to assess its validity.

Chapter 4 concerns the development of melting models for meteoroid entry applications. The melting model is based on the Stefan problem, and it can be applied to the phase-change of any material, e.g., oxides, and metals. Moreover, we extend the state-of-the-art shear removal based on glass materials to the materials mentioned above. Together with the models described in **Chapters 2 and 3**, we compare the ablation model by shear melting and evaporation with the experiments carried out in the Arc Jet facility at NASA Ames Research Center.

Chapter 5 depicts the radiative model employed in this thesis. We use a hybrid spectral reduction approach (Hybrid Statistical Narrow-Band (HSNB) model) due to the radiative transfer's complexity and computational cost. The chapter starts by describing the radiative features, the HSNB model, and the numerical methodology to solve the Radiative Transport Equation (RTE). Afterward, we examine the H5 chondrite experiment carried out in the Plasmatron facility at the VKI, and we rebuild it with the models explained in **Chapters 2 and 3**. Finally, we compare the spectral measurements with the numerical results using the HSNB model.

Chapter 6 combines all the models developed in the previous chapters to study the Lost City bolide. The first analysis regards the coupling of flow/radiation/evaporation (**Chapters 2, 3 and 5**) to estimate the luminosity at different trajectory points. Moreover, we compare these results with the observations carried out by astronomers. In the second analysis of the chapter, we include the shear ablation (**Chapter 4**) to a small part of the trajectory to understand the meteoroid ablation during flight. These results are also compared with the dynamic mass measurements.

Chapter 7 summarizes the results obtained through this thesis. We address the objectives laid out in this chapter, and we contextualize each chapter's importance for the modeling of meteoroid entry. We finalize the manuscript by providing perspectives on the work done and recommendations for future

studies.

The work shown in this thesis can be applied to understand the flow field details around meteors at a particular altitude, velocity, size, and object composition. Its limitations lie in the characterization of the full trajectory, and the initial conditions of the body at the boundary rarefied/continuum regime have to be assumed. Table (1.3) depicts a small description of the models presented in each chapter and its disadvantages and inputs/outputs.

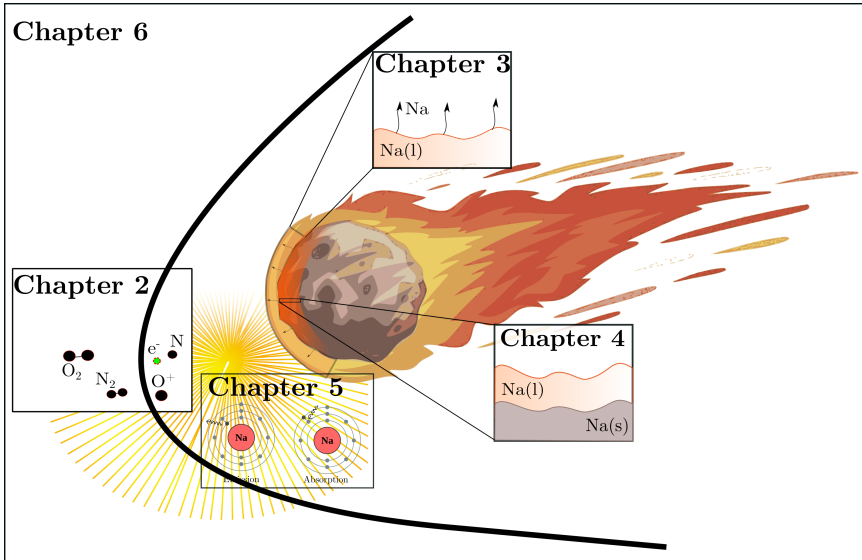


Figure 1.5.: Illustration of the thesis structure.

Table 1.3.: Description of the research milestone, general assumptions and input/output the models in each chapter.

	Research milestones	General assumptions	Model parameters	
			Input	Output
Chapter 2 ^a	<ul style="list-style-type: none"> • Stagnation-line simulation • Thermodynamic, transport, & chemical-kinetic models 	<ul style="list-style-type: none"> • Continuum regime • Single fragment • Equivalent spherical body • Point wise altitude simulations 	Surface temperature, object equivalent radius & velocity, atmosphere properties	Flow field properties
Chapter 3	<ul style="list-style-type: none"> • Thermo-chemical equilibrium evaporation model • Translational & chemical non-equilibrium evaporation model 	<ul style="list-style-type: none"> • Constant material composition at the surface • Boltzmann distribution at the Knudsen layer edge • Equal evaporation & condensation coefficients 	Surface temperature, ^b equilibrium vapor pressure, object equivalent radius, surface composition	Knudsen layer edge properties, evaporation rate
Chapter 4	<ul style="list-style-type: none"> • Melting & shear-ablation model 	<ul style="list-style-type: none"> • Constant molten thickness • Temperature independent molten material properties • Uniform recession • Uniform surface forces 	Shear forces, surface temperature, evaporation rate, material properties	Total ablation rate, molten thickness, material in-depth temperature

Continued on next page

Table 1.3 – *Continued from previous page*

	Research milestones	General assumptions	Model parameters	
			Input	Output
Chapter 5	<ul style="list-style-type: none"> Application of the HSNB model to meteor simulations 	<ul style="list-style-type: none"> Molecular & atomic radiative properties for air species & atomic properties for evaporation products 	Flow field properties, radiative properties	Radiative heat flux, spectral intensity, transmissivity, radiative source terms
Chapter 6	<ul style="list-style-type: none"> Estimation of the shock-layer meteor luminosity Flow/material coupling applied to meteor trajectories 	<ul style="list-style-type: none"> Constant velocity Non-fragmenting body Equivalent spherical body Rapidly tumbling Continuum regime 	Object equivalent radius & velocity, atmospheric properties, surface composition, radiative properties, material properties	Heat-transfer coefficient, luminosity, photographic magnitude, luminous efficiency, mass removal along trajectory, material in-depth temperature

^a The physico-chemical models employed in the flow field simulations require thermodynamic, transport and kinetic data. These data are described in Chapters [A](#) and [2](#).

^b In case the surface temperature T_w is not imposed, one can solve a Surface Energy Balance (SEB) (see Chapter [3](#)) where the wall heat flux q_w the emissivity ϵ are inputs and T_w is an output.

CHAPTER 2

Gas-phase modeling

Birds scream at the top of their lungs in horrified hellish rage every morning at daybreak to warn us all of the truth, but sadly we don't speak bird.

— Kurt Cobain

2.1. Introduction

The hypersonic flow environment is hard to predict because it involves complex physico-chemical models [15]. The complexity of these models is due to their interdisciplinary nature as they involve quantum mechanics, kinetic theory, and statistical thermodynamics.

The accuracy of the gas phase modeling determines how predictive is a hypersonic simulation. Anderson Jr. [7] gives an excellent example of the Apollo 11 re-entry, highlighting the importance of chemical reactions in thermodynamic quantities, such as the specific heat ratio γ . In his words, if one assumes a constant $\gamma = 1.4$ for air, the post-shock temperature is “*ungodly high, but also totally incorrect*”. As mentioned in Chapter 1, the meteor physics equations lack this detailed modeling and lump all the information into coefficients. These coefficients are hard to generalize for a broad range of flow conditions given such physico-chemical aspects. Therefore, an in-depth hypersonic simulation will allow us to understand better the meteor phenomena.

The objective of this chapter is to depict the physico-chemical models for simulating hypersonic flows. We start by examining the conservation equations for chemical reacting flows in Section 2.2. We consider a two-temperature model [193, 194] to describe the thermal state of the flow. This model assumes

Parts of this chapter have been published in

1. J. B. Scoggins, V. Leroy, G. Bellas-Chatzigeorgis, B. Dias and T. E. Magin, **Mutation++: Multicomponent Thermodynamic And Transport properties for IONized gases in C++**, *SoftwareX*, 12:100575, 2020.
1. B. Dias, A. Turchi and T. E. Magin, **Stagnation-Line Simulations of meteoroid ablation**, *45th AIAA Thermophysics Conference Proceedings AIAA 2015-2349*, 2015.

that the translational mode of the heavy species, atoms and molecules, and rotational mode of molecules follows a Boltzmann distribution at temperature T . In contrast, the vibrational mode of molecules, the electronic mode of heavy species, and the translational mode of the free electron follow a Boltzmann distribution at temperature T^{ve} . We employ state-of-the-art physico-chemical models (Section 2.3) for the closure of the Navier-Stokes equations. This closure contains fundamental properties and models suitable for high-temperature gas effects. Chemical and energy source terms due to radiation are included in the Navier-Stokes equations by following the work of Soucasse et al. [238]. We discretize the Navier-Stokes equations using a Finite Volume (FV) method (Section 2.4). In Section 2.5, we compare two flux-splitting schemes for a hypersonic simulation, and we analyze the physical details of the flow.

In essence, this chapter represents the foundation of the thesis since it supports the subsequent chapters. As the main contributions, we have derived and included the thermochemical properties of metals into the MUTATION⁺⁺ library. Furthermore, we have implemented a flux scheme to improve the robustness of the Computational Fluid Dynamics (CFD) solver at high Mach numbers.

2.2. Governing equation for hypersonic flows

Previously, we stressed the importance of chemical reactions in hypersonic flows. However, we must evaluate further physical aspects as the translational and internal energy modes of the gas can no longer be neglected. By internal energy modes, we imply that molecules have energy associated with the rotational and vibrational motion of the nuclei and electronic energy due to the electron shells surrounding them. On the other hand, atoms contain only an electronic energy mode. In the case of ionized flows, an additional mode is considered for the free-electron translational motion.

The conservation equations for a reacting gas flow yield,

$$\partial_t \begin{pmatrix} \rho_i \\ \rho \mathbf{u} \\ \rho E \end{pmatrix} + \nabla \cdot \begin{pmatrix} \rho_i \mathbf{u} \\ \rho \mathbf{u} \otimes \mathbf{u} \\ \rho H \mathbf{u} \end{pmatrix} + \nabla \cdot \begin{pmatrix} \mathbf{J}_i \\ p \bar{\mathbf{I}} + \bar{\boldsymbol{\tau}} \\ \bar{\boldsymbol{\tau}} \cdot \mathbf{u} + \mathbf{q} \end{pmatrix} = \begin{pmatrix} \dot{\omega}_i^{\text{chem}} \\ 0 \\ \mathcal{P}^{\text{rad}} \end{pmatrix}, \quad (2.1)$$

where the first, second and third equation are respectively the mass for species $i \in \mathcal{G}$, the mixture momentum and the mixture total energy. Equation (2.1) is valid both in thermal equilibrium and non-equilibrium. In thermal equilibrium, the energy of the internal modes is characterized with same temperature as the translational mode $T = T^{\text{R}} = T^{\text{V}} = T^{\text{E}} = T_e$. In this case, we say that the internal energy levels of the atoms and molecules follow Maxwell-Boltzmann distributions at temperature T .

In certain conditions, when the particles do not thermalize through collisions, the energy of every internal mode deviates from the equilibrium state. For such conditions, Eq. (2.1) is supplemented with additional equations do describe the energy of each internal mode. A simplified model for thermal non-equilibrium

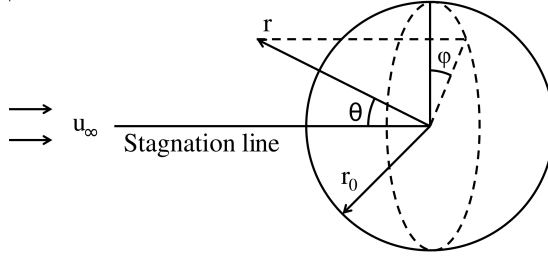


Figure 2.1.: Spherical body of radius r_0 subjected to a hypersonic flow at u_∞ . Azimuth and zenith angles are φ and θ , respectively.

flows is the two-temperature model proposed by Park [193, 194, 195]. In Park's model, the translational-rotational modes follow a Boltzmann distribution at temperature $T = T^R$, whereas vibrational-electronic-electron modes obeys a Boltzmann distribution at temperature $T^{\text{ve}} \equiv T^V = T^E = T_e$. The additional energy equation for the vibronic mode yields,

$$\frac{\partial}{\partial t} (\rho e^{\text{ve}}) + \nabla \cdot (\rho e^{\text{ve}} \mathbf{u}) + \nabla \cdot \mathbf{q}^{\text{ve}} = -p_e \nabla \cdot \mathbf{u} + \Omega^{\text{ve}} + \mathcal{P}^{\text{rad,ve}}, \quad (2.2)$$

where $p_e \nabla \cdot \mathbf{u}$ is the internal work done by the electron pressure. This term is non-conservative and is typically treated as a source term [94]. The remaining terms are detailed below.

The rationale behind this mode separation is: i) same relaxation timescale for the translational and rotational modes, whereas the vibrational relaxation is much slower; ii) fast energy transfer between the free-electron and vibrational mode; iii) most of the electronic excitation arises from the free-electron interaction, leading to an electron-electronic energy coupling.

Park [198] has mentioned a higher rotational relaxation than vibrational at greater temperatures. This effect implies a separate rotational equation, i.e., a three-temperature model. Panesi et al. [190] have observed a comparable relaxation between the translation-rotation and translation-vibration relaxation for a $\text{N}_2\text{-N}$ system at high temperature.

In this work, we use the two-temperature model due to the lack of data on the translation-rotation relaxation rates for the species of interest.

Stagnation-line formulation

We simulate the hypersonic flow around spherical bodies using a reduced form of the 2D axisymmetric Navier-Stokes equations to a quasi-1D approximation for the stagnation streamline [134] (see Fig. (2.1)). This reduction was achieved

$p_e \nabla \cdot \mathbf{u} = \nabla \cdot (p_e \mathbf{u}) - \mathbf{u} \cdot \nabla p_e$ where $\mathbf{u} \cdot \nabla p_e = -\mathbf{u} \cdot q_e n_e \mathbf{E}$ which represents the energy released during the work done by the electron flowing on a electric field \mathbf{E} , only valid for ambipolar assumption [195].

by using the following similarity transformation,

$$T = \bar{T}(r), \quad T^{\text{ve}} = \bar{T}^{\text{ve}}(r), \quad y_i = \bar{y}_i(r) \quad \forall i \in \mathcal{G}, \quad (2.3)$$

where the temperatures and mass fraction y_i of species i in the set of species \mathcal{G} depend only on the radial coordinate r , while the radial and azimuthal velocity components and the mixture pressure p and electron pressure p_e depend also on the polar angle θ such that,

$$\begin{aligned} u_r &= \bar{u}_r(r) \cos \theta, & u_\theta &= \bar{u}_\theta(r) \sin \theta, \\ p - p_\infty &= \bar{p}(r) \cos^2 \theta, & p_e - p_{e,\infty} &= \bar{p}_e(r) \cos^2 \theta. \end{aligned} \quad (2.4)$$

Taking the limit $\theta \rightarrow 0$, the stagnation streamline formulation referred to as the dimensionally reduced Navier Stokes equations (DRNSE), are written as

$$\frac{\partial}{\partial t} \mathbf{U} + \frac{\partial}{\partial r} \mathbf{F}^{\text{i}} + \frac{\partial}{\partial r} \mathbf{F}^{\text{v}} = \mathbf{S}^{\text{i}} + \mathbf{S}^{\text{v}} + \mathbf{S}^{\text{k}} + \mathbf{S}^{\text{rad}}, \quad (2.5)$$

where the vector \mathbf{U} denotes the volume-specific balance quantities, \mathbf{F}^{i} are the inviscid fluxes, and \mathbf{F}^{v} are the viscous terms. Vectors \mathbf{S}^{k} and the \mathbf{S}^{rad} are the kinetic and the radiative source terms, while \mathbf{S}^{i} and \mathbf{S}^{v} are the inviscid and viscous source terms arising from the DRNSE transformation. To ease the notation, we drop the the overline symbol do specify the stagnation-line quantities.

For the two-temperature model of Gnoffo et al. [94], this yields [238]:

$$\mathbf{U} = [\rho_i, \rho u_r, \rho u_\theta, \rho E, \rho e^{\text{ve}}]^T, \quad (2.6)$$

$$\mathbf{F}^{\text{i}} = [\rho_i u_r, \rho u_r^2 + p, \rho u_r u_\theta, \rho u_r H, \rho u_r e^{\text{ve}}]^T, \quad (2.7)$$

$$\mathbf{F}^{\text{v}} = [J_{r,i}, -\tau_{rr}, -\tau_{r\theta}, q_r - \tau_{rr} u_r, q_r^{\text{ve}}]^T, \quad (2.8)$$

$$\begin{aligned} \mathbf{S}^{\text{i}} &= -\frac{(u_r + u_\theta)}{r} \left[2\rho_i, 2\rho u_r, 3\rho u_\theta - 2\frac{p - p_\infty}{u_r + u_\theta}, \right. \\ &\quad \left. 2\rho H, 2\rho e^{\text{ve}} \right]^T, \end{aligned} \quad (2.9)$$

$$\begin{aligned} \mathbf{S}^{\text{v}} &= -\frac{1}{r} \left[2J_{r,i}, 2(\tau_{\theta\theta} - \tau_{rr} + \tau_{r\theta}), \right. \\ &\quad \left. \tau_{\theta\theta} - 3\tau_{r\theta}, 2(q_r - \tau_{rr} u_r - \tau_{\theta\theta} u_r - \tau_{r\theta} u_\theta), 2q_r^{\text{ve}} \right]^T, \end{aligned} \quad (2.10)$$

$$\mathbf{S}^{\text{k}} = [\dot{\omega}_i^{\text{chem}}, 0, 0, 0, \Omega^{\text{ve}}]^T, \quad (2.11)$$

$$\mathbf{S}^{\text{rad}} = [\dot{\omega}_i^{\text{rad}}, 0, 0, \mathcal{P}^{\text{rad}}, \mathcal{P}^{\text{rad,ve}}]^T, \quad (2.12)$$

where the total energy per unit volume is written as $\rho E = \rho e + \rho u_r^2/2$ with ρ being the mixture mass density. The total enthalpy is given as $H = E + p/\rho$.

The total internal energy of the mixture is defined as:

$$\rho e = \sum_{i \in \mathcal{H}} \rho_i e_i(T, T^{\text{ve}}) + \rho_e e_e^{\text{T}}(T^{\text{ve}}),$$

where ρ_e and e_e^{T} are respectively the electron density and the electron internal energy. The internal energy for the heavy species \mathcal{H} is defined as,

$$\begin{cases} e_i^{\text{T}}(T) + e_i^{\text{E}}(T^{\text{ve}}) + e_i^{\text{F}}, & \forall i \in \mathcal{A}, \\ e_i^{\text{T}}(T) + e_i^{\text{R}}(T) + e_i^{\text{V}}(T^{\text{ve}}) + e_i^{\text{E}}(T^{\text{ve}}) + e_i^{\text{F}}, & \forall i \in \mathcal{M}, \end{cases} \quad (2.13)$$

where the superscripts T, V, R, and E represent the translational, vibrational, rotational, and electronic modes, \mathcal{A} represents the set of atoms, and \mathcal{M} is the set of molecules. The term e_i^{F} represents the formation energy of the species i at 298 K. The pressure is retrieved with the perfect gas law as $p = \sum_{i \in \mathcal{H}} \rho_i R_i T + \rho_e R_e T^{\text{ve}}$, where R_i is the perfect gas constant of the species i . The total and internal heat flux on the radial direction read as:

$$q_r = \sum_{i \in \mathcal{G}} J_{r,i} h_i - \lambda^{\text{T}} \frac{\partial T}{\partial r} - \lambda^{\text{ve}} \frac{\partial T^{\text{ve}}}{\partial r}, \quad (2.14)$$

$$q_r^{\text{ve}} = \sum_{i \in \mathcal{G}} J_{r,i} h_i^{\text{ve}} - \lambda^{\text{ve}} \frac{\partial T^{\text{ve}}}{\partial r}, \quad (2.15)$$

where $J_{r,i}$ corresponds to the diffusion flux of species i (obtained by solving the Stefan-Maxwell system [160]), and λ^{T} and λ^{ve} are the heavy translation-rotation and electron-vibronic thermal conductivities, respectively. The different components of the viscous stress tensor read as,

$$\tau_{rr} = \frac{4}{3} \mu \left(\frac{\partial u_r}{\partial r} - \frac{u_r + u_\theta}{r} \right), \quad (2.16)$$

$$\tau_{r\theta} = \mu \left(\frac{\partial u_\theta}{\partial r} - \frac{u_r + u_\theta}{r} \right), \quad (2.17)$$

$$\tau_{\theta\theta} = -\frac{1}{2} \tau_{rr}, \quad (2.18)$$

where μ corresponds to the shear viscosity. Finally, the diffusion fluxes are defined as,

$$J_{r,i} = \rho_i V_{r,i} \quad (2.19)$$

where $V_{r,i}$ is the diffusion velocity on the radial direction.

The energy transfer between the translational and the vibration-electronic-electron energy is,

$$\Omega^{\text{ve}} = -p_e \left(\frac{\partial u_r}{\partial r} + 2 \frac{u_r + u_\theta}{r} \right) + \Omega^{\text{VT}} + \Omega^{\text{CV}} + \Omega^{\text{CE}} + \Omega^{\text{ET}} - \Omega^{\text{I}}. \quad (2.20)$$

and for convenience we include the work of the electron compression force

$p_e \nabla \cdot \mathbf{u}$ as a source term. The expressions for the transfer terms due to internal modes exchange and chemical reactions are given in Section 2.3.4.

2.3. Physico-chemical models for gas phase

The physico-chemical models used in CFD solvers have a direct impact on the closure the conservation laws governing the flow. These models include mixture thermodynamic and transport properties, species chemical production rates, and energy transfer rates. The properties depend a variety of specialized algorithms and data, such as species partition functions, binary collision integrals, and reaction rate coefficients.

The MUTATION⁺⁺ library [230, 232] has been built to centralize data and algorithms and provide accurate physico-chemical properties to CFD solvers. In this section, we describe the physico-chemical models implemented in the MUTATION⁺⁺ library that have been used in this thesis.

2.3.1. Thermodynamic properties

It is impossible to describe the presence of each microscopic particle in a system containing millions of atoms and molecules. Statistical thermodynamics fills this void by relating the behavior of a large number of particles to macroscopic thermodynamics of a system in equilibrium [262], i.e., this statistical treatment assumes that every internal mode is populated according to a Maxwell–Boltzmann distribution. An important quantity derived from statistical thermodynamics, which allows the derivation of the macroscopic thermodynamics properties, is the partition function,

$$Q = \sum_{j \in \mathcal{L}} a_j \exp\left(\frac{-\varepsilon_j}{k_B T}\right) \quad (2.21)$$

where ε_j and a_j are the energy and the degeneracy of the level $j \in \mathcal{L}$, respectively. The energy of the particle corresponds to the eigenvalues of the time-independent Schrödinger Equation, where,

$$\varepsilon_j = \varepsilon_j^T + \varepsilon_j^{\text{int}}, \quad \forall j \in \mathcal{L}, \quad (2.22)$$

ε_j^T is the energy linked to the translational motion and $\varepsilon_j^{\text{int}}$ is the internal energy of the particle. The Born-Oppenheimer approximation permits to separate the motion of the nuclei and the motion of the electrons which leads to,

$$\varepsilon_j^{\text{int}} = \varepsilon_j^E + \varepsilon_j^{\text{RV}}, \quad \forall j \in \mathcal{L}, \quad (2.23)$$

where ε_j^E is the electronic energy and $\varepsilon_j^{\text{RV}}$ is the energy associated to the ro-vibrational motion of the nuclei. Inserting Eqs. (2.22) and (2.23) into Eq. (2.21) allows to derive the macroscopic thermodynamic properties for each mode.

Remark. The Born-Oppenheimer approximation ceases to be valid for higher electronic states because the vibration of the nuclei might change the electronic configuration [69], inducing vibration-electronic coupling effects.

2.3.1.1. Rigid-Rotor Harmonic-Oscillator (RRHO)

The Rigid-Rotor Harmonic-Oscillator (RRHO) model is widely used for hypersonic simulations, despite its limitations at high temperatures. The rotational motion of the nuclei is computed as a rigid-rotor. This approximation implies that a fixed intermolecular distance separates the nucleus of the particles forming the molecule. The vibrational motion is determined with a harmonic potential as in classical mechanics. Furthermore, the harmonic potential assumes an equal vibrational energy gap. With this model, one neglects the coupling effects between the rotational and vibrational modes, which are essential at high temperatures. This is important to study phenomenon such as radiation but not for the balance of energy in the flow [189]. Additional effects include centrifugal distortion induced by the rotation of the nuclei widening the intermolecular distance between the atoms. Moreover, the vibrational and rotational constants derived from quantum mechanics are the same for excited and ground electronic states. For more details regarding the limitations of this model, the interested reader is directed to Vincenti and Kruger [262] and Demtröder [69].

The RRHO model allows to redefine the particle energy (Eq. (2.22)) as,

$$\varepsilon_j = \varepsilon_j^T + \varepsilon_j^R + \varepsilon_j^V + \varepsilon_j^E, \quad \forall j \in \mathcal{L}, \quad (2.24)$$

leading to the following partition function,

$$Q_i = Q_i^T Q_i^R Q_i^V Q_i^E, \quad \forall i \in \mathcal{G}.$$

The translational, rotational, vibrational, electronic and formation thermodynamic properties for each species are expressed according to Eqs. (2.25) to (2.30), respectively.

Translational mode: The translational partition function, energy, enthalpy and entropy are,

$$Q_i^T(T) = V \left(\frac{2\pi m_i T}{h^2} \right)^{3/2}, \quad \forall i \in \mathcal{G}, \quad (2.25a)$$

$$e_i^T(T) = \frac{3}{2} R_i T, \quad \forall i \in \mathcal{G}, \quad (2.25b)$$

$$h_i^T(T) = e_i^T(T) + R_i T, \quad \forall i \in \mathcal{G}, \quad (2.25c)$$

$$s_i^T(T) = \frac{h_i^T(T)}{T} + R_i \ln \left[\frac{k_B T}{p_i} \left(\frac{2\pi m_i T}{h^2} \right)^{3/2} \right], \quad \forall i \in \mathcal{G}, \quad (2.25d)$$

where V is the volume of the system.

Rotational mode: The rotational partition function, energy, enthalpy and entropy are,

$$Q_i^R(T) = \frac{1}{\sigma_i} \left(\frac{T}{\theta_i^R} \right)^{\mathfrak{L}/2}, \quad \forall i \in \mathcal{M}, \quad (2.26a)$$

$$e_i^R(T) = h_i^R(T) = \frac{\mathfrak{L}}{2} R_i T, \quad \forall i \in \mathcal{M}, \quad (2.26b)$$

$$s_i^R(T) = \frac{h_i^R(T)}{T} + R_i \left[\frac{\mathfrak{L}}{2} \ln \left(\frac{T}{\theta_i^R} \right) + \ln \left(\frac{1}{\sigma_i} \right) \right], \quad \forall i \in \mathcal{M}, \quad (2.26c)$$

where σ_i is the steric factor ($\sigma_i = 1$ for non-symmetric and $\sigma_i = 2$ for symmetric linear molecules) and \mathfrak{L} is related to the linearity of the molecule ($\mathfrak{L} = 2$ for linear molecules and $\mathfrak{L} = 3$ for non-linear molecules). The quantity $\theta^R = h/(8\pi^2 \mathfrak{I} k_B)$ is the rotational characteristic temperature where \mathfrak{I} is the rotor momentum of inertia.

Vibrational mode: The vibrational partition function, energy, enthalpy and entropy are,

$$Q_i^V(T^{\text{ve}}) = \prod_{k \in \mathcal{V}_i} \left[1 - \exp \left(\frac{\theta_{ki}^V}{T^{\text{ve}}} \right) \right], \quad \forall i \in \mathcal{M}, \quad (2.27a)$$

$$e_i^V(T^{\text{ve}}) = h_i^V(T^{\text{ve}}) = R_i \sum_{k \in \mathcal{V}_i} \theta_{ki}^V \left[\exp \left(\frac{\theta_{ki}^V}{T^{\text{ve}}} \right) - 1 \right]^{-1}, \quad \forall i \in \mathcal{M}, \quad (2.27b)$$

$$s_i^V(T^{\text{ve}}) = \frac{h_i^V(T^{\text{ve}})}{T^{\text{ve}}} - R_i \sum_{k \in \mathcal{V}_i} \ln \left[1 - \exp \left(\frac{\theta_{ki}^V}{T^{\text{ve}}} \right) \right], \quad \forall i \in \mathcal{M}, \quad (2.27c)$$

where $\theta_k^V = h\nu_k/k_B$ is the vibrational characteristic temperature and ν_k the vibrational quantum number for the mode $k \in \mathcal{V}$. Diatomic molecules have just one vibrational mode ($\theta_v = 3392.7$ K for N_2), whereas triatomic molecules have more (CO_2 has two modes plus one doubly degenerate bending mode).

Electronic mode: The electronic partition function, energy, enthalpy and entropy are,

$$Q_i^E(T^{\text{ve}}) = \sum_{k \in \mathcal{K}_i} a_{ki}^E \exp \left(\frac{-\theta_{ki}^E}{T^{\text{ve}}} \right), \quad \forall i \in \mathcal{G}, \quad (2.28a)$$

$$e_i^E(T^{\text{ve}}) = h_i^E(T^{\text{ve}}) = \frac{R_i}{Q_i^E} \sum_{k \in \mathcal{K}_i} a_{ki}^E \theta_{ki}^E \exp \left(\frac{-\theta_{ki}^E}{T^{\text{ve}}} \right), \quad \forall i \in \mathcal{G}, \quad (2.28b)$$

$$s_i^E(T^{\text{ve}}) = \frac{h_i^E(T^{\text{ve}})}{T^{\text{ve}}} - R_i \ln Q_i^E, \quad \forall i \in \mathcal{G}, \quad (2.28c)$$

where a_k^E is the degeneracy of the electronic level k , $\theta_k^E = E_k^E/k_B$ the electronic characteristic temperature and E_k^E is the electronic energy of level $k \in \mathcal{K}$.

The electronic partition function diverges as the electronic number tends to infinite [49]. Therefore, it is essential to choose the maximum number of electronic levels correctly. Figure (2.2) shows an example of the Na electronic partition function for different number of levels taken from Kramida and Ralchenko [138], where 139 is the maximum number of levels. This figure highlights the importance of including the high-lying electronic levels. These levels are essential at high temperatures because they become highly populated. The number of electronic levels has a direct impact on the evaluation of the partition function, thus on the thermodynamic properties.

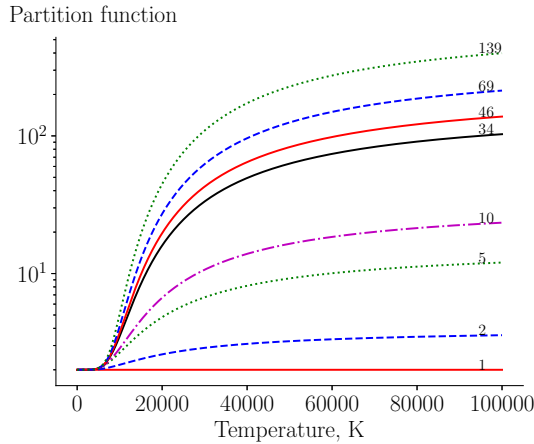


Figure 2.2.: Na Partition function for different amounts of energy levels. Increasing the number electronic levels does not guarantee the convergence of the partition function.

Electron mode: Electrons do not contain any internal structure; hence, they only have a translational mode. The electron translation energy, enthalpy, and entropy are,

$$e_e(T^{ve}) = \frac{3}{2}R_eT^{ve} + e_e^F, \quad (2.29a)$$

$$h_e(T^{ve}) = e_e + R_eT^{ve}, \quad (2.29b)$$

$$s_e(T^{ve}) = s_e^T(T) + R_e \ln 2, \quad (2.29c)$$

where e_e^F is the electron formation energy.

The formation energy of any heavy species $i \in \mathcal{G}$ is constant,

$$e_i^F(T) = \text{const}, \quad \forall i \in \mathcal{G}, \quad (2.30)$$

The electronic levels and degeneracy for atoms can be found in Kramida and Ralchenko [138]. For molecules, the internal mode properties can be found in Gurvich et al. [104] and Allison [6], Chase et al. [60].

Reduction of the electronic levels: Typically, alkali and metallic species have low ionization energy and hundreds of energy levels, making the evaluation of the partition function computationally expensive due to its exponential nature. To circumvent this problem, we use a binning strategy [163] which consists in grouping the energy levels into bins over an energy grid $[\varepsilon_k, \varepsilon_{k+1}[$, (Fig. (2.3)) as follows,

$$F_k = \{i \in F_e \text{ such that } (\varepsilon_k \leq E_i < \varepsilon_{k+1})\}, \quad k \in K_e,$$

where K_e is the set of the indices for the bins. An average energy for bin k

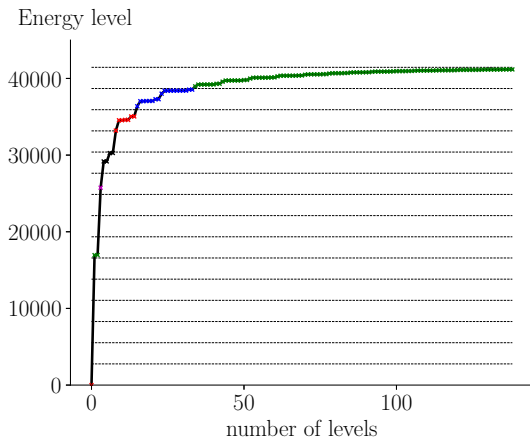


Figure 2.3.: Energy levels for Na.

follows,

$$\bar{E}_k = \frac{\sum_{i \in F_k} a_i^E E_i}{a_k^E}, \quad k \in K_e,$$

based on the degeneracy of the bin as $\bar{a}_k^E = \sum_{i \in F_k} a_i^E$.

Finally, the electronic partition function assuming a reduced amount of energy levels estimated for each bin is computed using,

$$\bar{Q}_i^E(T = T^{\text{ve}}) = \sum_{k \in K_e} \bar{a}_k^E \exp\left(\frac{-\bar{\theta}_k}{T}\right), \quad i \in \mathcal{A}, \quad (2.31)$$

where the characteristic temperature $\bar{\theta}_k = \bar{E}_k/k_b$ and k_b is the Boltzmann constant. As mentioned above, once the electronic partition function is known, the computation of the thermodynamic properties becomes trivial. The electronic

enthalpy follows,

$$h_i^E(T = T^{\text{ve}}) = R_i T^2 \frac{\partial \ln \bar{Q}_i^E}{\partial T}, \quad i \in \mathcal{A}. \quad (2.32)$$

The electronic levels for atoms are either observed through spectroscopy measurements or computed from quantum mechanics. The NIST database [138] comprises a large amount of data regarding the electronic levels for several atoms. Figure (2.3) shows all 139 electronic levels for Na. The bars shown in the same figure represent the bins, and the symbols concern the total number of electronic levels per bin. The reduction technique mentioned above allowed us to pass from 140 to 6 electronic levels. Figure (2.4a) shows the non-dimensional enthalpy for Na for the total number of electronic levels extracted from NIST [138] and for the reduced number.

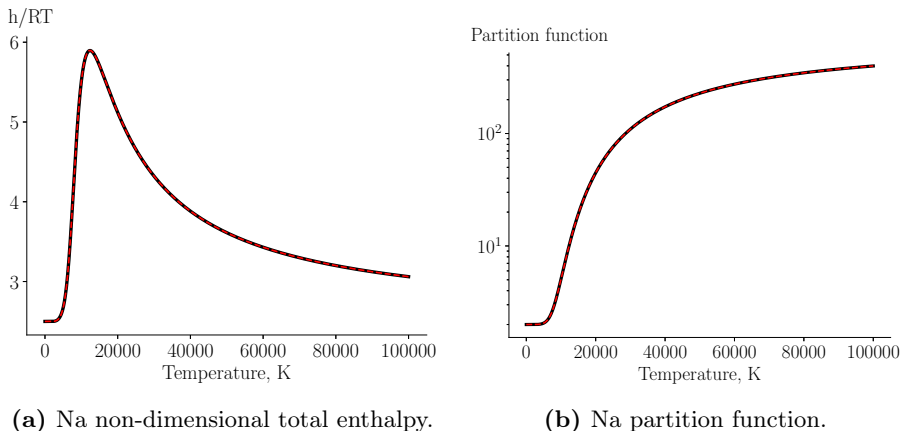


Figure 2.4.: Energy-level reduction of Na; solid line: 140 electronic levels, broken line: 6 electronic levels: - - - reduced model, — full model.

From the figure, the agreement of the reduced system can reproduce the same thermodynamic quantity as the whole number of electronic levels.

2.3.1.2. NASA-9 database

The NASA-9 database of McBride et al. [168] comprises the thermodynamic data of several species in the form of 9-coefficient polynomial. This data is accurate up to 20 000 K for the majority of the species and includes vibration-rotation coupling effect as well as anharmonicity corrections. The thermodynamic specific heat, enthalpy and entropy for species i are, respectively,

$$\frac{c_{p_i}}{R_i} = \sum_{j=0}^k a_{j,i} T^{j-2}, \quad \forall i \in \mathcal{G}, \quad (2.33a)$$

$$\frac{h_i}{R_i T} = \int \frac{c_{p_i} dT}{R_i T} + b_{1,i}, \quad \forall i \in \mathcal{G}, \quad (2.33b)$$

$$\frac{s_i}{R_i} = \int \frac{c_{p_i}}{R_i T} dT + b_{2,i}, \quad \forall i \in \mathcal{G}. \quad (2.33c)$$

where $a_{j,i}$, $b_{1,i}$ and $b_{2,i}$ are the species polynomial coefficient and R_i is the specific gas constant. The NASA-9 polynomial allows for a fast computation of the thermodynamic properties. However, these polynomials hinder the separation of the internal modes, which is necessary for the two-temperature model. A solution is to remove the translational and rotational contributions, e.g., Eqs. (2.25) and (2.26), from the polynomials above. Some CFD solvers already employ this strategy [94, 273].

Figure (2.5) shows the equilibrium composition based on the Gibbs free energy minimization [231] for an NaO system. We compare the RRHO model and the NASA polynomials, where the former includes the electronic level reduction explained above. Initially, only NaO is present in the mixture; around 2500 K, the species starts to dissociate, forming Na and O. Around 5000 K, Na starts to ionize, forming Na^+ , and finally, at 12000 K, the mixture becomes fully ionized. The agreement between both models is excellent up to 17000 K, corresponding to the limit of the NASA polynomials for these species.

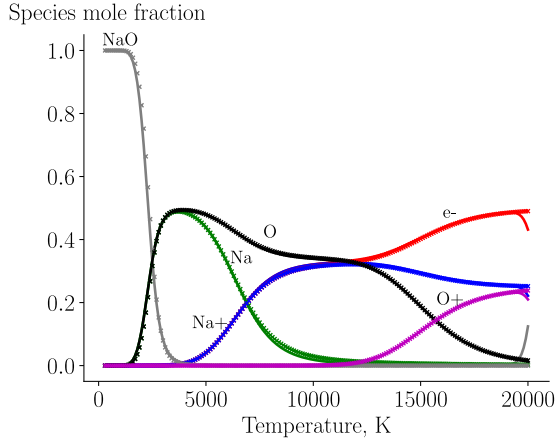


Figure 2.5.: Equilibrium composition for $\{\text{NaO}, \text{Na}, \text{O}, \text{Na}^+, \text{O}^+, \text{e}^-\}$; lines: NASA database, symbols: RRHO.

2.3.2. Transport properties

An intuitive physical interpretation of the transport fluxes is given by:

...the molecules in their random thermal movement from one region of the gas to another tend to transport with them the macroscopic properties of the region from which they come. If these macroscopic

properties are nonuniform, the molecules thus find themselves out of equilibrium with the properties of the region in which they arrive. The result of these molecular transport processes is the appearance at the macroscopic level of the well-know nonequilibrium phenomena of viscosity, heat conduction, and diffusion. (Vincenti and Kruger [262, pp. 15]).

The excerpt above relates the transport of microscopic quantities to macroscopic fluxes due to gradients within the flow. The closure of transport fluxes (Eqs. (2.14) to (2.19)) in the conservation laws is achieved through a multiscale Chapman-Enskog perturbative solution of the Boltzmann equation [82, 262]. This perturbation method yields the expressions of the transport coefficients, such as thermal conductivity, viscosity, and diffusion coefficients. The approximate solution of the perturbation functions is retrieved with a spectral Galerkin method with the Laguerre-Sonine polynomials as basis functions. Magin and Degrez [161, 162] derived expressions for the transport coefficients for weakly ionized and unmagnetized plasmas, based on this perturbation method.

The collision dynamics between particles are closely related to the transport coefficients, as this information appears in the linearized collision operator of the Boltzmann equation. The deflection angle χ_{ij} of a binary elastic collision (Fig. (2.6)) is given by,

$$\chi_{ij}(E, b) = \pi - 2b \int_{r_{\text{m}}}^{\infty} \frac{dr}{r^2 \sqrt{1 - \varphi_{ij}^{\text{E}}/E_{ij}}} \quad (2.34)$$

where b is the impact factor, $E_{ij} = 0.5\mu_{ij}g^2$ the relative kinetic energy between colliding particles, r and r_{m} are the distance between particles and the minimum possible distance, respectively. The effective potential φ_{ij}^{E} between particle i and j is given by,

$$\varphi_{ij}^{\text{E}}(E, b, r) = \varphi_{ij}(r) + E_{ij} \frac{b^2}{r}$$

where the first term is the spherical intermolecular potential and the second is a repulsive centrifugal term.

The relevant cross section is given by,

$$Q_{ij}^{(l)}(E) = 2\pi \int_0^{\infty} [1 - \cos^l(\chi_{i,j})] b db, \quad (2.35)$$

which relates the scattering angle with the impact factor. $Q_{ij}^{(1)}$ and $Q_{ij}^{(2)}$ represents respectively the momentum and viscosity cross sections [160]. The reduced collision integral yields,

$$\overline{Q}_{ij}^{(l,s)}(T) = \frac{2(l+1)}{(s+1)! [2l+1 - (-1)^l] (kT)^{s+2}} \int_0^{\infty} \exp\left(\frac{-E}{k_B T}\right) E^{s+1} Q_{ij}^{(l)} dE,$$

If b is large enough the particles do not collide

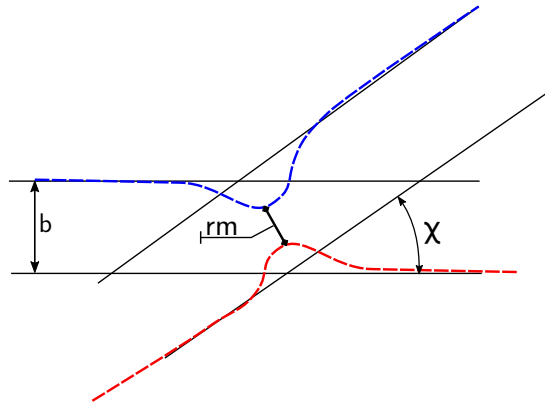


Figure 2.6.: Illustration of an elastic collision.

where (l, s) is the Laguerre-Sonine polynomial order.

In the case where both particles are considered rigid bodies or impenetrable spheres the collision integral reduces to,

$$\overline{Q}_{ij}^{(l,s)} = \pi d^2, \quad (2.36)$$

where $d = \frac{1}{2}(d_i + d_j)$ is the equivalent diameter for the i and j particles. The expression above is independent of the relative kinetic energy between particles i and j .

Most of the collision integrals for air species can be found directly in the literature [48, 242]. In the case this data is not available, one can use the non-dimensional tables of Monchick and Mason [180] provided with the correct neutral-neutral parameters for the Stockmayer potential.

2.3.2.1. Intermolecular potential

Neutral-neutral interactions: The Stockmayer and Lennard-Jones potentials are widely used for a neutral-neutral collision at low temperatures. The Stockmayer potential is given by,

$$\varphi_{ij}(r) = 4 \varphi_{ij}^0 \left[\left(\frac{\sigma_{ij}}{r} \right)^{12} - \left(\frac{\sigma_{ij}}{r} \right)^6 + \delta \left(\frac{\sigma_{ij}}{r} \right)^3 \right], \quad (2.37)$$

where φ_{ij}^0 is the depth of the potential well, σ_{ij} the distance of which the interparticle potential is zero and δ is related to the particle polarizability. The Stockmayer reduces to the Lennard-Jones potential for non-polar molecules ($\delta = 0$). These potentials provide accurate results for the transport properties at $T < 4000$ K, where long-range interactions are dominant [160]. At long-range, the potential has an attractive part (exponential 12), whereas at short-range (distances where $< \sigma_{ij}$), the interaction is dominated by repulsive forces (exponential 6). In the case of polar particles, the last term in the

Stockmayer potential corresponds to the forces that arise from the polarization of a particle by the electric field of a permanent multipole from another molecule. The potential parameters for the alkali metals were added to the MUTATION⁺⁺ library, and they are tabulated in Table (A.2).

The Born-Mayer is pure repulsive potential suitable for short-range interactions,

$$\varphi_{ij}(r) = \varphi_{ij}^0 \exp(-r/\sigma_{ij}). \quad (2.38)$$

At high temperatures, the kinetic energy of the particle is dominant over the attractive forces. Hence, the particles only feel each other through repulsive forces that occur at short ranges. This potential is usually used for temperatures higher than 4000 K as well for ion-neutral interactions [160].

Capitelli et al. [48] combined the Lennard-Jones and the Born-Mayer potential for air species, providing accurate transport data for many temperatures.

Ion-neutral interactions: In this work, we used the Langevin potential for this type of interaction [50], and it yields,

$$\varphi_{ij}(r) = -\frac{z_j^2 q_e^2 \alpha_i}{8\pi\epsilon_0 r^4}$$

where α_i is the dipole polarizability of the neutral species and z_j is the elementary charger of the ion. This potential is useful because it only requires α_i , which can be easily found in the literature. Moreover, it allows for a close form of the reduced collision integral [229],

$$\bar{Q}_{ij}^{(1,1)} = 424.443 z_j \pi \sqrt{\frac{\alpha_i}{T_h}}, \quad (2.39)$$

where the ratio with the reduced collision integral for the different Laguerre-Sonine polynomial orders is constant (refer to Scoggins [229]).

Charged interactions: A collision between charged particles is characterized by long-range forces represented by a Coulomb potential. In an ionized gas, the quasi-neutrality is maintained by the presence of an ambipolar electric field. This quasi-neutrality removes the long-range influence of the Coulomb potential. In this thesis we use the Debye-Hückel potential,

$$\varphi_{ij}(r) = \frac{z_i z_j}{r} \frac{q_e^2}{4\pi\epsilon_0} \exp\left(-\frac{r}{\lambda_D}\right),$$

which corresponds to a Coulomb potential shielded by the Debye length,

$$\lambda_D^2 = \frac{\epsilon_0 k_B / q_e^2}{n_e / T^{ve} + \sum_{j \in \mathcal{H}} z_j^2 n_j / T}.$$

2.3.2.2. Macroscopic properties

In many CFD solvers, the multicomponent transport coefficients are evaluated with mixture rules. The mixture rules are limited to low temperatures, and they lead to erroneous results for hypersonic conditions, e.g., meteoroid entry. As an example, the Fick diffusion model does not conserve mass. On the other hand, the Chapman-Enskog perturbation method is more rigorous, and it holds for a broad range of temperatures. The method provides expressions of the transport coefficients in terms of linear transport systems through a Laguerre-Sonine polynomial. These linear systems are functions of binary collision integrals and the local thermodynamic state-vector and may be solved through a variety of methods.

A single component viscosity is expressed as,

$$\mu_i = \frac{5}{16} \frac{\sqrt{\pi k_B T_h m_i}}{\overline{Q}_{ij}^{(2,2)}}, \quad \forall i \in \mathcal{H}, \quad (2.40)$$

where one sees the dependence on the reduced collision integral $\overline{Q}_{ij}^{(2,2)}$.

The monatomic thermal conductivity for a species i is related to the single component viscosity, and is given by,

$$\lambda_i = \frac{15}{4} \frac{k_B}{m_i} \mu_i, \quad \forall i \in \mathcal{H}. \quad (2.41)$$

Binary diffusion coefficient for heavy-heavy and heavy-electron are expressed as,

$$\mathcal{D}_{ij} = \frac{1}{n} \frac{3}{16} \sqrt{\frac{2\pi k_b T_h (m_i + m_j)}{m_i m_j}} \frac{1}{\overline{Q}_{ij}^{(1,1)}}, \quad \forall i, j \in \mathcal{H}, \quad (2.42)$$

$$\mathcal{D}_{ie} = \frac{1}{n} \frac{3}{16} \sqrt{\frac{2\pi k_b T_e}{m_e}} \frac{1}{\overline{Q}_{ie}^{(1,1)}}, \quad \forall i \in \mathcal{H}. \quad (2.43)$$

We briefly explain the linear system for multicomponent transport coefficients derived from the Chapman-Enskog perturbation method. The interested reader is directed to Magin [160] and Magin and Degrez [162] for a more thorough discussion. Details on transport algorithms to solve the linear systems are provided in Magin and Degrez [161].

Viscosity: The multicomponent shear viscosity μ is a solution of the following linear system,

$$\sum_{j \in \mathcal{H}} G_{ij}^\mu \alpha_j^\mu = x_i, \quad \forall i \in \mathcal{H},$$

$$\mu = \sum_{j \in \mathcal{H}} \alpha_j^\mu x_j,$$

where x is the species mole fraction and the multicomponent viscosity transport matrix is expressed as,

$$G_{ij}^\mu = G_{ji}^\mu = x_i x_j \frac{16}{5} \sqrt{\frac{2 m_i m_j}{\pi k_B T_h (m_i + m_j)^3}} \left(\overline{Q}_{ij}^{(2,2)} - \frac{5}{3} \overline{Q}_{ij}^{(1,1)} \right), \quad \forall i, j \in \mathcal{H}, \quad i \neq j$$

$$G_{ii}^\mu = \sum_{\substack{j \in \mathcal{H} \\ j \neq i}} x_i x_j \frac{16}{5} \sqrt{\frac{2 m_i m_j}{\pi k_B T_h (m_i + m_j)^3}} \left(\overline{Q}_{ij}^{(2,2)} \frac{m_j}{m_i} - \frac{5}{3} \overline{Q}_{ij}^{(1,1)} \right) + \frac{x_i^2}{\mu_i}, \quad \forall i \in \mathcal{H}.$$

Electrons do not contribute to the viscosity transport matrix due to its small mass, as a result of the electron-heavy scaling of the Boltzmann equation.

Thermal conductivity: Similarly to the shear viscosity, the thermal conductivity of the heavy particle translational mode is a solution of the following system,

$$\sum_{j \in \mathcal{H}} G_{ij}^\lambda \alpha_j^\lambda = x_i, \quad \forall i \in \mathcal{H},$$

$$\lambda^{\text{T}_h} = \sum_{j \in \mathcal{H}} \alpha_j^\lambda x_i,$$

where the multicomponent matrix is given by,

$$G_{ij}^\lambda = G_{ji}^\lambda = \frac{1}{25 k_B} \frac{x_i x_j}{n \mathcal{D}_{ij}} \frac{2 m_i m_j}{(m_i + m_j)^2} (16 A_{ij}^* + 12 B_{ij}^* - 55), \quad \forall i, j \in \mathcal{H}, \quad i \neq j$$

$$G_{ii}^\lambda = \frac{1}{25 k_B} \sum_{\substack{j \in \mathcal{H} \\ j \neq i}} \frac{x_i x_j}{n \mathcal{D}_{ij}} \frac{2 m_i m_j}{(m_i + m_j)^2} (30 m_i^2 + 25 m_j^2 - 12 m_j^2 B_{ij}^* + 16 m_i m_j A_{ij}^*)$$

$$+ \frac{4}{15 k_B} \frac{x_i^2 m_i}{\mu_i}, \quad \forall i \in \mathcal{H}$$

$$A_{ij}^* = \frac{\overline{Q}_{ij}^{(2,2)}}{\overline{Q}_{ij}^{(1,1)}}, \quad \forall i, j \in \mathcal{H}$$

$$B_{ij}^* = \frac{5 \overline{Q}_{ij}^{(1,2)} - 4 \overline{Q}_{ij}^{(1,3)}}{\overline{Q}_{ij}^{(1,1)}}, \quad \forall i, j \in \mathcal{H}$$

The thermal conductivity for each internal mode is given by the Eucken correction,

$$\lambda^{\text{R}} = \sum_{j \in \mathcal{M}} \frac{\rho_i c_i^{\text{R}}}{\sum_{j \in \mathcal{H}} x_j / \mathcal{D}_{ij}},$$

$$\lambda^{\text{V}} = \sum_{j \in \mathcal{M}} \frac{\rho_i c_i^{\text{V}}}{\sum_{j \in \mathcal{H}} x_j / \mathcal{D}_{ij}},$$

$$\lambda^E = \sum_{j \in \mathcal{H}} \frac{\rho_i c_i^E}{\sum_{j \in \mathcal{H}} x_j / \mathcal{D}_{ij}},$$

where c_i^R , c_i^V and c_i^E are the rotational, vibrational, and electronic species specific heats per particle, respectively. Expressions for the thermal conductivity of the electron translational mode λ^{Te} are provided by Magin [160] and Scoggins [229].

The thermal conductivity in Eqs. (2.14) and (2.15) is given by,

$$\begin{aligned} \lambda^T &= \lambda^{Th} + \lambda^R, \\ \lambda^{ve} &= \lambda^V + \lambda^E + \lambda^{Te}. \end{aligned}$$

Diffusion velocity: The diffusion velocity vector \mathbf{V} is given by the generalized Stefan-Maxwell system that can be written as,

$$\sum_{j \in \mathcal{G}} G_{ij}^V \mathbf{V}_j = \mathbf{d}_i^{\Theta'} + k_i^{\Theta} \mathbf{E} \quad (2.44)$$

where $\mathbf{d}_i^{\Theta'} = \mathbf{d}_i^{\Theta} \Theta_i$, $k_i^{\Theta} = k_i \Theta_i$, $\Theta_i = T_h / T_i$ $i \in \mathcal{G}$. The grouping parameter k is,

$$\begin{aligned} k_j &= \frac{x_j q_j}{k_B T_h} - \frac{y_i q}{k_B T_h}, \quad \forall j \in \mathcal{G}, \quad \text{and} \\ q &= \sum_{i \in \mathcal{G}} x_i q_i, \end{aligned}$$

where the last equation refers to the mixture charge. Neglecting thermo- and barodiffusion, the modified driving force follows,

$$\mathbf{d}_i' = \frac{p}{n k_B T_h} \nabla x_i, \quad \forall i \in \mathcal{G}. \quad (2.45)$$

The multicomponent diffusion matrix \mathbf{G}^V is given by,

$$\begin{aligned} G_{ij}^V &= G_{ji}^V = -\frac{x_i x_j}{\mathcal{D}_{ij}} (1 + \psi_{ij}), \quad \forall i, j \in \mathcal{G}, \quad i \neq j \\ G_{ii}^V &= \sum_{\substack{j \in \mathcal{H} \\ j \neq i}} \frac{x_i x_j}{\mathcal{D}_{ij}} (1 + \psi_{ij}) + \left(\frac{T_e}{T_h} \right)^2 \frac{x_i x_e}{\mathcal{D}_{ie}} (1 + \psi_{ie}), \quad \forall i \in \mathcal{G} \end{aligned}$$

where ψ_{ii} and ψ_{ie} are correction functions to consider a higher order Sonine polynomial. The expressions for the correction functions are provided by Magin [160] and Scoggins [229].

The multicomponent diffusion matrix \mathbf{G}^V is singular. The solution of the

linear system in Eq. (2.44) is obtained by adding a mass constraint,

$$\sum_{j \in \mathcal{G}} y_j \mathbf{V}_j = 0.$$

The singular matrix \mathbf{G}^V can be regularized by incorporating the constraint such that $\mathbf{G}^{V'} = \mathbf{G}^V + \alpha \mathbf{y} \otimes \mathbf{y}$ where $\alpha = 1/\max(\mathcal{D}_{ij})$ [161].

In this thesis, we assume ambipolar diffusion, meaning that an electric field develops naturally to keep quasi-neutrality between the charge species such that,

$$\sum_{i \in \mathcal{G}} x_i q_i \mathbf{V}_j = 0. \quad (2.46)$$

This assumption leads to a diffusion velocity of electrons and ions of the same order. The ambipolar assumption combined with the mass constraint yields,

$$\sum_{j \in \mathcal{G}} k_j \mathbf{V}_j = 0,$$

where this expression is preferred to Eq. (2.46) to keep a symmetric formulation of the Stefan–Maxwell system in thermal equilibrium.

The final Stefan–Maxwell system supplied with the mass constraint and the ambipolar assumption yields,

$$\begin{bmatrix} \mathbf{G}^{V'} & -\mathbf{k}^\ominus/s \\ -\mathbf{k}^\ominus/s & 0 \end{bmatrix} \begin{bmatrix} \mathbf{V} \\ s\mathbf{E} \end{bmatrix} = \begin{bmatrix} \mathbf{d}^{\ominus'} \\ 0 \end{bmatrix}$$

where \mathbf{E} is the ambipolar electric field and $s = \|\mathbf{k}\|$ is a scaling factor to improve the robustness of the system.

2.3.3. Chemical kinetic

A reversible chemical reaction $r \in \mathcal{R}$ can be expressed as,

$$\sum_{i \in \mathcal{G}} \nu'_{ir} X_i \rightleftharpoons \sum_{i \in \mathcal{G}} \nu''_{ir} X_i, \quad \forall r \in \mathcal{R}$$

where X_i is the chemical symbol for species $i \in \mathcal{G}$, and ν'_{ir} and ν''_{ir} are the forward and backward stoichiometric coefficients for species i in reaction r .

From the Law of Mass Action, the chemical production rate is given by,

$$\dot{\omega}_i^{\text{chem}} = M_i \sum_{r \in \mathcal{R}} \nu_{ir} \mathfrak{R}_r, \quad \forall i \in \mathcal{G} \quad (2.47)$$

where $\nu_{ir} = \nu''_{ir} - \nu'_{ir}$ and the symbol M_i stands for the species molar mass.

The rate of progress for reaction r is given by

$$\mathfrak{R}_r = k_r^f \prod_{i \in \mathcal{G}} \left(\frac{\rho_i}{M_i} \right)^{\nu_{ir}'} - k_r^b \prod_{i \in \mathcal{G}} \left(\frac{\rho_i}{M_i} \right)^{\nu_{ir}''}, \quad \forall r \in \mathcal{R}, \quad (2.48)$$

and it represents the direction of the reaction, i.e, going towards the destruction of the reactants ($\mathfrak{R}_r > 0$) or products ($\mathfrak{R}_r < 0$). A zero rate of progress means a chemical equilibrium condition which leads to $\dot{\omega}_i^{\text{chem}} = 0$

The forward rate k_r^f follows an Arrhenius-type empirical law given by,

$$k_r^f(T_r^f) = AT_f^\beta \exp\left(-\frac{E_a}{k_B T_r^f}\right), \quad \forall r \in \mathcal{R}$$

where E_a is the activation energy. The pre-exponential term represents to the collision frequency between particles, whereas the exponential part is the probability for the reaction to occur based on the collision energy. The backward rate is evaluated as

$$k_r^b = \frac{k_r^f(T_r^b)}{K_{\text{eq},r}(T_r^b)},$$

where T^f and T^b are the forward and backward temperature, respectively. In thermal non-equilibrium these temperatures are not the same for certain reactions. For instance, the forward rate of the *heavy particle impact dissociation* reaction is controlled by a geometrical temperature $\sqrt{TT^{\text{ve}}}$ to account for vibration-chemistry coupling effects [193, 194]. As for the *electron impact ionization/dissociation*, both rates are controlled by the electron temperature T^{ve} , since the free-electrons are the ones providing the necessary energy to ionize the heavy particle. Table (A.1) shows the reaction type and the choice of temperature used in this work. This temperature controlling parameter is an *ad hoc* solution to the fact that the macroscopic rates are derived from kinetic theory assuming a Maxwellian distribution.

The equilibrium constant $K_{\text{eq},r}$ the reaction r is defined in terms of chemical concentrations,

$$K_{\text{eq},r} = \left(\frac{p^\circ}{\mathcal{R}T} \right)^{\nu_r} \exp\left(-\frac{\Delta G_r^\circ}{\mathcal{R}T}\right),$$

where $\nu_r = \sum_{i \in \mathcal{S}} \nu_{ir}$. Quantity ΔG_r° is the difference of the molar Gibbs energy between products and reactants at standard condition (1 atm and 273.15 K),

$$\Delta G_r^\circ = \sum_{i \in \mathcal{S}} \nu_{ir} G_i^0,$$

where G_i^0 is the standard state molar Gibbs energy of species $i \in \mathcal{S}$,

$$G_j^0 = H_j^0 + TS_j^0, \quad \forall j \in \mathcal{S},$$

being H^0 and S^0 the molar enthalpy and entropy at standard condition, re-

spectively.

2.3.4. Energy transfer mechanisms

A collision between particles results in the energy transfer between the species modes. In the two-temperature model, this energy transfer is accounted for as Ω^{ve} in Eq. (2.11) [94]. Elastic collisions entail energy transfer between translational and internal modes, and in the two-temperature model used in this work it accounts for: i) vibration-translation energy exchange (Ω^{VT}), and ii) free electron and heavy translation energy exchange (Ω^{ET}). Additional energy exchange terms must be included in case the other modes are solved separately, e.g., a rotational-translation energy exchange (Ω^{RT}) if these two modes are separated (for more details refer to Panesi [189]). The elastic transfer terms described here assume that each internal mode follows Boltzmann distribution at their temperature. They vanish when the internal modes equilibrate with translational-rotational mode, i.e., follow a Boltzmann distribution at T . Inelastic collisions alter the energy of the internal modes by adding or removing energy from chemical reactions. In this work, we consider: i) electron-impact ionization (Ω^{I}), ii) chemical-vibration coupling (Ω^{CV}), iii) chemical-electronic-electron coupling (Ω^{CE}).

Vibration-translation energy exchange (Ω^{VT}) follows a Landau-Teller expression,

$$\Omega^{\text{VT}} = \sum_{j \in \mathcal{M}} \rho_j \frac{e_j^{\text{V}}(T) - e_j^{\text{V}}(T^{\text{ve}})}{\tau_j^{\text{VT}}}$$

where $e_j^{\text{V}}(T)$ and $e_j^{\text{V}}(T^{\text{ve}})$ are the average vibrational energy that follows a Boltzmann distribution at T and T^{ve} , respectively. A $\Omega^{\text{VT}} > 0$ represents a translational \rightarrow vibrational energy transfer and *vice versa*. The quantity τ_j^{VT} is the necessary kinetic time for both modes to relax to the same temperature. Millikan and White [176] derived a phenomenological relaxation time which is accurate for $T < 8000$ K,

$$1.01325 \times 10^5 p \tau_j^{\text{MW}} = \sum_{m \in \mathcal{G}} x_m \exp \left[a_{jm} \left(T^{-\frac{1}{3}} - b_{jm} \right) - 18.42 \right], \quad \forall j \in \mathcal{M}$$

with $a_{jm} = 0.00116 \mu_{jm}^{1/2} \theta_j^{\text{V}4/3}$ and $b_{jm} = 0.015 \mu_{jm}^{1/4}$, where μ_{jm} is the reduced mass between the vibrator j and the collision partner m .

The expression above considers an infinitely large cross-section (or relaxation time) at high temperatures, leading to a sudden equilibrium between the two modes. Park [195, 196] added a correction to the Millikan and White [176] relaxation time by limiting the cross-section at high temperatures,

$$\tau_j^{\text{P}} = \left(n_j \sqrt{\frac{8k_B T_h}{\pi m_j}} \sigma_j^{\text{V}} \right)^{-1}, \quad \forall j \in \mathcal{M}$$

where σ_j^Y is an effective cross-section. This correction to the standard Landau-Teller expression yields the Ω^{VT} final expression,

$$\Omega^{\text{VT}} = \sum_{j \in \mathcal{M}} \rho_j \frac{e_j^Y(T) - e_j^Y(T^{\text{ve}})}{(\tau_j^{\text{MW}} + \tau_j^{\text{P}})}.$$

Free electron and heavy translation energy exchange (Ω^{ET}) corresponds to the energy transfer due to elastic collisions between the free electron and the heavy particle. Similar to the Ω^{VT} , this energy exchange follows a Landau-Teller relaxation,

$$\Omega^{\text{ET}} = \rho_e \frac{e_e^{\text{T}}(T) - e_e^{\text{T}}(T^{\text{ve}})}{\tau^{\text{eT}}}$$

and the relaxation time,

$$\frac{1}{\tau^{\text{eT}}} = \sum_{i \in \mathcal{H}} \frac{8}{3} \frac{m_e}{m_i} n_i \sqrt{\frac{8k_B T^{\text{ve}}}{\pi m_e}} \bar{Q}_{ei}^{(1,1)},$$

is derived from kinetic theory, where $\bar{Q}_{ei}^{(1,1)}$ is the reduced collision integral for the electron-heavy interaction.

Electron-impact ionization (Ω^{I}) corresponds to the energy provided by the electron bath during electron-impact ionization reactions \mathcal{I} . The necessary energy to ionize a heavy species is removed from the electron, resulting in a loss of the electron translation mode,

$$\Omega^{\text{I}} = \sum_{r \in \mathcal{I}} \Delta H^r \mathfrak{R}_r,$$

where \mathfrak{R}_r is the rate of progress Eq. (2.48). The term ΔH^r corresponds to the necessary energy to ionize an atom from its ground state. Hartung et al. [105] suggest taking the ionization energy for the electron-impact ionization reactions of N and O from an excited state; therefore, we use $4.05 \times 10^8 \text{ J kg}^{-1} \text{ mol}^{-1}$ for the reaction (39) and $4.3 \times 10^8 \text{ J kg}^{-1} \text{ mol}^{-1}$ for the reaction (40) of Table (A.1).

Chemical-vibration coupling (Ω^{CV}) corresponds to the energy added or removed to the vibration-electronic mode due to chemical reactions. This coupling can be divided into preferential and non-preferential empirical models [189]. The former model assumes that dissociation most likely occurs from the higher vibrational states. Through collisions, molecules in the lower vibrational states are excited to a higher state before dissociating. Scoggins [229] and Panesi [189] present a detailed review of this model.

In this work, we use the non-preferential model, which assumes an equal probability for the dissociation to occur from any vibrational energy state.

The energy transfer term is given by,

$$\Omega^{CV} = \sum_{j \in \mathcal{M}} e_j^V \dot{\omega}_j^{\text{chem}},$$

where e^V represents the average vibrational energy.

Chemical-electronic-electron coupling (Ω^{CE}) corresponds to the energy added to electronic-electron mode due to chemical reactions. We add this term to represent the production/destruction of species that are already electronically excited [195],

$$\Omega^{\text{CE}} = \sum_{j \in \mathcal{H}} e_j^{\text{E}} \dot{\omega}_j^{\text{chem}} + e_e^T \dot{\omega}_e^{\text{chem}},$$

where the second term on right-hand side represents the electron-chemistry coupling effect.

Remark. In the work of Graille et al. [98], the Ω^{I} and $e_e^T \dot{\omega}_e^{\text{chem}}$ were derived rigorously from kinetic theory. This derivation includes a proper scaling of the Boltzmann equation to account for the electron mass disparity. Such rigorous derivation of the other exchange terms is not available yet in the literature.

2.4. Numerical methods

In this section we describe the numerical discretization of Eq. (2.5) using the Method-Of-Lines (MOL) [117]. This method separates the spatial and the temporal dependence of the Partial Differential Equation (PDE) leading to an Ordinary Differential Equation (ODE). The spatial integration of the ODE is performed with a cell-centered FV method, whereas the temporal part is integrated with the Backward-Euler (BE) method.

The quasi-1D nature of Eq. (2.5) allows for a fast numerical solution of flows containing complex physico-chemical properties. The stagnation-line solver was initially developed by Munafò [181], Munafò and Magin [182] to study nitrogen State-To-State (STS) flows. Since then, the code has been extended to study Gas-Surface Interaction (GSI) [19–21, 71, 255], flow-radiation coupling [73, 74, 228, 238] and flow-material coupling [72, 226].

2.4.1. Stagnation-line discretization

Equation (2.5) is discretized both in space and time yielding,

$$\begin{aligned} \frac{\delta \mathbf{U}_i^n}{\Delta t_i} \Delta r_i + \mathbf{F}_{i+\frac{1}{2}}^{\mathbf{i}^{n+1}} - \mathbf{F}_{i-\frac{1}{2}}^{\mathbf{i}^{n+1}} + \mathbf{F}_{i+\frac{1}{2}}^{\mathbf{v}^{n+1}} - \mathbf{F}_{i-\frac{1}{2}}^{\mathbf{v}^{n+1}} = \\ (\mathbf{S}_i^{\mathbf{i}^{n+1}} + \mathbf{S}_i^{\mathbf{v}^{n+1}} + \mathbf{S}_i^{\mathbf{k}^{n+1}} + \mathbf{S}_i^{\text{rad}^n}) \Delta r_i, \end{aligned} \quad (2.49)$$

where the superscript n corresponds to the temporal index, subscript i to the spatial index (cell center location) and Δr_i the cell length. The local time-step is based on the Courant-Friedrichs-Lewy (CFL) number such that,

$$\Delta t_i = \frac{\text{CFL} \Delta r_i}{\left[|u_r| + a + \frac{1}{\Delta r} \max\left(\frac{4}{3} \frac{\mu}{\rho}, \frac{\lambda}{c_v}\right) \right]_i},$$

where the viscous contribution on the denominator prevents numerical instabilities on diffusion dominated regions, such as the boundary layer. Equation (2.49) reaches a steady-state solution when $\delta \mathbf{U}^n = \mathbf{U}^{n+1} - \mathbf{U}^n \rightarrow 0$.

The non-linear fluxes and source terms in Eq. (2.49) are linearized by means of a Taylor-Series expansion around time n . The inviscid flux is linearized by an upwind splitting of the positive and negative eigenvalue contributions of the Jacobian matrix [149] such that $\mathbf{A}^\pm = \mathbf{R}\mathbf{\Lambda}^\pm\mathbf{L}$,

$$\mathbf{F}_{i+\frac{1}{2}}^{i,n+1} \simeq \mathbf{F}_{i+\frac{1}{2}}^{i,n} + (\mathbf{A}^+)_i^n \delta \mathbf{U}_i^n + (\mathbf{A}^-)_{i+1}^n \delta \mathbf{U}_{i+1}^n, \quad (2.50)$$

where \mathbf{R} and \mathbf{L} are the right and left eigenvector matrices and $\mathbf{\Lambda}$ the eigenvalue matrix. The kinetic and the inviscid source terms simple yields,

$$\mathbf{S}_{i+\frac{1}{2}}^{i,n+1} \simeq \mathbf{S}_{i+\frac{1}{2}}^{i,n} + \left(\frac{\partial \mathbf{S}^i}{\partial \mathbf{U}} \right)_i^n \delta \mathbf{U}_i^n, \quad \mathbf{S}_{i+\frac{1}{2}}^{k,n+1} \simeq \mathbf{S}_{i+\frac{1}{2}}^{k,n} + \left(\frac{\partial \mathbf{S}^k}{\partial \mathbf{U}} \right)_i^n \delta \mathbf{U}_i^n.$$

The viscous fluxes and source terms are linearized in two steps. The first step consists in writing these two quantities by separating terms which depend on the gradient of conservative variables and terms which are non-linear (for more details refer to Munafò [181]). In the second step, the viscous flux and source term are linearized by means of a Taylor-Series expansion. The final expression for the viscous fluxes yields,

$$\mathbf{F}_{i+\frac{1}{2}}^{\mathbf{v},n+1} = \mathbf{F}_{i+\frac{1}{2}}^{\mathbf{v},n} + 2\mathbf{A}_{i+\frac{1}{2}}^{\mathbf{v},n} \left(\frac{\delta \mathbf{U}_{i+1}^n - \delta \mathbf{U}_i^n}{\Delta r_{i+1} + \Delta r_i} \right) + \left(\frac{\partial \mathbf{B}^{\mathbf{v}}}{\partial \mathbf{U}} \right)_i^n \delta \mathbf{U}_i^n + \left(\frac{\partial \mathbf{B}^{\mathbf{v}}}{\partial \mathbf{U}} \right)_{i+1}^n \delta \mathbf{U}_{i+1}^n,$$

and the viscous source terms,

$$\mathbf{S}_{i+\frac{1}{2}}^{\mathbf{v},n+1} = \mathbf{S}_{i+\frac{1}{2}}^{\mathbf{v},n} + 2\mathbf{A}_{s,i}^{\mathbf{v},n} \left(\frac{\delta \mathbf{U}_{i+1}^n - \delta \mathbf{U}_{i-1}^n}{\Delta r_{i+1} + 2\Delta r_i + \Delta r_{i-1}} \right) + \left(\frac{\partial \mathbf{B}_s^{\mathbf{v}}}{\partial \mathbf{U}} \right)_i^n \delta \mathbf{U}_i^n.$$

The works of Munafò [181] and Scoggins [229] provide the analytical expressions for the Jacobian matrices \mathbf{A} , $\mathbf{A}^{\mathbf{v}}$, $\mathbf{A}_s^{\mathbf{v}}$, $\partial_{\mathbf{U}} \mathbf{S}^i$, $\partial_{\mathbf{U}} \mathbf{S}^k$, $\partial_{\mathbf{U}} \mathbf{B}^{\mathbf{v}}$, $\partial_{\mathbf{U}} \mathbf{B}_s^{\mathbf{v}}$.

Inserting the linearized expressions aforementioned into Eq. (2.49) yields the following block-tridiagonal linear system which can be solved with the Thomas algorithm,

$$\mathbf{M}_{\mathbf{L}i} \delta \mathbf{U}_{i-1}^n + \mathbf{M}_{\mathbf{C}i} \delta \mathbf{U}_i^n + \mathbf{M}_{\mathbf{R}i} \delta \mathbf{U}_{i+1}^n = -\mathbf{R}_i^n \quad (2.51)$$

where,

$$\begin{aligned} \mathbf{M}_{\mathbf{L}i} &= \frac{2 \Delta r_i \mathbf{A}_{\mathbf{s}i}^{\mathbf{v}}}{(\Delta r_{i+1} + 2\Delta r_i + \Delta r_{i-1})} - \frac{2\mathbf{A}_{i-1/2}^{\mathbf{v}}}{(\Delta r_{i-1} + \Delta r_i)} + \left(\frac{\partial \mathbf{B}^{\mathbf{v}}}{\partial \mathbf{U}} \right)_{i-1} + (\mathbf{A}^+)_{i-1} \\ \mathbf{M}_{\mathbf{C}i} &= \left[\frac{\bar{\mathbf{I}}}{\Delta t_i} - \left(\frac{\partial \mathbf{S}^{\mathbf{i}}}{\partial \mathbf{U}} + \frac{\partial \mathbf{S}^{\mathbf{k}}}{\partial \mathbf{U}} + \frac{\partial \mathbf{B}_{\mathbf{s}}^{\mathbf{v}}}{\partial \mathbf{U}} \right) \right]_i \Delta r_i + |\mathbf{A}_i| + \\ &\quad \frac{2\mathbf{A}_{i+1/2}^{\mathbf{v}}}{(\Delta r_{i+1} + \Delta r_i)} + \frac{2\mathbf{A}_{i-1/2}^{\mathbf{v}}}{(\Delta r_{i-1} + \Delta r_i)} \\ \mathbf{M}_{\mathbf{R}i} &= -\frac{2 \Delta r_i \mathbf{A}_{\mathbf{s}i}^{\mathbf{v}}}{(\Delta r_{i+1} + 2\Delta r_i + \Delta r_{i-1})} - \frac{2\mathbf{A}_{i=1/2}^{\mathbf{v}}}{(\Delta r_{i+1} + \Delta r_i)} + \left(\frac{\partial \mathbf{B}^{\mathbf{v}}}{\partial \mathbf{U}} \right)_{i+1} + (\mathbf{A}^-)_{i+1} \\ \mathbf{R}_i &= \mathbf{F}_{i+\frac{1}{2}}^{\mathbf{i}} - \mathbf{F}_{i-\frac{1}{2}}^{\mathbf{i}} + \mathbf{F}_{i+\frac{1}{2}}^{\mathbf{v}} - \mathbf{F}_{i-\frac{1}{2}}^{\mathbf{v}} - (\mathbf{S}_i^{\mathbf{i}} + \mathbf{S}_i^{\mathbf{v}} + \mathbf{S}_i^{\mathbf{k}} + \mathbf{S}_i^{\mathbf{rad}}) \Delta r_i. \end{aligned}$$

The radiative source term $\mathbf{S}^{\mathbf{rad}}$ is solved explicitly and updated after a certain number of iterations. We give more details in Chapter 6.

The viscous fluxes and source terms are evaluated in terms of primitive variables,

$$\mathbf{V} = [\rho_i, u_r, u_\theta, T, T^{\text{ve}}]^T,$$

where their value and gradients at the volume interfaces are computed by a weighted average and a central finite difference approximation, respectively,

$$v_{i+\frac{1}{2}} = \frac{v_{i+1} \Delta r_{i+1} + v_i \Delta r_i}{\Delta r_{i+1} + \Delta r_i}, \quad \left(\frac{\partial v}{\partial r} \right)_{i+\frac{1}{2}} = 2 \left(\frac{v_{i+1} - v_i}{\Delta r_{i+1} + \Delta r_i} \right)$$

and the gradients in the viscous source term are evaluated at the cell center with a two point central finite difference,

$$\left(\frac{\partial v}{\partial r} \right)_i = 2 \left(\frac{v_{i+1} - v_{i-1}}{\Delta r_{i+1} + 2\Delta r_i + \Delta r_i} \right).$$

The primitive variables are reconstructed at the interface using the Monotone Upstream Centered Schemes for Conservation Laws (MUSCL) method of van Leer [256] to reach second order accuracy in space,

$$\begin{aligned} v_{\mathbf{L},i+\frac{1}{2}} &= v_i + \frac{1}{2} \phi(r_{\mathbf{L},i})(v_i - v_{i-1}), & v_{\mathbf{R},i+\frac{1}{2}} &= v_{i+1} + \frac{1}{2} \phi(r_{\mathbf{R},i+1})(v_{i+2} - v_{i+1}), \\ r_{\mathbf{L},i} &= \frac{v_{i+1} - v_i}{v_i - v_{i-1}}, & r_{\mathbf{R},i+1} &= \frac{v_{i+2} - v_{i+1}}{v_{i+1} - v_i}, \end{aligned}$$

where $\phi(r)$ is the slope limiter function and r is the ratio of consecutive differences. The numerical inviscid fluxes at the interface are computed based on the reconstructed primitive variables $\mathbf{F}_{i+\frac{1}{2}}^{\mathbf{i}} = \mathbf{F}^{\mathbf{i}}(\mathbf{V}_{\mathbf{L},i+\frac{1}{2}}, \mathbf{V}_{\mathbf{R},i+\frac{1}{2}})$.

2.4.2. Flux splitting methods

The Roe's approximate Riemann solver [218] is one of the most popular methods to solve the inviscid fluxes and yields,

$$\mathbf{F}^i_{i+\frac{1}{2}} = \frac{1}{2} [\mathbf{F}^i(\mathbf{U}_{i+1}) + \mathbf{F}^i(\mathbf{U}_i)] - \frac{1}{2} \left| \tilde{\mathbf{A}}(\tilde{\mathbf{U}}) \right| (\mathbf{U}_{i+1} - \mathbf{U}_i) \quad (2.52)$$

where $\left| \tilde{\mathbf{A}}(\tilde{\mathbf{U}}) \right|$ is a dissipation matrix and corresponds the eigensystem of the inviscid flux Jacobian ($\mathbf{A} = \partial_{\mathbf{U}} \mathbf{F}^i$ as in Eq. (2.50)) aforementioned. The quantity $\tilde{\mathbf{U}}$ is the conservative variable vector evaluated by the Roe's average state, where Prabhu [212] extended the original scheme to multi-temperature models.

This scheme belongs to the Flux Difference Splitting (FDS) family, and due to its low dissipative nature, it is accurate in the viscous region of the flow field. This is an important feature in order to have a correct heating profiles at the wall. Moreover, the Roe scheme has excellent shock capturing properties [27]. However, this scheme becomes highly unstable in presence of strong shocks [12].

The high entry velocities endured by meteors has motivated the implementation of a more suitable scheme to perform in such flow conditions. A family of schemes known for performing well at low and high velocities is the AUSM-family. In this chapter, we have implemented the latest version into the stagnation-line solver.

2.4.2.1. AUSM⁺-up2 scheme

The AUSM-family has been developed by Liou [148] with the intention of having reliable schemes at low speeds. The stability of these schemes was obtained by introducing a numerical speed of sound, re-scaling the Mach number to unity in the subsonic range. The AUSM-family schemes has proven to work for different range of velocities without the need of preconditioning the time derivative terms in the governing equations. Despite this flexibility, the primordial versions of the AUSM-family suffer from non-smoothness in the pressure split function, which was remedied in AUSM⁺-up by introducing dissipation in the pressure flux. The proper scaling for the numerical fluxes makes the AUSM⁺-up a low dissipative scheme, yielding accurate predictions of the surface heat flux. The dissipation in the pressure flux works only for low speeds and it vanishes in the supersonic region, meaning that for strong shocks this scheme might become unstable; as the Roe scheme aforementioned. Kitamura and Shima [133] developed the AUSM⁺-up2 scheme to overcome this deficiency. This scheme combines mass flux of AUSM⁺-up and the pressure flux of SLAU2 scheme.

As for all AUSM-family schemes, the inviscid flux is split into a convective and a pressure flux,

$$\mathbf{F}^i_{i+\frac{1}{2}} = \dot{m}\psi + p\mathbf{N}$$

where the scalar mass flux $\dot{m} = \rho u_r$ and,

$$\begin{aligned}\boldsymbol{\psi} &= [y_i, u_r, u_\theta, H, e^{\text{ve}}]^T, \\ \mathbf{N} &= [0, 1, 0, 0, 0]^T.\end{aligned}$$

The upwind inviscid flux is approximated as,

$$\mathbf{F}^i_{i+\frac{1}{2}} = \frac{\tilde{m} + |\tilde{m}|}{2} \boldsymbol{\psi}_R - \frac{\tilde{m} - |\tilde{m}|}{2} \boldsymbol{\psi}_L + \tilde{p} \mathbf{N}$$

where \tilde{p} is interface pressure flux and \tilde{m} the upwind interface mass flux,

$$\tilde{m} = a_{1/2} M_{1/2} \begin{cases} \rho_L & u_r > 0, \\ \rho_R & u_r \leq 0. \end{cases}$$

The interface Mach number is given by,

$$M_{1/2} = f_M^+ + f_M^- + M_p$$

where the split Mach numbers functions are,

$$f_M^\pm = \begin{cases} \pm \frac{1}{4} (M \pm 1)^2 [1 \mp 2(\mp \frac{1}{4} (M \mp 1)^2)] & |M| \leq 1, \\ \frac{1}{2} (M \pm |M|) & |M| > 1, \end{cases}$$

and the pressure diffusion term to insure stability a low speeds,

$$M_p = \frac{0.25}{f_a} \max(1 - \bar{M}^2, 0) \frac{p_R - p_L}{\bar{\rho} a_{1/2}^2},$$

with the scaling factor,

$$f_a = M_0(2 - M_0)$$

where the reference Mach number is

$$M_0^2 = \min\left(1, \max\left(\bar{M}^2, \bar{M}_\infty^2\right)\right).$$

Up to this point, the numerical mass flux \tilde{m} is identical as the AUSM⁺-up scheme. The numerical pressure flux \tilde{p} is given by the SLAU2 scheme [133],

$$\tilde{p} = \frac{p_L + p_R}{2} + \frac{f_P^+|_{\alpha=0} - f_P^-|_{\alpha=0}}{2} (p_L - p_R) + P_u$$

where the pressure split functions are,

$$f_P^\pm|_{\alpha=0} = \begin{cases} \pm \frac{1}{4} (M \pm 1)^2 [(\mp 2 - M)] & |M| \leq 1, \\ \frac{1}{2} \frac{(M \pm |M|)}{M} & |M| > 1, \end{cases}$$

and the dissipation term is proportional to the Mach number at supersonic

speeds,

$$P_u = \sqrt{\frac{u_{r,L}^2 + u_{r,R}^2}{2}} (f_P^+|_{\alpha=0} + f_P^-|_{\alpha=0} - 1) \bar{\rho} a_{1/2}.$$

Finally, the average density and Mach number are given by,

$$\bar{\rho} = \frac{\rho_L + \rho_R}{2} \quad \text{and} \quad \bar{M}^2 = \frac{M_L^2 + M_R^2}{2}.$$

2.5. Results

In this section, we verify the AUSM⁺-up2 implementation in the stagnation-line solver against the pre-implemented Roe scheme. The objective is to study the differences between both schemes for meteoroid entry conditions. We carry out a numerical simulation of a non-ablative 1 m radius body with an entry velocity of 15 km s⁻¹ at 50 km altitude. For simplicity, the flow is composed by eleven air species (see Table (2.1)).

Table 2.1.: Gaseous species used in this chapter.

air species										
e ⁻	N	NO	N ₂	O	O ₂	N ⁺	O ⁺	NO ⁺	N ₂ ⁺	O ₂ ⁺

Figure (2.7) shows the thermodynamic properties computed along the stagnation streamline with the AUSM⁺-up2 and the Roe scheme. The match between both schemes is excellent especially at the shock location, ≈ 47 mm from the surface. A quantity of interest is the surface heat flux and the percent relative error between both schemes is $\delta \approx 3\%$. The AUSM⁺-up2 has proven to be more stable during the converge allowing us to reach higher CFL values.

It is interesting to analyze these results from a physico-chemical point of view, which lay ground for the flow interpretation in the following chapters. Figures (2.7a) and (2.7b) show the T and T^{ve} along the stagnation streamline, respectively. The translational-rotational temperature quickly rise at the shock location and immediately drops. This drop is owed to: i) chemical reactions at the shock which alter the mixture energy, ii) energy transfer between to the translation-rotational to vibrational-electronic-electron modes. Past the shock, one can observe a thermal equilibrium $T = T^{\text{ve}}$ in the shock layer. This equilibrium is owed to the high pressure after the shock, shown in Fig. (2.7c), which results in a highly collisional gas. The high collisional frequency leads to a chemical equilibrium and, thus, to a zero net energy transfer between the internal modes in the shock layer.

Figure (2.8) shows the composition along the stagnation streamline. Upstream the shock, where the temperature is low, the mixture is only composed by N₂ and O₂. At the shock, the temperature rises to 50 000 K (see Fig. (2.7a)) inducing the first reactions, *heavy particle impact dissociation* in Table (A.1).

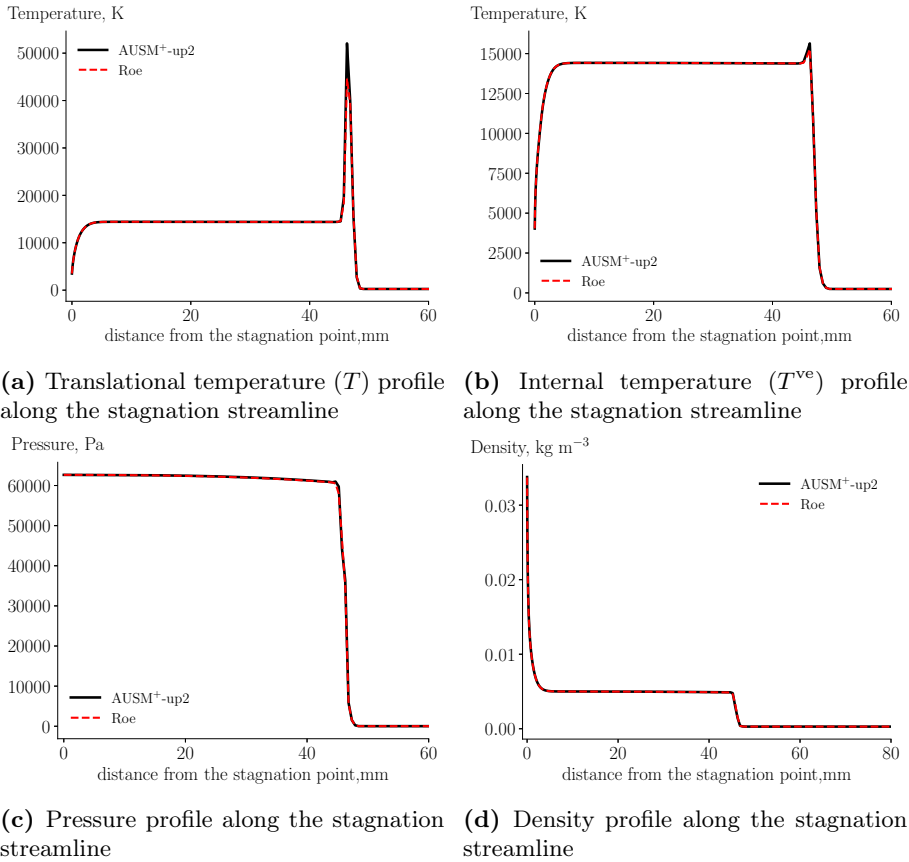


Figure 2.7.: Comparison of the thermodynamic properties between Roe and AUSM⁺-up2 scheme.

The creation of electron starts with the *associative ionization* reaction,



and once the first electrons are formed, a so-called electron avalanche occurs due to *electron impact ionization*. For the test case presented in this section, all these reactions occur close to the shock. The system quickly gets into chemical equilibrium in the shock layer, as we can see from the plateau in Fig. (2.8). As the temperature cools down in the boundary layer, the ionized species recombines into neutrals and atoms into molecules.

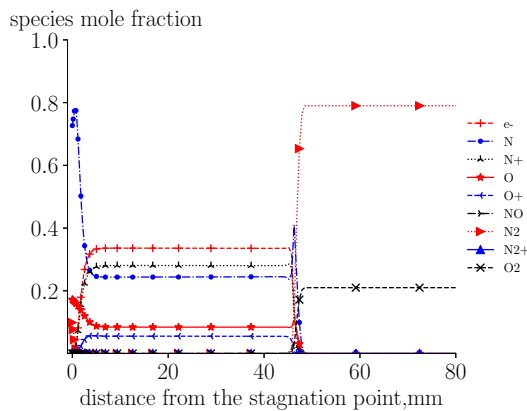


Figure 2.8.: Composition along the stagnation streamline computed with AUSM⁺-up2 scheme.

The energy transfer terms due to chemical reaction and the internal modes relaxation at the shock is shown in Fig. (2.9). The dominant terms are Ω^{ET} and Ω^{I} . The former occurs due to a collision between heavy and electrons which results in the acceleration of the electron, whereas the latter term results into a deceleration. This energy exchange can be seen from the internal temperature profile in Fig. (2.7b), where the initial rise is due to the positive energy transfer terms and the small drop is due to Ω^{I} .

2.6. Conclusion

In this chapter, we have presented the governing equations for hypersonic flows applied to meteoroid entry. We have used state-of-the-art physico-chemical models to close the governing equations. The models include accurate thermodynamic, transport, kinetic, and energy transfer properties for high-temperature flows. We have included the properties of metallic species in the open-source MUTATION⁺⁺ library. These properties are essential for the following chapters to study the surface evaporation and the flow radiation.

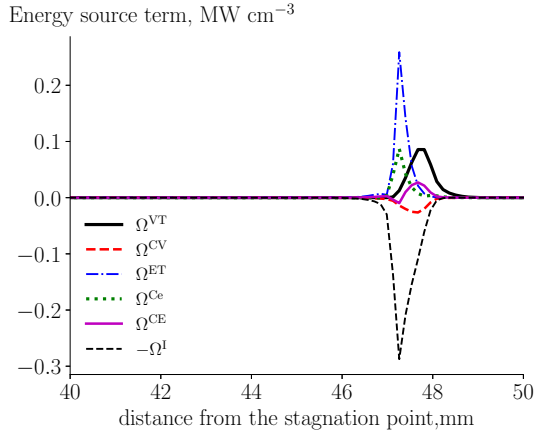


Figure 2.9.: Energy transfer source terms computed with AUSM⁺-up2 scheme.

Even though these models are accurate and standard in the hypersonic community, they are limited to a certain level of non-equilibrium. We have simulated a spherical body at 50 km altitude with a 15 km s^{-1} entry velocity. At these conditions, we have observed a quick thermalization of the internal modes right past the shock. This effect is owed to the high post-shock pressure, which results in a large number of collisions between particles. Therefore, we do not expect large deviations from equilibrium for the conditions of interest in this thesis. Moreover, the flow composition is mostly dissociated and ionized aftershock, meaning that the limitations of RRHO do not apply in this case.

We have used the stagnation-line solver developed at von Karman Institute for fluid dynamics (VKI) to compute the discretized version of the governing equations. This solver is quite fast since it solves the dimensionally reduced Navier Stokes equations. Finally, we have implemented the AUSM⁺-up2 splitting scheme, which has proven to have the same accuracy as the Roe scheme but is more stable at higher Mach numbers.

Concerning the collision integral data, the potential of Pirani et al. [205] requires less data even though it provides accurate properties. Therefore, we recommend this potential for upcoming studies.

CHAPTER 3

Surface evaporation

What we can do is to establish a bridge between the various levels in order to form a coherent picture; the whole of Boltzmann's work is a masterpiece of this procedure, i.e., how to construct, starting from atoms, a description that explains everyday life.

— Carlo Cercignani, *Ludwig Boltzmann: The Man Who Trusted Atoms.*

3.1. Introduction

The evaporation of a liquid surface is one of the most common phenomena present in our daily lives, from making a cup of tea to fuel combustion. This phenomenon has been studied since the 19th century, and yet it is a challenging problem. Although hydrodynamic equations can describe the liquid phase well, this is not the case for the vapor due to non-equilibrium close to the interface. This non-equilibrium results in a kinetic layer called the Knudsen layer for which the continuum assumption does not hold, i.e., the Navier-Stokes equations are not valid [57]. At a macroscopic level, the presence of this layer creates a jump of macroscopic variables such as temperature, density, and velocity at the vapor-liquid interface.

Different modeling approaches have been adopted to predict evaporation over the years with distinct levels of approximation. The *heat-of-ablation* method is a simplified approach in the engineering community. It assumes that the gas/liquid interface is at the saturation temperature, and the evaporation rate is obtained by energy balance at the surface [25, 130, 178]. Another approach used by the aerospace community is to presume chemical equilibrium between the gas/liquid interface and to estimate the mass transfer based on transfer coefficients [65, 177]. These approaches are simplified because they do not simulate the dynamics between evaporation and condensation, causing the non-equilibrium at the interface.

On the other hand, kinetic theory provides a more detailed and physically sound approach to solve this non-equilibrium at the interface. The first known and most popular evaporation model based on kinetic theory is from Hertz [115] and Knudsen [135]; initially intended to study evaporation of mercury

into a vacuum. A half-century later, Schrage [224] improved the Hertz-Knudsen model by including non-linear convective terms. Since that period, this problem has received considerable attention, and researchers have used several approaches to study it from a mesoscopic and microscopic level. At the mesoscopic scale, the Boltzmann [84, 85] and the Enskog-Vlasov equations [86, 88, 89] were numerically solved using the Direct Simulation Monte Carlo (DSMC) method, where the latter equation considers both the liquid and gas phase. The solution of the Boltzmann equation with the moment methods is presented by Aursand and Ytrehus [8], Bond and Struchtrup [28], Yasuda et al. [276], Ytrehus [278], Ytrehus and Østmo [279]. At the microscopic level, the gas-liquid interface was solved with Molecular Dynamics (MD) in the work of Kon et al. [137], Meland et al. [172]. Frezzotti and Barbante [87] gives an extensive review of the existing kinetic models for evaporation and condensation flows. For large-scale problems and when the external flow approaches the continuum condition, using the first three methods is unfeasible due to the computational cost. Hence, the only possible solution is to derive macroscopic properties from the moments of the Boltzmann equation to model the Knudsen layer. This method is relatively easy for the evaporation of a single component [279], but it becomes mathematically complex for the evaporation of multicomponent mixtures; see Yasuda et al. [276].

The objective of this chapter is twofold: i) to present an overview of the evaporation models with distinct levels of approximation; ii) to develop a multicomponent evaporation model under translational non-equilibrium (rarefied gas effects) as well as chemical equilibrium and non-equilibrium of the gas-liquid interface. We start by expressing the balance equations between the gas and the surface, derived from Navier-Stokes equations, in Section 3.2. The closure of these balances under the equilibrium assumption is given in Section 3.3, where we extend the state-of-the-art engineering models to address multicomponent evaporation. Section 3.4 shows a closure, for multicomponent evaporation, derived from the kinetic theory that includes the jump of macroscopic properties across the Knudsen layer. We apply both equilibrium and non-equilibrium models to the evaporation of a multicomponent surface under continuum flow conditions (Section 3.6) then we compare the latter model with the DSMC reference solutions (Section 3.5). We stress that the balance equations can consider both the evaporation of liquids and the ablation of carbon-based materials. The latter is essential to describe the experiments shown in Chapter 5.

This work represents the first step to derive the evaporation of multicomponent surfaces. It is original on the development of the non-equilibrium model without the mathematical complexity present in the moment method of the Boltzmann equation for this problem. This chapter is general for any evaporation problem in the sense that its outcome goes beyond meteor entry.

3.2. Flux balances at the surface

At steady state, the balances between the flow and the surface are formulated by transforming the volumetric governing equations of mass, momentum, and energy into an infinitesimal control volume attached to the surface. In the case of a reactive surface — such as ablation of carbon-based materials and evaporation of liquid surfaces — one must consider source terms which represent the creation or destruction of mass at the surface. Equation (3.1) shows the generic surface balance for mass, momentum and energy,

$$[\mathbf{F}_g - \mathbf{F}_c] \cdot \mathbf{n} = \dot{\Omega}_{\text{surf}}, \quad (3.1)$$

where \mathbf{F}_g represents the flux from the gas side, \mathbf{F}_c is the flux from the material side, \mathbf{n} the unit vector normal to the surface and $\dot{\Omega}_{\text{surf}}$ the surface source term.

Generally, the momentum balance is neglected because the velocity boundary condition is obtained from Eq. (3.4). Note that in the case of significant surface forces, such as surface tension due to thermo-capillary effects, a momentum balance should be considered [44, 79].

3.2.1. Surface mass balance

In the case of reactive flows where one needs to solve a mass conservation equation for each species $i \in \mathcal{G}$ a Surface Mass Balance (SMB) for each species must be considered, as illustrated in Fig. (3.1). This balance represents a system of

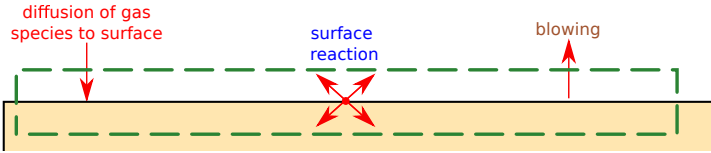


Figure 3.1.: Illustration of the mass balances on the surface.

non-linear equations whereby the solution is the species gas composition created by surface reactions given by the species mass density at the wall $\rho_{w,i}$. The mass balance of species $i \in \mathcal{G}$ writes as

$$\begin{cases} \mathbf{F}_{g,i} = \rho_{w,i}(\mathbf{u}_w - \mathbf{u}_\Gamma) + \mathbf{J}_{w,i}, \\ \mathbf{F}_{c,i} = 0, \\ \dot{\Omega}_{\text{surf},i} = \dot{m}_{\text{ablat},i} + \dot{m}_{\text{vap},i} = \dot{m}_i. \end{cases} \quad \forall i \in \mathcal{G}, \quad (3.2)$$

On the gas side ($\mathbf{F}_{g,i}$), \mathbf{u}_w is the blowing velocity, \mathbf{u}_Γ is the surface recession velocity and $\mathbf{J}_{w,i}$ the species diffusion flux. It is worthwhile to note that $\mathbf{u}_\Gamma \cdot \mathbf{n} \ll \mathbf{u}_w \cdot \mathbf{n}$; thus, this term is usually neglected. On the material side ($\mathbf{F}_{c,i}$), a term such as $\rho_{s,i}\mathbf{u}_s$ can be added to represent the flux of gases going towards

the surface, e.g., the pyrolysis gases in the case of an carbon-based ablators that contain resin. In this case, $\rho_{s,i}$ would be the density of the pyrolysis gases and \mathbf{u}_s the blowing velocity. The surface source term accounts for thermochemical carbon-ablation $\dot{m}_{\text{ablat},i}$, and/or evaporation $\dot{m}_{\text{vap},i}$. It is possible to include catalytic reactions [21], which are not considered in this work. The definition of each source term is

$$\dot{m}_{\text{ablat},i} = \sum_{r \in \mathcal{R}^{\text{ablat}}} \dot{m}_{\text{ablat},i}^r, \quad \dot{m}_{\text{vap},i} = \sum_{r \in \mathcal{R}^{\text{vap}}} \dot{m}_{\text{vap},i}^r \quad \forall i \in \mathcal{G}, \quad (3.3)$$

where the set $\mathcal{R}^{\text{ablat}}$ corresponds to all carbon ablation reactions and \mathcal{R}^{vap} to all evaporation reactions. By summing Eq. (3.2) over the set of species \mathcal{G} , one obtains the total mass blowing rate,

$$\sum_{i \in \mathcal{G}} \dot{m}_i = \dot{m} = \rho_w \mathbf{u}_w \cdot \mathbf{n} = \rho_s \mathbf{u}_\Gamma \cdot \mathbf{n} \quad (3.4)$$

with,

$$\mathbf{u}_w \cdot \mathbf{n} = \frac{\dot{m}}{\rho_w} \quad (3.5)$$

where ρ_w and ρ_s are the mass density of the gas and condensed phase, respectively. From Eq. (3.4), it is obvious that $\mathbf{u}_\Gamma \cdot \mathbf{n} \ll \mathbf{u}_w \cdot \mathbf{n}$ due to the density difference of both phases.

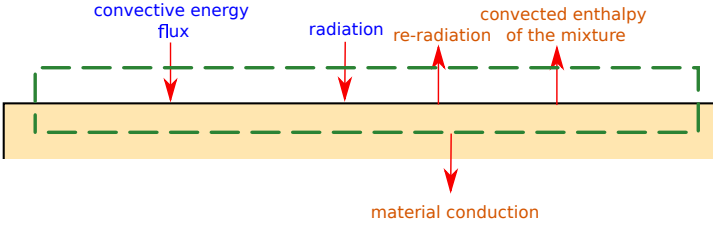


Figure 3.2.: Illustration of the energy balances on the surface.

3.2.2. Surface energy balance

The Surface Energy Balance (SEB) illustrated in Fig. (3.2) is a non-linear equation for the surface temperature T_w , and it writes as,

$$\begin{cases} \mathbf{F}_g = \dot{m}L_{\text{heat}} + \mathbf{q}^{\text{cond}}, \\ \mathbf{F}_c = k \nabla T_w, \\ \dot{\Omega}_{\text{surf}} = \epsilon(\sigma T_w^4 - \mathbf{q}_{\text{in}}^{\text{rad}} \cdot \mathbf{n}). \end{cases} \quad (3.6)$$

On the gas side, the term $\dot{m}L_{\text{heat}}$ represents the flux of energy released from the surface into the gas phase due to reactions, where L_{heat} is the latent heat

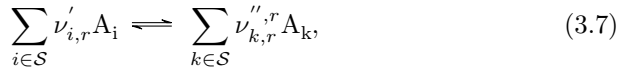
of vaporization and/or the latent heat of ablation for carbon-based ablators [25]. Quantity \mathbf{q}^{cond} is the conductive heat flux from the gas into the surface (Fourier's law). On the material side, the term $k\nabla T_w$ represents the conductive heat flux in the material. This term is estimated with a steady-state model [254] or by solving the thermal response of the material numerically [72, 74]. The latter requires a coupling between the flow and the material (Chapter 4). Quantity $\dot{\Omega}_{\text{surf}}$ represents the balance of radiative fluxes on the surface, ϵ is the material emissivity, σT_w^4 is the radiative flux from the material and $\mathbf{q}_{\text{in}}^{\text{rad}}$ is the radiative flux from the boundary layer.

The solution of the coupled system Eqs. (3.2) and (3.6) provides the surface composition and temperature, which serve as boundary conditions to the flow solver.

3.2.3. Equilibrium vapor pressure

The closure of the \dot{m}_i in Eqs. (3.2) and (3.6) is based on the surface reactions considered, i.e., thermochemical carbon-ablation and/or evaporation. For the thermochemical ablation of carbon-based materials, three types of reactions at the material-vapor interface are considered: oxidation, nitridation, and sublimation. The rates for the three reactions were derived by Park et al. [202] from experimental results. In the case of an evaporating surface, the $\dot{m}_{\text{vap},i}^r$ is the net evaporation/condensation flux for reaction $r \in \mathcal{R}$. The evaporation and condensation fluxes based on kinetic theory are modeled with different approaches, which will be shown later. The evaporation flux depends on the equilibrium vapor pressure p_{vap} , which is a pure thermodynamic property.

Consider the following generic reaction,



where $\mathcal{S} = \{\mathcal{G}, \mathcal{C}\}$ is the full set of species and \mathcal{C} the set of condensed species. Quantities $\nu'_{i,r}$ and $\nu''_{i,r}$ are the forward and backward stoichiometric coefficient for the species $i \in \mathcal{S}$. The equilibrium constant for such reaction writes as

$$K_{p,r} = \frac{\prod_{k \in \mathcal{S}} a_k^{\nu''_{k,r}}}{\prod_{i \in \mathcal{S}} a_i^{\nu'_{i,r}}} = \exp\left(\frac{-\Delta G_r^0}{\mathcal{R}T}\right), \quad (3.8)$$

where ΔG_r^0 is the difference of the molar Gibbs energy between products and reactants at standard condition (1 atm and 273.15 K). The activity a_i for species $i \in \mathcal{S}$ in Eq. (3.8), writes as,

$$\begin{cases} a_i = p_{\text{vap},i}, & \forall i \in \mathcal{G}, \\ a_i = \gamma_i x_i, & \forall i \in \mathcal{C}, \end{cases} \quad (3.9)$$

where $p_{\text{vap},i}$ is the equilibrium vapor pressure of species $i \in \mathcal{G}$, x_i the mole fraction in the condensed phase and γ_i the activity coefficient; for ideal mixtures $\gamma_i = 1$. Figure (3.3) shows the equilibrium vapor pressure for the reaction,



where the ΔG_r^0 was computed with the thermodynamic module of MUTATION⁺⁺ and the vapor pressure was compared with the experiments carried out by Bowles and Rosenblum [39].

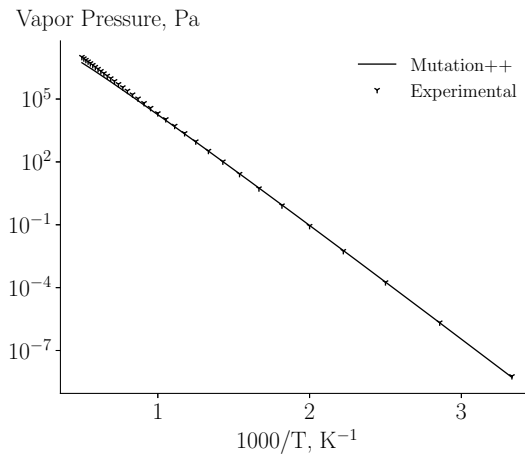
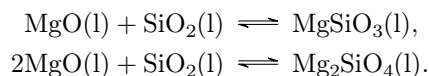


Figure 3.3.: Saturation vapor pressure of Na; comparison of MUTATION⁺⁺ with experimental measurements.

Multi-element vapor pressure

Most of the meteoroids are composed of a mixture of oxides. Table (3.1) shows the composition of the most common meteoroids, the H5 chondrite. Once the material reaches the melting point, the species in the liquid phase interact forming new ones. The following set of reactions is an example,



MgO(l) and SiO₂(l) create new pseudo-species which has strong intermolecular bonds. The creation of these pseudo-species effectively decreases the mole fraction of the unbound oxides, deviating from the ideal mixture (*Rault's Law*), leading to $\gamma_i < 1$ and for the reaction above

$$\gamma_{\text{MgO}} = \frac{a_{\text{MgO}}}{a_{\text{MgO}} + a_{\text{MgSiO}_3} + 2a_{\text{Mg}_2\text{SiO}_4}}. \quad (3.10)$$

Species	H5 wt%
SiO ₂	38.36
TiO ₂	0.12
Al ₂ O ₃	2.12
Na ₂ O	1.03
K ₂ O	0.13
CaO	1.75
FeO	11.28
MgO	24.22

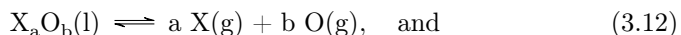
Table 3.1.: Major oxides present in an H5 chondrite in weight percentage. This composition is taken from Jarosewich [122] and the remaining major species are H₂O and Fe(s). The latter corresponds to bands of pure iron. MAGMA only considers oxide compositions, thus, the weight fractions are rescaled here to sum to 100%.

MAGMA is a multiphase-equilibrium solver developed by Fegley and Cameron [80] to provide equilibrium vapor pressure $p_{\text{vap},i}$ to mixture of metal oxides such as the one shown in Table (3.1). The solver uses the Ideal Mixing of Complex Components (IMCC) model [109] and accounts for the deviation from the ideal mixture in the molten phase. In the IMCC model, one considers all the possible species that may be formed in the molten layer, and the equilibrium solution is obtained by minimizing the Gibbs free energy of the system. MAGMA has been extensively validated for liquid-silicate compositions [223]. Figure (3.4) shows the equilibrium vapor pressure of the possible related species for many temperatures fitted in the form of,

$$p_{\text{vap},i}(T_w) = \exp\left(A - \frac{B}{T_w}\right), \quad \forall i \in \mathcal{G}, \quad (3.11)$$

and the coefficients A and B can be found in Section A.3.

According to thermodynamics, multiphase chemical equilibrium is reached once the chemical potential of both phases are the same, meaning that the material is oxidized/reduced depending on the oxygen fugacity. However, MAGMA disregards the excess of oxygen existent in the surrounding environment to compute the multiphase reactions; thus, considering oxidation/reduction reactions is impossible at this stage. To be consistent with the reactions present in MAGMA, $\dot{m}_{\text{vap},i}$ in Eq. (3.3) considers all the possible reactions of type,



where X represents any element present in the condensed phase such as Mg, Fe, Na, Si and K. Equation (3.12) is a dissociative reaction and occurs for species

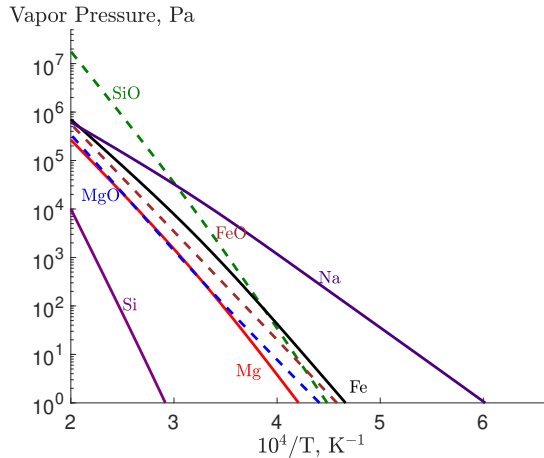


Figure 3.4.: Saturation vapor pressure computed by MAGMA using the composition from Table (3.1). The dashed and solid lines represent to the products of reactions 3.12 and 3.13. Bellow 2800 K, Na is the most abundant species in the flow field since it is a volatile.

with low dissociation energy. Oxygen is also present in the free stream, but it is difficult to quantify precisely how much of it condensates. The rate of oxygen condensation is assumed to follow the stoichiometry ratio in Eq. (3.12), as suggested by Alexander [4], such that

$$\dot{m}_{\text{vap},\text{O}} = \sum_{r \in \mathcal{R}^*} \frac{b_r}{a_r} \frac{M_{\text{O}}}{M_{X_r}} \dot{m}_{\text{vap},X_r}^r, \quad (3.14)$$

where \mathcal{R}^* corresponds to the subset of reactions given in Eq. (3.12) and M is the molecular weight.

3.3. Equilibrium evaporation models

Equilibrium models were developed by engineers in the 60s to overcome the absence of surface reactions data describing the ablation of Thermal Protection System (TPS). This problem was solved by considering the heterogeneous mixture (hot gas phase and material surface) to be in thermochemical equilibrium at the local conditions of pressure and temperature [25]. Lately, this approach has also been used to study evaporation [65, 130]. When such equilibrium approach is considered, it is useful to rewrite Eq. (3.2) in terms of elements such

that

$$\sum_{i \in \mathcal{S}} \alpha_{ki} (3.2) = \begin{cases} \mathbf{F}_{\mathbf{g},k} = \rho_{\mathbf{w},k} \mathbf{u}_{\mathbf{w}} + \mathbf{J}_{\mathbf{w},k}, \\ \mathbf{F}_{\mathbf{c},k} = 0 \\ \dot{\Omega}_{\text{surf},k} = \dot{m}_{\text{ablat},k} + \dot{m}_{\text{vap},k} = \dot{m}_k, \end{cases} \quad \forall k \in \mathcal{E}_{\text{cond}}, \quad (3.15)$$

where $\mathcal{E}_{\text{cond}}$ corresponds to the non-zero set of elements in the condensed phase, and

$$\alpha_{ki} = \sigma_{ik} \frac{M_k}{M_i} \quad (3.16)$$

where σ_{ik} is the formation matrix coefficient of elements k in species i and M the molecular weight, finally,

$$\sum_{k \in \mathcal{E}_{\text{cond}}} \dot{m}_k = \dot{m} = \rho_{\mathbf{w}} \mathbf{u}_{\mathbf{w}}.$$

Equation (3.15) is called Elemental Surface Mass Balance (ESMB) and $\rho_{\mathbf{w},k} \mathbf{u}_{\mathbf{w}}$ (or $y_{\mathbf{w},k} \rho_{\mathbf{w}} \mathbf{u}_{\mathbf{w}}$) is the elemental mass flux, $\mathbf{J}_{\mathbf{w},k}$ the elemental diffusion flux and \dot{m}_k the production of elements k at the surface. This equation is directly coupled with the flow solver serving as a boundary condition, meaning that $\rho_{\mathbf{w}}$ and $\mathbf{J}_{\mathbf{w},k}$ are a solution of the thermochemical state of the flow.

Differently from Eq. (3.2), the surface composition $y_{\mathbf{w},k}$ is computed via a multiphase-equilibrium approach by minimizing the Gibbs free energy of the system \mathcal{S} . Scoggins and Magin [231] developed a multiphase-equilibrium solver based on the Gibbs function continuation method of Pope [210]. The continuation method ensures the convergence of the Gibbs free energy minimization by converting it into an initial value problem, which can be easily integrated. Furthermore, the method has the capability of imposing any constraint to treat multiple surface components. Figure (3.5) shows an example of the multiphase-equilibrium solution whereby the condensed composition is made of 50% Na and 50% Mg in a background gas of nitrogen atoms N. Na evaporates at a lower temperature (650 K) than Mg, and it is depleted from the condensed phase at 750 K. It is worth to highlight that this composition corresponds to the surface composition $y_{\mathbf{w},k}$ of the balance Eq. (3.15).

The remaining variable, \dot{m}_k , is the solution of the following linear system,

$$\begin{cases} \dot{m} y_{\mathbf{w},k} + \mathbf{J}_{\mathbf{w},k} = \dot{m}_k, & \forall k \in \mathcal{E}_{\text{cond}}, \\ \sum_{k \in \mathcal{E}_{\text{cond}}} \dot{m}_k = \dot{m}. \end{cases} \quad (3.17)$$

This closure, i.e., to enforce the equilibrium composition at the surface, is equivalent to imposing the saturated properties for an evaporation case, leading to a zero net evaporation flux [87–89]). The physical interpretation of this model, more specifically the equilibrium \dot{m} , might be seen as the necessary integrated mass for which the surface has to lose to establish an equilibrium condition.

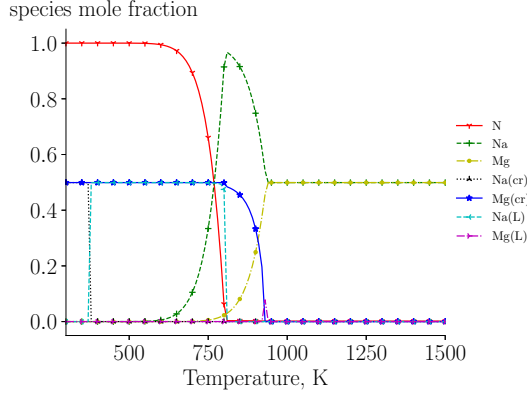


Figure 3.5.: Multiphase equilibrium composition for pure Na, Mg and N, for a condensed composition of Na = 0.5 and Mg = 0.5.

B' formulation

We recall that Eqs. (3.2) and (3.17) are tightly coupled with the flow, i.e., the boundary conditions and the thermochemical state of the flow have to be solved simultaneously. However, another approach is widely used for engineering purposes based on transfer-coefficient correlations [25], decoupling the material-response from the thermochemical state of the flow. The diffusion flux across the boundary is approximated with the mass transfer coefficient C_m as

$$\mathbf{J}_{w,k} = \rho_e \mathbf{u}_e C_m (y_{w,k} - y_{e,k}), \quad (3.18)$$

where the subscript e corresponds to the flow conditions on the edge of the boundary layer, w to the conditions at the wall and s to the condensed state. At this stage, it is noteworthy to highlight that:

- the mass C_m and heat C_h transfer coefficients are related via the Chilton-Colburn relation $C_m = C_h (Le)^\alpha$, where Le is the Lewis number and $\alpha \simeq 3/2$. Duffa [77] suggests that $\alpha \simeq 1$ for significant blowing rates.
- the heat transferred to the surface depends on the material injected into the boundary layer, due to “blocking effects” [25]. Therefore, C_h has to be corrected based on the mass blowing rate.

Bianchi [25] gives a thorough review of the transfer-coefficient approach.

Inserting Eq. (3.18) in Eq. (3.17) and dividing the latter by $\rho_e \mathbf{u}_e C_m$, one gets

$$\begin{aligned} B' y_{w,k} + y_{w,k} - y_{e,k} &= B' y_{c,k} \Rightarrow \\ \Rightarrow B' &= \frac{y_{e,k} - y_{w,k}}{y_{w,k} - y_{c,k}}, \quad \forall k \in \mathcal{E}_{\text{cond}}; \end{aligned} \quad (3.19)$$

note that we define $\dot{m}_k = \dot{m}y_{c,k}$ and $y_{c,k}$ corresponds to the in-depth elemental composition of element k . Equation (3.19) constitutes the non-dimensional mass blowing rate $B' = \dot{m}/\rho_e \mathbf{u}_e C_m$ [177], and it has been extensively employed for the design of Thermal Protection System (TPS) [139, 173, 177, 178]. Mainly, it represents the ratio of mass across the boundary layer ($y_{e,k} - y_{w,k}$) and the ablated mass ($y_{w,k} - y_{c,k}$), and it can be obtained directly from an equilibrium solution such as the one in Fig. (3.5). This approach is popular because of its simplicity, since B' can be tabulated for a range of pressures and temperatures to be used in the Computational Fluid Dynamic (CFD) simulations.

For TPS composed by a single element, such as carbon graphite, the material response modeling is rather simplified since $y_{c,k} = 1.0$. On the other hand, when the material is composed of multiple elements that have different ablation behaviors, this response modeling becomes more complicated because Eq. (3.19) might have multiple solutions. The thermochemistry ablation of multiple surface elements was first addressed by Milos and Chen [177], and they handled this problem by constraining the surface element ratios. As mentioned before, the multiphase-equilibrium solver can include any constraint. Therefore, we impose that the ratio of the elements $k \in \mathcal{E}_{\text{cond}}$ in the gas phase is the same as the in-depth elemental composition. By applying this constraint, it is possible to assume that all elements are removed, from the condensed phase, with the same rate leading to a unique Eq. (3.19).

Figure (3.6) shows an example of a multiphase constrained equilibrium composition; where the condensed composition is the same as the one in Fig. (3.5). In this example, the phase change of Na and Mg occurs at the same temperature, and the elemental ratio of Na/Mg is always the same, as opposed to the unconstrained case.

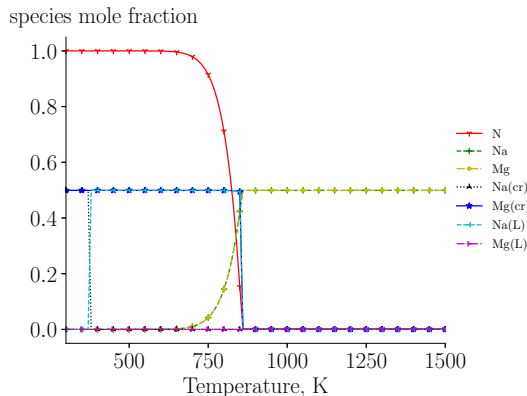


Figure 3.6.: Multiphase constrained equilibrium composition for pure Na, Mg and N, for a condensed composition of $\text{Na} = 0.5$ and $\text{Mg} = 0.5$.

In this work, we formulate a unique B' to account for the volatilization of the different elements. This formulation consists in writing Eq. (3.17) in the non-dimensional form, using the approximate diffusion fluxes from Eq. (3.18),

yielding the linear system,

$$\begin{cases} B' y_{w,k} + y_{w,k} - y_{e,k} = B'_k, & \forall k \in \mathcal{E}_{\text{cond}}, \\ \sum_{k \in \mathcal{E}_{\text{cond}}} B'_k = B', \end{cases} \quad (3.20)$$

where elemental non-dimensional mass blowing rate $B'_k = \dot{m}_k / \rho_e \mathbf{u}_e C_m$, $\forall k \in \mathcal{E}_{\text{cond}}$.

Figure (3.7) shows the comparison between the B' approach resulting from the unconstrained (Eq. (3.20)), and constrained (Eq. (3.19)) multiphase-equilibrium solution and the *NASA formulation* [164]

$$B' = \sum_{k \in \mathcal{E}_{\text{cond}}} (y_{e,k} - y_{w,k}) / \sum_{k \in \mathcal{E}_{\text{cond}}} (y_{w,k} - y_{c,k}). \quad (3.21)$$

The abrupt increase of B' occurs at the onset of the strong evaporation, and the corresponding temperature is the equilibrium vapor temperature. Quantity B' reaches its maximum when all the elements in the condensed phase are depleted (see Figs. (3.5) and (3.6)). Figure (3.7a) shows a lower equilibrium vapor temperature for the constrained multiphase B' . Figure (3.7b) shows a discontinuity for the unconstrained multiphase (or linear system in Eq. (3.20)) around 800 K, which represents the depletion of Na. The strong increase of the function around 950 K represents the depletion of Mg (see Fig. (3.5)). From Figs. (3.5) to (3.7), we observe that imposing a constraint in the multiphase equilibrium solution decreases the equilibrium vapor temperature of the less volatile elements. Finally, the linear system in Eq. (3.20) and the *NASA formulation* gives the same results, despite the different formulation.

Constraining or not, the multiphase-equilibrium solution has several implications in the flow and material compositions. By constraining the solution, we are enforcing all elements to have the same equilibrium vapor temperature. Moreover, we enforce that the condensed phase composition does not change due to the depletion of elements, contradicting the results of Pittarello et al. [206] where depletion of volatile elements has been observed. Hence, this method does not account for the volatilization, which is an important feature for meteoroid entry analysis [265]. On the other hand, in the unconstrained case, one should consider a transient deficit of the most volatile elements on the surface. To consider this, one must solve the diffusion of the elements in the material to define the surface composition accurately.

3.4. Kinetic-based evaporation models

Evaporation occurs when the flow pressure or temperature is lower than the saturation condition at the surface. The opposite situation results in condensation. In Section 3.2, we have shown generalized mass and energy balances across the surface. In this section, we model the non-equilibrium \dot{m}_{vap} in Eq. (3.2). This approach accounts for translational non-equilibrium effects at

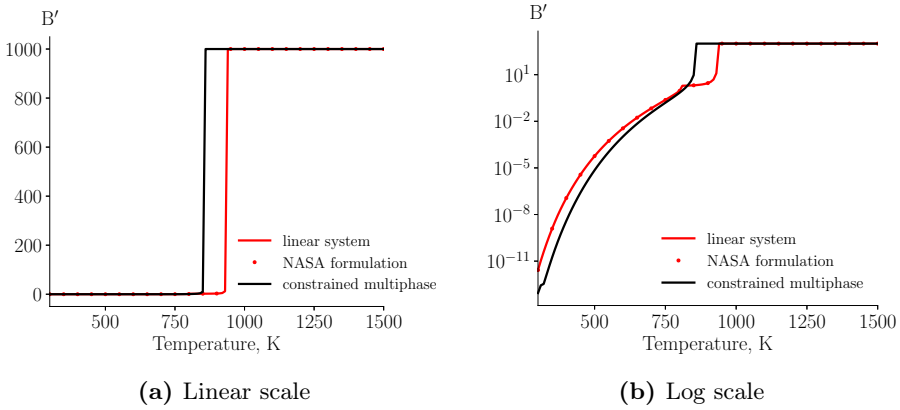


Figure 3.7.: B' comparison at 1000 Pa between unconstrained (Eq. (3.20)), and constrained (Eq. (3.19)) multiphase-equilibrium solutions and the *NASA formulation*.

the surface, by considering the jump in the macroscopic properties across the Knudsen layer.

3.4.1. The Knudsen layer

The Knudsen layer is the region where the two families of particles emerging from the free stream and the surface thermalize, i.e., relax to equilibrium or follow a Maxwellian Velocity Distribution (VDF) (drawing in Fig. (3.8)). Its length might reach a hundred mean free paths, and inside this region, the Navier-Stokes equations are not valid. Evaporating particles of species $i \in \mathcal{G}$

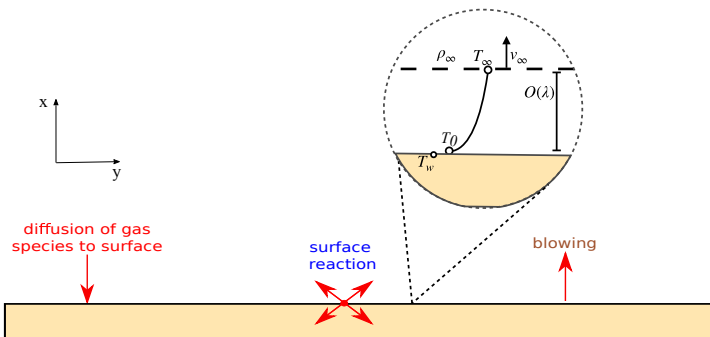


Figure 3.8.: Illustration of the Knudsen layer jump conditions on the surface.

from the surface ($x = 0$) follow a half-space Maxwellian distribution $f_i(x, \xi)$

with the molecular velocity $\boldsymbol{\xi}$ described as,

$$f_{e,i}(0, \boldsymbol{\xi}) = \frac{n_{e,i}}{(2\pi R_i T_w)^{3/2}} \exp\left(-\frac{|\boldsymbol{\xi}|^2}{2R_i T_w}\right), \quad \boldsymbol{\xi} \cdot \mathbf{n} > 0, \quad \forall i \in \mathcal{G}, \quad (3.22)$$

where x is the normal component to the surface, $n_{e,i}(p_{\text{vap},i}, T_w)$ the species equilibrium vapor density, $p_{\text{vap},i}$ the species vapor pressure, T_w the temperature of the surface and R_i the specific gas constant of species i . At the edge of the Knudsen layer, $x = x_\infty$, the particles follow a Maxwellian distribution function at the local pressure $p_{\infty,i}$ and temperature $T_{\infty,i}, \forall i \in \mathcal{S}$,

$$f_{\infty,i}(\infty, \boldsymbol{\xi}) = \frac{n_{\infty,i}}{(2\pi R_i T_\infty)^{3/2}} \exp\left(-\frac{|\boldsymbol{\xi} - \mathbf{u}_\infty|^2}{2R_i T_\infty}\right), \quad \forall i \in \mathcal{G}, \quad (3.23)$$

where $n_{\infty,i}(p_{\infty,i}, T_\infty)$ is the species number density. At the edge of the Knudsen layer, the particles share the same temperature since the flow is thermalized, hence, $T_{\infty,i} = T_\infty, \forall i \in \mathcal{S}$. The particles represented by the distribution function in Eq. (3.23) follow the hydrodynamic velocity \mathbf{u}_∞ (drift velocity) at the edge of the Knudsen layer. Both distribution functions are illustrated in Fig. (3.9).

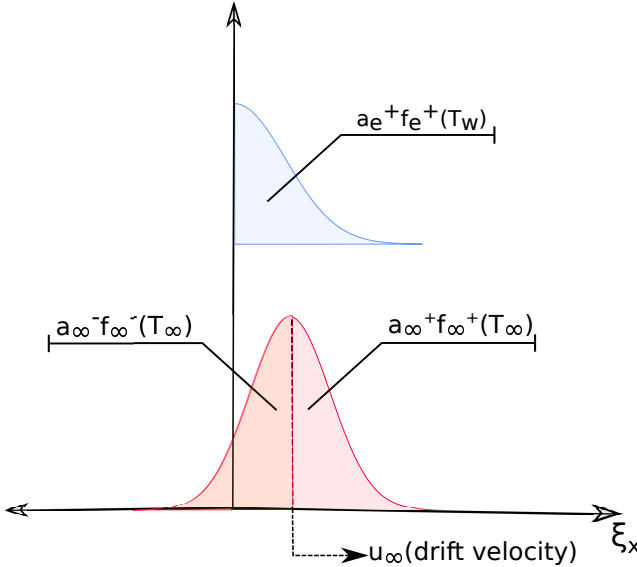


Figure 3.9.: Illustration of the Maxwellian distribution function in the Knudsen layer; the red curve illustrates the VDF of particles at Knudsen layer's edge, the blue curve illustrates the distribution of particles emerging from the surface.

Due to few collisions within the layer, the two families of particles, emerging

from both ends and traveling with opposite directions, generate a bimodal distribution function, which largely deviates from a Maxwellian distribution. Moreover, the anisotropy of the distribution function close to the surface leads to a temperature jump [89, 172], illustrated in Fig. (3.8) as $T_0 \neq T_w$. The significant deviation from a Maxwellian distribution is precisely the condition by which the Navier-Stokes equations do not hold; thus, one has to resort to the Boltzmann equation to solve the structure of the Knudsen layer.

When the Knudsen layer thickness is much smaller than the vapor-liquid interface curvature, it behaves as a second "skin" adhering to the vapor-liquid interface. In this case, the hydrodynamic equations can still be applied to describe most of the vapor phase, and jump relations are used to model the Knudsen layer. These jumps are obtained through the conservation of mass, momentum, and energy across the kinetic layer [279]. In reality, the boundary conditions of the Navier-Stokes equations correspond to the edge state of the Knudsen layer.

3.4.2. Multicomponent non-equilibrium model

In this section, we derive the jump conditions across the Knudsen layer based on the Moment Method to solve the Boltzmann equation. This method has been used by Ytrehus and Østmo [279] for a single evaporation component. We use their methodology to derive a solution for multicomponent evaporation, which later will be compared with the numerical solution of the Boltzmann equation using DSMC.

We start by defining the one-particle distribution function for species $i \in \mathcal{G}_{\text{vap}}$ neglecting the internal degrees of freedom, where \mathcal{G}_{vap} corresponds to the evaporation and condensation set of species. The three-modal ansatz [279] is applied to define the distribution function along the Knudsen layer,

$$f_i(x, \boldsymbol{\xi}) = a_{e,i}^+(x) f_{e,i}^+(\boldsymbol{\xi}) + a_{\infty,i}^+(x) f_{\infty,i}^+(\boldsymbol{\xi}) + a_{\infty,i}^-(x) f_{\infty,i}^-(\boldsymbol{\xi}), \quad \forall i \in \mathcal{G}_{\text{vap}} \quad (3.24)$$

where $f_{e,i}^+$ is the half-Maxwellian distribution of the evaporated particles, and $f_{\infty,i}^+$ and $f_{\infty,i}^-$ are respectively the positive and negative part of the Maxwellian distribution at the Knudsen layer edge, illustrated by Fig. (3.9). The amplitude functions on both extremes of the Knudsen layer are,

$$x = 0 \begin{cases} a_{e,i}^+ = 1, \\ a_{\infty,i}^+ = 0, \\ a_{\infty,i}^- = \beta_i, \end{cases} \quad \text{and} \quad x = x_{\infty} \begin{cases} a_{e,i}^+ = 0, \\ a_{\infty,i}^+ = 1, \\ a_{\infty,i}^- = 1, \end{cases} \quad \forall i \in \mathcal{G}_{\text{vap}}; \quad (3.25)$$

where β_i is an unknown parameter obtained by solving the jump conditions.

The one-dimensional, steady-state Boltzmann equation writes as,

$$\xi_x \frac{\partial f_i}{\partial x} = \sum_{j \in \mathcal{G}_{\text{vap}}} \mathbf{Q}_{i,j}(f_i, f_j), \quad \forall i \in \mathcal{G}_{\text{vap}}. \quad (3.26)$$

The left-hand side corresponds to the streaming operator and the right-hand side to the collision operator, expressing the distribution function change due to collisions between particles. We define collision invariants Ψ^k such that for a binary collision of particles $ij \in \mathcal{G}_{\text{vap}}$

$$\Psi_i^k + \Psi_j^k = \Psi_i^{k'} + \Psi_j^{k'}$$

where the superscript $'$ denotes the post collision quantity. Collision invariants of mass, x-momentum and kinetic energy for species $i \in \mathcal{G}_{\text{vap}}$ are,

$$\Psi_i^k = \left\{ m_i \delta_{ik}, m_i \xi_x, -\frac{1}{2} m_i |\xi|^2 \right\}, \quad \forall i \in \mathcal{G}_{\text{vap}}, \quad k = 1, \dots, \#\mathcal{G}_{\text{vap}} + 2, \quad (3.27)$$

where m_i is the mass species. The moments of the Boltzmann equation are obtained by multiplying Eq. (3.27) with Eq. (3.26) and integrating over the velocity space such that,

$$\frac{\partial}{\partial x} \sum_{i \in \mathcal{G}_{\text{vap}}} \int \Psi_i^k \xi_x f_i d\xi = 0 \quad k = 1, \dots, \#\mathcal{G}_{\text{vap}} + 2, \quad (3.28)$$

due to the orthogonality between the collision invariant space and collision operator space, in other words, species mass, mixture momentum and energy are conserved through collisions. Hence we write Eq. (3.28) as,

$$\sum_{i \in \mathcal{G}_{\text{vap}}} \int \Psi_i^k \xi_x f_i d\xi \Big|_{x=0} = \sum_{i \in \mathcal{G}_{\text{vap}}} \int \Psi_i^k \xi_x f_i d\xi \Big|_{x=x_\infty}, \quad k = 1, \dots, \#\mathcal{G}_{\text{vap}} + 2, \quad (3.29)$$

which represents the conservative quantities on both sides of the Knudsen layer.

Inserting Eq. (3.24) into Eq. (3.29), with the amplitude functions defined in Eq. (3.25) and $\mathbf{u}_\infty = u_\infty \hat{\mathbf{e}}_x$ in Eq. (3.23), one obtains the mass balance for species i , momentum balance and energy balance for the mixture across the Knudsen layer,

$$\rho_{e,i} \sqrt{\frac{R_i T_w}{2\pi}} - \rho_{\infty,i} \sqrt{\frac{R_i T_\infty}{2\pi}} F_i^- \beta_i = \rho_{\infty,i} u_\infty, \quad \forall i \in \mathcal{G}_{\text{vap}}, \quad (3.30)$$

$$\sum_{i \in \mathcal{G}_{\text{vap}}} \left(\frac{1}{2} \rho_{e,i} R_i T_w + \frac{1}{2} \rho_{\infty,i} R_i T_\infty G_i^- \beta_i \right) = \sum_{i \in \mathcal{G}_{\text{vap}}} (\rho_{\infty,i} u_\infty^2 + \rho_{\infty,i} R_i T_\infty), \quad (3.31)$$

$$\sum_{i \in \mathcal{G}_{\text{vap}}} \left[2\rho_{e,i} R_i T_w \sqrt{\frac{R_i T_w}{2\pi}} - 2\rho_{\infty,i} R_i T_\infty \sqrt{\frac{R_i T_\infty}{2\pi}} H_i^- \beta_i \right] = \sum_{i \in \mathcal{G}_{\text{vap}}} \left[\rho_{\infty,i} u_\infty \left(\frac{1}{2} u_\infty^2 + \frac{5}{2} R_i T_\infty \right) \right], \quad (3.32)$$

where the velocity ratio is,

$$S_{\infty,i} = \frac{u_\infty}{\sqrt{2R_i T_\infty}}, \quad (3.33)$$

and the half-range integration of the distribution function $f_{\infty,i}^-$ leads to the following [41],

$$F_i^\pm = \sqrt{\pi} S_{\infty,i} (\pm 1 + \text{erf}(S_{\infty,i})) + \exp(-S_{\infty,i}^2), \quad (3.34)$$

$$G_i^\pm = (2S_{\infty,i}^2 + 1)(1 \pm \text{erf}(S_{\infty,i})) \pm \frac{2}{\sqrt{\pi}} S_{\infty,i} \exp(-S_{\infty,i}^2), \quad (3.35)$$

$$H_i^\pm = \frac{\sqrt{\pi} S_{\infty,i}}{2} \left(S_{\infty,i}^2 + \frac{5}{2} \right) (\pm 1 + \text{erf}(S_{\infty,i})) + \frac{1}{2} (S_{\infty,i}^2 + 2) \exp(-S_{\infty,i}^2). \quad (3.36)$$

The left-hand side of Eq. (3.30) is the net of species evaporation/condensation i analogous to $\dot{m}_{\text{vap},i}$ in Eq. (3.3).

To retrieve the same formulation as Ytrehus and Østmo [279], we approximate Eqs. (3.30) to (3.32) as,

$$\sum_{i \in \mathcal{G}_{\text{vap}}} (3.30) \Rightarrow \rho_e \sqrt{\frac{RT_w}{2\pi}} - \rho_\infty \sqrt{\frac{RT_\infty}{2\pi}} F^- \beta = \rho_\infty u_\infty, \quad (3.37)$$

$$\frac{1}{2} \rho_e RT_w + \frac{1}{2} \rho_\infty RT_\infty G^- \beta = \rho_\infty u_\infty^2 + \rho_\infty RT_\infty, \quad (3.38)$$

$$2\rho_e RT_w \sqrt{\frac{RT_w}{2\pi}} - 2\rho_\infty RT_\infty \sqrt{\frac{RT_\infty}{2\pi}} H^- \beta = \rho_\infty u_\infty \left(\frac{1}{2} u_\infty^2 + \frac{5}{2} RT_\infty \right), \quad (3.39)$$

which might not be exactly equivalent due to the non-linear terms of Eqs. (3.34) to (3.36), meaning that we make an approximation on averaging F_i^- , G_i^- and H_i^- . Later we evaluate the accuracy of the approximation by comparing with the DSMC simulations. Using of the equation of state $p = \rho RT$, such $\rho_e(p_{\text{vap}}, T_w)$ and $\rho_\infty(p_\infty, T_\infty)$, and defining the following ratios,

$$\mathcal{Z} = \frac{p_{\text{vap}}}{p_\infty}, \quad \mathcal{R} = \sqrt{\frac{T_\infty}{T_w}}, \quad (3.40)$$

where R is the specific gas constant of the vapor mixture, $p_{\text{vap}} = \sum_{i \in \mathcal{G}_{\text{vap}}} p_{\text{vap},i}$

and $p_\infty = \sum_{i \in \mathcal{G}_{\text{vap}}} p_{\infty,i}$; we write Eqs. (3.37) to (3.39) as,

$$\mathcal{L}\mathcal{R} - \beta F^- = 2\pi^{1/2} S_\infty, \quad (3.41)$$

$$\mathcal{L} + \beta G^- = 4S_\infty^2 + 2, \quad (3.42)$$

$$\mathcal{L} - \mathcal{R}\beta H^- = \mathcal{R}\pi^{1/2} S_\infty \left(S_\infty^2 + \frac{5}{2} \right). \quad (3.43)$$

From the system of Eqs. (3.41) to (3.43) is possible to define \mathcal{L} , \mathcal{R} , β and M_∞ as function of $S_\infty = u_\infty/\sqrt{2RT_\infty}$ (see Cercignani [57] for the detailed derivation) which leads to the following table:

Table 3.2.: Evaporation parameters

S_∞	\mathcal{L}	\mathcal{R}^2	β	$M_\infty = (6/5)^{1/2} S_\infty$
0.0	1.000	1.000	1.000	0.000
0.1	1.231	0.957	1.020	0.110
0.2	1.500	0.915	1.060	0.219
0.3	1.812	0.876	1.135	0.329
0.4	2.170	0.838	1.271	0.438
0.5	2.577	0.802	1.511	0.548
0.6	3.037	0.767	1.928	0.657
0.7	3.553	0.734	2.644	0.767
0.8	4.127	0.703	3.862	0.876
0.9	4.764	0.673	5.932	0.986
0.907	4.813	0.671	6.132	0.994

The system of Eqs. (3.41) to (3.43) were derived by Ytrehus [278], Ytrehus and Østmo [279] for a single evaporating species. They compared the accuracy of the model with experiments carried out in a low-density wind tunnel at the von Karman Institute for fluid dynamics (VKI), where the flow was created by molecular effusion from a punctured wall (around 10^5 m^{-2} perforations). Figure (3.10) shows the downstream velocity ratio as function of the driving force \mathcal{L} .

3.4.3. The Hertz-Knudsen model

The net evaporation/condensation (left-hand side of Eq. (3.37)) derived by Hertz [115] and Knudsen [135] writes as,

$$\dot{m}_{\text{vap}} = \sum_{i \in \mathcal{G}_{\text{vap}}} \left(\rho_{e,i} \sqrt{\frac{R_i T_w}{2\pi}} - \rho_{\infty,i} \sqrt{\frac{R_i T_\infty}{2\pi}} \right). \quad (3.44)$$

$M_\infty = u_\infty/\sqrt{\gamma RT_\infty}$ and for monoatomic gases $\gamma = 5/3$

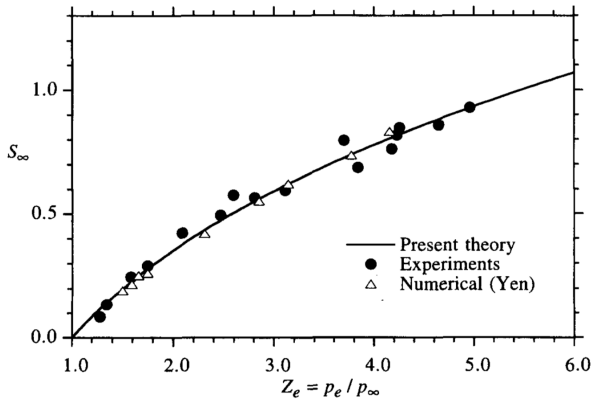


Figure 3.10.: Velocity ratio vs. pressure jump \mathcal{Z} from Ytrehus and Østmo [279]. Note that $p_e = p_{\text{vap}}$.

This model only considers the conservation of mass across the Knudsen layer, and compared to Section 3.4.2 it disregards: i) the drift velocity represented by F^- , meaning that the Maxwellian distribution function on the edge of the Knudsen layer is centered in zero; ii) the non-equilibrium parameter β at the surface, denoting that the backscatter of particles, due to collisions on the Knudsen layer, is neglected. Moreover, for weak evaporation problems it is usually assumed that $T_\infty = T_w$ [204].

3.4.4. The Schrage model

Schrage [224] improved the Hertz-Knudsen model by including non-linear convective effects in the Knudsen layer. They considered the drift velocity effect, but in turn, omitted the non-equilibrium parameter β . The Schrage model writes as,

$$\dot{m}_{\text{vap}} = \sum_{i \in \mathcal{G}_{\text{vap}}} \left(\rho_{e,i} \sqrt{\frac{R_i T_w}{2\pi}} - \rho_{\infty,i} \sqrt{\frac{R_i T_\infty}{2\pi}} F_i^- \right). \quad (3.45)$$

Contrarily to the Hertz-Knudsen model, it does consider the conservation of momentum and energy. Similarly to the previous model, the thermochemical state of the flow at the edge of the Knudsen layer cannot be obtained by the Schrage equation itself, as Ytrehus and Østmo [279] stated.

Notice that Eq. (3.30) can be written in a general form,

$$\dot{m}_{\text{vap},i} = \rho_{\infty,i} u_\infty, \quad \forall i \in \mathcal{G}_{\text{vap}}, \quad (3.46)$$

regardless of which non-equilibrium model is used. We can relate the similarities of this expression with the SMB written in Eq. (3.2), with the exception that the former excludes the diffusion fluxes $\mathbf{J}_{w,i}$. The diffusion fluxes aren't

present in Eq. (3.46) precisely because the particles follow a Maxwellian distribution on the edge of the Knudsen layer, leading to zero transport fluxes.

Remark. In the case of reactive surfaces (ablative, catalytic, or both), the state-of-the-art surface reactions [21, 202, 254] depend on an impinging particles flux following Maxwellian distribution, and yet the diffusion fluxes are considered in the SMB. This inconsistency is mentioned by Barbante [12], and it should be reviewed in the future.

3.5. Numerical methods

Section 3.4 shows the derivation of the balances across the Knudsen layer using the Moment Method to solve the Boltzmann equation. In this section, we solve the structure of the Knudsen layer using the DSMC technique.

3.5.1. The DSMC method

In DSMC [26], the trajectories of a group of representative particles are simulated in the physical space. Each time-step alternates the execution of three phases: i) a free-advection phase, where particles are displaced in the physical space without interacting. Evaporating molecules are generated at the wall according to the VDF prescribed by Eq. (3.22) and at infinity particles are generated according to Eq. (3.23); ii) a collision phase, where particles in proximity can collide and change their velocity because of the binary encounters. For this purpose, a background mesh is used for the efficient choice of collisions partners. The employed 1-D code of Frezzotti [84] implements elastic collisions for monatomic species and variable-hard-sphere cross-sections. iii) a sampling phase, where macroscopic quantities are obtained as averages of the molecular properties in each cell of the grid. At steady state, time-averaging allows evaluating the macroscopic properties accurately.

3.5.2. Comparison with non-equilibrium evaporation models

We study the structure of the Knudsen layer formed by the evaporation of a binary mixture with different mass ratios $\mu = m_2/m_1$. The surface vapor composition and the molecular diameter are the same for both species. We compare the normalized evaporation rate using Hertz-Knudsen, Schrage, and Ytrehus and Østmo [279] models with the numerical simulations. It is important to mention that Ytrehus and Østmo [279] model and the one described in Section 3.4.2 are equivalent for $\mu = 1$. Moreover, the model described in Section 3.4.2 requires the pressure jump across Knudsen layer as a driving parameter. Therefore, this model is omitted in the following comparison, and we compare all the models in Section 3.6.

The jump of macroscopic properties across the Knudsen layer – density, temperature, and other non-equilibrium parameters – are directly provided to the

models by the DSMC simulations. Furthermore, the DSMC results serve as reference to compare with the multicomponent non-equilibrium model, described in Section 3.4.2, applied to an evaporation problem in continuum flow conditions, shown in Section 3.6. We provide the expressions of the different temperature components to aid the discussion [41],

$$T_{\parallel,i} = \frac{m_i}{\rho_i R_i} \int C_{\parallel,i} f_i d\xi, \quad (3.47a)$$

$$T_{\perp,i} = \frac{m_i}{2\rho_i R_i} \int C_{\perp,i} f_i d\xi, \quad \forall i \in \mathcal{G}, \quad (3.47b)$$

$$T_i = \frac{m_i}{3\rho_i R_i} \int C_i f_i d\xi, \quad (3.47c)$$

were $C_i = |\xi_i - \mathbf{u}|^2$, $\xi_{\parallel} = \xi_x \hat{\mathbf{e}}_x$ and $\xi_{\perp} = \xi_y \hat{\mathbf{e}}_y + \xi_z \hat{\mathbf{e}}_z$. The total mixture temperature yields,

$$T = \sum_{i \in \mathcal{G}} y_i T_i, \quad (3.48)$$

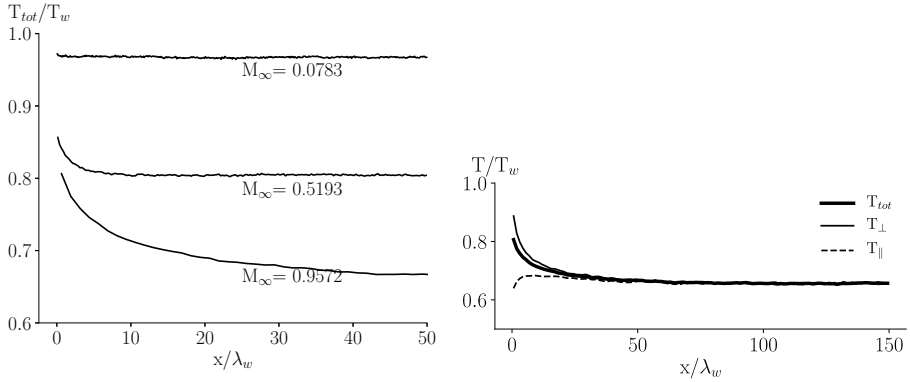
where y_i is the mass fraction for species $i \in \mathcal{G}$.

Evaporation of a binary mixture of mass ratio $\mu = 1$

We start by showing the Knudsen layer structure of a binary mixture with equal mass, being equivalent to single component evaporation. Figure (3.11a) shows the temperature relaxation in the Knudsen layer for different downstream Mach numbers M_{∞} . At the surface, $x = 0$, we observe a jump between the mixture temperature T_{tot} and the surface temperature T_w , as depicted in Fig. (3.8). This jump is due to the backscatter of particles that arrive to the surface with a different VDF than the particles evaporating [88]. As mentioned by Aursand and Ytrehus [8], the interface jump temperature corresponds to the majority of temperature jump across the Knudsen layer.

The Knudsen layer is present due to an anisotropy of the distribution function. Its thickness is the distance by which T_{tot} reaches an asymptotic value. For bigger M_{∞} , the thickness Knudsen layer becomes larger, meaning that the particles require more mean-free paths λ_w to relax. This relaxation of particles is better grasped by Fig. (3.11b), which shows the different temperature components. T_{\perp} and T_{\parallel} are respectively, the temperature due to the kinetic energy of the perpendicular and parallel components of the VDF. One can observe that the two temperature components are different in the Knudsen layer, which originates from an anisotropic VDF. After several mean-free paths, the particles thermalize by collisions, and as a consequence, both temperatures reach the asymptotic T_{tot} . The temperature ratio at the edge of the Knudsen layer corresponds to \mathcal{R}^2 given in Table (3.2).

Figure (3.12) shows the normalized density in the Knudsen layer with a similar behavior as the temperature. For strong evaporation conditions, i.e., high M_{∞} the temperature downstream of the Knudsen layer can reach 70% of T_w while the density can attain 40% of ρ_w . With the DSMC temperature and



(a) Normalized temperature profile in the Knudsen layer for different edge Mach number. (b) Different temperature components in the Knudsen layer at $M_\infty = 0.9572$.

Figure 3.11.: Temperature for $\mu=1$.

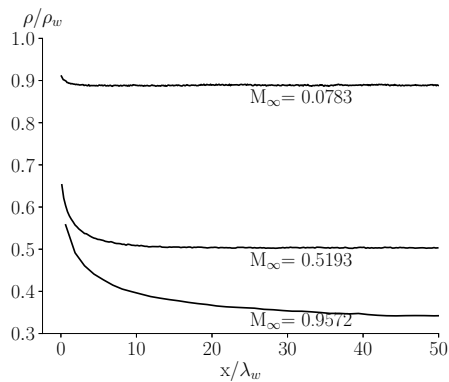
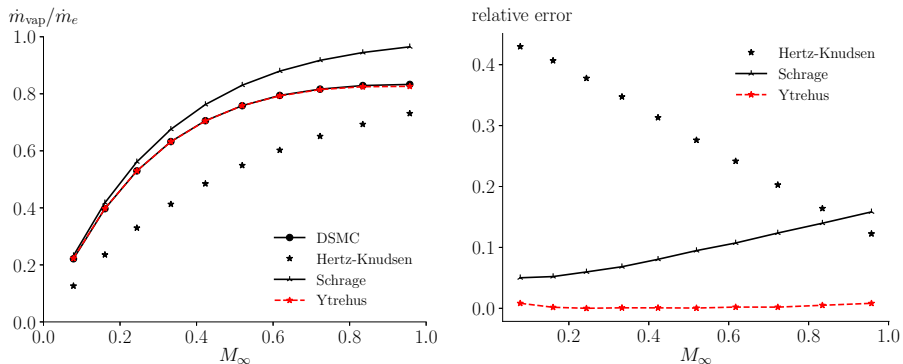


Figure 3.12.: Normalized density profile in the Knudsen layer for different M_∞

density, we compute the evaporation rate using Eqs. (3.37), (3.44) and (3.45) for each species i . Figure (3.13a) shows the normalized evaporation rate of the different non-equilibrium models and DSMC, with $\dot{m}_e = \rho_e \sqrt{(RT_w/2\pi)}$, and Fig. (3.13b) shows the respective relative error compared to DSMC. One



(a) Normalized evaporation rate for different M_∞ .

(b) Relative error of the non-equilibrium models compared with DSMC.

Figure 3.13.: Comparison of the evaporation rate between DSMC and non-equilibrium models for $\mu=1$.

observes a perfect agreement between Ytrehus and Østmo [279] and DSMC. We recall that this model is accurate for a single evaporating component. The error of the Schrage model increases at high M_∞ , and in the subsonic limit, it predicts almost zero condensation. This effect is a combination of: i) $\beta = 1$ in Eq. (3.37) which means that all condensing particles follow a half-Maxwellian with the conditions edge at the Knudsen layer; ii) high M_∞ it means a large drift velocity u_∞ which in turn will prevent the condensation of particles. In Eq. (3.37), $\lim(S_\infty \rightarrow +\infty)F^-(S_\infty) = 0$ which means that the distribution function, described by the red curve in Fig. (3.9), is shifted to $+\infty$; hence, it becomes entirely positive in the velocity space. The Hertz-Knudsen evaporation behaves almost linearly with the M_∞ . We recall this model assumes $\beta = 1$ and that the VDF of the condensing particles is centered in zero, meaning that unlike the Schrage model, the particles condense at high M_∞ .

Evaporation of a binary mixture of mass ratio $\mu \neq 1$

We extend the previous analysis to a binary mixture of the different mass ratios, namely $\mu = 2$ and $\mu = 10$. Figure (3.14) shows the normalized temperature profile in the Knudsen layer for $\mu = 2$, like the one shown in Fig. (3.11a). Furthermore, Frezzotti [84] has shown that the normalized temperature jump in the Knudsen layer depends weakly on the mass ratio. Figure (3.15) shows the temperature components for the light and heavy species for the different mass ratios. Figs. (3.15a) and (3.15b) shows a similar behavior in the late relaxation of the T_{\parallel} for the heavy species, being more predominant in the latter figure.

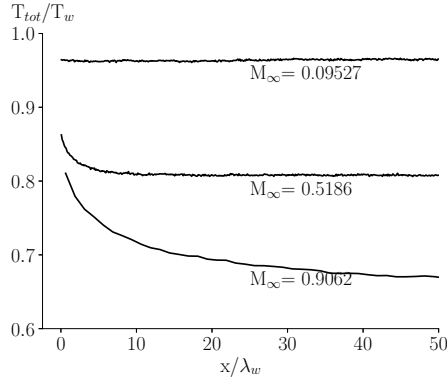
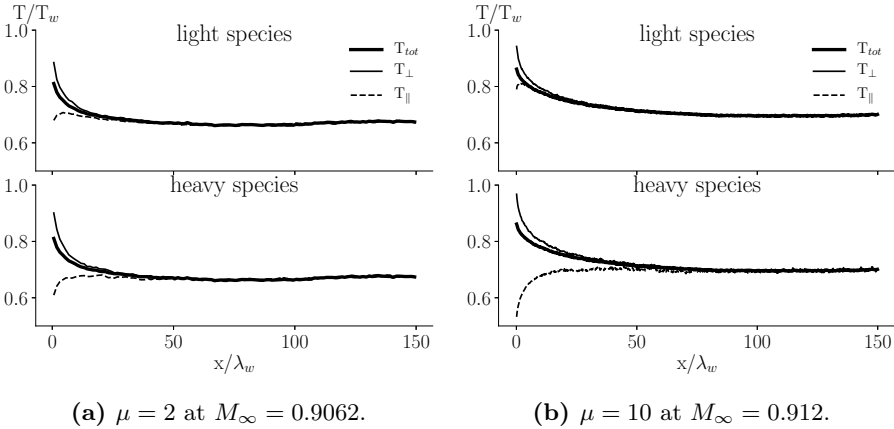


Figure 3.14.: Normalized temperature profile in the Knudsen layer for different edge Mach number, for $\mu=2$.

Both particles leave the surface with different thermal velocities, where the light owns a higher velocity. Close to the surface, Fig. (3.15b) shows a slight increase of the parallel velocity of the light particle. It quickly drops and thermalizes due to the collisions within the Knudsen layer. The opposite is observed for the heavy particle because the collisions are less effective, resulting in a later thermalization.



(a) $\mu = 2$ at $M_\infty = 0.9062$.

(b) $\mu = 10$ at $M_\infty = 0.912$.

Figure 3.15.: Temperature components of the light and heavy species in the Knudsen layer.

The different thermal velocity of the particles results in a dissimilar composition downstream of the Knudsen layer. Figs. (3.16a) and (3.16b) shows an enrichment and deficit of the light and heavy particle, respectively, compared to the surface, which is stronger for high M_∞ .

Figs. (3.17) and (3.18) show the normalized evaporation rate and the relative

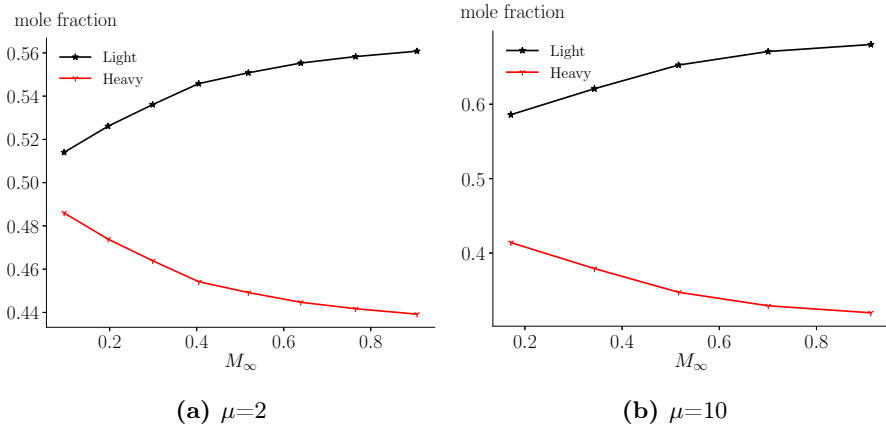
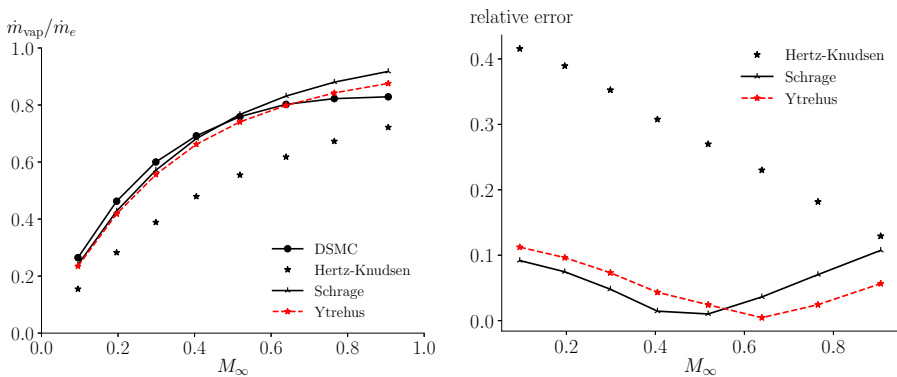


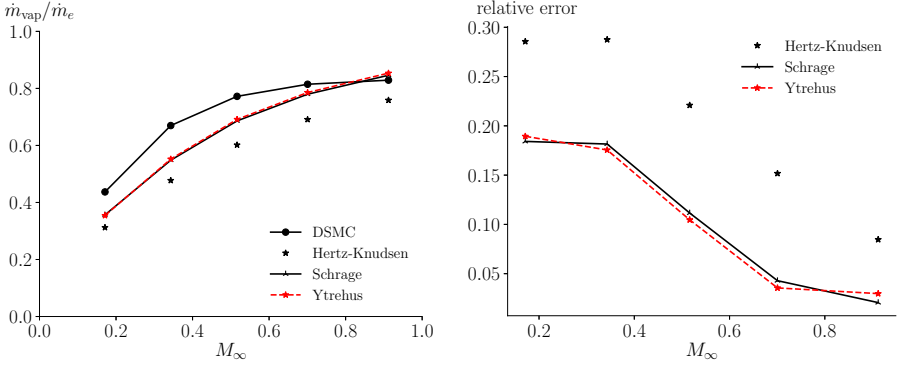
Figure 3.16.: Species mole fraction downstream of the Knudsen layer for different M_∞ .

error for $\mu = 2$ and $\mu = 10$. Contrarily to $\mu = 1$, the Ytrehus and Østmo [279] model does not show a perfect agreement with the DSMC results. The mismatch arises because the Ytrehus and Østmo [279] model does not account for the interaction of many species in the Knudsen layer. This lack of interaction is also present in the Hertz-Knudsen and Schrage models.



(a) Normalized evaporation rate for different M_∞ . **(b)** Relative error of the non-equilibrium models compared with DSMC.

Figure 3.17.: Comparison of the evaporation rate between DSMC and non-equilibrium models for $\mu=2$.



(a) Normalized evaporation rate for different M_∞ . (b) Relative error of the non-equilibrium models compared with DSMC.

Figure 3.18.: Comparison of the evaporation rate between DSMC and non-equilibrium models for $\mu=10$.

3.6. Results

In the previous section, we have shown that state-of-the-art non-equilibrium models do not agree with the numerical Boltzmann solution for multi-species evaporation problems. In this section, we apply the multicomponent non-equilibrium model, described in Section 3.4.2. We model the evaporation of a 0.1 dm radius sphere – composed of atomic species with different mass ratios – into atomic nitrogen using the stagnation-line solver. The inlet velocity is 5 km s^{-1} and the free-stream pressure and temperature correspond to 60 km altitude. The inlet conditions are irrelevant to this problem since the objective is to study the evaporation with an imposed surface temperature T_w . Furthermore, the flow is considered frozen, meaning that we ignore chemical reactions in the gas phase. We impose the evaporation boundary condition at the surface by solving the following system,

$$\left\{ \begin{array}{l} \rho_{e,i} \sqrt{\frac{R_i T_w}{2\pi}} - \rho_{\infty,i} \sqrt{\frac{R_i T_\infty}{2\pi}} F_i^- \beta_i = \rho_{\infty,i} u_\infty, \quad \forall i \in \mathcal{G}_{\text{vap}}, \\ \sum_{i \in \mathcal{G}_{\text{vap}}} \dot{m}_{\text{vap},i} = \dot{m}_{\text{vap}} = \rho_\infty u_\infty, \\ T_\infty = T_w \mathcal{R}^2, \end{array} \right. \quad (3.49)$$

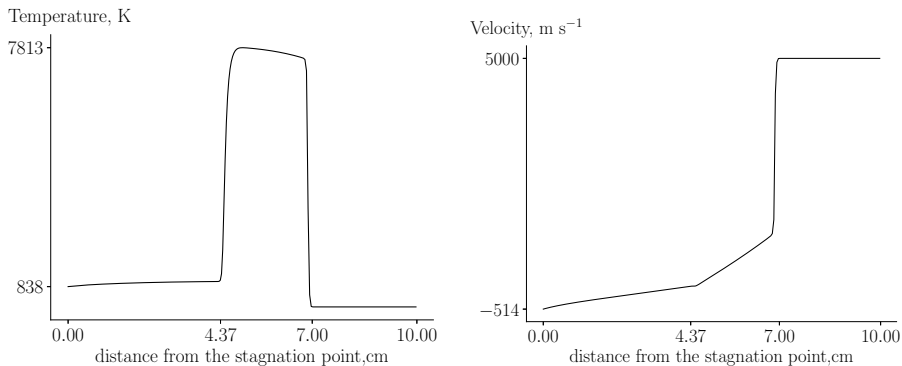
where $\rho_e(p_{\text{vap}}, T_w)$ and $\rho_\infty(p_\infty, T_\infty)$ are related via the perfect gas equation-of-state. As mentioned before, the Navier-Stokes boundary conditions correspond to the conditions at the edge of the Knudsen layer. Hence, we impose the quantities with subscript ∞ as the “surface” of the Stagnation-line solver. In the derivation of Table (3.2) the driving parameter is S_∞ , but in this case the driving parameter is the pressure ratio $\mathcal{L} = p_{\text{vap}}/p_\infty$, because the p_{vap} is retrieved from Eq. (3.8) and p_∞ is a direct solution of the Navier-Stokes

equations. Therefore, the variables $\mathcal{R}^2(\mathcal{L})$, $\beta_i(\mathcal{L}_i)$ and $F_i^-(S_{\infty,i}(\mathcal{L}_i))$, to close Eq. (3.49), are obtained from Table (3.2), both for the properties of the mixture and the species i .

3.6.1. Navier-Stokes solution for evaporation

Evaporation of a binary mixture Na and Mg, $\mu = m_{\text{Mg}}/m_{\text{Na}} \approx 1.0$

We start by simulating the evaporation of pure Na and Mg into atomic nitrogen. We choose this surface composition for two reasons: i) both Na and Mg are significant species for meteoroid ablation, more specifically, Na is an important element to understand light curves ii) both species have similar mass ratio, meaning that the original model of Ytrehus and Østmo [279] holds for this problem. Figure (3.19a) indicates the temperature profile along the stagnation streamline for an imposed surface temperature of $T_w = 1125$ K. The shock wave is at 7 cm from the surface and the shock layer thickness is around 3 cm, reaching a maximum of 7813 K. After the shock layer, we observe a large plateau of 4.37 cm where the temperature at the ‘‘Computational Fluid Dynamics (CFD) surface’’ is $T_\infty = 838$ K. Figure (3.19b) shows the velocity profile along the stagnation streamline and at the surface the blowing velocity is $u_\infty = 514$ m s⁻¹.



(a) Temperature profile along the stagnation streamline.

(b) Radial velocity profile along the stagnation streamline.

Figure 3.19.: Physical properties along the stagnation streamline due to the evaporation of Na and Mg into N for $T_w = 1125$.

Figure (3.20) shows the composition along the stagnation streamline where a vapor layer, between 0 and 4.37 cm, contains only Na and Mg. Note that the concentration of Na is larger than Mg due to a higher equilibrium vapor pressure p_{vap} , or in other words, Na is more volatile than Mg. The temperature jump is $\mathcal{R}^2 = T_\infty/T_w = 0.745$ for a Mach number of $M_\infty = 0.726$ and an evaporation rate of $\dot{m}_{\text{vap}} = 17.51$ kg m⁻² s⁻¹. These conditions represent a

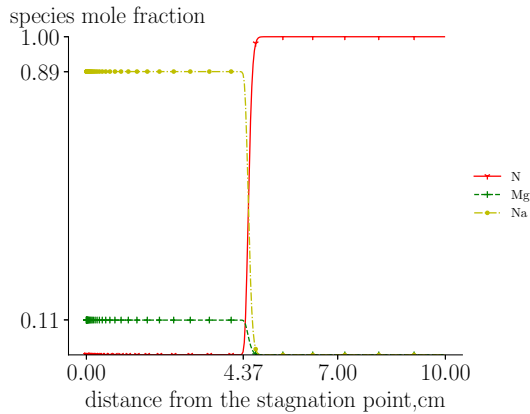


Figure 3.20.: Composition along the stagnation streamline due to the evaporation of Na and Mg into N for $T_w = 1125$.

strong evaporation case whereby a large vapor layer develops, due to the massive evaporation rate. This large vapor layer moves the shock upstream and it is the cause of the temperature plateau in Fig. (3.19a).

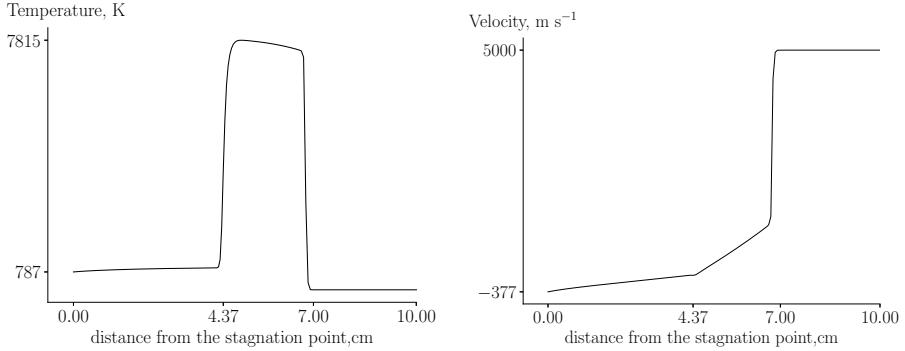
Evaporation of a binary mixture Na and Fe, $\mu = m_{\text{Fe}}/m_{\text{Na}} = 2.5$

We extend the conditions above to a surface composition of Na and Fe, which represents a mass ratio $\mu = 2.5$. Na has higher volatility concerning Fe, and to avoid a vapor layer comprised only by the former, we enforced the same equilibrium vapor pressure to each element. The fact that both elements have equal vapor pressure does not affect the non-equilibrium evaporation because the primary impact parameter is the mass ratio. Figs. (3.21a) and (3.21b) show, respectively, the temperature and velocity profile along the stagnation streamline, for an imposed surface temperature of $T_w = 1067$ K, where the flow properties have a similar behavior as the previous case.

Figure (3.22) shows the composition along the stagnation streamline. Like the previous case, we examine a large vapor layer composed only by Na and Fe. An interesting remark is that although both elements have the same equilibrium vapor pressure, we observe an enrichment of Na in the vapor layer due to its lighter mass compared to Fe, and therefore, higher thermal velocity. In this case, the temperature jump is $\mathcal{R}^2 = T_\infty/T_w = 0.738$ for a Mach number of $M_\infty = 0.697$ and an evaporation rate of $\dot{m}_{\text{vap}} = 22.26 \text{ kg m}^{-2} \text{ s}^{-1}$.

Evaporation of a ternary mixture Na, K and Fe, $\mu_1 = m_{\text{K}}/m_{\text{Na}} = 1.25$ & $\mu_2 = m_{\text{Fe}}/m_{\text{Na}} = 2.5$

The final analysis regards the evaporation of pure Na, K and Fe into atomic N. The objective is to access the fidelity of the multicomponent evaporation model for more than two species with different mass ratios. As in the previous



(a) Temperature profile along the stagnation streamline.

(b) Radial velocity profile along the stagnation streamline.

Figure 3.21.: Physical properties along the stagnation streamline due to the evaporation of Na and Fe into N for $T_w = 1067$.

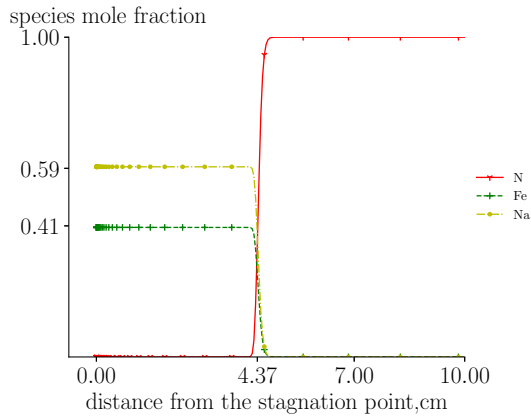
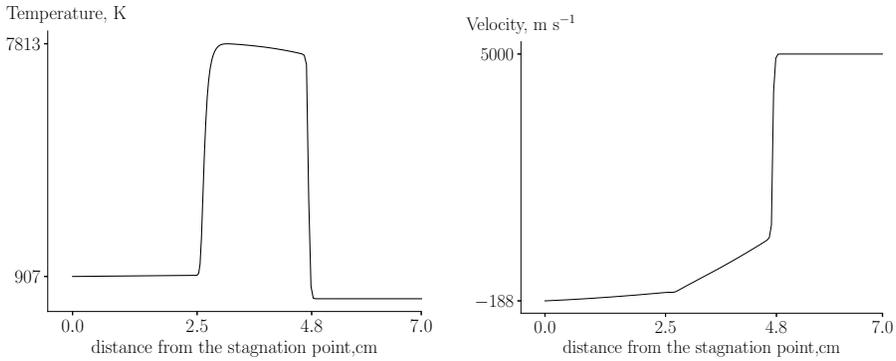


Figure 3.22.: Composition along the stagnation streamline due to the evaporation of Na and Fe into N for $T_w = 1067$.

case, the vapor pressure is the same for all elements. Figs. (3.23a) and (3.23b) show the temperature and velocity for an imposed surface temperature of $T_w = 1040$ K.



(a) Temperature profile along the stagnation streamline.

(b) Radial velocity profile along the stagnation streamline.

Figure 3.23.: Physical properties along the stagnation streamline due to the evaporation of Na, K and Fe into N for $T_w = 1040$.

Figure (3.24) shows the composition along the stagnation streamline where, from lighter to heavier, Na is the richer component at the surface, followed by K then, Fe. For the ternary evaporation case, the temperature jump is

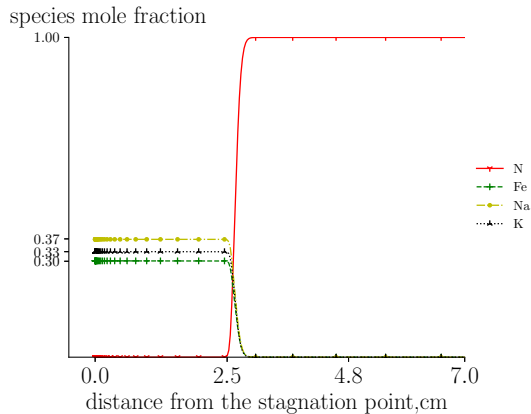


Figure 3.24.: Composition along the stagnation streamline due to the evaporation of Na, K and Fe into N for $T_w = 1040$.

$\mathcal{R}^2 = T_\infty/T_w = 0.872$ for a Mach number of $M_\infty = 0.331$ and an evaporation rate of $\dot{m}_{\text{vap}} = 13.41 \text{ kg m}^{-2} \text{ s}^{-1}$.

3.6.2. Comparison with the equilibrium and non-equilibrium evaporation model

In the previous sections, we present different approaches to simulate evaporation using equilibrium (Section 3.3) – widely employed by the engineering community – and non-equilibrium models (Section 3.4). Here, we correlate the two models developed in this thesis shown in Eq. (3.17) and Eq. (3.49). The test case is the same as the one in Section 3.6.1, corresponding to Na and Mg evaporating into N. Figure (3.25) compares the \dot{m}_{vap} with the equilibrium (*red*) and the non-equilibrium (*blue*) model for different surface temperatures T_w . We observe a significant deviation between the two models for higher temperatures, where the equilibrium calculates more than the double \dot{m}_{vap} at $T_w=975$ K, compared to the non-equilibrium approach. The equilibrium model overestimates the \dot{m}_{vap} because it excludes condensation due to the saturation of the vapor at the surface.

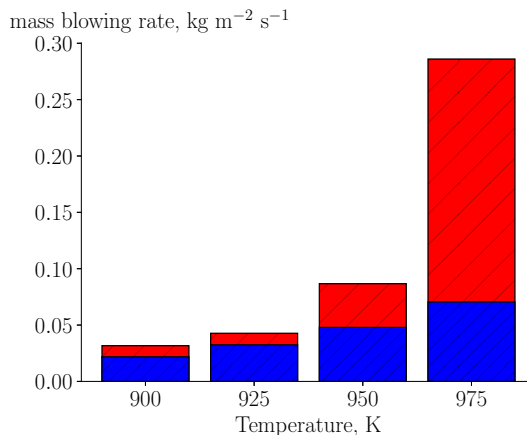
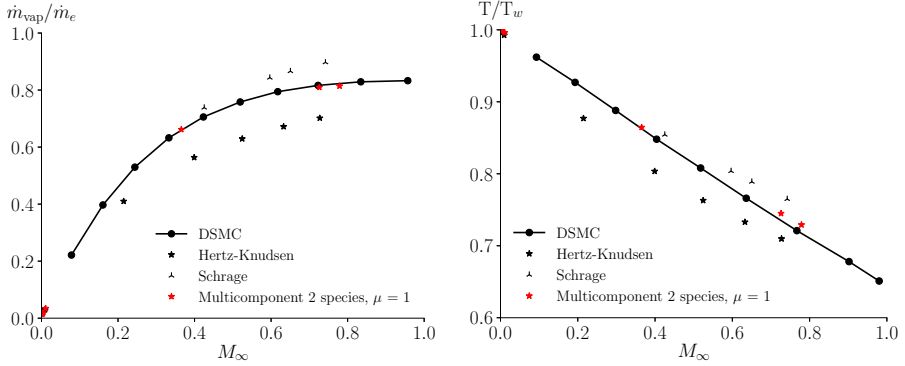


Figure 3.25.: Evaporation rate of Na and Mg into N for different surface temperatures; (*red*): equilibrium model, (*blue*): non-equilibrium model.

3.6.3. Comparison with the Navier-Stokes and Boltzmann solution

In Section 3.5.2, we show that state-of-the-art non-equilibrium models, such as Schrage, Hertz-Knudsen and Ytrehus and Østmo [279], do not correlate well with the DSMC for binary mixtures with $\mu > 1$. Here, we compare the DSMC solution with the test cases indicated in Section 3.6.1 for various surface temperatures T_w , employing the multicomponent non-equilibrium model described by Eq. (3.49). Figure (3.26a) compares the normalized evaporation rate of the different non-equilibrium models with DSMC, for the evaporation of Na and Mg into N. The Hertz-Knudsen and Schrage rates are computed using the closure of Eqs. (3.44) and (3.45) in Eq. (3.49), instead of the closure of the

multicomponent model. Figure (3.26a) shows a similar behavior to Fig. (3.13a) from which Ytrehus and Østmo [279] model is exact. Figure (3.26b) shows the temperature jump across the Knudsen layer where a good agreement with the DSMC solution is also found. The multicomponent model and the Ytrehus and Østmo [279] are the same for an $\mu = 1$ evaporation, which is supported by Figs. (3.13) and (3.26). Figure (3.27a) shows the normalized evaporation



(a) Normalized evaporation rate for different M_∞ . (b) Normalized temperature jump across the Knudsen layer for different M_∞ .

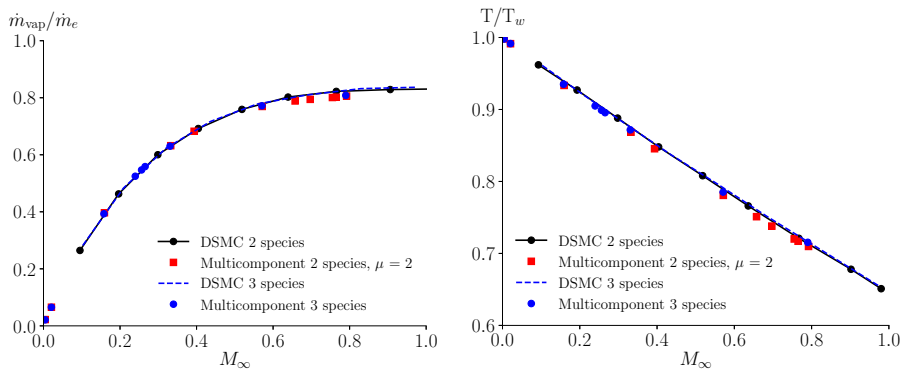
Figure 3.26.: Comparison of the evaporation properties between DSMC and multicomponent non-equilibrium model for $\mu=1$.

of the multicomponent case, shown in Section 3.6.1. The figure shows a good agreement concerning the DSMC solution for the same conditions. Moreover, the temperature jump across Knudsen layer, shown in Fig. (3.27b), also agrees well with the numerical solution of the Boltzmann equation. We recall that at these conditions, the Ytrehus and Østmo [279] model does not hold, as we show in Section 3.5.2.

The reasons why the multicomponent non-equilibrium model (Section 3.4.2) agrees with DSMC results for $\mu > 2$ have to be thoroughly investigated in the future. Intuitively, the two last equations in the system Eq. (3.49) acts as a mixture constraint to the multicomponent evaporation.

3.7. Conclusion

In this chapter, we have developed two models to treat the evaporation of multicomponent elements. The first model assumes the chemical equilibrium between the gas and the surface, and it is an extension of state-of-the-art models widely used by the engineering community to design TPS. The second model includes the jump of properties across the Knudsen layer. This model is derived from the solution of the Boltzmann equation, and it is an extension of Ytrehus and Østmo [279] work, which is only able to treat single component evaporation.



(a) Normalized evaporation rate for different M_∞ . (b) Normalized temperature jump across the Knudsen layer for different M_∞ .

Figure 3.27.: Comparison of the evaporation properties between DSMC and multicomponent non-equilibrium model for binary and ternary surface composition.

We have compared the equilibrium and the non-equilibrium model for the evaporation of a surface composed by Na and Mg (mass ratio equal to one) into N. The former model predicts more than the double of the evaporation rate, compared to the latter. Since the equilibrium model imposes the saturation conditions at the surface, it does not simulate the dynamics of evaporation and condensation of particles.

Finally, we have compared the multicomponent non-equilibrium model with the DSMC method, where we observe an excellent agreement. This comparison includes evaporation of elements with mass ratios higher than one, from which the state-of-the-art models fail. [84] showed that the jump of mixture macroscopic properties across the Knudsen layer is weakly related to the mass ratio of evaporating components. Leveraging from those results, we have developed our models to approximate the vapor mixture as a single evaporation component allowing the macroscopic mixture jumps to be treated with the method of [279]. However, this model is not appropriate to analyze the Knudsen layer structure.

The evaporation phenomenon is present in several different areas, from combustion to the ablation of meteors. The multicomponent non-equilibrium model developed in this chapter represents a step forward to increase the fidelity of evaporation modeling. This model is relevant to study the evaporation of surfaces exposed to intensive radiative fields, such as laser or meteoroid ablation. Moreover, we express the model in a general form suitable to weak and strong evaporation conditions.

As future work, we plan to compare the multicomponent non-equilibrium model with the DSMC for larger mass ratios. Finally, we propose to extend this model to the evaporation of molecules, where the species internal degrees of freedom must be considered. The evaporation of a polyatomic gas has been

studied by Frezzotti [85] using DSMC methods. The author observed thermal non-equilibrium effects at the edge of the Knudsen layer, which might be relevant for space applications such as reentry vehicles.

CHAPTER 4

Material melting

We need science education to produce scientists, but we need it equally to create literacy in the public. Man has a fundamental urge to comprehend the world about him, and science gives today the only world picture which we can consider as valid. It gives an understanding of the inside of the atom and of the whole universe, or the peculiar properties of the chemical substances and of the manner in which genes duplicate in biology. An educated layman can, of course, not contribute to science, but can enjoy and participate in many scientific discoveries which are constantly made. Such participation was quite common in the 19th century, but has unhappily declined. Literacy in science will enrich a person's life.

— Hans A. Bethe

4.1. Introduction

Recent laboratory experiments [2, 113, 151] yield insights into meteoroid ablation and emission phenomena at entry conditions. From these experiments, it was clear that a substantial ablation mechanism was due to the shear ablation process. Stony meteorites recovered from the ground typically present a fusion crust layer [206, 207] of condensed molten material, which is clear evidence that the material underwent a melting process during its entry. In the literature of meteoroid ablation [45, 130, 265], little attention is given to modeling the melt of meteoritic material, and the shear ablation by aerodynamic forces. This might have the effect of biasing inference of meteor size and composition from observations. For materials that undergo melting, an effective heat of ablation can be derived to consider the mass loss of the molten layer due to aerodynamic

Parts of this chapter have been published in

1. B. Dias, A. Turchi, E. Stern, and T. E. Magin, **A model for meteoroid ablation including melting and vaporization**, *Icarus*, 345(2020) 113710.
1. B. Dias, F. Bariselli, A. Turchi, A. Frezzotti, P. Chatelain, and T. E. Magin, **Development of a melting model for meteors**, *AIP Conference Proceedings* 1786(1) 160004, 2016 .

forces [1]. The heuristic coefficients (heat transfer, ablation and luminosity), used in meteor trajectory models to infer the size of a meteoroid from observations, are influenced by the mechanisms of ablation. Recent work account for melting effects, Girin [93] developed a melt-spraying model to represent the fragmentation of the molten layer which is proposed to explain high-altitude flares observed in many bolides. In this model, the molten thickness is estimated using the boundary-layer theory and not by solving the phase-transition. Capek et al. [47] also used a melt-spraying model to interpret light curves of iron meteoroids. They solve the material response at which the molten layer is assumed to be removed in the form of spray immediately after the surface reaches the melting temperature.

Bethe and Adams [24] presented a model based on the incompressible Navier-Stokes equations which estimated the shear ablation for glassy materials. Glassy materials do not have a definite melting point, and a change of viscosity characterizes the material. The liquid thickness is defined by the authors as the distance from which the viscosity increases one order of magnitude. In the case of stony materials or metals such as ordinary chondrites and iron meteorites, the phase-transition occurs when the energy of the material overcomes the latent heat of fusion [44]. Nevertheless, Bronshten [42] applied the model of Bethe and Adams [24] to meteoroid ablation. The most advanced model to simulate materials that undergo phase-transition is presented by Chen et al. [65]. They use the model of Bethe and Adams [24] together with a coupling of a material/flow solver to study the evaporation and shear ablation of quartz experiments, presented in Agrawal et al. [2]. The equilibrium model used for evaporation lacks accuracy because evaporation is intrinsically a non-equilibrium phenomenon [87]. Therefore, without modification, this model is unsuitable for modeling the melt flow ablation of meteoritic material.

The objective of this chapter is to develop an ablation model for meteoroids which accounts for the solid-liquid phase transition, as well as the removal of the molten layer by evaporation and shear ablation. This methodology aims to study meteor trajectories with low computational resources, where flow and material behavior are considered. Within this methodology, we assume that the surface temperature is uniform which leads to a uniform molten layer, and that the aerodynamic forces, promoting the removal of the molten layer, are averaged along the surface. In this work, we develop a finite-differences material solver which estimates the phase-transition for stony/metal materials (Section 4.2). From this solver, we compute the mass loss of the molten layer at the stagnation point due to aerodynamic forces using a steady-state incompressible Navier-Stokes model as Bethe and Adams [24]. Moreover, we derive a boundary condition to estimate the overall recession of the meteoroid at entry conditions; assuming average aerodynamic forces, uniform temperature and constant molten layer around the surface. The aerodynamic forces from the flow to the material are obtained by solving the chemically reacting, compressible Navier-Stokes equations using the stagnation-line solver (Section 2.2). We use a Hertz-Knudsen law (assuming $T_\infty = T_w$ in Eq. (3.44)) to compute the rates of evaporation/condensation of the molten layer as a boundary condition

for the flow governing equations. We compare our material/flow coupling approach using ablation data for the Tamdakht H5 ordinary chondrite, to the experimental results of Agrawal et al. [2], from which we assume an equivalent radius from the sphere-cone sample, described in Section 4.3. We first analyze the flow around the material and the influence of evaporation in Section 4.4.1, and in Section 4.4.2 we study the material behavior. Finally, we compare the stagnation point recession with the experimental measurements, and we derive the effective heat of ablation from our results.

4.2. Multi-phase model

4.2.1. Material phase-transition

The phase-transition of a multicomponent material occurs in a range of temperatures where the material is in an intermediate state of pure liquid and solid since the different components have distinct melting temperatures. In a transient problem, the enthalpy method is one of the simplest ways to simulate the moving solid-liquid boundary due to the phase-transition, since it does not require deformation of the numerical grid. This method considers the thermodynamic properties of both phases and a mushy region where the material is in a combination of solid and liquid state because of the melting point of the different components. Below the solidus temperature (T_{solidus}), the material is in a pure solid-state, and above the liquidus temperature (T_{liquidus}), the material is in a pure liquid-state, up to the evaporation point. Fig. (4.1) illustrates the thermodynamic properties: on the top, we see the behavior of the enthalpy with the temperature; on the bottom the specific heat at constant pressure ($c_p = \partial_T h$). The phase-transition enthalpy is defined as [44]:

$$h(T) = \int_{T_{ref}}^T c_p(\tau) d\tau + f_l(T) L_m \quad (4.1)$$

where L_m is the latent heat of fusion and f_l the liquid volume fraction:

$$f_l = \frac{1}{2} \left[\tanh \left(\frac{T - T_m}{\delta T} \right) + 1 \right] \quad (4.2)$$

with the melting temperature $T_m = (T_{\text{solidus}} + T_{\text{liquidus}})/2$ and the mushy temperature range $\delta T = T_{\text{liquidus}} - T_{\text{solidus}}$. In Eq. (4.2), the hyperbolic tangent allows for a smooth transition between phases, ensuring continuity of the enthalpy function, also observed on the specific heat c_p plot (bottom of Fig. (4.1)). It is worthwhile to mention that we choose constant thermodynamic properties for the solid and liquid phase due to the lack of experimental data, but the model can be used for any type of non-linear properties.

We estimate the molten thickness of the material (δ_m) by solving the energy

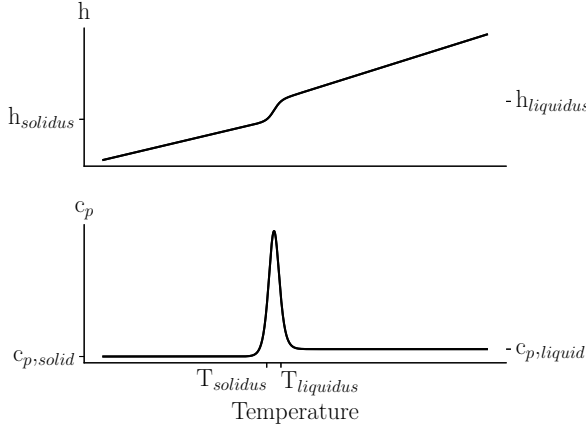


Figure 4.1.: Enthalpy method: top - enthalpy function; bottom - specific heat at constant pressure. This figure represents a constant c_p in temperature for the solid and liquid phases. The peak in c_p arises from the $\partial h/\partial T$ due to the latent heat of fusion, which is important to consider when solving the one-fluid equation (liquid and solid phase in the same domain). This method is also known as the “Equivalent Heat Capacity Method”[79].

equation. The energy equation in conservation form is written as,

$$\begin{aligned} \frac{\partial \rho h}{\partial t} &= \frac{1}{\xi^n} \frac{\partial}{\partial \xi} \left(\xi^n k(T) \frac{\partial T}{\partial \xi} \right), & (4.3) \\ h(\xi, t = 0) &= h_0(T_0), \quad \forall \xi \in \Omega \\ \nabla T(\xi_0, t > 0) &= 0, \quad \forall \xi_0 \in \Gamma_0 \\ h(\xi_w, t > 0) &= h_w(T_w), \quad \forall \xi_w \in \Gamma_w \end{aligned}$$

where ξ is a generic variable depending on the coordinate system, i.e., if $n = \{0, 1, 2\}$ then $\xi = \{\text{cartesian, cylindrical, spherical}\}$, Ω corresponds to the domain of integration, Γ_0 is the back-surface or the center of a sphere and Γ_w is the surface exposed to the flow. In this work, we assume only heat conduction of the material and we neglect the thermo-capillary effects in the molten layer. The solution of the energy equation allows for identification of the phase-transition by locating the solidus temperature through post-processing. The conservative variable h is converted into the primitive variable T by iteratively solving the non-linear Eq. (4.1). The solid and liquid phases have different values of thermal conductivity. Similar to the thermodynamic quantities above, we define the thermal conductivity as having a smooth transition from the solid to the liquid phase in Eq. (4.4), also shown by Fig. (4.2). In this figure, we show a constant solidus and liquidus thermal conductivity. The assumption of the constant thermal conductivity is due to the lack of experimental measurements

of this property at high temperatures. The recent work of Haskins et al. [108] aims to fill this experimental gap by deriving models using ab-initio methods. These calculations have been proven efficient for less complex mixture than the one studied in this chapter and for time being this approach is inapplicable for the complex mixture analyzed here.

$$k(T) = (1 - f_l)k_{\text{solid}} + f_l k_{\text{liquidus}} \quad (4.4)$$

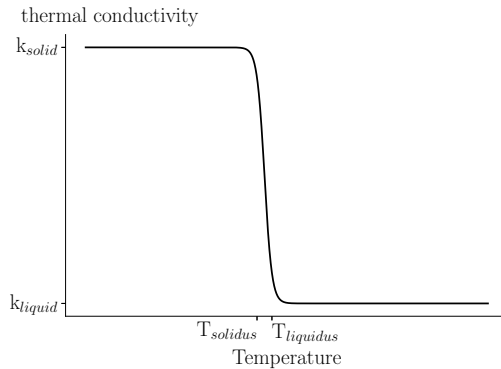


Figure 4.2.: Thermal conductivity as a function of temperature. As in the c_p , we defined a constant k for the solid and liquid phase.

Remark. The model above refers to an equilibrium phase-transition. This model has limitations for materials that endure short high-heating rates, such as laser ablation or erosion of the Arc Jet electrodes. In such conditions, the heating pulse time might be of the same order as the lattice excitation time; thus, the phase-transition should be treated with a non-equilibrium model [267]. In practice, these non-equilibrium effects might change the solidus, liquidus, and melting temperatures.

4.2.2. Removal of the molten material

The molten removal by aerodynamic forces is estimated by using a quasi-steady Stokes flow derived by Bethe and Adams [24] for silicate materials. Starting from the incompressible momentum equation, Bethe and Adams [24] retrieved the velocity along the molten thickness by neglecting the inertial terms, postulating that the viscous forces are predominant (Stokes flow). The velocity along the molten layer in steady-state reads as,

$$u_x(x, y) = \tau_w(x) \int_{-R}^y \frac{1}{\mu} d\eta + \frac{\partial P(x)}{\partial x} \Big|_w \int_{-R}^y \frac{\eta}{\mu} d\eta, \quad (4.5)$$

where the details are in Section B.2. In Eq. (4.5), the y and x are the normal and tangential coordinates at the surface, respectively (see Fig. (4.4)). The distance δ_m is defined based on the solidus temperature. Therefore, we integrated Eq. (4.5) from the center at location $-R$, where the velocity is zero (or the viscosity is infinite), to the gas-liquid interface where $y = 0$. The aerodynamic forces τ_w and $\partial P/\partial x$ are the shear stress and pressure gradient, respectively, at the gas-liquid interface. These variables are boundary conditions obtained from the flow solver (Section 2.2).

As the temperature of the molten layer increases, the material becomes less viscous facilitating its removal due to aerodynamic forces. In Fig. (4.3) we present two viscosity models and their behavior with the temperature. The “BA” concerns an empirical viscosity model derived by Baldwin and Allen [11], where the viscosity is linear with temperature in the log scale (the coefficients can be found in Bronshten [42]). In the Vogel–Fulcher–Tammann (“VFT”) model, the viscosity has a non-Arrhenian temperature dependence (Eq. (4.6)).

$$\log \mu(T) = A + \frac{B}{T - C} \quad (4.6)$$

Giordano et al. [92] retrieved the VFT parameters from more than 1770 measurements, for silicates mixtures. The parameters are computed based on the abundance of each component. For the composition considered in this work (Table (3.1)), the VFT parameters are $A = -4.55$, $B = 4723.94$ and $C = 576.16$. Once we solve for the in-depth temperature of the material and the flow properties around the object, the velocity profile of the molten thickness and mass flux removed by aerodynamic forces can be estimated.

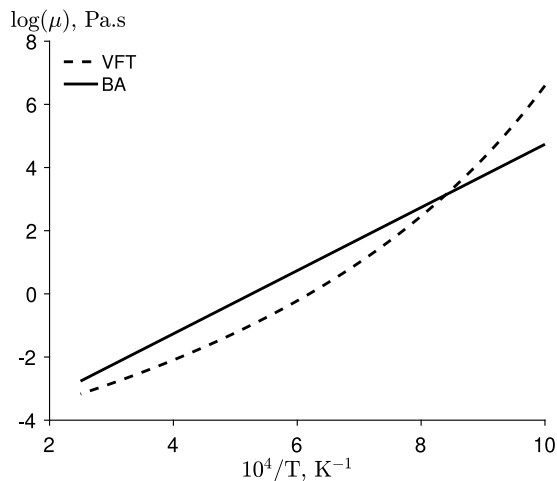


Figure 4.3.: Viscosity of the material (solid and liquid phase) as a function of temperature. We compared two empirical methods to compute the viscosity: the “BA” is found in Bronshten [42] and the “VFT” is found in Giordano et al. [92].

The stagnation point recession, i.e, the normal velocity on the surface is derived by solving the equation for mass conservation together with Eq. (4.5). The details of the derivation can be found in Section B.2. The general recession velocity at the stagnation point reads as,

$$u_y = -2 \int_{-R}^0 \partial_x u_x(y) dy, \quad (4.7)$$

where u_y is the normal velocity at the surface and $\partial_x u_x(y)$ writes as,

$$\partial_x u_x(y) = \partial_x \tau_w \int_{-R}^y \frac{1}{\mu} d\eta + \partial_{xx} P|_w \int_{-R}^y \frac{\eta}{\mu} d\eta. \quad (4.8)$$

This derivation is similar to the one given by Bronshten [42], and the difference comes from the numerical integration of Eq. (4.5). Moreover, we do not enforce that the molten thickness corresponds to a distance whereby the viscosity increases by one exponential factor. Therefore, this formulation is more general, and it can be applied to any material, rather than just silicates. The pressure forces along the surface were computed assuming a Newtonian pressure distribution, and the Reynolds analogy was used for the shear distribution [77].

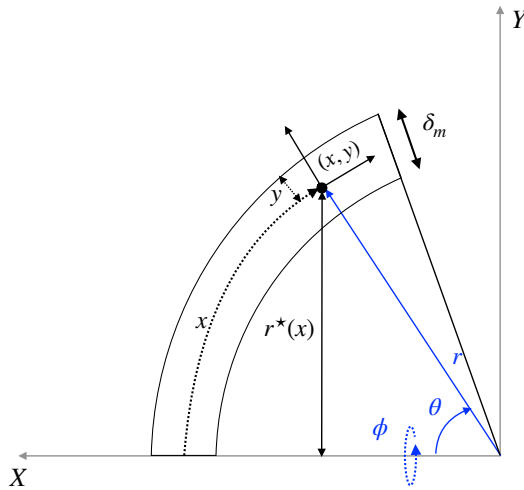


Figure 4.4.: Illustration of a half-sphere from which the mass flux is integrated. We assume that the molten thickness (δ_m) is constant over the half-sphere.

It becomes troublesome to use this 1D model for studying the overall meteoroid recession during a trajectory. The main issue arises from the change of shape due to the non-uniform surface recession, leading to a loss of the spherical shape. We propose to build a formulation that captures the overall recession by estimating an effective constant recession, i.e., it estimates an uniform recession velocity on the surface. It is possible to build such formulation if we

assume a uniform surface temperature (an assumption made for tumbling bodies [45]), a constant molten thickness around the surface. The distribution of the aerodynamic forces along the surface are approximated as average values. As shown in Section B.3, by doing a balance of fluxes on the body represented in Fig. (4.4), the average recession velocity \bar{u}_r is obtained by,

$$\int_{-R}^0 \bar{u}_x(y+R) dy = \bar{u}_r \left(R^2 \int_0^{\frac{\pi}{2}} \sin \theta d\theta + \frac{\pi}{2} \int_{-R}^0 (y+R) dy \right), \quad (4.9)$$

where R is the radius of the sphere and $\bar{u}_x(y)$ writes as:

$$\bar{u}_x(y) = \bar{\tau}_w \int_{-R}^y \frac{1}{\mu} d\eta + \left. \frac{\partial \bar{P}}{\partial x} \right|_w \int_{-R}^y \frac{\eta}{\mu} d\eta \quad (4.10)$$

$\bar{\tau}_w$ and $\overline{\partial_x P}$ are the average aerodynamic forces around the surface.

The total recession velocity of the material is obtained by summing the recession velocity by aerodynamic forces, u_y given by Eq. (4.7) or \bar{u}_r by Eq. (4.9), and the recession velocity due evaporation.

4.2.3. Finite-differences method

We solve the phase-transition problem using a finite-difference method in spherical coordinates, where Section 4.2.1 is spatially discretized as,

$$\frac{\partial \rho h_i}{\partial t} = \frac{k_{i+\frac{1}{2}}(T_{i+1} - T_i) - k_{i-\frac{1}{2}}(T_i - T_{i-1})}{\Delta r^2} + \frac{2}{r_i} \frac{k_{i+\frac{1}{2}}(T_{i+1} - T_i)}{\Delta r}. \quad (4.11)$$

The time dependent term is discretized with a forward Euler method. Since the thermal conductivity is temperature dependent, we evaluate the average quantity between two nodal points using a harmonic average (Eq. (4.12)).

$$k_{i+\frac{1}{2}} = \frac{2k_{i+1}k_i}{k_{i+1} + k_i} \quad (4.12)$$

Moreover, one can notice the singularity when $r_i \rightarrow 0$ on the last term of Eq. (4.11). To overcome this singularity, we used the approach of Versypst and Braatz [260] for spheres where the last node of the domain is computed as,

$$\frac{\partial \rho h_0}{\partial t} = \frac{6k_0(T_1 - T_0)}{\Delta r_1^2}. \quad (4.13)$$

This correction still respects the adiabatic boundary condition (third condition of Section 4.2.1). The mass removal of the material leads to a reduction of the computational domain at each time step. This reduction is simulated by removing nodes from the surface and remapping the old solution into a new computational domain. In the work of Chen and Milos [64], a convective term is added to the energy equation as change of the reference frame, and the last node is dropped to take into account the recession. Our approach and the

latter are compatible; but in spherical coordinates it is essential that the last node is fixed at the center to respect the symmetry boundary condition. The verification of the material solver is shown in Section B.1.

4.3. Arc Jet validation experiment

Quantitative data on meteoroid ablation, with sufficient fidelity to aid in the development and validation of detailed models, is scarce. Interrogation of bolide observational data, because of the complex and highly coupled entry phenomena, can only help inform the relatively simple heuristic models in common use. Therefore, there is a need for controlled experiments, performed at entry-relevant conditions, to provide data that you can be used to assess the accuracy of detailed ablation models, such as that in the current work. To this end, NASA's Asteroid Threat Assessment Project (ATAP) has performed a series of experiments [2] in the Arc Jet (high-enthalpy wind tunnels) facilities at NASA Ames Research Center to investigate meteoroid ablation and emission. A detailed description of the experimental apparatus and full data-set is beyond the scope of the current work. For more detail the reader is referred to the work of Agrawal et al.[2]. A brief description of the relevant elements of the experiment follows.

One of the stated goals of the experimental campaign was to obtain quantitative data on meteorite ablation at entry-relevant conditions. To achieve this, test articles were machined to precise specifications such that the flow environment around the model could be accurately computed, as well as make simulations more feasible. Figure (4.5) shows a schematic of the model used in the Arc Jet experiment. The model consists of a 45° sphere-cone with 3.070cm base diameter, and a 0.635cm nose radius. The meteorite sample that will be simulated in the current work is the Tamdakht H5 ordinary chondrite[268]. The sphere-cone design was selected to provide higher heat fluxes at the stagnation point, as well as significant shear stresses on the conic flank. The aerothermal environment in the Arc Jet was computed using the DPLR computational fluid dynamics (CFD) solver [273], resulting in a predicted cold wall stagnation point heat flux of $\approx 3.4 \text{ kW/cm}^2$, and a stagnation pressure of 126 kPa. Pre- and post-test laser scans were done on all models to provide accurate recession profiles. Additionally, edge detecting image processing techniques were applied to high-speed video from the experiment to obtain *in situ* measurement of the stagnation point recession during exposure. The model was inserted into the flow for approximately 2s, which yielded significant shape change of the model. Figure (4.6) shows a frame from 1000fps high-speed video after $\approx 1.49\text{s}$ from model insertion. It is evident from this image that shear ablation plays an important role in the overall ablation of the model.

We compare the experimental ablation of the H5 chondrite with the ablation model, where the material boundary conditions are provided by the flow solver. The aerodynamic forces are primarily computed with the stagnation-line solver as a series of steady-state solutions for a time interval of 0.4 seconds.

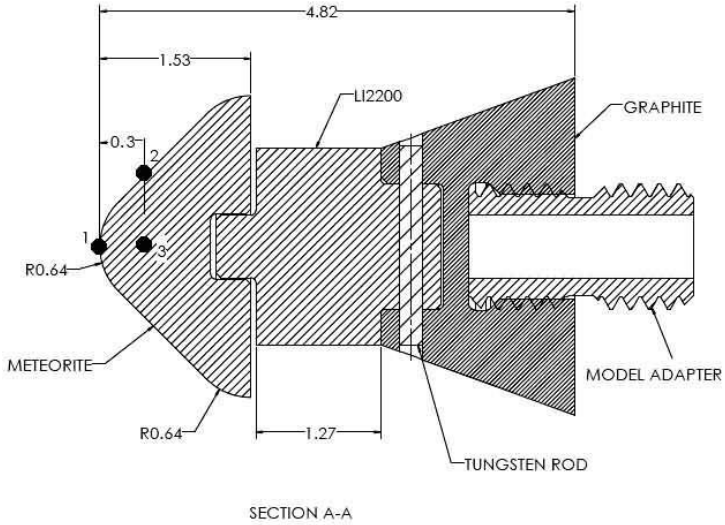


Figure 4.5.: Model assembly for Arc Jet experiment. All dimensions in cm.

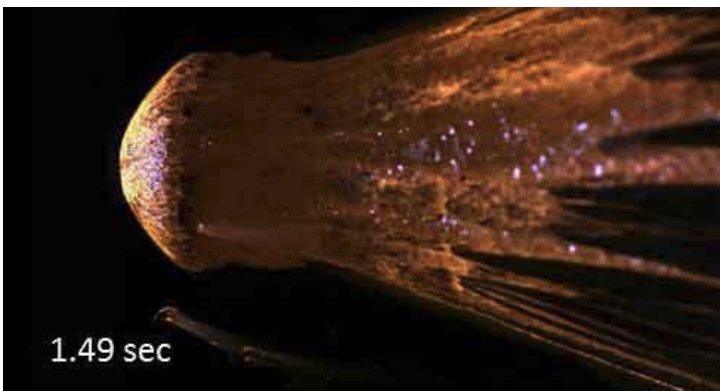


Figure 4.6.: Frame from high-speed video captured at 1.49 seconds from model insertion.

After, these forces are fitted with a 4th order polynomial and passed to material solver as time-dependent properties. We imposed the surface temperature measured by the pyrometer as a boundary condition for the energy equation (Section 4.2.1). The procedure described above is only possible due to prior knowledge of the sample recession as each steady-state flow field computation considers an updated geometry (i.e., updated radius of curvature).

Since the focus of this validation is to compare the recession of the stagnation point, and we can only work in spherical coordinates, it was necessary to transform the original 2D sphere-cone sample into a 1D symmetric sphere. This transformation was possible by fitting the nose to a sphere. Figure (4.7) shows an increase of the effective radius of curvature (6.83 mm pre-test and 12.5 mm post-test). The shock wave location - which is directly affected by the curvature of the sphere - affect the aerodynamic forces at the surface, thus the need to simulate the same radial curvature as in the experiment. The increase of the effective radius was interpolated linearly in time from the pre and post shape.

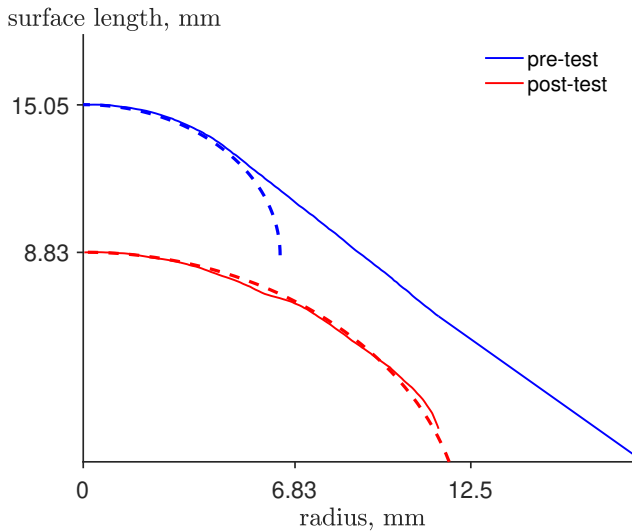


Figure 4.7.: Sample shape pre and post test: solid lines - measured shape; dashed lines - spherical fit.

4.4. Results

The set of species \mathcal{S} use in this chapter is given in table Table (4.1). The thermodynamic properties are computed from a polynomial database of McBride et al. [168].

For the present study, we use the Roe inviscid-flux scheme implemented in the stagnation-line solver. The Hertz-Knudsen evaporation model (Section 3.4.3)

Table 4.1.: Gaseous species used in this chapter. The evaporation products contain only the major species according to their saturated vapor pressure.

air species N NO N ₂ O O ₂ Ar
H5 chondrite evaporation products Mg MgO FeO Si SiO SiO ₂ Na NaO K Fe

served as boundary condition to the flow field simulations which is coupled to the MUTATION⁺⁺ library.

4.4.1. Flow results

Figure (4.8) shows the temperature profile along the stagnation streamline at test start and after 2 seconds. For the numerical simulations, we impose an isothermal boundary condition meaning that surface temperature is the one measured by the pyrometer at the stagnation point. We can observe a sharp increase in the temperature representing the shock wave located at a different position for different times. For example, at 0 seconds, the shock layer thickness is almost half the one at 2 seconds. The increase of the shock layer in time is due to an increase of effective radius leading to a decrease of heat flux in time, as shown by Fig. (4.9). The heat flux presented in this work is within the catalytic and non-catalytic heat flux estimated by the 2D axisymmetric simulations of Agrawal et al. [2], where evaporation is not considered. Assuming a fully catalytic boundary condition, they estimated a pre-test heat flux of 2700 W cm⁻² and a post-test heat of 2200 W cm⁻². For a non-catalytic boundary condition, they estimated a heat flux of ~1000 W cm⁻².

The aerodynamic forces acting on the molten later, $\partial_{xx}P$ and $\partial_x\tau_w$, are highly dependent on the radius of the body. We recall that these properties are evaluated with the Newtonian pressure distribution and the Reynolds analogy, similarly to Bethe and Adams [24]. The behavior of these quantities are shown in Fig. (4.10); where they decrease in time as a result of an increase of the effective radius.

The gas composition along the stagnation streamline at the beginning of the experiment is shown in figures Figs. (4.11) and (4.12a). The plasma composition in Fig. (4.11) shows that the free-stream is mostly composed by N₂ and O with some traces of N and Ar. Figure (4.12a) shows the gas composition along the stagnation streamline. Note that the most abundant evaporation product is sodium – which is also the most volatile component on the H5 composition [208]– followed by iron. Moreover, SiO quickly dissociates into silicon further upstream and K is shown as a trace, due to its small presence in the oxide composition. Figure (4.12b) shows the evaporation species along the stagnation streamline at 2 seconds. The same conclusions can be withdrawn from Fig. (4.12a) but in this case the vapor layer is larger. The vapor layer is larger than the 0 seconds result due to the increase of the effective radius. This larger

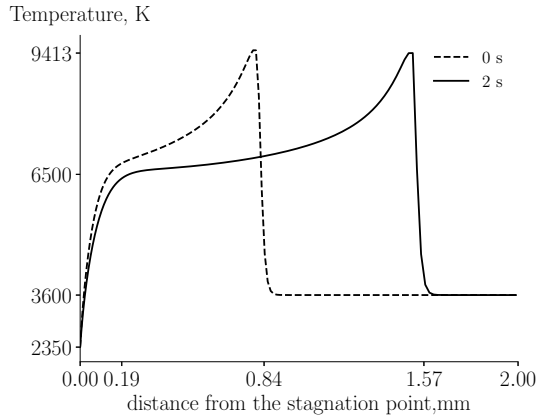


Figure 4.8.: Stagnation-streamline temperature profile at different times.

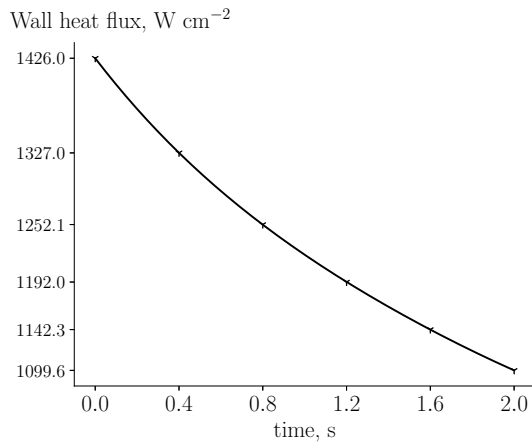


Figure 4.9.: Stagnation point heat flux in time taking into account the evaporation of the molten layer.

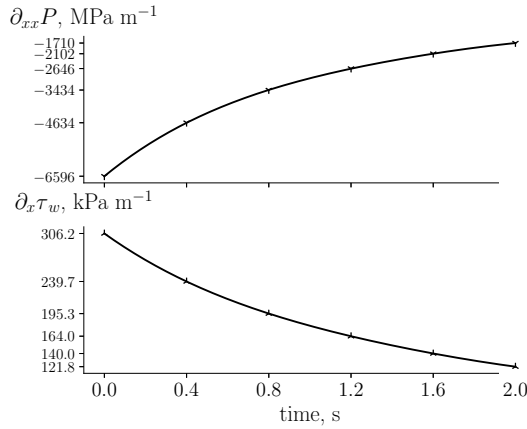


Figure 4.10.: Gradient of the aerodynamic forces in time around the sphere: top - $\partial_{xx}P$; bottom - $\partial_x\tau_w$.

vapor layer results in a decreases of the diffusion fluxes due to a lower concentration gradient. The spectral measurements by Agrawal et al. [2] support the presence of these species. However, Agrawal et al. [2] reports the non-appearance of the MgO molecular bands as it is theoretically predicted. The present results show that the presence of evaporated MgO is almost inexistent from chemical recombination, thus, justifying why it does not appear in the spectrum.

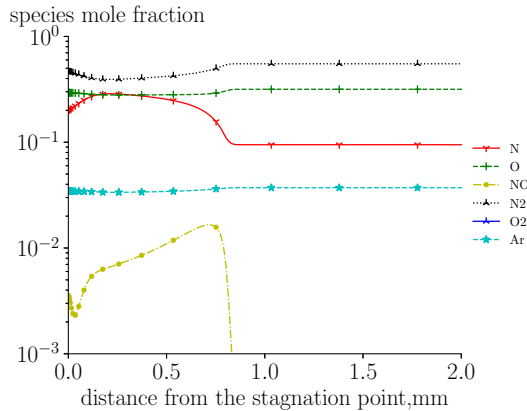
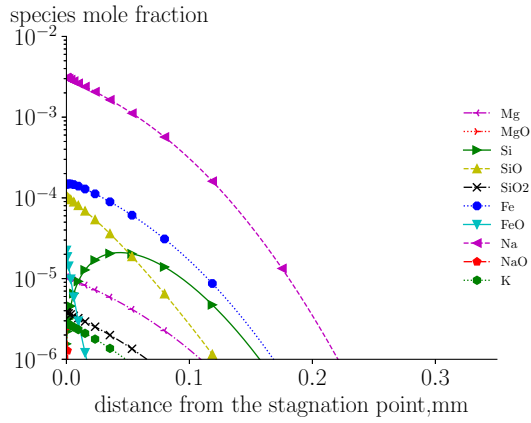
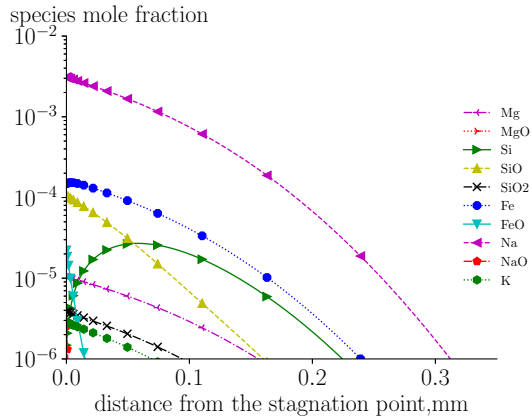


Figure 4.11.: Plasma composition along the stagnation streamline at 0 seconds.

An increase of radius leads to an increase of the gas pressure on the surface and a decrease of the diffusion fluxes. This effect translates into a significant amount of particles that can condensate lowering the net evaporation flux



(a) Evaporation species along the stagnation streamline at 0 seconds. Note that 0 seconds it corresponds to few instants right after the injection of the material.



(b) Evaporation species along the stagnation streamline at 2 seconds.

Figure 4.12.: Evaporation species at the beginning and at the end of the test. Sodium is the most abundant component due to its volatilization and the vapor layer increases due to the increase of the effective radius.

(Fig. (4.13)). It is important to stress that overall mass loss due to evaporation is small due to a combination of high pressure at the surface, and low surface temperature, explaining the low content of the evaporated species in Fig. (4.12a).

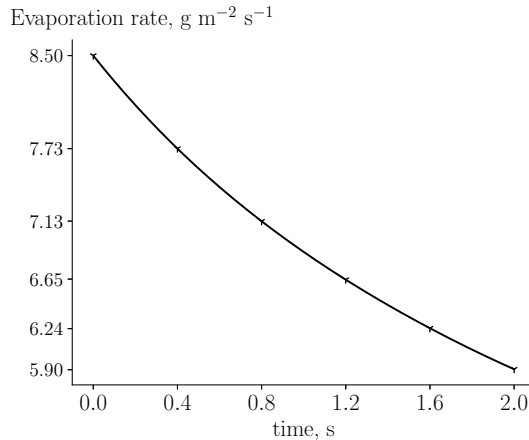


Figure 4.13.: Decrease of the evaporation mass blowing rate in time. This decrease is due to a combined effect of a small increase of stagnation pressure - increasing the condensation flux of the particles - and a lowering of the diffusive flux.

4.4.2. Multi-phase results

Generally speaking, the necessary properties for a flow/material coupling are the aerodynamic forces (Fig. (4.10)), evaporation mass loss (Fig. (4.13)) and heat flux (Fig. (4.9)) [226]. In this work, the latter becomes superfluous since we imposed the measured stagnation point temperature. The underlying assumption is that the surface temperature is uniform. The thermal conductivity of the Tamdakht H5 in the solid state is taken from Opeil et al. [188], which is equal to $3.0 \text{ W m}^{-1}\text{K}^{-1}$. Due to the lack of data for the material properties at high temperatures (see Loehle et al. [150] for EL6 enstatite chondrite properties), it is merited to examine the impact of these uncertainties on the material response analysis. Therefore, we make a sensitivity analysis on those properties considered relevant for the mechanical mass removal due to the aerodynamic forces, which as explained before represents the major contribution to the overall mass loss. We use Eq. (4.7) to compute the stagnation point recession and we compared with the experimental results.

Thermal conductivity

Figure (4.14a) shows the strong dependence of the stagnation point recession on the thermal conductivity even though the molten thickness is small

(Fig. (4.14b)). The sensitivity analysis revealed a good agreement with the experimental measurement if we assume a molten thermal conductivity of $0.85 \text{ W m}^{-1}\text{K}^{-1}$ for the liquid phase together with the VFT model for viscosity. The molten thickness increases linearly for most of the heating period (Fig. (4.14b)), and it becomes maximal for the case of $k_s = 3.0$ and $k_l = 1.0$. We assumed that the sample does not lose mass during the cooling period, i.e., when the arc-jet is shut down.

A comparison of Fig. 13 and Fig. 16 confirms that the mechanical mass removal is the dominant process under the present conditions (four orders of magnitude larger than the evaporation mass removal). The mechanical removal trend over time (Fig. (4.14c)) presents an initial growth followed by a slight decrease; the combination of the rapidly increasing molten thickness and the maximal aerodynamic forces is responsible for the growth, whereas the decreasing trend of the aerodynamic forces over time causes the decrease.

Viscosity

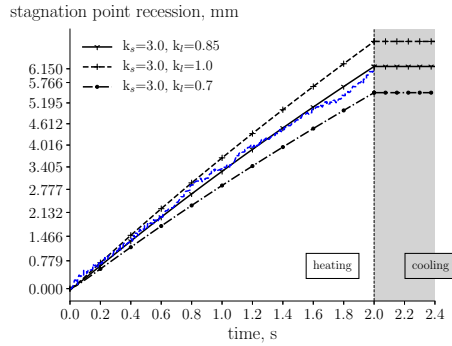
The material viscosity is another important parameter to estimate the mechanical removal (Eq. (4.8)). We compared the VFT and the BA model presented in Section 4.2 for the nominal condition $k_s = 3.0$ and $k_l = 0.85$. The comparison of both models shows that the BA model underpredicts the surface recession by nearly 50% (Fig. (4.15a)). This under-prediction is due to a higher viscosity at higher temperatures; leading to a lower recession velocity. A thermal conductivity much higher than $0.85 \text{ W m}^{-1}\text{K}^{-1}$ would be needed to match the experimental data with the BA model, which might not be physical for these type of materials. The lower-mass removal predicted by the BA model leads to an increase in the molten thickness seen in Fig. (4.15b).

Mushy zone

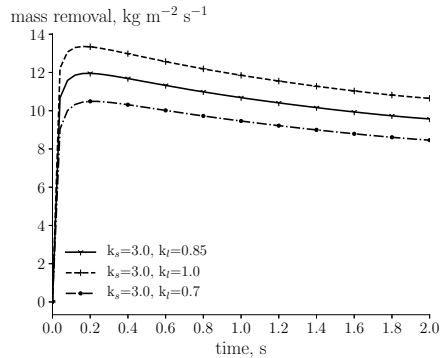
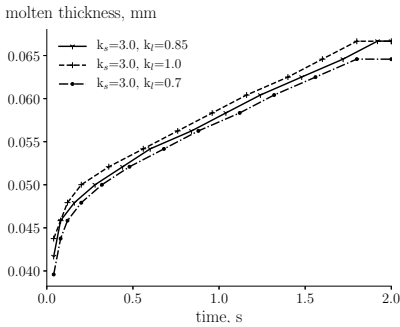
Figures (4.16a) and (4.16b) show that, for different mushy temperatures range, the stagnation point recession and the mass removal is the same as in the nominal conditions ($k_s = 3.0/k_l = 0.85$ and VFT model for viscosity). The different temperature range in the mushy zone have a negligible effect on the growth of the molten thickness which leads to an equal recession velocity at the stagnation point. For a sharp phase change a small difference is observed mainly due to a smaller molten thickness. It is important to remark that the difference between the solidus and liquidus temperatures is reported to have substantial importance in geochemistry. However, as discussed, we did not observe any significant impact in our analysis.

Thermal behaviour of the material

The fast recession at the stagnation point and the low thermal diffusion rate of the material results in a steep temperature profile close to the surface. Figure (4.17) shows the material in-depth temperature for different time instants assuming $k_s = 3.0$ and $k_l = 0.85$, the VFT model for viscosity and $\delta T = 100 \text{ K}$.

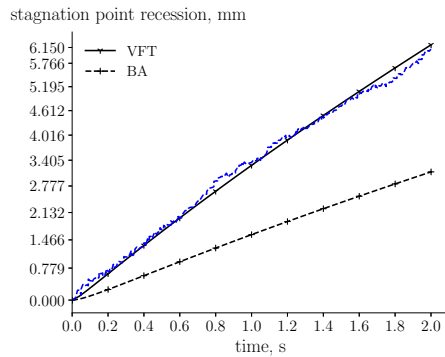


(a) Recession of the stagnation point during the test and after the test. The (---) curve is the recession of the stagnation point determined from the video camera data.

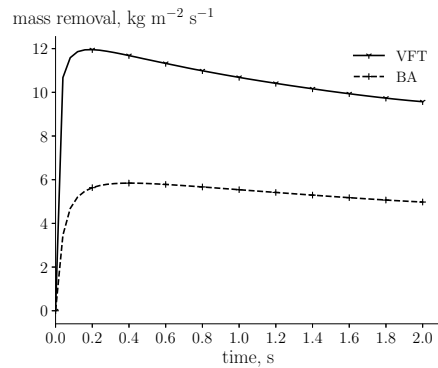
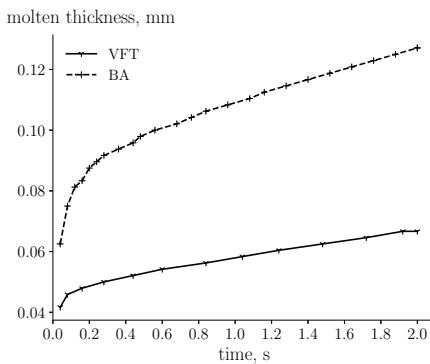


(b) Growth of the molten thickness in time. (c) Mass removal rate of the molten layer.

Figure 4.14.: Parametric study on the thermal conductivity of the material. The study shows that the thermal conductivity on the solid has little influence on the overall shear ablation.

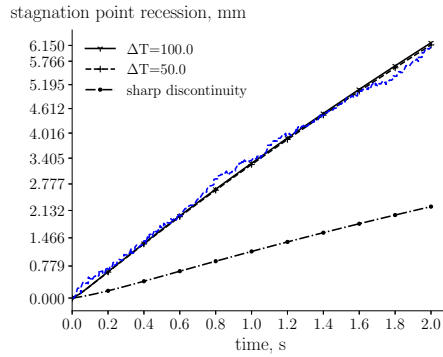


(a) Recession of the stagnation point during the test. The (---) curve is the recession of the stagnation point determined from the video camera data.

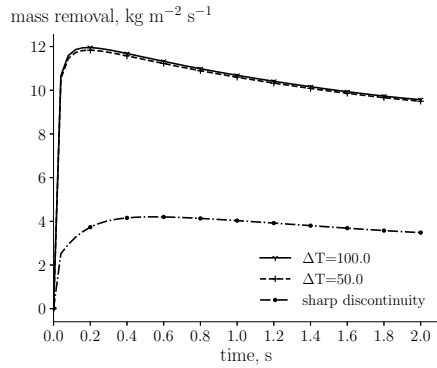
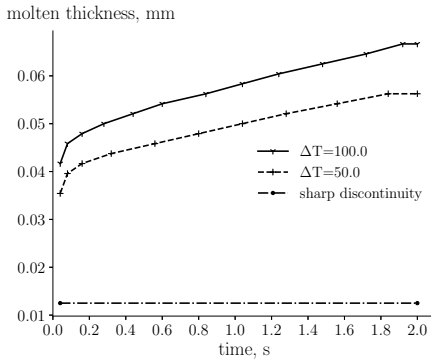


(b) Growth of the molten thickness in time. (c) Mass removal rate of the molten layer.

Figure 4.15.: Study on the empirical viscosity models. The BA model predicts a lower stagnation point recession because it estimates a higher viscosity compared to the VFT model. The BA model could only match the experimental results by prescribing nonphysical thermal conductivities.



(a) Recession of the stagnation point during the test. The (---) curve is the recession of the stagnation point determined from the video camera data.



(b) Growth of the molten thickness in time. (c) Mass removal rate of the molten layer.

Figure 4.16.: Parametric study on the mushy temperature range. The different mushy temperature range have a negligible impact on the overall mass removal.

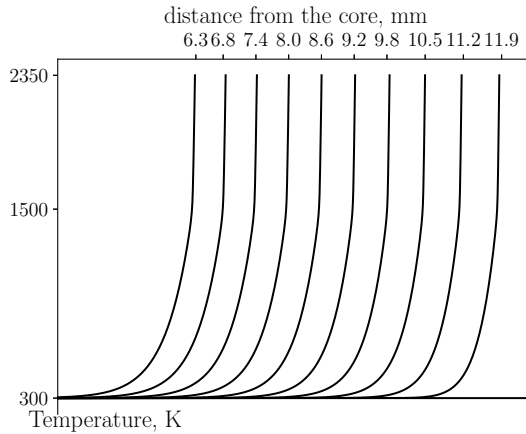


Figure 4.17.: In-depth material temperature along the centerline. The curves are 0.2 seconds apart (from test start to test end). The low thermal-diffusivity of the material prevents the thermal wave from reaching the core of the sample.

A substantial increase of the temperature is observed close to the surface while the core remains at 300 K as the initial condition. The large temperature gradients at the surface are due to the relatively slow diffusion of the heat wave, mainly driven in turn by the low thermal conductivity of the material and the high mass removal of the molten layer. The permanent removal of the molten layer also implies a loss of energy in the material, effectively dissipating energy from the flow before it can be used to heat the core.

The cooling down of the material has an essential effect on the creation of the fusion crust. As seen by the large temperature gradient in Fig. (4.17), during the heating period (2 seconds), i.e., while the sample is exposed to the plasma flow, the material accumulates energy. When the sample is removed from the plasma flow, this energy diffuses inside the material allowing the solid/liquid interface to propagate. As shown in Fig. (4.18), the surface temperature was imposed constant (isothermal boundary condition) during the heating phase and estimated by a radiative boundary condition ($k_l \nabla T_w = -\sigma \epsilon T_w^4$, where $\epsilon = 0.85$) during the cooling phase. We use a radiative boundary condition during the cooling phase because the sample was immediately removed from the testing position, not allowing the pyrometer and the mid-Infra-Red camera to measure the surface temperature. After the experiment, we find a rapid drop-off of the surface temperature due to the large temperature gradient inside the material, as well as the initially high surface temperature. The rate of cooling changes around the melting temperature, where the energy inside the material is overcoming the latent heat of fusion and the thermal conductivity increases. As the heat wave propagates inside the material, the cooling rate at the surface decreases, and the core temperature slowly increases.

State-the-art meteor physics models typically disregard the shear ablation by

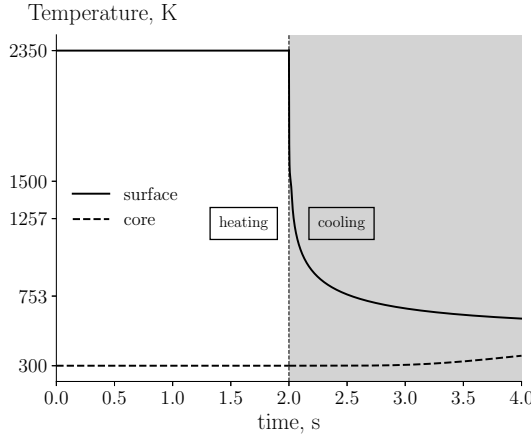


Figure 4.18.: Surface and core temperature for the heating and cooling period of the experiment.

aerodynamic forces, and instead is based on the theoretical heat of vaporization for an ideal mixture of meteoritic constituents. Melting, and subsequent removal due to aerodynamic forces, is energetically more favorable than vaporization. Therefore, in instances where melting is important, the effective heat of ablation may be overestimated. By knowing the heat flux and the total mass loss one can estimate the effective heat of ablation for a given scenario. The mass loss is the sum of the evaporation and mechanical removal, where the evaporation is negligible. Figure (4.19) shows the evolution of the effective heat of ablation of the stagnation point in time for the validation case used in this work. As can be seen in this figure, the value peaks at the test start and then decreases, quickly reaching a fairly steady-state value. The abrupt decrease is due to the initial high heat flux and low mass loss, as time and energy are required to bring the material to its melting point. We computed the average effective heat of ablation following the definition given by Adams et al. [1],

$$\overline{h_{\text{eff}}} = \frac{\int_0^{t_f} \dot{q}(t) dt}{\int_0^{t_f} \dot{q}(t)/h_{\text{eff}}(t) dt}. \quad (4.14)$$

The value obtained for our validation exercise is 1.16 MJ kg^{-1} , whereas the state-of-the-art effective heat of ablation is 8.0 MJ kg^{-1} . It should be noted that, while the conditions in the Arc Jet are among the most extreme achievable in a ground test, they are still not necessarily representative of the flow environment for a given meteor. Indeed, in the case of a large meteoroid at low altitudes, the heat fluxes (mostly due to radiative heating) will far exceed that simulated in the current work, and in those cases, with such extreme heating, the melt layer would conceivably be vaporized before it could be removed by aerodynamic forces. In those cases, such as the one of Johnston and Stern [125],

it would be reasonable to expect the effective heat of ablation to approach the classical value.

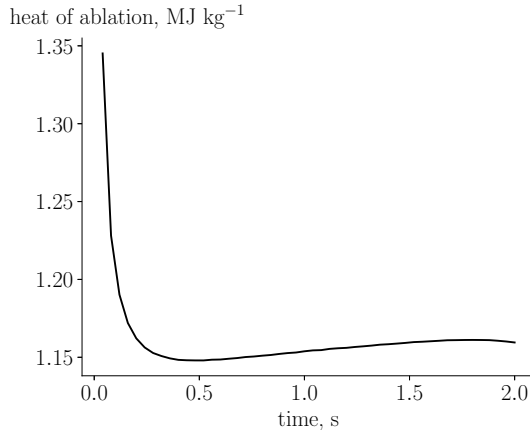


Figure 4.19.: Heat of ablation at the stagnation point in time (h_{eff}). We estimated the heat of ablation from the total heat flux computed by the flow solver and by the total mass loss due to evaporation and shear ablation. The effective heat of ablation (Eq. (4.14)) is computed by integrating this profile.

Comparison of the stagnation point shear and the surface average shear

As mentioned in the Section 4.2, an assumption was made to derive a formulation able to capture the overall recession of a meteoroid during its trajectory. Different from the stagnation point shear (Eq. (4.7)), the surface average shear (Eq. (4.9)) depends on the average aerodynamic forces along the surface. Figure (4.20) shows the average aerodynamic forces for the Tamdakht H5 experiment assuming a perfect sphere with the equivalent radius shown in Fig. (4.7).

Figure (4.21a) shows the comparison of the stagnation point recession by using the two formulations. From the figure, the surface average shear predicts nearly half of the stagnation point recession compared to stagnation point shear, due to a lower mass removal seen in Fig. (4.21b). It is important to stress that this comparison does not serve as a validation of the surface average shear formulation but more as a qualitative one. To properly validate this formulation, it is necessary to perform a 2D axisymmetric computation, which is beyond the scope of this chapter.

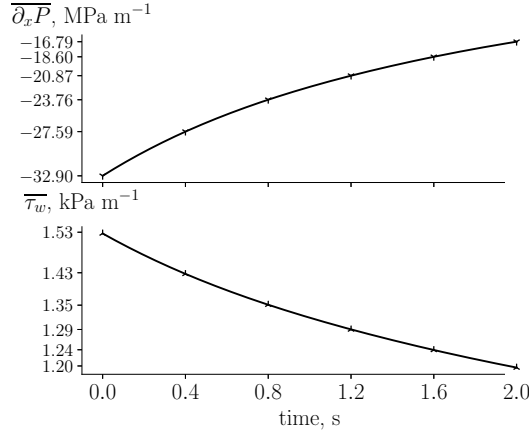


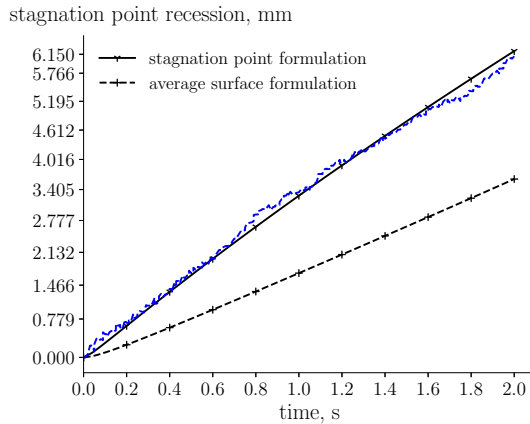
Figure 4.20.: Average aerodynamic forces in time around the sphere: top - $\overline{\partial_x P}$; bottom - $\overline{\tau_w}$.

4.5. Conclusion

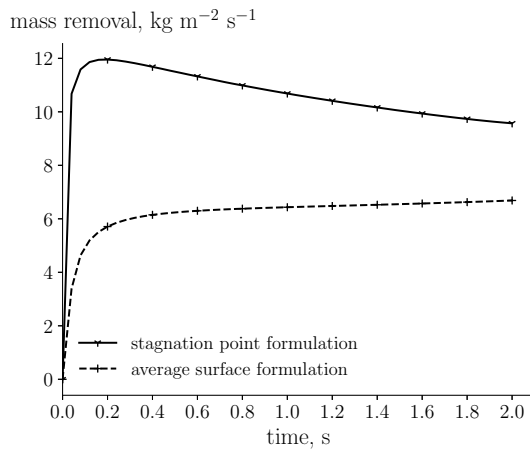
This work has proposed a coupled material/flow methodology for meteoroid entry modeling, accounting for vaporization, and shear ablation of the melting layer. The flow solver computes the evaporation rate, provided by a non-equilibrium evaporation model, and provides boundary conditions (aerodynamic forces) to the material solver. In contrast, the latter computes the thermal behavior and the liquid layer's mass removal due to aerodynamic forces. We have compared the numerical methodology with an H5 ordinary chondrite's experimental data from a campaign carried out at NASA Ames in a high enthalpy facility.

The stagnation point's numerical recession agrees with the experimental results where the shear ablation is the dominant process of ablation (four orders of magnitude higher than the evaporation mass loss). Moreover, this process is sensitive to the molten compound's viscosity and thermal conductivity, which is poorly characterized. We have performed a sensitivity analysis due to the lack of data on the thermal conductivity at high temperatures. Although a low evaporation rate is estimated, we have observed that the evaporation of more volatile elements is consistent with the spectral measurements shown by Agrawal et al. [2].

From our results, we have quantified an effective heat of ablation 1.16 MJ kg^{-1} , which is roughly eight times smaller than the one reported in the literature [42, 265]. We have deduced the effective heat of ablation considering the mass loss due to evaporation and the shear ablation. This outcome is regarded as primary importance as the heat of ablation affects the interpretation of visual and photometric observations, meaning that a lower heat of ablation results in a different estimation of the meteoroid mass derived from trajectory equations.



(a) Comparison of the stagnation point recession for both models. The (---) curve is the recession of the stagnation point determined from the video camera data.



(b) Mass removal rate of the molten layer.

Figure 4.21.: Comparison of two mass removal models; the stagnation point removal and the average removal on the surface.

Although our findings show that the shear ablation is the primary source of mass loss, the evaporation rate might increase at the condition of higher heat flux, balancing the importance of both ablation mechanism. The estimate of meteoroid's mass from photometric observations, based on the measured luminosity and an approximated heat transfer analysis (i.e., transfer coefficient approach), considers evaporation as the primary mass-removal mechanism. Consequently, it is essential to consider the coupled effects between the material and the flow to understand the ablation mechanism during a meteor trajectory to derive these coefficients, which can be later used to interpret photometric observations.

The material thermochemical properties are an uncertainty source to study the melting of meteoroids. At present, these properties have not been measured experimentally for molten meteoritic material at high temperatures. As shown in relevant works in this field (i.e., Haskins et al. [108]), Molecular Dynamics (MD) is a promising method to fill the experimental gap and gain knowledge on these properties.

Finally, we believe that the current model can be extended to account for the break-up and spraying of the molten layer by following the work of Girin [93] and Capek et al. [47]. In the derivation of the uniform recession presented in this chapter, we have inferred that the melting layer is lost on the sample's shoulder as it occurs in the experiment. Our assumption is supported by the fact that the surface forces have an inflection point at $\theta = \pi/2$. As future work, we recommend analyzing this assumption through multidimensional simulations.

CHAPTER 5

Flow radiation

All the fifty years of conscious brooding have brought me no closer to answer the question, “What are light quanta?” Of course today every rascal thinks he knows the answer, but he is deluding himself.

— Albert Einstein

5.1. Introduction

One important characteristic of the meteor phenomenon is the light emitted during the entry. This light is owed to the radiative process inherent to hypersonic entries. It is caused by the excitation of air components and alkali metals arising from meteoroid ablation. The radiative signal of the latter allows to classify the meteoroid, enabling astronomers to understand their origin. The spectral analysis of the meteor phenomenon is the first step to understand its composition. However, there are still several uncertainties related to unknown physics during flight [264] – spraying of the molten layer is one example. This uncertainty can be minimized with ground experiments on real meteorites since the testing conditions and material composition are known. Moreover, ground experiments provide measurements that cannot be inferred from flight observations, such as surface temperature and an in-depth spectral diagnostic of the flow with spatio-temporal resolution.

Parts of this chapter have been published in

1. B. Helber, B. Dias, F. Bariselli, L. F. Zavalan, L. Pittarello, S. Goderis, B. Soens, S. J. McKibbin, P. Claeys and T. E. Magin, **Analysis of Meteoroid Ablation Based on Plasma Wind-tunnel Experiments, Surface Characterization, and Numerical Simulations**, *The Astrophysical Journal*, 876:120-134 2019.
2. L. Pittarello, S. Goderis, B. Soens, S. J. McKibbin, G. Giuli, F. Bariselli, B. Dias, B. Helber, G. O. Lepore, F. Vanhaecke, C. Koeberl, T. E. Magin and P. Claeys, **Meteoroid atmospheric entry investigated with plasma flow experiments: Petrography and geochemistry of the recovered material**, *Icarus*, 331:170-178, 2019.

On the modeling side, the classic meteor physics equations, described in Chapter 1, do not simulate the radiative field in detail, hindering the classification of these objects. Simulating the radiative field is a tremendous task due to its complexity and costly computations. The hypersonic community has a strong knowledge of coupled flow, radiation, and ablation phenomena [229] for the design of Thermal Protection System (TPS), where several approximated models were established to solve the radiative field. One of these is the Hybrid Statistical Narrow-Band (HSNB) (Section 5.2.2), developed by Lamet et al. [140], which has proven to be precise and computationally fast.

In this chapter, we replicate the radiative field of the El Hammami H5 ordinary chondrite ground experiment carried out at von Karman Institute for fluid dynamics (VKI), where we compare the results obtained by means of the HSNB model with the spectral measurements. The objective is to assess the accuracy of the HSNB model to simulate radiative meteor fields. The ground experiments (Section 5.3) are performed in an inductively-coupled plasma wind-tunnel (Plasmatron). The subsonic 1.2 MW Plasmatron facility can reproduce the aero-thermodynamic environment of atmospheric entry in the boundary layer of a test object for many pressures and heat fluxes [38]. We use the stagnation-line solver to recreate the flow field, and we compare the simulated and observed spectral intensity (Section 5.4) by integrating the Radiative Transport Equation (RTE) along lines-of-sight, representing the spectrometers measurements. The simulations include an evaporation boundary condition described in Chapter 3.

The experimental results shown in this chapter were carried out by Dr. Helber. This chapter's original contribution concerns the inclusion of several atomic bound-bound and bound-free processes for alkali metals to the High Temperature Gas Radiation (HTGR) database. Moreover, we develop a systematic approach to reproduce ground experiments with simulation tools and to perform spectral diagnostics.

5.2. Flow radiation modeling

In this section, we analyze the radiative processes in a participating media and how they influence the flow field. After, we describe the HSNB model and the 1D tangent slab method, which allows for an efficient and fast solution of the radiative source terms.

5.2.1. Radiative transfer in participating media

The quantized nature of atoms and molecules might create or annihilate electromagnetic radiation, also known as photons. The interaction of photons with matter leads to radiative processes that are divided in three categories (see Fig. (5.2)): i) bound-bound, ii) bound-free and iii) free-free (also known as *Bremsstrahlung*). As mentioned in Chapter 2, molecules and atoms contain internal energy modes. In the case of molecules, an electronic level n contains

vibrational levels v , which in turn are composed by rotational levels j . The energy of a molecule ro-vibronic level is,

$$E = E^E(n) + E^V(n, v) + E^R(n, v, j)$$

where n , v and j are the electronic, vibration and rotation quantum number, respectively. An energy transition is represented as $(n', v', j') \rightarrow (n'', v'', j'')$ in Fig. (5.2). In some instances, the transition might overcome the ionization energy level I resulting in the loss of an electron from the molecule/atom-shell.

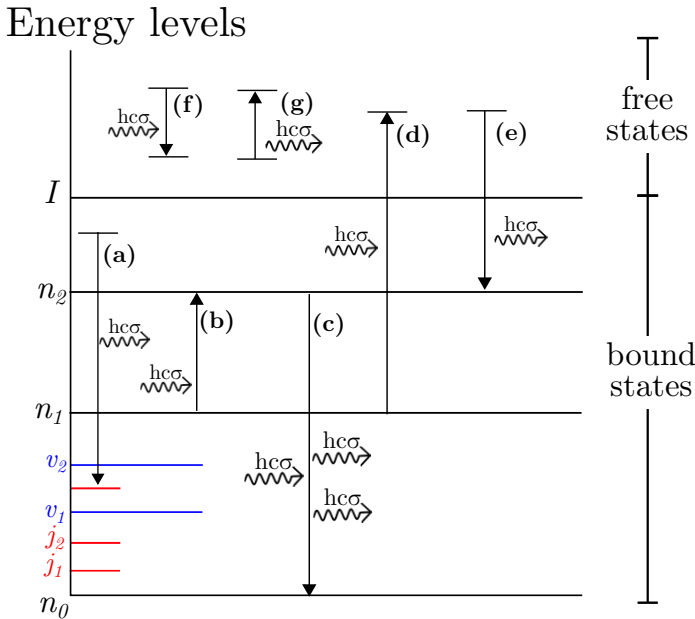


Figure 5.1.: Radiative processes in participating media.

Bound-Bound

These processes occur within the bound states of the atom/molecules internal modes. The collision between heavy particles can lead to an excitation of the upper internal energy levels E_u [163, 189, 191]. After a characteristic lifetime τ_{ul} , the atom or molecule spontaneously relax to a lower energy E_l releasing a photon [69] described as,

$$hc\sigma_{ul} = E_u - E_l. \quad (5.1)$$

where σ_{ul} is the photon wavenumber. This decay of energy, $u \rightarrow l$, is called spontaneous emission and is depicted as transition (a) in Fig. (5.2). In molecules, the ro-vibrational transitions within the same electronic state result in a weak energy release, meaning that the photon wavenumber is in the InfraRed (IR) part of the electromagnetic spectrum [247]. The electronic state

decay results in the photon emission with higher energy (or high-wavenumber), corresponding to UltraViolet (UV) / Visible (VIS) or Vacuum-Ultraviolet (VUV) emission [179]. The radiation field leads to the emission of photons by inducing the decay of energy levels. This process called induced or stimulated emission, is depicted by the process (c), and results in the emission of two photons that have identical propagation direction [69, 250]. The inverse process of induced emission is called absorption, process (b) in Fig. (5.2), where the atom/molecule absorbs a photon leading to an excitation of the upper level such as $l \rightarrow u$. Both absorption and induced emission depend on the spectral energy density, thus, they are similar in nature but with opposite behaviour.

Line-shape: Although the ro-vibronic and electronic transitions are discrete, the emission/absorption of photons results in broadened spectral lines centered in σ_{ul} . The causes of the line broadening, in our applications, are mostly due to Doppler effects and collisions of the radiating particles (Lorentz) such that,

$$\int_0^\infty f_{D,L}(\gamma_{ul}^{D,L}, \sigma - \sigma_{ul}) d\sigma = 1.$$

where γ_{ul}^D and γ_{ul}^L are line half-width for the Doppler and Lorentz broadening, respectively.

Doppler broadening, f_D leads to a wavenumber shift because of the particle movement concerning the observer reference frame. The shift in wavenumber is given by,

$$\sigma - \sigma_{ul} = \sigma_{ul} \frac{v}{c} \quad (5.2)$$

where $v = \mathbf{v} \cdot \hat{\mathbf{s}}$ is the relative velocity between emitting/absorbing particle and the observer and $\hat{\mathbf{s}}$ the unit direction vector. The velocity of the particles can be derived from Kinetic Theory (KT) and they are assumed to follow Maxwell's velocity distribution. In Section C.2, we give more details regarding the line profile due to Doppler effect.

The collision broadening is due to the collision frequency between particles, and it arises when the radiator collides with a perturber. This broadening is divided into several contributions, where the line shape follows a Lorentzian f_L . Neutral-Neutral collisions generate van der Waals broadening (Section C.2.2.1). Resonance broadening (Section C.2.2.2) happens only for collisions where the perturber is the same as the radiator. Lastly, the Stark broadening (Section C.2.2.3) occurs in the presence of an electric field. This electric field is either induced externally or due to the collisions of charged particles (free electrons and ions).

For hypersonic applications, both Doppler and collision broadening are essential. The convolution of the two line-profiles gives rise to the Voigt profile. In this work, we use the method of S.R. Drayson [241] to compute the convolution, where the details are presented in Scoggins [229]. The line profiles are depicted in Fig. (5.2).

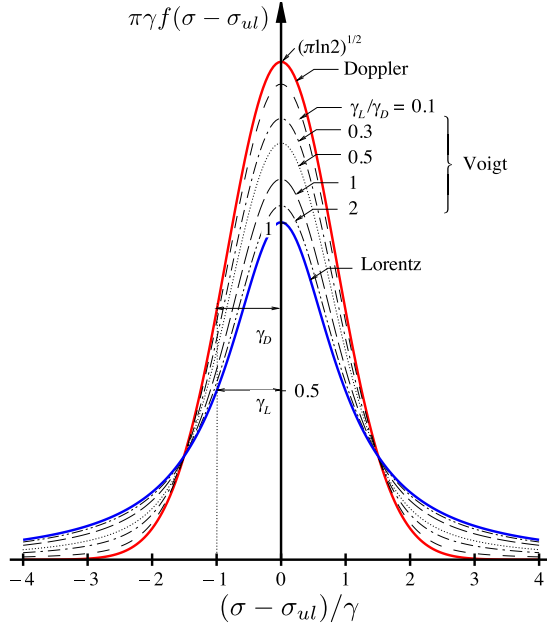


Figure 5.2.: Doppler, Lorentz and Voigt line shape. This figure has been adapted from Modest [179].

Master equation: We write the master equation of an isolated line, describing above processes in a wavenumber range $[\sigma, \sigma + d\sigma]$, as

$$\partial_t n_l|_\sigma = n_u A_{ul}^{bb} f_{ul}^{se}(\sigma - \sigma_{ul}) - u_\sigma [n_l B_{lu}^{bb} f_{ul}^{ab}(\sigma - \sigma_{ul}) - n_u B_{ul}^{bb} f_{ul}^{ie}(\sigma - \sigma_{ul})] d\sigma \quad (5.3)$$

where n is the number density, the probabilities A_{ul}^{bb} , B_{ul}^{bb} and B_{lu}^{bb} are the Einstein coefficients for spontaneous emission, induced emission and absorption, respectively, and u_σ is the radiative energy density. The line profiles f^{se} , f^{ab} , and f^{ie} are associated with spontaneous emission, absorption, and induced emission [97]. The relation between the Einstein coefficient will be given later, but for now we define the spontaneous emission coefficient as,

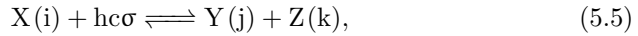
$$A_{ul}^{bb} = \frac{1}{\tau_{ul}} = \frac{2\pi\sigma_{ul}^2 q_e^2 a_l}{\epsilon_0 m_e c a_u} f_{lu}. \quad (5.4)$$

where a is the degeneracy of the level and f is the oscillator strength of a line.

Bound-free

When a high-energy photon collides with a gaseous particle, it might break the molecular bonds (photodissociation) or remove electrons from the atomic/molecular electron shells (photoionization). These photochemical processes alter the composition of the flow, and they usually appear on the VUV part of

the spectrum. A general formula for photochemistry writes as,



where X, Y and Z are the species involved in the reaction and i, j and k represent their respective energy level. Lamet et al. [142] generalized the energy conservation for reaction Eq. (5.5) such that,

$$\frac{1}{2}\mu g^2 = hc\sigma + E_i^X - E_j^Y - E_k^Z, \quad (5.6)$$

where g and μ are respectively the relative velocity and the reduced mass of Y and Z, E_l^s is the energy of species s at the level l . In Fig. (5.2), photochemistry process is depicted as (d) while its inverse, radiative recombination, is depicted as (e).

Master equation: Analogous to Eq. (5.3), we write a master equation of this process such that,

$$\partial_t n_i^X|_\sigma = n_j^Y n_k^Z A_{jk}^{\text{bf}} - u_\sigma [n_i^X B_i^{\text{bf}} - n_j^Y n_k^Z B_{jk}^{\text{bf}}] \quad (5.7)$$

where n_l^s is the number density of species s at level l and the rates A_{jk}^{bf} , B_i^{bf} and B_{jk}^{bf} are similar to the Einstein coefficients and write as,

$$\begin{aligned} A_{jk}^{\text{bf}} &= g \mathfrak{S}_{jk,i}^{\text{se}}(\sigma) f^0(g) d^3g d\Omega \\ B_{jk}^{\text{bf}} &= g \mathfrak{S}_{jk,i}^{\text{ie}}(\sigma) f^0(g) d^3g d\Omega \\ B_i^{\text{bf}} &= \mathfrak{S}_{i,jk}^{\text{abs}}(\sigma) d\Omega \end{aligned}$$

where $\mathfrak{S}_{jk,i}^{\text{se}}$, $\mathfrak{S}_{jk,i}^{\text{ie}}$ and $\mathfrak{S}_{i,jk}^{\text{abs}}$ are the effective cross-sections on spontaneous emission, induced emission and absorption, respectively. $f^0(g)$ is the distribution function of the relative velocity between the products of Eq. (5.6).

Free-free

The collision between an electron and a heavy species may result in the deceleration of the electron. This loss of kinetic energy translates into the emission of a photon, and this mechanism is called Bremsstrahlung, process (g) in Fig. (5.2). On the other hand, the collision of a photon with an electron leads to an increase of the electron kinetic energy (inverse Bremsstrahlung); this corresponds to process (f).

Since the translational energy of the particles is not quantized, the bound-free and free-free processes result in a near-continuum spectrum. In the case of bound-free radiation, the continuum absorption and emission appear above the ionization/dissociation energy. At the same time, for the free-free, it can span the entire spectrum because the photon released or absorbed does not have a specific wavenumber. Continuum radiation is relevant when dissociation and

ionization become substantial.

Radiative field

We derive the power due to the bound-bound process, of an isolated line, from the master equation. The same method is general for the bound-free. The radiative power per unit volume in a spectral range $[\sigma, \sigma + d\sigma]$ is retrieved by multiplying the master equation, Eq. (5.3), with the photon energy $hc\sigma_{ul}$ yielding,

$$d\mathcal{P}^{\text{rad}} = hc\sigma_{ul} \partial_t n_l|_{\sigma} = \int_{4\pi} hc\sigma_{ul} \left[\frac{1}{4\pi} n_u A_{ul}^{\text{bb}} f_{ul}^{\text{se}}(\sigma - \sigma_{ul}) - \frac{I_{\sigma}}{c} \left[n_l B_{lu}^{\text{bb}} f_{ul}^{\text{ab}}(\sigma - \sigma_{ul}) - n_u B_{ul}^{\text{bb}} f_{ul}^{\text{ie}}(\sigma - \sigma_{ul}) \right] \right] d\Omega d\sigma. \quad (5.8)$$

where the radiative density energy is,

$$u_{\sigma} = \frac{1}{c} \int_{4\pi} I_{\sigma}(\hat{s}) d\Omega, \quad (5.9)$$

and I_{σ} is the radiant intensity.

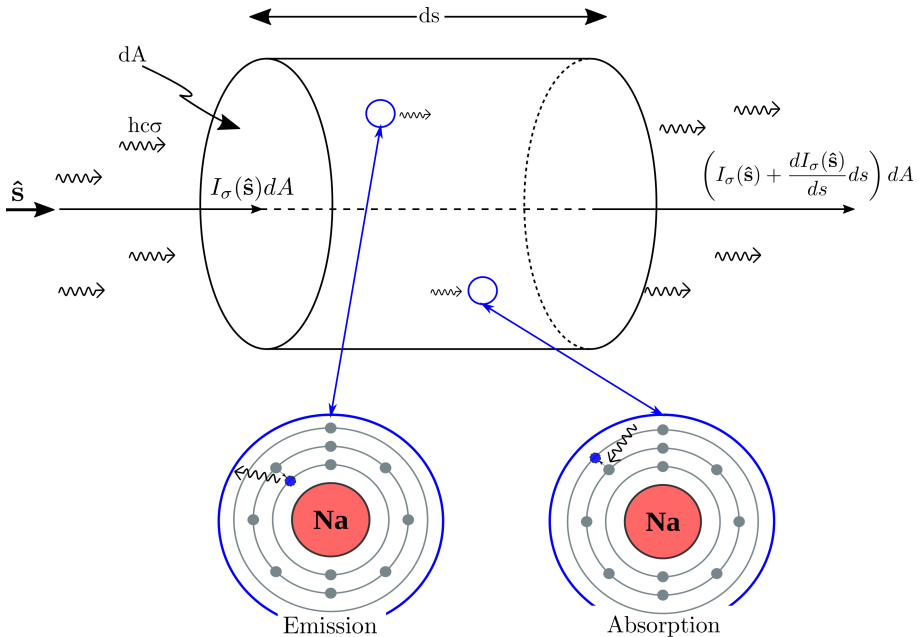


Figure 5.3.: Energy balance in an infinitesimal pencil of rays.

The power in an elementary volume dV (shown in Fig. (5.3)), in an elemen-

tary solid angle $d\Omega$ and in a spectral range $[\sigma, \sigma + d\sigma]$ is,

$$\begin{aligned} d\mathcal{P}^{\text{rad}}dV &= \frac{dI_\sigma}{ds} ds dA d\sigma d\Omega \Rightarrow \\ d\mathcal{P}^{\text{rad}} &= \frac{dI_\sigma}{ds} d\sigma d\Omega, \end{aligned} \quad (5.10)$$

and substituting the above equation in Eq. (5.8) yields,

$$\frac{dI_\sigma}{ds} = \hat{\mathbf{s}} \cdot \nabla I_\sigma(\hat{\mathbf{s}}) = \eta_{\sigma,ul}^{\text{bb}} - \kappa_{\sigma,ul}^{\text{bb}} I_\sigma(\hat{\mathbf{s}}). \quad (5.11)$$

This is known as the steady Radiative Transfer Equation (RTE) and represents the steady-state transport of the photon energy flux at certain wavenumber σ , in a certain direction $\hat{\mathbf{s}}$ along an optical path s . The quantities $\eta_{\sigma,ul}$ and $\kappa_{\sigma,ul}$ are, respectively, the absorption and emission coefficient of an isolated line and the sum over all transitions is,

$$\eta_\sigma^{\text{bb}} = \sum_{ul} \eta_{\sigma,ul}^{\text{bb}} = \sum_{ul} n_u \frac{A_{ul}^{\text{bb}}}{4\pi} hc\sigma_{ul} f_{ul}^{\text{se}}(\sigma - \sigma_{ul}) \quad (5.12)$$

$$\kappa_\sigma^{\text{bb}} = \sum_{ul} \kappa_{\sigma,ul}^{\text{bb}} = \sum_{ul} \left[n_l B_{lu}^{\text{bb}} f_{ul}^{\text{ab}}(\sigma - \sigma_{ul}) - n_u B_{ul}^{\text{bb}} f_{ul}^{\text{ie}}(\sigma - \sigma_{ul}) \right] h\sigma_{ul}, \quad (5.13)$$

and the same coefficients for bound-free processes are,

$$\eta_\sigma^{\text{bf}} = \sum_{ijk} \eta_{\sigma,ijk}^{\text{bf}} = \sum_{ijk} n_j^Y n_k^Z hc\sigma g \mathfrak{S}_{jk,i}^{\text{se}}(\sigma) 4\pi g^2 f^0(g) \frac{dg}{d\sigma}, \quad (5.14)$$

$$\kappa_\sigma^{\text{bf}} = \sum_{ijk} \kappa_{\sigma,ijk}^{\text{bf}} = \sum_{ijk} \left[n_i^X \mathfrak{S}_{i,jk}^{\text{abs}}(\sigma) - n_j^Y n_k^Z g \mathfrak{S}_{jk,i}^{\text{ie}}(\sigma) 4\pi g^2 f^0(g) \frac{dg}{d\sigma} \right] h\sigma. \quad (5.15)$$

Without loss of generality, we extend Eq. (5.11) to all radiative mechanisms $k \in \mathcal{R}$ such that,

$$\eta_\sigma = \sum_{k \in \mathcal{R}} \eta_\sigma^k, \quad \kappa_\sigma = \sum_{k \in \mathcal{R}} \kappa_\sigma^k.$$

The HTGR database [9, 61, 62, 240] provides all the radiative mechanisms used in this work, shown in Table (C.1). The database includes bound-bound (atomic and molecular transitions), bound-free and free-free mechanisms for several species; it covers a spectral range from 1000 to 200 000 cm^{-1} valid to temperatures up to 30 000 K.

The formal solution of the RTE, which includes all mechanisms in \mathcal{R} is [247],

$$I_\sigma(s) = I_\sigma(0) \prod_{k \in \mathcal{R}} \tau_\sigma^k(0, s) + \sum_{k \in \mathcal{R}} \int_0^s \eta_\sigma^k(s') \tau_\sigma^k(s', s) \prod_{k' \neq k} \tau_\sigma^{k'}(s', s) ds', \quad (5.16)$$

where $I_\sigma(0)$ is the spectral intensity at the boundary of the optical path s , the term $\eta_\sigma^k(s')\tau_\sigma^k(s', s)$ represents the self-absorption of the mechanism k and $\tau_\sigma(s', s)$ is the spectral transmissivity between points s' and s given by,

$$\tau_\sigma(s', s) = \exp\left(-\int_{s'}^s \kappa_\sigma(s'') ds''\right). \quad (5.17)$$

The transmissivity is related to the opacity of the gas, i.e., in optically thin medium this property is close to the unity while for optically thick it approaches zero.

In a homogenous medium under Local Thermodynamic Equilibrium (LTE) [250], the RTE equation reduces to Kirchhoff's law,

$$\eta_\sigma = I_\sigma^b \kappa_\sigma \quad (5.18)$$

where the spectral intensity is given by Planck's law,

$$I_\sigma = I_\sigma^b \equiv 2hc^2\sigma^3 \left[\exp\left(\frac{hc\sigma}{k_B T}\right) - 1 \right]^{-1}. \quad (5.19)$$

Inserting Eqs. (5.12) and (5.13) into Eq. (5.18) allows to derive the relationship between the Einstein coefficients and line shapes for the bound-bound [97],

$$B_{ul}^{bb} f_{ul}^{ie}(\sigma - \sigma_{ul}) = \frac{1}{8\pi hc\sigma^3} A_{ul}^{bb} f_{ul}^{se}(\sigma - \sigma_{ul}), \quad (5.20)$$

$$B_{lu}^{bb} f_{ul}^{ab}(\sigma - \sigma_{ul}) = \frac{1}{8\pi hc\sigma^3} A_{ul}^{bb} f_{ul}^{se}(\sigma - \sigma_{ul}) \frac{a_u}{a_l} \exp\left[\frac{hc(\sigma - \sigma_{ul})}{k_B T}\right]. \quad (5.21)$$

and the relationship between bound-free cross-sections using Eqs. (5.14) and (5.15),

$$\begin{aligned} \mathfrak{S}_{jk,i}^{se}(\sigma) &= 2hc\sigma^3 \mathfrak{S}_{jk,i}^{ie}(\sigma), \\ \mathfrak{S}_{jk,i}^{ie}(\sigma) &= \frac{h^2}{4\pi\mu^2 g^2 c} \frac{a_i}{a_j a_k} \mathfrak{S}_{i,jk}^{abs}(\sigma). \end{aligned} \quad (5.22)$$

5.2.2. The Hybrid Statistical Narrow-Band method

The integration of the RTE (Eq. (5.16)) over the spectral space is the real bottleneck for engineering applications because of the large number of rovibrational and electronic transitions. Essentially, some mechanisms contain millions of lines. The spectral integration is usually done via Line-By-Line (LBL), which is computationally costly due to the spectral resolution required to capture the fine structures of these transitions. This method becomes almost impractical for 2D or 3D problems, especially for coupled radiation/flow simulations. Since the 60s, approximated methods are being developed to overcome this computational issue. Approximated methods include the mean absorption coefficient –

the boundaries of the RTE will be shown later

such as the Rosseland mean used by Park [199, 200, 201] described in Chapter 1 – Smeared-Rotational-Band [129] and narrow-band models, among others.

In the narrow-band models, the radiative properties are averaged around a small enough band, $\Delta\sigma$, which contains numerous spectral lines and the Planck function (Eq. (5.19)) is nearly constant. These models can be divided into two families [97, 250]: i) regular band models or the Elsasser model, ii) and Statistical Narrow-Band (SNB) models or the Mayer-Goody model [97]. The Elsasser model assumes equally spaced lines with the same intensity. In contrast, the Mayer-Goody model assumes a random distribution of similar shape lines, and the line intensity S follows a probability distribution function $P(S)$. The former model overestimates the absorption coefficient at high temperatures due to less overlap between the lines, compared to the statistical model.

In this thesis, we use the HSNB model of Lamet et al. [140], which combines a statistical model for optically thick molecular systems and a box model for optically thin molecular systems and continua. The small number of atomic lines in a narrow-band prevents atomic systems from being treated with a statistical approach; hence, it is treated with the classic LBL method. Scoggins [229], Soucasse et al. [238] used the HSNB method to perform coupled flow/radiation simulations showing reduction of the computational cost, while retaining the accuracy of the full LBL method.

The RTE for the HSNB model is derived by averaging Eq. (5.16) over a narrow-band using the following definition,

$$\overline{X}^{\Delta\sigma} \equiv \frac{1}{\Delta\sigma} \int_{\Delta\sigma} X \, d\sigma, \quad (5.23)$$

yielding,

$$\overline{I_\sigma(s)}^{\Delta\sigma} = \overline{I_\sigma(0)}^{\Delta\sigma} \prod_{k \in \mathcal{R}} \overline{\tau_\sigma^k(0, s)}^{\Delta\sigma} + \sum_{k \in \mathcal{R}} \int_0^s \overline{\eta_\sigma^k(s') \tau_\sigma^k(s', s)}^{\Delta\sigma} \prod_{k' \neq k} \overline{\tau_\sigma^{k'}(s', s)}^{\Delta\sigma} ds'. \quad (5.24)$$

The main assumptions of Eq. (5.24) are:

- all the mechanisms in \mathcal{R} are statistically uncorrelated. In other words, the spectra between the different species are weakly correlated [247]; hence, the mean transmissivity yields,

$$\overline{\tau_\sigma}^{\Delta\sigma} = \prod_{k \in \mathcal{R}} \overline{\tau_\sigma^k}^{\Delta\sigma}.$$

- the boundary intensity is approximated as,

$$\overline{I_\sigma(0) \prod_{k \in \mathcal{R}} \tau_\sigma^k(0, s)}^{\Delta\sigma} = \overline{I_\sigma(0)}^{\Delta\sigma} \prod_{k \in \mathcal{R}} \overline{\tau_\sigma^k(0, s)}^{\Delta\sigma},$$

which according to Taine and Soufiani [247] is reasonable for weakly reflecting walls (or high wall ϵ).

At this stage, it is important to separate the set of mechanism \mathcal{R} in Eq. (5.24) according to their radiative contribution such that,

$$k \in \mathcal{R} = \mathcal{R}^{\text{thick}} \cup \mathcal{R}^{\text{thin}} \cup \mathcal{R}^{\text{continua}} \cup \mathcal{R}^{\text{atom}}.$$

A radiative mechanism is a priori considered thick if its optical depth $\kappa_\sigma l > 0.1$ on a slab $l = 10$ cm at the LTE conditions of $T = 8000$ K and $p = 2$ atm, otherwise it is considered thin. Figure (5.4) shows all molecular systems present in the SNB database according to their optical thickness

Statistical narrow-band for optically thick molecular systems

From Eq. (5.24), the spectral intensity for optically thick systems can be written as,

$$\overline{I_\sigma^{\text{thick}}(s)}^{\Delta\sigma} = \sum_{k \in \mathcal{R}^{\text{thick}}} \int_0^s \frac{\eta_\sigma^k(s')}{\kappa_\sigma^k(s')} \frac{\partial}{\partial s'} \overline{\tau_\sigma^k(s', s)}^{\Delta\sigma} \prod_{k' \neq k} \overline{\tau_\sigma^{k'}(s', s)}^{\Delta\sigma} ds', \quad (5.25)$$

and Lamet et al. [140] approximated the self-absorption term as,

$$\frac{\eta_\sigma^k(s')}{\kappa_\sigma^k(s')} \frac{\partial}{\partial s'} \overline{\tau_\sigma^k(s', s)}^{\Delta\sigma} \approx \frac{\eta_\sigma^k(s')}{\kappa_\sigma^k(s')} \frac{\partial}{\partial s'} \overline{\tau_\sigma^k}^{\Delta\sigma}(s', s). \quad (5.26)$$

This approximation is consistent under LTE conditions because the ratio of emission and absorption coefficients follow the Planck function, which is uncorrelated to the transmissivity over a narrow-band. Under non-LTE conditions, Lamet et al. [140] verified the validity of Eq. (5.26), and they observed an error less than 1 % for most of the thick mechanisms at maximum temperature ratio of $T^r/T^{\text{ve}} = 2$.

We discretize Eq. (5.26) in a homogenous slab $\Delta s_i = s_{i+1} - s_i$,

$$\overline{I_\sigma^{\text{thick}}(s_j)}^{\Delta\sigma} = \sum_{k \in \mathcal{R}^{\text{thick}}} \sum_{i=1}^{j-1} \left[\overline{\tau_\sigma^k(s_{i+1}, s_j)}^{\Delta\sigma} - \overline{\tau_\sigma^k(s_i, s_j)}^{\Delta\sigma} \right] \frac{\eta_\sigma^k(s_i)}{\kappa_\sigma^k(s_i)} \prod_{k' \neq k} \overline{\tau_\sigma^{k'}(s_i^*, s_j)}^{\Delta\sigma}, \quad (5.27)$$

and to simplify the spatial integration in Eq. (5.25), we introduce a mean equivalent point s_i^* , such that

$$\overline{\tau_\sigma^k(s_i^*, s_j)}^{\Delta\sigma} \equiv \sqrt{\overline{\tau_\sigma^k(s_i, s_j)}^{\Delta\sigma} \overline{\tau_\sigma^k(s_{i+1}, s_j)}^{\Delta\sigma}}. \quad (5.28)$$

As cited by Soucasse et al. [238], Taine and Soufiani [247], the aim of the SNB is to provide an expression of the mean transmissivity on a homogenous slab of length l ,

$$\overline{\tau_\sigma(l)}^{\Delta\sigma} = \frac{1}{\Delta\sigma} \int_{\Delta\sigma} \exp(-\kappa_\sigma l) d\sigma. \quad (5.29)$$

Under the assumptions of the SNB model mentioned above, Goody and Yung

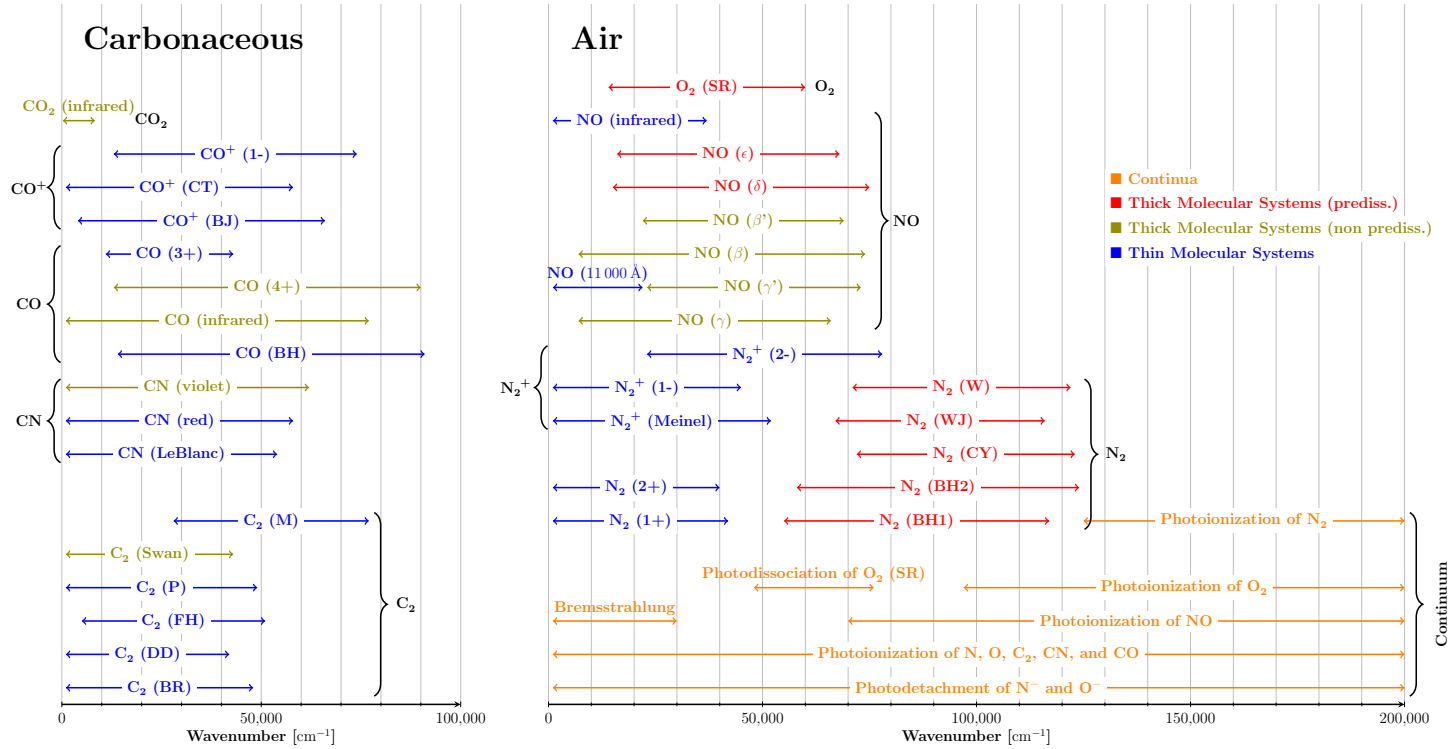


Figure 5.4.: Graphical summary of the molecular systems and continuum processes included in the SNB database. This figure was adapted from Scoggins [229].

[97] provided an expression of the mean transmissivity,

$$\overline{\tau_\sigma(l)}^{\Delta\sigma} = \exp(-\overline{W}/\delta), \quad (5.30)$$

where δ is the average line spacing,

$$\delta = \frac{\Delta\sigma}{N},$$

and N is the number of lines within the narrow-band $\Delta\sigma$. The absorption coefficient follows the definition [179],

$$\kappa_\sigma = f(\sigma - \sigma_{ul})S,$$

where S is the line intensity, leading to the expression of the mean black equivalent line width given by [97, 140, 247],

$$\begin{aligned} \overline{W} &= \frac{1}{N} \sum_i^N \int_0^{+\infty} \left[1 - \exp(-S_i f(\sigma - \sigma_{ul})l) \right] d\sigma \\ &= \int_0^{+\infty} P(S)W(S)dS \end{aligned}$$

From the expression above, the mean black equivalent line width depends on the probability distribution function of the line intensity, and a unique spectral line shape for all the lines. The line intensity PDFs $P(S)$ can be described by the Goody exponential distribution [97] or by the Malkmus inverse-exponential distribution [156].

Soucasse et al. [238] provides expressions for the mean black equivalent width, for a uniform and non-uniform media. They are a function of the mean absorption coefficient $\overline{\kappa_\sigma}^{\Delta\sigma}$, the partial pressure of the species, and the line overlapping parameters $\overline{\beta}_D$ and $\overline{\beta}_L$ related to the Doppler and Lorentz broadening. In this manuscript, we only describe the mean black equivalent width for a non-uniform media using the Lindquist-Simmon approximation, see Table (5.1). The interested reader is referred to Lamet et al. [140], Lamet [141], Scoggins [229], Soucasse et al. [238] for more information related to the statistical treatment for uniform media and for non-uniform media with the Curtis-Godson approximation.

The Lindquist-Simmons provides a better approximation for non-uniform paths with strong variations of the line widths since it accounts for its derivative, as opposed to the Curtis-Godson which assumes uniform path-averages properties. The expression for the broadening regime is given by,

$$\frac{\overline{W}_{L/D}}{\delta}(s', s) = - \int_{s'}^s \frac{1}{\delta} \frac{\partial}{\partial s''} \overline{W}_{L/D}(s'', s) ds'', \quad (5.31)$$

where the derivatives can be found Table (5.1) provided by Rivière and Soufiani

Table 5.1.: Summary of analytical relationships for mean black equivalent line widths for a non-uniform path o using the Lindquist-Simmons approximation (adapted from Scoggins [229]), corresponding to different probability distribution functions $P(S)$ of line strength S and the mean line intensity $S_0 = \int SP(S)dS$. \bar{k} is the mean absorption coefficient per partial pressure p_a of species a , and $\bar{W}^* = -1/\delta \partial_{s''} \bar{W}(s'', s) [p_a(s'')\bar{k}(s'')]^{-1}$.

$P(S)$	\bar{k}	Lorentz profile:		Doppler profile:	
		$x = uk^*/2\bar{\beta}_L^*, \rho = \bar{\beta}_L(s'')/\bar{\beta}_L^*$		$x = uk^*/\bar{\beta}_D^*, \rho = \bar{\beta}_D(s'')/\bar{\beta}_D^*$	
		$\bar{\beta}_L$	\bar{W}_L^*	$\bar{\beta}_D$	\bar{W}_D^*
<i>Goody exponential</i>					
$\frac{1}{S_0} \exp\left(-\frac{S}{S_0}\right)$	$\frac{S_0}{\delta}$	$\frac{\gamma_0^L}{\delta}$	—————	$\frac{\gamma_0^D}{\delta} \sqrt{\frac{\pi}{\ln 2}}$	$\frac{1}{\sqrt{\pi}} \int_{-\infty}^{+\infty} \frac{\exp(-\xi^2)}{[1+x \exp(-\rho^2 \xi^2)]^2} d\xi$
<i>Malkmus tail inverse-exponential</i>					
$\frac{\exp\left(-\frac{S}{S_{\max}}\right) - \exp\left(-\frac{RS}{S_{\max}}\right)}{S \ln R}$	$\frac{S_{\max}}{\delta \ln R}$	$\frac{\pi \gamma_0^L}{\delta \ln R}$	$\frac{2x\rho + (1-\rho^2)\sqrt{1+2x}}{(1-\rho^2+2x)\sqrt{1+2x}}$	$\frac{\gamma_0^D}{\delta \ln R} \sqrt{\frac{\pi}{\ln 2}}$	$\frac{1}{\sqrt{\pi}} \int_{-\infty}^{+\infty} \frac{\exp(-\xi^2)}{1+x \exp-\rho^2 \xi^2} d\xi$

[216].

The Voigt mean black equivalent width is obtained by [229],

$$\begin{aligned} \frac{\overline{W}_V}{\delta} &= u\overline{k}^* \sqrt{1 - \Omega^{-1/2}}, \\ \Omega &= \left[1 - \left(\frac{1}{u\overline{k}^*} \frac{\overline{W}_D}{\delta}\right)^2\right]^{-2} + \left[1 - \left(\frac{1}{u\overline{k}^*} \frac{\overline{W}_L}{\delta}\right)^2\right]^{-2} - 1. \end{aligned} \quad (5.32)$$

where the pressure path length u , mean absorption coefficient \overline{k}^* per partial pressure p_a of the absorbing species, and mean overlap parameter $\overline{\beta}^*$ are given by,

$$u = \int_{s'}^s p_a(s'') ds'', \quad (5.33)$$

$$\overline{k}^* = \frac{1}{u} \int_{s'}^s p_a(s'') \overline{k}(s'') ds'', \quad (5.34)$$

$$\overline{\beta}^* = \frac{1}{u\overline{k}^*} \int_{s'}^s p_a(s'') \overline{k}(s'') \overline{\beta}(s'') ds''. \quad (5.35)$$

When compared to the LBL method, Scoggins [229] found that the Malkmus distribution provides a better match for the Lorentz broadening of all systems. In the case of Doppler broadening, he observed that the Goody distribution provides a better match for the air systems, while the Malkmus distribution is better for the carbonaceous systems.

The SNB formulation allows to tabulate the radiative parameters for optically thick systems $\overline{\eta}_\sigma/\overline{\kappa}_\sigma^{\Delta\sigma}$, $\overline{\kappa}_\sigma^{\Delta\sigma}$, $\overline{\beta}_D$ and $\overline{\beta}_L$ enabling a fast computation of the radiative field. These parameters have been tabulated [140, 229, 238] based on the rotational T^r (500–50 000K) and the vibronic T^{ve} (500–25 000K) temperatures for constant band-widths of $\Delta\sigma = 1000 \text{ cm}^{-1}$ for 1000–200 000 cm^{-1} .

Box model for optically thin molecular systems and continua

Lamet [141] showed that the curve of growth ($-\ln[\overline{\tau}_\sigma^{\Delta\sigma}(l)]$) for a slab of characteristic length l for optically thin systems behaves linearly, which allows the following approximation,

$$-\ln(\overline{\tau}_\sigma^{\Delta\sigma}(l)) = -\ln\left(\frac{1}{\Delta\sigma} \int_{\Delta\sigma} \exp(\kappa_\sigma l) d\sigma\right) \approx \overline{\kappa}_\sigma^{\Delta\sigma} l.$$

This approximation is called the Box model [179] and holds for continua since these contributions have a weak spectral dynamic, due to the continuum behavior of bound-free processes. Since both optically thin and continua systems are treated with the Box model, we write both sets of mechanism \mathcal{R} into a single one such that,

$$\mathcal{R}^{\text{box}} = \mathcal{R}^{\text{think}} \cup \mathcal{R}^{\text{continua}}$$

For these mechanisms, the absorption and emission coefficient are weakly correlated which simplifies the self-absorption term to,

$$\overline{\eta_{\sigma}^k \tau_{\sigma}^k}^{\Delta\sigma} = \overline{\eta_{\sigma}^k}^{\Delta\sigma} \overline{\tau_{\sigma}^k}^{\Delta\sigma}.$$

allowing to write Eq. (5.24) as,

$$\overline{I_{\sigma}^{\text{box}}(s)}^{\Delta\sigma} = \sum_{k \in \mathcal{R}^{\text{box}}} \int_0^s \overline{\eta_{\sigma}^k(s')}^{\Delta\sigma} \prod_{k' \in \mathcal{R}} \overline{\tau_{\sigma}^{k'}(s', s)}^{\Delta\sigma} ds', \quad (5.36)$$

and the average transmissivity is given by the Box model,

$$\overline{\tau_{\sigma}^k(s', s)}^{\Delta\sigma} = \exp\left(-\int_{s'}^s \overline{\kappa_{\sigma}^k(s'')}^{\Delta\sigma} ds''\right), \quad \forall k \in \mathcal{R}^{\text{box}}. \quad (5.37)$$

Equation (5.36) is discretized as,

$$\overline{I_{\sigma}^{\text{box}}(s_j)}^{\Delta\sigma} = \sum_{k \in \mathcal{R}^{\text{box}}} \sum_{i=1}^{j-1} \overline{\eta_{\sigma}^k(s_i)}^{\Delta\sigma} \prod_{k' \in \mathcal{R}} \overline{\tau_{\sigma}^{k'}(s_i^*, s_j)}^{\Delta\sigma} \Delta s_i \quad (5.38)$$

and the pseudo-mean transmissivity simplifies to,

$$\begin{aligned} \overline{\tau_{\sigma}^k(s_i^*, s_j)}^{\Delta\sigma} = \\ \exp\left(-\frac{(s_{i+1} - s_i)}{2} \overline{\kappa_{\sigma}^k(s_i)}^{\Delta\sigma} - \sum_{k=i+1}^{j-1} (s_{k+1} - s_k) \overline{\kappa_{\sigma}^k(s_k)}^{\Delta\sigma}\right), \quad \forall k \in \mathcal{R}^{\text{box}}. \end{aligned} \quad (5.39)$$

Similarly to the optically thick systems, the radiative properties for the Box systems ($\overline{\eta_{\sigma}^{\Delta\sigma}}$ and $\overline{\kappa_{\sigma}^{\Delta\sigma}}$) are also tabulated for many temperatures.

One contribution of this thesis is the addition of photoionization processes for atomic alkali to the HTGR database; hence, we proceed to the derivation of the absorption and emission coefficient for photoionization. We recall that Eqs. (5.14) and (5.15) are general coefficients for any bound-free process, given by Eq. (5.5). Photoionization is a case of Eq. (5.5) and the radiative coefficients are obtained by inserting the electron Maxwellian distribution

$$\begin{aligned} f^0(v_e) &= \frac{m_e^3}{h^3 \xi(m_e, T^{\text{ve}})} \exp\left(-\frac{m_e v_e^2}{2 k_B T^{\text{ve}}}\right) \\ &= \frac{m_e^3}{h^3 \xi(m_e, T^{\text{ve}})} \exp\left(\frac{E_{\text{ion}}^{\text{at}} - hc\sigma}{k_B T^{\text{ve}}}\right), \end{aligned} \quad (5.40)$$

into Eqs. (5.14) and (5.15), using the relation provided by Eq. (5.22). Quantities m_e , v_e and $E_{\text{ion}}^{\text{at}}$ are respectively the electron mass, velocity and the ionization

energy and the electron volumetric translational partition function is

$$\xi(m_e, T^{\text{ve}}) = \left(\frac{2\pi m_e k_B T^{\text{ve}}}{h^2} \right)^{3/2}.$$

The population of the atomic electronic energy levels is expressed as,

$$n_i = \theta_i^B \frac{n_{\text{at}}}{Q_{\text{at}}^{\text{E}}(T^{\text{ve}})} a_k \exp\left(-\frac{E_i^{\text{at}}}{k_B T^{\text{ve}}}\right), \quad (5.41)$$

where Q_{at}^{E} is the electronic partition function, and θ_i^B represents a non-Boltzmann parameter of the electronic energy level i . In the case of the atomic species N, N⁺, O and O⁺ the θ_i^B is taken from the Quasi-Steady-State (QSS) method of Johnston [126]. To the author's best knowledge, these data are currently not available for the alkali atoms; thus, we assume $\theta_i^B = 1$, which represents a Boltzmann distribution of the electronic levels.

Finally, inserting Eq. (5.41) into Eqs. (5.14) and (5.15) yields the radiative coefficients associated with atomic photoionization,

$$\eta_{\sigma}^{\text{at},bf} = 2hc^2\sigma^3 \exp\left(-\frac{hc\sigma}{k_B T^{\text{ve}}}\right) \frac{n_{\text{at}}}{Q_{\text{at}}^{\text{E}}} \chi^{\text{neq}} \sum_i a_i \exp\left(-\frac{E_i^{\text{at}}}{k_B T^{\text{ve}}}\right) \mathfrak{S}_i^{\text{abs}}(\sigma), \quad (5.42)$$

$$\kappa_{\sigma}^{\text{at},bf} = \frac{n_{\text{at}}}{Q_{\text{at}}^{\text{E}}} \left[\sum_i a_i \exp\left(-\frac{E_i^{\text{at}}}{k_B T^{\text{ve}}}\right) \mathfrak{S}_i^{\text{abs}}(\sigma) \right] \left[1 - \chi^{\text{neq}} \exp\left(-\frac{hc\sigma}{k_B T^{\text{ve}}}\right) \right], \quad (5.43)$$

where the non-equilibrium factor is given by

$$\chi^{\text{neq}} = \frac{n_{\text{ion}} n_e}{n_{\text{at}}} \frac{Q_{\text{at}}^{\text{E}}}{2\xi(m_e, T^{\text{ve}}) Q_{\text{ion}}^{\text{E}}} \exp\left(\frac{E_{\text{ion}}^{\text{at}}}{k_B T^{\text{ve}}}\right). \quad (5.44)$$

The absorption cross-sections $\mathfrak{S}_i^{\text{abs}}$ are obtained from The Opacity Project atomic database (TOPBASE) [67] and they are,

$$\mathfrak{S}_i^{\text{abs}}(\sigma) = h\sigma \sum_{jk} \mathfrak{S}_{i,jk}^{\text{abs}}(\sigma), \quad (5.45)$$

where j and k represent the ion electronic level and the unique electron energy level, respectively.

Atomic lines

The atomic lines are solved with the LBL method because their weak spectral density prevents a statistical narrow-band treatment [140]. The atomic emission $\eta_{\sigma}^{\text{at}}$ and the absorption $\kappa_{\sigma}^{\text{at}}$ coefficients and transmissivity $\tau_{\sigma}^{\text{at}}$ are computed on the fly with the LBL approach and subsequently averaged over a narrow-bands of $\Delta\sigma = 1000 \text{ cm}^{-1}$. The intensity contribution to the RTE, for all

atomic systems in $\mathcal{R}^{\text{atom}}$, is

$$\overline{I_\sigma^{\text{atom}}(s)}^{\Delta\sigma} = \int_0^s \overline{\frac{\eta_\sigma^{\text{at}}(s')}{\kappa_\sigma^{\text{at}}(s')} \frac{\partial}{\partial s'} \tau_\sigma^{\text{at}}(s', s)}^{\Delta\sigma} \prod_{k' \neq \mathcal{R}^{\text{atom}}}^{\mathcal{R}} \overline{\tau_\sigma^{k'}(s', s)}^{\Delta\sigma} ds', \quad (5.46)$$

and is discretized as,

$$\overline{I_\sigma^{\text{atom}}(s_j)}^{\Delta\sigma} = \sum_{i=1}^{j-1} \left[\overline{\tau_\sigma^{\text{at}}(s_{i+1}, s_j) - \tau_\sigma^{\text{at}}(s_i, s_j)} \right] \overline{\frac{\eta_\sigma^{\text{at}}(s_i)}{\kappa_\sigma^{\text{at}}(s_i)}}^{\Delta\sigma} \prod_{k' \neq \mathcal{R}^{\text{atom}}}^{\mathcal{R}} \overline{\tau_\sigma^{k'}(s_i^*, s_j)}^{\Delta\sigma}. \quad (5.47)$$

Scoggins [229] developed a spectral mesh algorithm to accelerate the the LBL integration. This algorithm optimizes the number of spectral points required based on a bisection method.

The emission and absorption coefficients for atomic bound-bound processes are obtained by inserting Eqs. (5.4), (5.20) and (5.21) along with the distribution of Eq. (5.41) into Eqs. (5.12) and (5.13),

$$\eta_\sigma^{\text{at,bb}} = \sum_{ul} \eta_{\sigma,ul}^{\text{at,bb}} = \frac{h\sigma q_e^2}{2\epsilon_0 m_e} \frac{n_{\text{at}}}{Q_{\text{at}}^{\text{E}}} \sum_{ul} \theta_u^B \exp\left(\frac{-E_u^{\text{at}}}{k_B T^{\text{ve}}}\right) a_l f_{lu} \sigma_{ul}^2 f_{ul}^{\text{se}}(\sigma - \sigma_{ul}), \quad (5.48)$$

$$\kappa_\sigma^{\text{at,bb}} = \sum_{ul} \kappa_{\sigma,ul}^{\text{at,bb}} = \frac{1}{2hc^2\sigma^3} \sum_{ul} \left[\frac{\theta_l^B}{\theta_u^B} \exp\left(\frac{hc\sigma}{k_B T^{\text{ve}}}\right) - 1 \right] \eta_{\sigma,ul}^{\text{at}}. \quad (5.49)$$

The atomic line data ($a_l f_{lu}$, E_u^{at} , and σ_{ul}) of the alkali metals — added to the HTGR database in Table (C.1) — is taken from the NIST database [138].

5.2.3. Radiative source terms and HSNB tangent-slab

The radiative processes, described above, alter both the energy and the composition of the flow field, and they are accounted for as a radiative source term \mathbf{S}^{rad} in Eq. (2.12). The radiative powers \mathcal{P}^{rad} and $\mathcal{P}^{\text{rad,ve}}$ indicate the energy source terms due to radiative processes that contribute to the total energy and the vibronic modes, respectively. Photochemical mass production rate of species i , ω_i^{rad} , represents the creation or destruction of species i during bound-free radiative processes, such as photoionization ($X + hc\sigma \rightleftharpoons X^+ + e^-$) or photodissociation ($X + hc\sigma \rightleftharpoons Y + Z$).

In one dimension, the total radiative source term is given as the negative

divergence of the radiative heat flux, \mathbf{q}^{rad} ,

$$\begin{aligned} \mathcal{P}^{\text{rad}}(r) &= -\frac{\partial}{\partial r} \mathbf{q}^{\text{rad}}(r), \\ &= 2\pi \int_0^\infty \int_0^{\frac{\pi}{2}} \cos \theta \frac{\partial I_\sigma(r, \theta)}{\partial r} \sin \theta \, d\theta \, d\sigma, \\ &= 2\pi \int_0^\infty \int_0^{\frac{\pi}{2}} [\kappa_\sigma I_\sigma(r, \theta) - \eta_\sigma] \sin \theta \, d\theta \, d\sigma. \end{aligned} \quad (5.50)$$

where r is the radial coordinate and θ is the angle between the stagnation line and the ray direction.

The vibronic radiative energy source term is estimated by neglecting radiative energy exchanges with translational and rotational modes. Specifically, we assume

$$\begin{aligned} \mathcal{P}^{\text{rad,ve}}(r) &= \mathcal{P}^{\text{rad}}(r) - \sum_{p \in \mathcal{J}} \Delta h_p \dot{\omega}_{p,e}^{\text{rad}}(r) \\ &\quad - (\mathcal{P}_{\text{SR}}^{\text{rad}} - \dot{\omega}_{\text{SR}}^{\text{rad}}(E_{\text{O}^1\text{D}}^{\text{el}} - \bar{E}_{\text{O}_2}^{\text{vib}})), \end{aligned} \quad (5.51)$$

where \mathcal{J} is the set of photoionization processes, $\dot{\omega}_{p,e}^{\text{rad}}$ is the electron mass production rate for the bound-free process p , and Δh_p is the ionization energy per unit mass of the electron. The terms $\mathcal{P}_{\text{SR}}^{\text{rad}}$ and $\dot{\omega}_{\text{SR}}^{\text{rad}}$ are the radiative power and production rate of O^1D , respectively, associated with the Schumann-Runge photodissociation process, $\text{O}_2(\text{X}) + \text{hc}\sigma \rightleftharpoons \text{O}^3\text{P} + \text{O}^1\text{D}$. Finally, $E_{\text{O}^1\text{D}}^{\text{el}}$ and $\bar{E}_{\text{O}_2}^{\text{vib}}$ are the electronic energy of the first excited state of atomic oxygen and the average vibrational energy of the ground electronic state of O_2 , respectively. The summation on the right-hand side accounts for the part of the photon energy transformed into formation energy during photoionization processes [154], while the remaining terms regard for the formation and translational energy production due to the Schumann-Runge O_2 -photodissociation. To our knowledge, these last terms are a novel contribution; they proved to be crucial for the stability of the numeric solver when significant photodissociation occurs in front of the shock. The photochemistry production is obtained from Eq. (5.7) with the relations given by Eqs. (5.14) and (5.15),

$$\dot{\omega}_j^{\text{rad}} = m_j \frac{2\pi}{hc} \sum_{p \in \mathcal{R}^{\text{photo}}} \nu_{pj} \int_0^\infty \frac{1}{\sigma} \int_0^{\frac{\pi}{2}} (\kappa_\sigma^p I_\sigma - \eta_\sigma^p) \sin \theta \, d\theta \, d\sigma. \quad (5.52)$$

where $\mathcal{R}^{\text{photo}}$ represents the set of all photochemical processes and ν_{pj} is the stoichiometry coefficient of species j in process p . Equation (5.52) is the net number of photons multiplied by the species mass m_j .

The tangent slab approximation [127] allows to solve the RTE (Eq. (5.11)) in a simple and fast manner. Johnston et al. [130] has shown that this approximation compared fairly well the \mathcal{P}^{rad} regarding more complex techniques such as Ray-tracing. The tangent-slab divides the flow field into infinity slabs

with constant properties, depicted in Fig. (5.5), reducing the RTE calculation to one dimension.

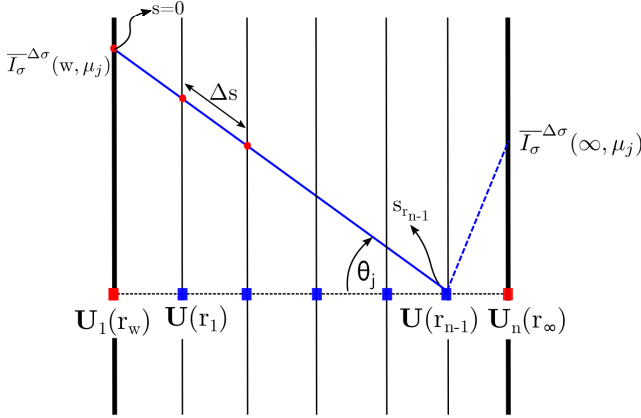


Figure 5.5.: Illustration of the tangent-slab approximation. U represents the stagnation line solution which is extended along infinite constant slabs. θ is the angle between the ray path s and the stagnation line.

The RTE in one dimension is,

$$\cos \theta \frac{\partial I_\sigma(r, \theta)}{\partial r} = \eta_\sigma(r) - \kappa_\sigma(r) I_\sigma(r, \theta), \quad (5.53)$$

and the radiative heat flux is,

$$\begin{aligned} \mathbf{q}^{\text{rad}}(r_i) &= \int_0^\infty \int_{4\pi} I_\sigma(\hat{\mathbf{s}}) \hat{\mathbf{s}} d\Omega d\sigma \\ &= 2\pi \int_0^\infty \int_{-1}^1 I_\sigma(r_i, \mu) \mu d\mu d\sigma \\ &= 2\pi \sum_{\Delta\sigma} \sum_1^{\#\mu} \bar{I}_\sigma^{\Delta\sigma}(r_i, \mu_i) \mu_i \Delta\mu \Delta\sigma \end{aligned} \quad (5.54)$$

where the last equation represents the discretized heat flux with the HSNB formalism. Scoggins [229] observed that 20 equal points were enough to divide $-1 < \mu < 1$, leading to a $\Delta\mu = 0.1$. We recall that the average spectral intensity $\bar{I}_\sigma^{\Delta\sigma}(r_i, \mu_i)$ is given by Eq. (5.24) for a ray starting at a boundary, with a direction θ_i (where $\mu_i = \cos \theta_i$), and ending at the location r_i

The spectral intensity at the free-stream boundary is treated as a black wall at the local temperature,

$$\bar{I}_\sigma^{\Delta\sigma}(r_\infty, \mu_i) = \bar{I}_\sigma^b(T_\infty), \quad \mu_i < 0 \quad (5.55)$$

and at the wall boundary is,

$$\bar{I}_\sigma^{\Delta\sigma}(r_w, \mu_i) = \epsilon \bar{I}_\sigma^b(T_w) + \frac{1-\epsilon}{\pi} \sum_{\mu_j < 0} \bar{I}_\sigma^{\Delta\sigma}(r_w, \mu_j) |\mu_j| \Delta\mu, \quad \mu_i > 0 \quad (5.56)$$

where the first part of the right-hand side is the Planck intensity, Eq. (5.19), and the second is the reflection of the spectral irradiance. This boundary is known as a diffusely emitting and reflecting opaque wall which assumes equal emissivity and absorptivity, as shown in Modest [179].

Inserting the wall spectral intensity, Eq. (5.56), into Eq. (5.54),

$$q_{\text{out}}^{\text{rad}} = \sum_{\Delta\sigma} \sum_{\mu_i > 0} \bar{I}_\sigma^{\Delta\sigma}(r_w, \mu_i) |\mu_i| \Delta\mu \Delta\sigma \quad (5.57)$$

and considering the incoming heat flux from the flow as,

$$q_{\text{in}}^{\text{rad}} = \sum_{\Delta\sigma} \sum_{\mu_i < 0} \bar{I}_\sigma^{\Delta\sigma}(r_w, \mu_i) |\mu_i| \Delta\mu \Delta\sigma \quad (5.58)$$

we write a balance of radiative heat flux at the surface,

$$q_w^{\text{rad}} = q_{\text{out}}^{\text{rad}} - q_{\text{in}}^{\text{rad}} = \epsilon(\sigma T_w^4 - q_{\text{in}}^{\text{rad}}). \quad (5.59)$$

which contributes to the Surface Energy Balance (SEB) in Eq. (3.6). It is important to model this balance with a certain accuracy because the ablation of large bodies is mostly driven by radiative heating.

5.3. H5 Chondrite Plasmatron experiment

In this section, we describe the Plasmatron facility and the experimental set-up to test the H5 Chondrite. Thereafter, we highlight the main experimental results that serve as a comparison with numerical simulations. We recall that the experiments were carried out by Dr. Helber and they have been published in Helber et al. [113].

5.3.1. Plasmatron facility description

The VKI Plasmatron facility has been used for the reproduction of the aerothermodynamic environment of atmospheric entry plasma flows, creating a high-enthalpy, highly dissociated subsonic gas flow [38]. It is equipped with a 160 mm diameter Inductively Coupled Plasma (ICP) torch powered by a high frequency, high power, high voltage (400 kHz, 1.2 MW, 2 kV) generator (MOS technology). The gas is heated by induction through a coil, creating a high purity plasma flow. Three probe holders are installed in the Plasmatron facility next to each other, which can be exchanged independently by a pneumatic mechanism. One holds the test sample, while the other two are used for heat flux

and Pitot pressure measurements in the same experimental run as the ablation test. The cold-wall (~ 350 K) stagnation point heat flux \dot{q}_{cw} is measured with a water-cooled calorimeter having a sensing surface of 14 mm in diameter made of copper. A water-cooled Pitot probe, connected to a Validyne variable reluctance pressure transducer, is used to determine the dynamic pressure of the plasma flow. Atmospheric air at a mass flow of $\dot{m} = 16 \text{ g s}^{-1}$ was used to create the plasma flow. For the results presented throughout this chapter, the time indication $t = 0$ s corresponds to the injection of the test sample into the plasma flow. The sample was attached to a sample holder located 445 mm downstream of the plasma jet exit. After reaching the target testing condition (testing chamber static pressure and heat flux), the sample was inserted using the pneumatic mechanism. We used a two-color Raytek Marathon MR1S-C pyrometer to determine the surface temperature at a 1 Hz acquisition rate (1300 K to 3300 K). A broadband infrared radiometer (KT19 HEITRONICS Infrarot Messtechnik GmbH, Wiesbaden, Germany) recorded the surface radiance in a broad spectral range (0.6 – 39 μm), which allows the estimation of the hot wall emissivity by using the two-color pyrometer surface temperature as black body radiance reference. The front surface was monitored by a 14 bit Charge-Coupled Device (CCD) camera (pco.pixelfly developed by PCO AG) providing snap shots throughout the experiment. Synchronized with the camera were Optical Emission Spectroscopy (OES) measurements, which consisted of three low-resolution, wide-range Ocean Optics HR4000 spectrometers, providing information of the emission spectrum upstream of the test specimen. The HR4000 spectrometers cover a wide spectral range (200 nm to 1000 nm) within a single acquisition and a minimum integration time of 5 ms. A schematic of the experimental setup for in-situ ablation measurements can be found in Fig. (5.6) [110, 112].

5.3.2. Test sample and holder

The H5 chondrite sample was cut into a cylindrical shape with diameter $d = 16$ mm and length, $l = 6$ mm, using a commercial diamond-embedded drill bit, and it was embedded in a hemispherical holder of 50 mm diameter and 45 mm length made out of cork-composite ablative material (Fig. (5.7)). This sample holder had two main objectives: firstly, insulating the test sample from side-wall heating, allowing a one-dimensional heat conduction approach; and secondly, to provide a test shape of known geometry in order to be able to perform an extensive plasma flow characterization by intrusive probes and numerical rebuilding. The employed cork composite material is highly insulating and the only source of heat delivered to the test sample can be assumed to be coming from the stagnation region. The main drawback of using a cork housing was the pollution of the boundary layer with cork ablation products as detected by the spectrometers, as will be seen in Section 5.3.3. Another possibility for future experiments could be investing in a water-cooled metallic housing of the meteor sample. This would provide the desired test shape (for example, hemisphere) without polluting the boundary layer, and at the same time would

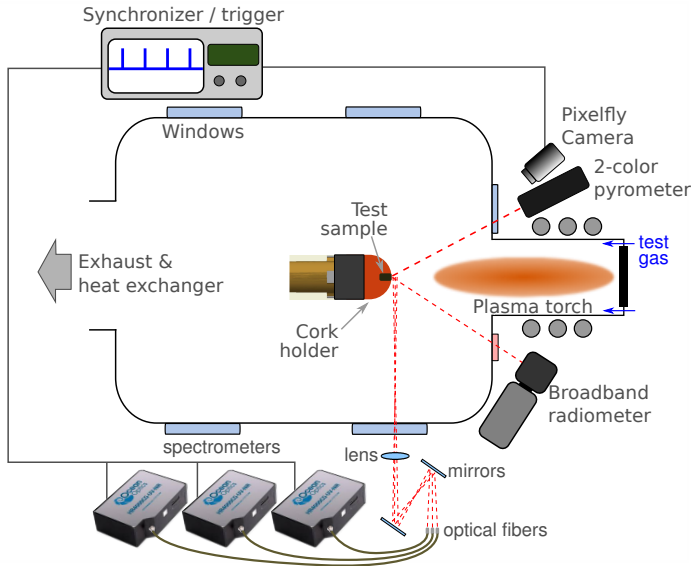


Figure 5.6.: Schematic of experimental setup (not to scale) with diagnostics for meteoroid ablation analysis.

provide 1D thermal conduction inside the sample if well insulated from the cooled holder walls. Unfortunately, such thermal insulation from the sidewalls would not be trivial as ablation of the sample was one main objective, which would lead to destruction of the insulation material as well, again polluting the test material and boundary layer. We suggest using a pure test sample, as done by Loehle et al. [151], without any additional interfaces that could contaminate the recorded data, such as a single sample in the desired test shape (e.g., hemisphere). However, meteorite samples for such destructive tests are difficult to obtain, especially on a reasonable size to be machined into the desired shape, and the strong sidewall heating in such case would make the thermal analysis more difficult compared to the one-dimensional approach we applied in this work. In addition, such a sample might be completely destroyed during the experiment because of the fast heating, hampering recovery and further analyses of the resulting material (no material remainders have been analyzed in Loehle et al. [151]).

Their main characteristics of the (OC) are reported in Table (5.2). The density was obtained by weighing the samples and assuming a perfectly cylindrical shape. The chemical characterization of a silicate portion of the sample, obtained via Laser Ablation-Inductively Coupled Plasma-Mass Spectrometry (LA-ICP-MS) [206], is reported in Table (5.3), where the average composition of H chondrites reported by [122] is also presented as a reference. Yomogida and Matsui [277] computed bulk densities in a range between 3350 and 3690 kg m⁻³ for H chondrites

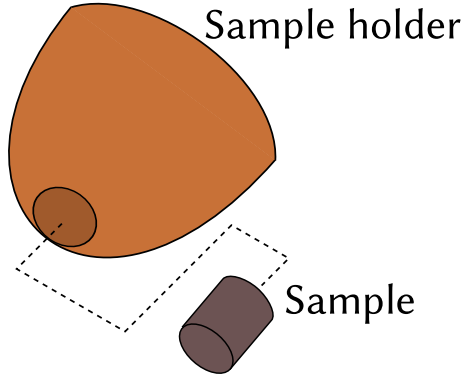


Figure 5.7.: Schematic of the sample and its cork holder. Material sample of 16 mm diameter embedded in the sample holder in stagnation point configuration.

Table 5.2.: Characteristics of the El Hammami H5 ordinary chondrite

l	d	m	ρ
mm	mm	g	kg m^{-3}
6	16	3.65	3026

5.3.3. Experimental results

In Table (5.4), we present an overview of the main results in terms of maximum surface temperature, test time and total mass loss. The sample withstood the plasma flow during the entire test time of 21 s without fracturing, probably because of a predominantly granular metamorphic texture (rather than igneous). In fact, the ordinary chondrite sample only lost 3 mg during those 21 s, starting from an original weight of 3.65 g. This illustrates that, although the surface appeared to be boiling and frothing (Fig. (5.8)), only a little material volatilization took place and not much mass was injected into the boundary layer, allowing the recovery of the ablated material.

Photographs taken before and after each experiment are shown in Fig. (5.9) and Fig. (5.10). The sample displayed a reddish color change, which probably indicates a change of the oxidation state of the high iron content with formation of hematite (Fe_2O_3) at the surface. Global oxidation of the sample is also suggested based on petrographic observations of the resulting material, which contains magnetite [206].

Surface temperature measurements

The plateau temperature reached during these test conditions 2360 K for the ordinary chondrite (Fig. (5.11)). Although the pyrometers measuring surface area of 11 mm diameter mostly covered the OC sample surface, some addi-

Table 5.3.: Major species chemical composition before the experiments

Species	OC wt%	OC-Ref. wt%
SiO ₂	50.71	36.6
TiO ₂	0.07	0.1
Al ₂ O ₃	1.74	2.1
Na ₂ O	1.55	0.8
K ₂ O	0.10	-
CaO	2.33	1.7
FeO	15.93	11.9
MgO	26.03	23.1

NOTE: Chemical composition was determined by means of LA-ICP-MS for the ordinary chondrite (OC-silicate portion). For the latter, a reference value from literature is also provided [122].

Table 5.4.: Overview of Plasmatron results for condition (1)

Material	τ s	T_w K	Δm mg	ϵ -
OC	21	2360	3	0.69

NOTE: Data for ordinary chondrite (OC) includes test sample exposure time τ , mean surface temperature T_w , total mass loss Δm , and surface emissivity ϵ .

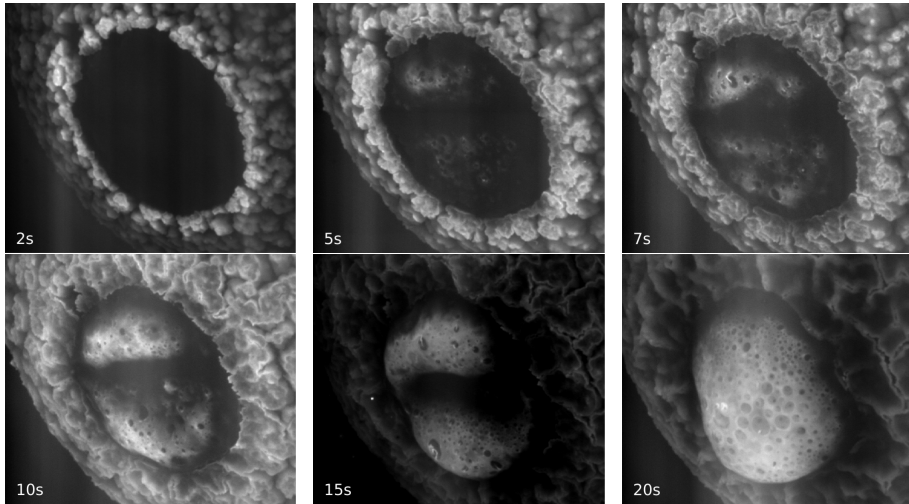
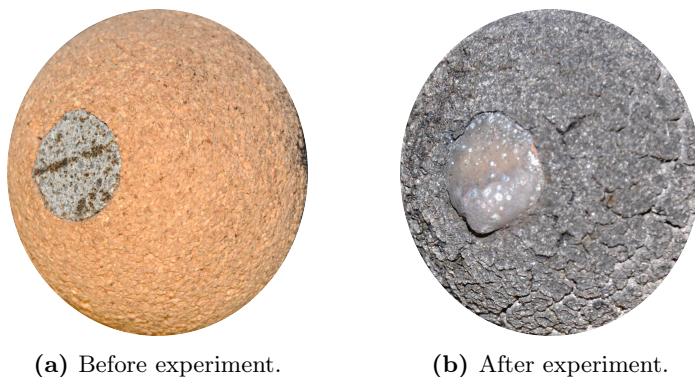


Figure 5.8.: Snap shots (upper left to lower right) during ordinary chondrite test at 1.2 MW m^{-2} and 200 hPa highlighting boiling of the surface after 5 s (time from injection indicated in each image); a melted surface state remained present throughout the remaining 15 s of the test.

tional radiation, coming from the cork housing, may have been recorded by the pyrometer. This cork housing is likely to have resulted in a different surface



(a) Before experiment.

(b) After experiment.

Figure 5.9.: Ordinary chondrite samples before (a) and after (b) plasma exposure.



Figure 5.10.: Samples after plasma exposure. The change of color, probably a sign of the change in the oxidation state of iron, is visible.

temperature than the held sample, as well as in different apparent emissivity, affecting the measured temperature to a small degree.

Optical emission spectroscopy

We present emission spectra recorded in front of the test sample during plasma exposure in Fig. (5.12). The two plots present the radiative signature of the air plasma free-stream (red) together with radiation mostly coming from the ablating cork holder just at injection (a), and emission spectrum recorded in front of the ordinary chondrite sample several seconds into the test (b), when radiative emission was highest. The free-stream emission spectrum presents expected CN violet and N_2^+ radiation, both strong radiators and generally present in atmospheric air plasmas at such gas temperatures (5000 K - 10000 K). The ablating cork sample, in addition, led to much stronger CN violet emission due to ablation, as well as sodium (Na) and potassium (K). Traces of the volatile elements sodium and potassium in this spectrum may also result from the ablation of the test sample. Sodium has been found in the cork material as a result of either the supplier's manufacturing process, or in-house machining

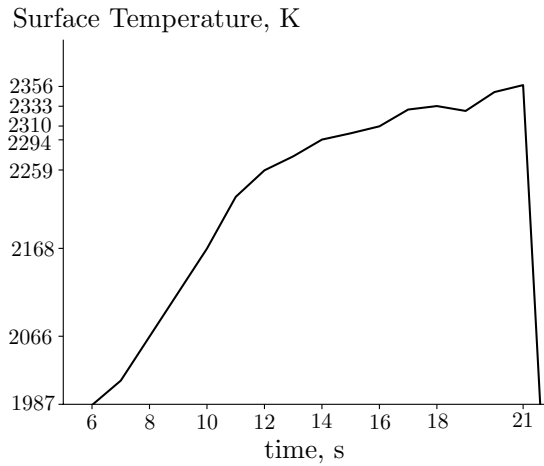


Figure 5.11.: Surface Temperature of the H5 sample measured by the two-color pyrometer.

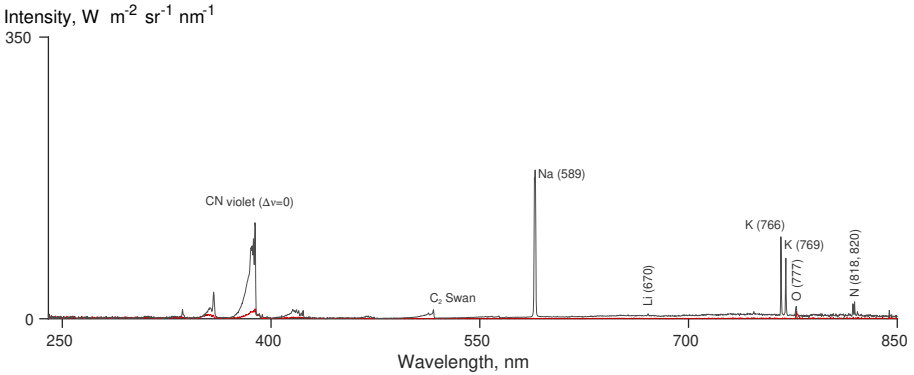
of the test sample.

The spectral intensity signal observed by the spectrometers strongly changed during the ablation of the ordinary chondrite. The spectrum is mainly dominated by iron emission (Fe), with several strong lines in the UV and visible range of the spectrum, as indicated by the fine markers. As seen in Table (5.3), high concentrations of iron are present in the sample. The recorded emission signals of sodium (589 nm) actually saturated during the measurement. The saturation is not apparent from the plots of Fig. (5.12) as emission lines at lower and higher wavelengths are well captured (at higher calibrated intensity); this comes from the lower quantum efficiency of the HR4000 sensor towards its wavelength wings below 400 nm and above 750 nm.

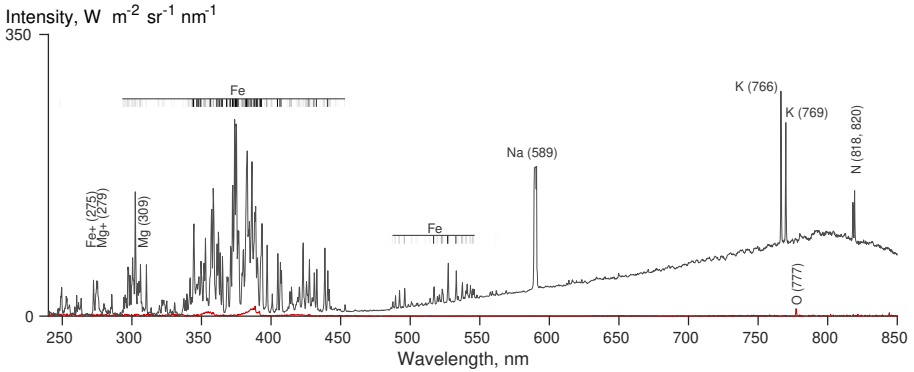
Interestingly, although the sample is predominantly composed of SiO_2 , it did not show any silicon emission during the whole experiment. In general, moderately refractory elements like Si, Mg, and truly refractory elements such as Al, which are part of the ordinary chondrite elemental composition, are not strongly present in the spectrum. The emission of iron lines produced by an ablating ordinary chondrite sample in plasma flows was also reported by Loehle et al. [151], together with traces of silicon, sodium, potassium, and manganese.

In addition to the radiative species emission, continuum radiation, emitted by the hot surface, was recorded by the spectrometer close to the surface (Fig. (5.12)). This might have been caused by the cork material that tends to swell upon heating up, with emission of the hot surface reaching the optics of the closest spectrometer.

Potassium and sodium emission during ablation of meteoritic samples is of particular importance and high interest to the community. However, several constraints limited the possibility of obtaining unpolluted emission spectra from the observed material alone. One limiting factor was the available test sample



(a) Air plasma free-stream (red) and cork holder (gray) at injection



(b) Ordinary chondrite after 16 s (gray) and air plasma free-stream (red)

Figure 5.12.: Emission spectra overview of air plasma and cork holder (a), and ordinary chondrite (b) tests; the air free-stream spectrum for each test run is given in red, while the spectrum recorded in front of the ablating material sample is given in gray, highlighting the presence of additional radiative contributors ejected by the material (all spectra recorded by spectrometer closest to surface).

dimension, which was a cylinder of 16 mm diameter, thus, an adequate sample holder needed to be used. We decided to embed the test sample in a sample holder of known shape (i.e., a hemisphere) in order to be able to perform an extensive plasma flow characterization by intrusive probes and numerical rebuilding.

Test parameters and rebuilding of flight free-stream condition

The Local Heat Transfer Simulation (LHTS) methodology was originally developed by [136] allowing us to duplicate flight conditions at the stagnation point by matching the boundary layer edge total enthalpy h_e , pressure p_e and and the radial velocity gradient in radial direction at the wall ($\beta_e = (\partial u / \partial x)_e$) between ground experimental and flight conditions.

The subsonic Plasmatron flow field was numerically simulated by solving the Navier-Stokes equations coupled with the Maxwell equations for the electromagnetic field created by the coil (*VKI ICP code* [68, 160, 257]). This provides the boundary layer velocity gradient β and boundary layer thickness δ , as well as an initial stream-wise velocity v for the characterization of the boundary layer around the test sample under local thermodynamic equilibrium and axisymmetric flow assumptions [13]. The hydrodynamic boundary layer edge parameters (temperature T_e , density ρ_e , and velocity v_e) are determined through an iterative procedure using the *VKI boundary layer code* [14], which takes as input conditions the flow quantities determined from the *VKI ICP code*, as well as the experimental heat flux and Pitot pressure measurements. The *VKI boundary layer code* consists of solving the chemically-reacting stagnation line boundary layer over a catalytic surface under chemical non-equilibrium conditions, assuming fixed wall catalytic properties for copper and a cold-wall temperature for the heat flux probe. A more detailed description of this procedure applied to ablation tests can be found in [111].

We chose three test conditions, often used for TPS testing, which are characterized by a high level of confidence in terms of repeatability and flow behavior. In addition, these experimental conditions were chosen to allow the recovery of the sample for surface characterization analysis after the tests. The experimental conditions are listed in Table (5.5). In this work, we present results for condition (1), while conditions (2) and (3) are relevant for the surface characterization presented in [206]. Notice that the cold-wall heat flux \dot{q}_{cw} was measured by means of a cylindrical calorimeter probe for condition (1) and a hemispherical calorimeter probe for conditions (2) and (3). The values presented in Table (5.5) are given for a hemispherical calorimeter, or its equivalent for condition (1).

A numerical procedure was used to infer flight conditions from the experimental ones. By solving the Rankine-Hugoniot jump relations, assuming a thermally perfect gas, a contour map of post-shock enthalpy h_e , and pressure p_e , was defined for a range of free-stream velocities and altitudes. An equivalent flight radius can also be computed by means of the modified Newtonian

Table 5.5.: Plasmatron test conditions

Condition ID	Experimental			Numerical				
	p_s hPa	P_{el} kW	\dot{q}_{cw} MW m ⁻²	h_e MJ kg ⁻¹	ρ_e g m ⁻³	T_e K	v_e m s ⁻¹	β 1 s ⁻¹
(1)	200	206	1.2	24	7.0	6293	26	1230
(2)	220	310	3.0	42	4.3	8079	55	4480
(3)	15	373	3.1	54	0.3	9229	687	29790

NOTE: Data include experimentally measured static pressure p_s , generator electric power P_{el} , and mean cold-wall heat flux \dot{q}_{cw} , as well as numerically rebuilt boundary layer edge values of enthalpy h_e , gas density ρ_e , gas temperature T_e , velocity v_e , and boundary layer gradient β_e .

theory [7]:

$$R_{\text{equ},f} = \frac{1}{\beta} \sqrt{\frac{2(p_e - p_\infty)}{\rho_{e,f}}} \quad (5.60)$$

where p_∞ represents the atmospheric pressure at the flight altitude and $\rho_{e,f}$ the flight boundary layer edge density obtained from the Rankine-Hugoniot jump relations. The three experimental conditions are shown in Fig. (5.13). For the experimental results reported here, condition (1) corresponds to a 3.8 m diameter object ($2 \times R_{\text{equ},f}$), flying at a velocity of 6.9 km s⁻¹, at an altitude of 54.7 km. Fireball trajectories for two well-known events are also reported in Fig. (5.13): one can observe that the range of velocities of the two bolides, Benešov and Chelyabinsk, are higher than our experimental conditions. We chose a lower heat flux condition than what can be assumed from existing meteor observations to avoid complete destruction of the samples and ensure successful recovery of the modified basaltic and chondritic materials. Recovery of modified experimental samples enabled us to set a further objective in this experimental campaign, which was a complete petrographic and geochemical characterization and comparison with natural meteorite fusion crust. Future work may include testing at higher heat fluxes, reproducing smaller meteoroids at higher entry velocities.

It should be noted here that most of the mass of extraterrestrial material falling on Earth consists of micrometeorites (between 50 and 2000 μm producing $40,000 \pm 20,000$ metric tons of extraterrestrial matter to Earth every year [155]). But the largest fraction of significant discoveries about meteorite parent bodies and the early stages of the solar system formation have so far been made focusing on actual meteorites. It is, therefore, important to constrain the modifications induced on this material during atmospheric entry. Micrometeorites, including their innermost parts, undergo degassing, melting, and evaporation, with limited material remaining required for high-precision analytical studies. To amplify the detectable effects of atmospheric passage on geological materials and at the same time recover material required to make our observations, we opted for the experimental design described above.

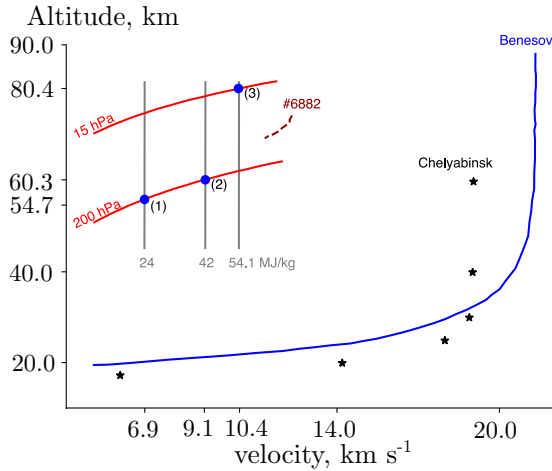


Figure 5.13.: Duplication of the Plasmatron test conditions to flight conditions. The Benešov fireball reported by Borovička et al. [33] has an estimated value at entry conditions of 2.3 m diameter body with 21.3 km s^{-1} velocity. The Chelyabinsk event [35] is estimated to be 18 m in size, with an entry velocity of 19 km s^{-1} . The trajectory #6882 is one of the 413 photographic meteors reported by [233] and [121]. The sizes of these bodies are not reported.

5.4. Comparison with Plasmatron experiments

In this section, we simulate the experiment of the El Hammami H5 sample using the stagnation-line solver (Section 2.2). Earlier we mention the *ICP code* and the *Boundary layer code* to rebuild the plasmatron conditions, but for this case the stagnation-line solver is preferred due to the following:

ICP code solves the 2D axisymmetric Navier-Stokes coupled with the Maxwell equations. However, it presupposes local thermal and chemical equilibrium in the boundary layer, which are strong assumptions in this region. It ignores any boundary condition for the gas-surface interaction. Lastly, it is computationally costly, which becomes cumbersome for parametric studies.

Boundary layer code considers chemical non-equilibrium, and it is fast since it only solves the boundary layer equations. On the other hand, it only includes catalytic reactions as part of gas-surface interaction, and it does not account for ablative or evaporation boundary conditions. Furthermore, it does not resolve the external flow since the physical domain is confined to the boundary layer.

Using the flow solution as input, we integrate the RTE along three lines-of-sight – which represent the three spectrometers – allowing us to correlate the simulated radiative emission of the vapor species with spectroscopy measure-

ments (Fig. (5.12)) at different time instants. We focus our comparison at the 6 s and 14 s of the experiment.

5.4.1. Numerical set-up

The flow exiting the Plasmatron torch is at low Mach number, thus, we use the AUSM⁺-up2 flux-splitting scheme due to its excellent properties at this flow regime. Moreover, instead of imposing a subsonic boundary condition, we decided to employ a supersonic inlet with a sufficiently large domain, where the Riemann problem automatically screens the information needed from the boundary.

We consider three important aspects to compare the simulated radiative intensity with the experimental measurements, using the stagnation-line solver:

- the boundary conditions and how to include the presence of the cork holder;
- the fact that the spectrometers assess the integrated radiative intensity across the plasmatron chamber while the stagnation-line solver can only resolve the stagnation streamline;
- the swelling of the cork which appears as continuum radiation in the experimental data.

Boundary condition: The stagnation-line solver requires an inlet and a wall boundary condition. The numerical rebuilding explained in Section 5.3.3 provided the inlet boundary conditions. The inlet static-pressure is 20 000 Pa, the temperature is 6293 K and the free-stream velocity is 70 m s⁻¹. The species partial densities are imposed according to the equilibrium composition at the local pressure and temperature. On the wall side, we impose an isothermal boundary condition, which corresponds to the surface temperature measured by the pyrometer, Fig. (5.11). Furthermore, we impose a gas-surface boundary condition, which contains both the evaporation of the sample and the ablation of the cork.

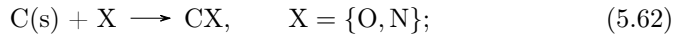
As in Chapter 4, we use the Hertz-Knudsen model (Section 3.4.3) to simulate the evaporation of the El Hammami H5 sample, but in turn, Eq. (3.44) includes an evaporation coefficient α_{evap} and a condensation coefficient α_{cond} , such that,

$$\dot{m}_{\text{vap},i} = \alpha_{\text{evap},i} \rho_{e,i} \sqrt{\frac{R_i T_w}{2\pi}} - \alpha_{\text{cond},i} \rho_{\infty,i} \sqrt{\frac{R_i T_w}{2\pi}}, \quad \forall i \in \mathcal{G}_{\text{vap}}. \quad (5.61)$$

In the previous chapters, we consider the evaporation/condensation coefficient α equal to one. A unity α_{cond} indicates that all the particles impinging on the surface condensate, and a unity α_{evap} means all the particles leaving the surface follow a half-Maxwellian distribution function at the saturation conditions. Typically, these coefficients are derived either by experimental measurements [165, 204] or by numerical simulations with Molecular Dynamics

(MD) [28, 137, 172, 183]. From experimental results, Ogasawara et al. [186], Safarian and Engh [219] show a unity α_{evap} for the evaporation of pure substances into vacuum; Meland et al. [172] concluded the same with MD. The α_{evap} of polyatomic species do not follow any trend [17]. Alexander [4] shows an evaporation coefficient far from unity when compared with the experimental results of Hashimoto [106]. It is cumbersome to derive the condensation coefficient from experiments because they are carried out under vacuum conditions. The gas expands into the void without back flow; hence, few particles condensate. Furthermore, this coefficient depends on numerous parameters, such as the energy of the particle colliding with the surface, the surface temperature, the surface morphology, and many others [28]. We consider $\alpha_{\text{evap}} = \alpha_{\text{cond}} = 1$ for all species evaporating from the surface and $\alpha_{\text{cond}} = 0.3$ for the evaporation of Fe, for reasons that we will mention after.

The cork housing ablation results in the appearance of carbonaceous species detected by the spectrometers, consequence of surface oxidation and nitridation reactions,



where C(s) represents a carbon atom in the condensed phase. The reaction in Eq. (5.62) stands for the production of CO and CN in the flow field, where the latter species emits strongly. The mass blowing rate for these types of reactions,

$$\dot{m}_{\text{ablat},\text{X}} = \gamma_{\text{X}}^{\text{CX}} \rho_{\text{X}} \sqrt{\frac{R_{\text{X}} T_{\text{w}}}{2\pi}}, \quad \text{X} = \{\text{O}, \text{N}\}; \quad (5.63)$$

where γ_{X} is the recombination probability of the impinging atom – e.g., a $\gamma_{\text{X}} = 1$ means that every X atom that impinges the surface results in a CX molecule. In this work, we used the nitridation probability from Suzuki et al. [244],

$$\gamma_{\text{N}}^{\text{CN}} = 0.003, \quad (5.64)$$

and the oxidation probably from Park [192]

$$\gamma_{\text{O}}^{\text{CO}} = 0.63 \exp(-1160/T_{\text{w}}). \quad (5.65)$$

Together with Eq. (5.61), the mass blowing rate of the cork (Eq. (5.63)) is included into the Surface Mass Balance (SMB) (Eq. (3.2)) to simulate the ablation of the holder.

Finally, cork contains natural resin that under high heat loads it decomposes, originating the blowing of carbonaceous species into the boundary layer, known as pyrolysis gases [251, 252]. For simplicity, we ignore the pyrolysis gases in our analysis.

Two-dimensional flow field projection: Although the stagnation-line solver utilizes high-fidelity physico-chemical models, it only solves the stagnation streamline. This hinders the spectral diagnostics of the plasma. Hence, to compare the numerical with the experimental results, we need a full thermochemical description of the flow surrounding the sample. Therefore, we project

the stagnation streamline field in two dimensions using spherical slabs, meaning that the physical property at the cell-center is assumed to be constant along the slab, see Fig. (5.14).

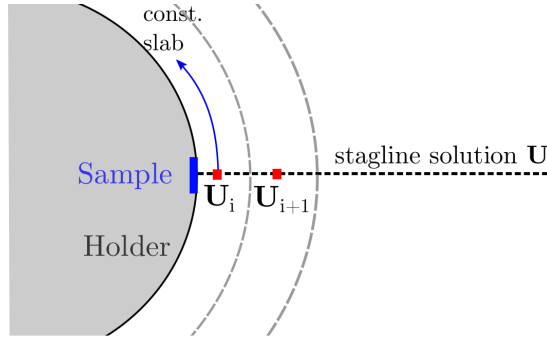


Figure 5.14.: Projection of stagnation streamline field using spherical caps with constant properties.

Apart from the boundary layer, one must consider the plasma jet that surrounds the sample. This plasma jet is at high temperature, and it might contain atomic and ionized species that determine the RTE integration. Following the work of Bellas-Chatzigeorgis [19], we specify the energy along the plasma jet radius r as,

$$e(r) = A + B \operatorname{erf}(Cr + D). \tag{5.66}$$

where the constants $C = -37.29$ and $D = 1.526$ define the shape of the jet.

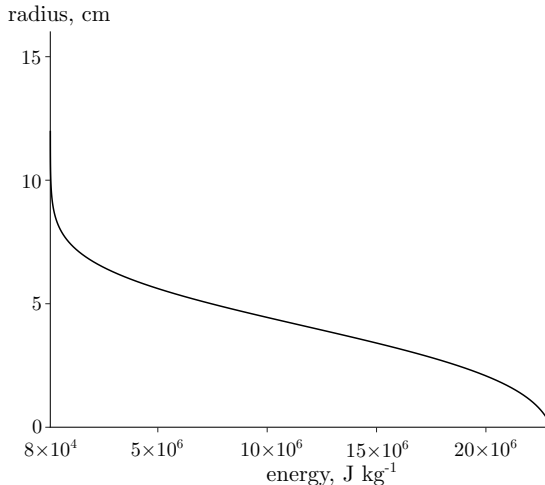


Figure 5.15.: Energy profile along the plasma jet radius.

The constants A and B are found by imposing the stagnation-line energy at $r = 0$ and the corresponding energy at 300 K when $r \rightarrow \infty$. The temperature

distribution along the plasma radius is computed by solving the non-linear energy equation (Section 2.2), assuming LTE conditions, and subsequently appended to the projection mentioned before. As a final remark, it is important to consider the full plasmatron chamber because the medium might absorb part of the radiative intensity in the cold region of the test section, due to the Schumann-Runge mechanism.

Figure (5.16) shows an illustration of the temperature contour obtained by projecting the stagnation-line solution – from 0.0 to ± 2.5 cm on the transversal coordinate – and the plasma jet profile – above 2.5 cm. The sample stagnation point is at the (0,0) position.

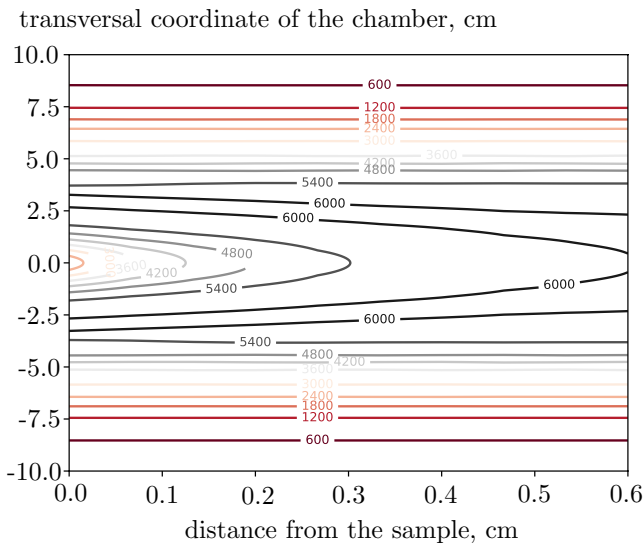


Figure 5.16.: Contour of the temperature field (not to the scale) around the sample, at the position (0, 0).

Swelling of the cork: The three spectrometers are at different positions, and they collect the integrated emission along a line-of-sight crossing the entire chamber (see Fig. (5.6)). The time-resolved spectra of the distinct spectrometers show the appearance of a Planck curve at different moments, with a similar temperature as the one recorded by the pyrometer. This temperature equivalence suggests that the holder is in the line-of-sight of the different spectrometers at an instant, due to the cork swelling. From the measurements recorded by each spectrometer (Fig. (5.12)), we estimate the transient swelling of the cork, as shown in Fig. (5.17), and we observe that three spectrometers point to the cork surface after 15 seconds of the experiment. This information leads to a more accurate comparison between the numerical and experimental results.

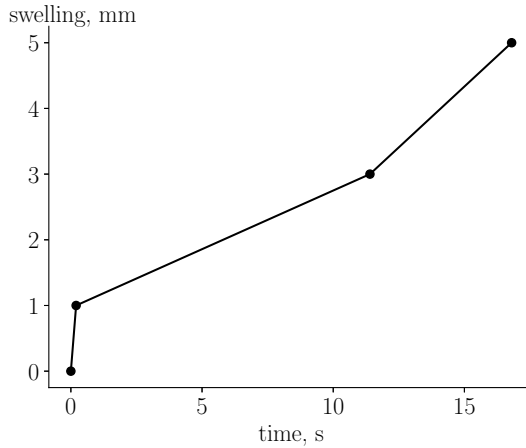


Figure 5.17.: Swelling of the cork holder derived from the time-resolved data spectra. The points represent the location of the three spectrometers, and after 15 seconds, the cork holder is in the line-of-sight of all.

5.4.2. 6 seconds

We choose this instant because of the low surface temperature, which means a weak evaporation rate, but in turn, the oxidation and nitridation reactions are relevant. Hence, these conditions allow us to study the influence of the cork ablation in the spectroscopy measurements. We cannot directly model the presence of the holder because the surface is not normal to the stagnation streamline (see Fig. (5.14)) – for that, a multidimensional solver is needed. Therefore, to include the presence of the carbon species, we do a sensitivity analysis on the nitridation $\gamma_{\text{N}}^{\text{CN}}$ and oxidation $\gamma_{\text{O}}^{\text{CO}}$ coefficients. The results in this section correspond to 10 % of the coefficients in Eqs. (5.64) and (5.65) and in Section C.3, we show the results concerning the original values.

The chemical mixture of our flow is composed by the species in Table (5.6), and the reaction rates can be found in Table (A.1).

Table 5.6.: Gaseous species used to simulate the plasmatron experiment. The evaporation products contain only the major species according to their saturated vapor pressure. For simplicity of the analysis, the cork holder products do not contain hydrocarbon species arising from the pyrolysis gases.

air species												
e^-	N	NO	N ₂	O	O ₂	N ⁺	O ⁺	NO ⁺	N ₂ ⁺	O ₂ ⁺		
H5 chondrite evaporation products												
Mg	Mg ⁺	MgO	FeO	Si	SiO	SiO ₂	Na	Na ⁺	NaO	K	Fe	Fe ⁺
cork holder products												
	C	CO ₂	CO	CN	C ₂							

Flow field

Figures (5.18a) and (5.18b) show the two temperatures and the velocity along the stagnation streamline, respectively. Figure (5.18a) shows a thermal equilibrium between translational and internal modes. In Fig. (5.18b), the negative velocity at the surface corresponds to the gas blowing from the ablation products.

Figure (5.18c) shows the composition due to the surface reactions. The mole fraction of the species produced by evaporation is negligible compared to the ablation of cork, due to the lower equilibrium vapor pressure at this surface temperature. The major species at the surface is CO, a result of the oxidation reactions, followed by C. The gas reactions lead to a substantial change of CN in the boundary layer, reaching a maximum value further upstream of the surface. The dominant evaporation species is Na, due to its volatilization, followed by Fe; while the other species appear as mere traces.

Figure (5.18d) shows the air composition along the stagnation streamline. At the inlet, the air mixture is mostly dissociated due to the high temperature. In the boundary layer, we observe the decay of O, due to surface oxidation, and decay of N due to nitridation and recombination of N₂.

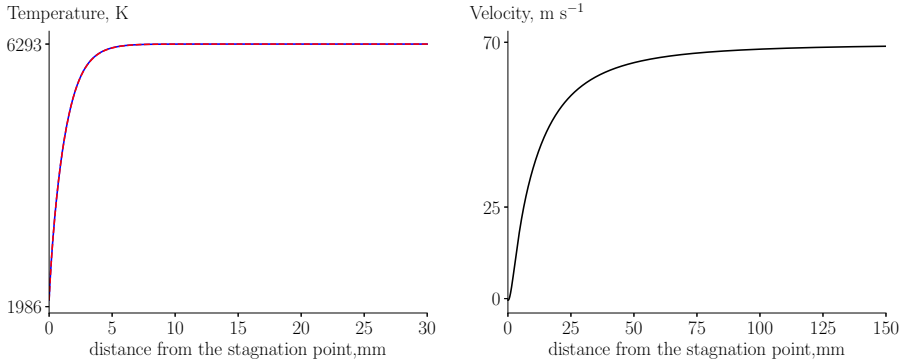
Radiative field

As mentioned before, the Na appears saturated in the spectra, meaning that we cannot compare the numerical and the experimental results for these lines. Therefore, we remove the saturated Na doublet from the experimental spectra, and we omitted it in our numerical simulations.

Figure (5.19) shows the intensity on several lines-of-sight normal to the stagnation streamline and the intensity measured by the different spectrometers. Based on the cork swelling derived in Fig. (5.17), the holder is in the line-of-sight of the closest spectrometer. We include the error bars in Fig. (5.19) because it is not clear if the closest spectrometer was positioned at 1 or 2 mm from the surface at the beginning of the experiment.

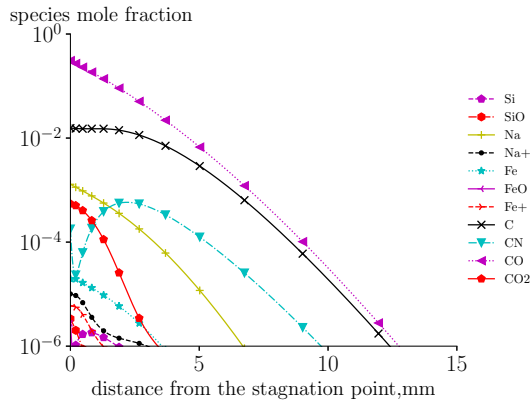
The total intensity reaches its maximum at 2 mm from the surface, and by analyzing the radiative intensity of each mechanism, Fig. (5.19b), we conclude that CN violet is the major contributor. The intensity of this species is bigger at 2 mm due to the combination of temperature and concentration increase upstream the surface (see Figs. (5.18a) and (5.18c)). Although the composition of CN is smaller than CO, the intensity of the former species is stronger. The second most relevant evaporation species, Fe, shows a negligible intensity due to its small presence in the boundary layer.

Figure (5.19) indicates a good agreement between the numerical and the experimental intensity which can be better appreciated in Fig. (5.20). The top part of Fig. (5.20a) reveals the spectral intensity reproduced at 1 mm from the surface compared to the intensity measured by the middle spectrometer. We observe a small discrepancy around 25 000 cm⁻¹, but the tendency is well captured, as we can see from the cumulative intensity on the bottom part of the figure. Moreover, we observe a weak dependence of the atomic mechanisms

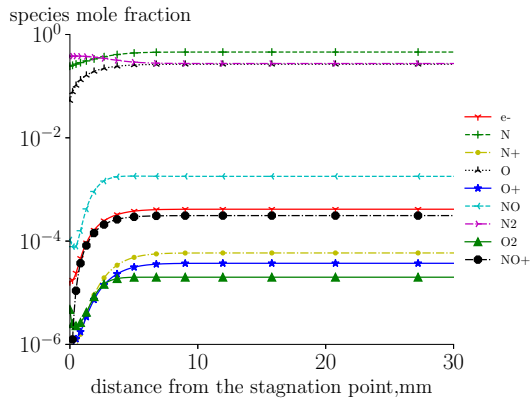


(a) Temperature profile: — T , - - - T^{ve} .

(b) Velocity profile.

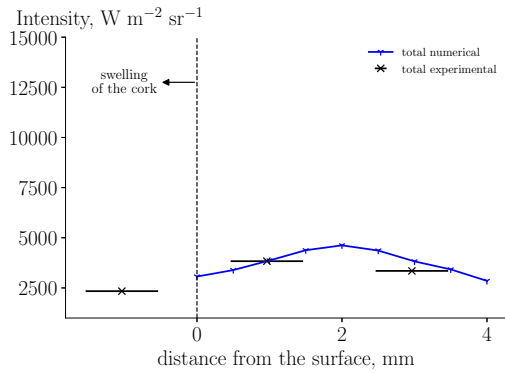


(c) Species composition regarding the evaporation of the H5 sample and the ablation of the cork.

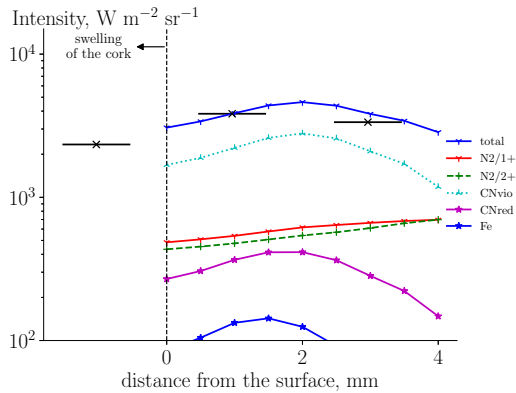


(d) Air species composition.

Figure 5.18.: Flow field properties along the stagnation streamline at 6s.



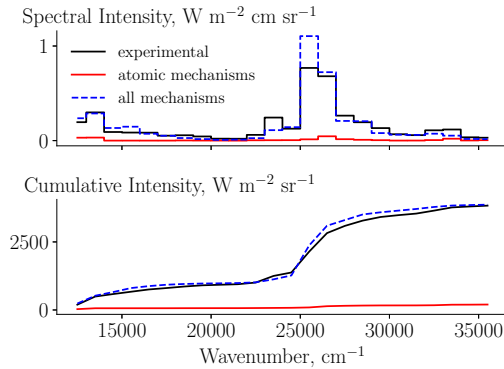
(a) Intensity based on the sum of all mechanisms.



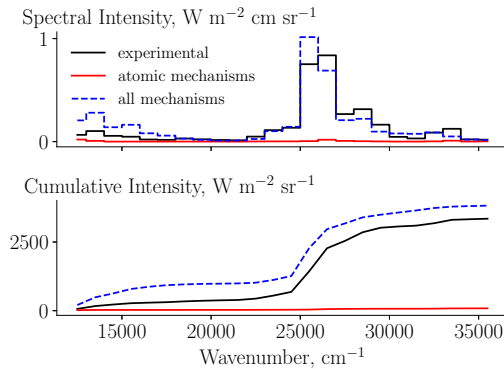
(b) Intensity of the individual mechanism.

Figure 5.19.: Comparison of the integrated intensity at different locations with the data recorded by the three spectrometers. The spectrometer data is represented by \times and the horizontal bar represents the error due to its location. The cork swelling is linearly interpolated from Fig. (5.17).

on the intensity. Figure (5.20b) shows to the spectral (top), and the cumulative (bottom) intensity simulated 3 mm from the surface and the comparison with the furthest spectrometer. At this location, we observe a more significant deviation at wavenumber $< 20\,000\text{ cm}^{-1}$, but the cumulative intensity shows a similar trend between the numerical and the experimental results.



(a) Comparison of the intensity simulated at 1 mm from the surface with the middle spectrometer: (top) spectral and (bottom) cumulative intensity.



(b) Comparison of the intensity simulated at 3 mm from the surface with the furthest spectrometer: (top) spectral and (bottom) cumulative intensity.

Figure 5.20.: Comparison of the simulated intensity with the spectrometer data at a certain location.

Figure (5.21) shows the contribution of the most important mechanisms discussed in Fig. (5.20a). We notice a weak spectral intensity on the evaporation products, Fe and K. CN violet is the most intensive species, as shown in Fig. (5.21d), while CN red has a stronger radiative emission more at low

wavenumber. From these results, one notes that we are slightly overestimating the radiative emission of CN violet regarding the experimental data of both spectrometers. It is challenging to provide reasons for this overestimation because the radiative intensity of a mechanism depends on several parameters.

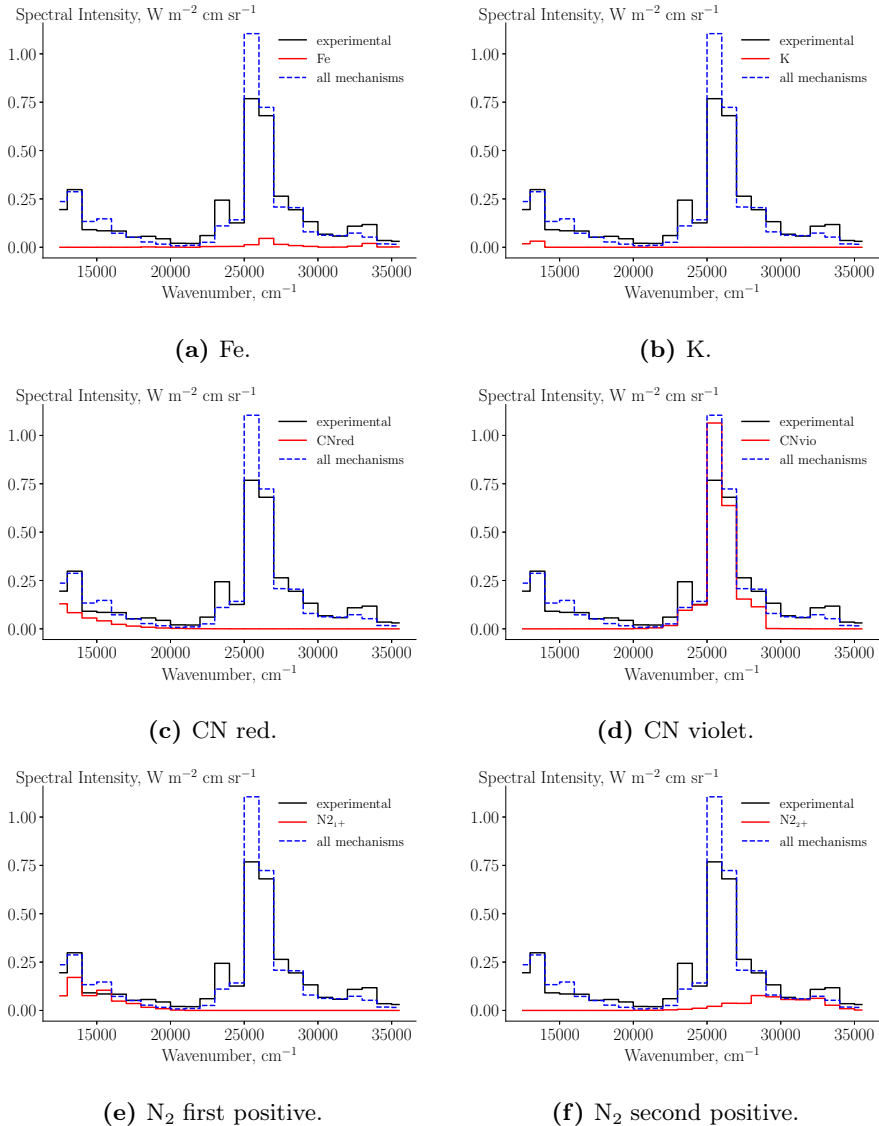


Figure 5.21.: Spectral intensity of the individual mechanisms compared with the data recorded by the middle spectrometer at 6s. The numerical results correspond to location of Fig. (5.20a)

Lastly, in Section C.3 we present the numerical results obtained with the ni-

tridation and oxidation coefficients from Eqs. (5.64) and (5.65). We observe an overestimation of the numerical intensity compared to the measured one. This overestimation arises from a stronger radiative emission of both CN red and violet, observed by comparing the individual mechanisms intensity Figs. (C.2b) and (5.19b).

5.4.3. 14 seconds

In this case, the numerical conditions are the same as the 6 s case, except for the surface temperature.

Flow field

The higher surface temperature leads a stronger evaporation the H5 sample. The flow field properties indicated in Fig. (5.22) are like the previous case apart from the boundary layer composition. In this case, we observe a stronger presence of Na, Fe, K and Si as shown in Fig. (5.22c).

Radiative field

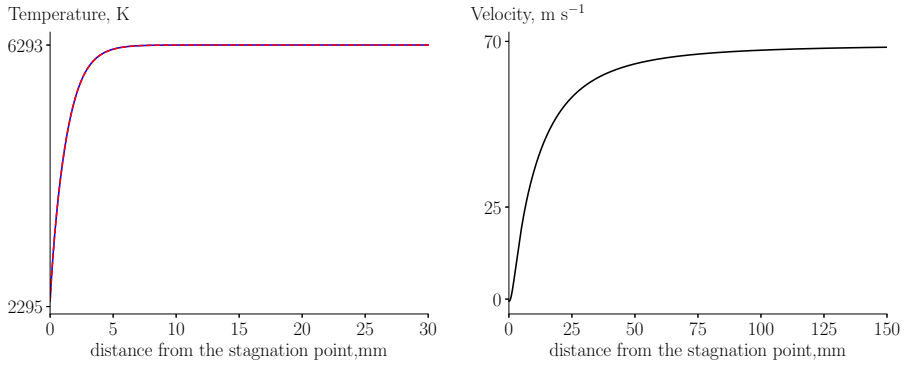
Figure (5.23) shows the integrated intensity at different locations and the comparison with furthest spectrometer; since, the swelling of the cork prevents the comparison with the other two. The maximum intensity is at 2 mm from the surface and almost the double of the 6 s case. This increase of intensity is explained by a stronger radiative emission of Fe and K while the radiative emission of CN violet is approximately the same as the previous case, as indicated in Fig. (5.23b).

Figure (5.24) shows in more detail the spectral (top) and cumulative (bottom) intensity 1 mm far from the surface. As the 6 s case, we slightly overestimate the radiative intensity around $25\,000\text{ cm}^{-1}$ but we obtain a good comparison of the cumulative intensity. Moreover, we get an excellent agreement above $32\,500\text{ cm}^{-1}$, between the numerical and experimental results. This match is only possible by imposing a $\alpha_{\text{cond}} = 0.3$ for the evaporation of Fe, since the emission of its lines are the most important at this wavenumber range.

5.5. Conclusion

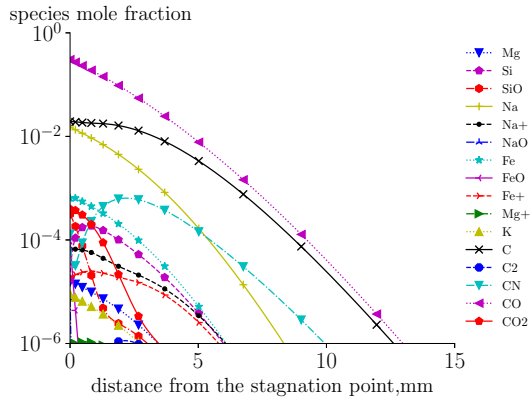
In this chapter, we have reproduced the El Hammami H5 ordinary chondrite experiment carried out at the VKI Plasmatron facility. We have computed the spectral intensity at different locations from the simulated flow field, integrating the RTE using the HSNB model, and we have compared it with the experimental results. This comparison has allowed us to assess the accuracy of the HSNB model and to understand if the evaporation model is representative of the ground experiment.

We have encountered additional difficulties in simulating this experiment due to the presence of the cork holder. The holder causes the presence of

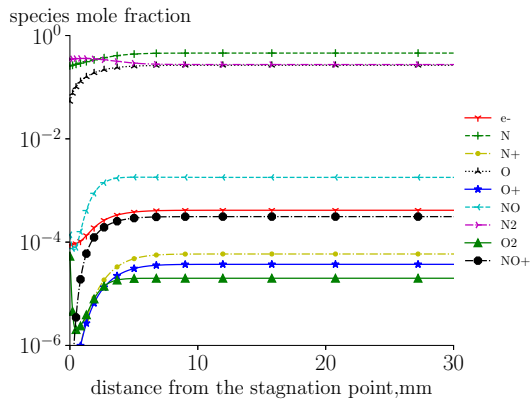


(a) Temperature profile: — T , - - - T^{ve} .

(b) Velocity profile.

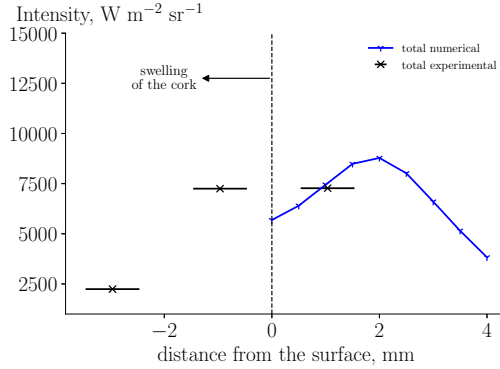


(c) Species composition regarding the evaporation of the H5 sample and the ablation of the cork.

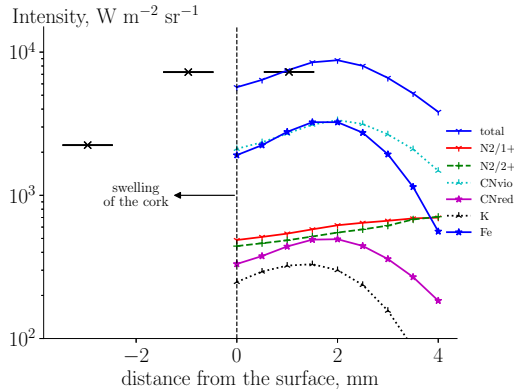


(d) Air species composition.

Figure 5.22.: Flow field properties along the stagnation streamline at 14 s.



(a) Intensity based on the sum of all mechanisms.



(b) Intensity of the individual mechanism.

Figure 5.23.: Comparison of the integrated intensity at different locations with the data recorded by the three spectrometers. The spectrometer data is represented by \times and the horizontal bar indicates the error due to its location. The cork swelling is linearly interpolated from Fig. (5.17).

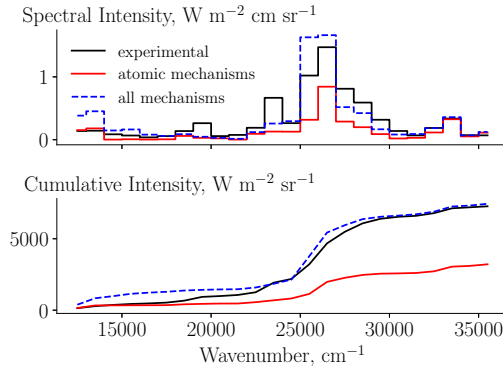
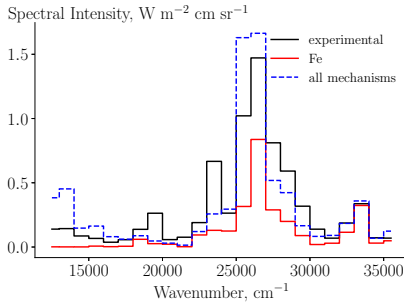


Figure 5.24.: Comparison of the intensity simulated at 1 mm from the surface with the furthest spectrometer: (top) spectral and (bottom) cumulative intensity

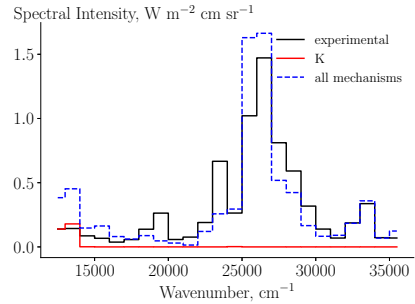
carbonaceous species in the flow field and hinders the analysis of the evaporation products. Furthermore, the strong presence of Na has resulted in the saturation of the spectral measurements. Nonetheless, the spectral intensity of the following stronger species, Fe, and K, has been well resolved. We have observed a good agreement of the cumulative intensity between the simulation and experimental results when the carbonaceous mechanisms have been included.

The analysis we have performed in this chapter gives us high confidence to apply the HSNB model to study the radiative field of meteoroid entry. Additionally, we have developed a methodology that can be used to compare simulations and ground experiments quickly.

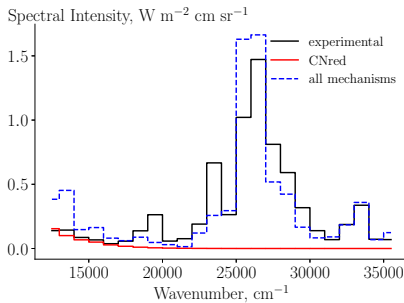
This chapter's main contribution is the development of a methodology that allows for a comparison of simulations with experimental measurements. More specifically, our methodology allows us to perform a spectral analysis of the flow without resorting to multi-dimensional Computational Fluid Dynamics (CFD) solvers. This methodology can be applied for future Plasmatron experiments as well as experiments in other high-enthalpy facilities, where the experiment carried out by [151] is one example. We recall that using a cork holder hinders the comparison with the numerical results regarding the specific experiment mentioned in this chapter. Initially, the holder's objective was to insulate the material so that the material melting could be considered a 1-D problem. For future experiments, we suggest not to use the holder and to use a sample with a spherical shape.



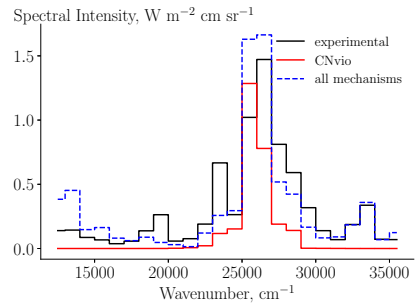
(a) Fe.



(b) K.



(c) CN red.



(d) CN violet.

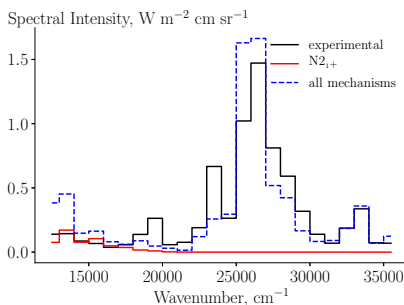
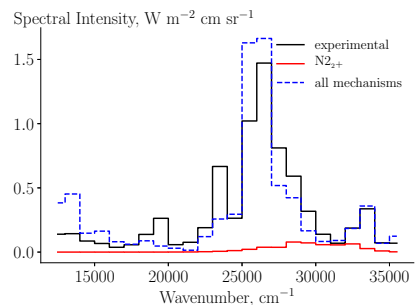
(e) N₂ first positive.(f) N₂ second positive.

Figure 5.25.: Spectral intensity of the individual mechanisms compared with the data recorded by the furthest spectrometer at 14s. The numerical results correspond to location of Fig. (5.24).

CHAPTER 6

Lost City case study

We can easily forgive a child who is afraid of the dark; the real tragedy of life is when men are afraid of the light.

— *Plato*

6.1. Introduction

Meteor phenomena involve a series of complex aspects, from multiphase physics of the meteoroid to non-equilibrium effects within the flow. The complexity significantly increases when one tries to couple all physical aspects in multi-dimensional simulations, where Golub et al. [96], Johnston and Stern [128], Johnston et al. [130], Shuvalov and Artemieva [235], Svetsov et al. [246] show some examples, as mentioned in Chapter 1.

The objective of this chapter is to simulate the entry of meteoroids with a quasi-1D approach by coupling all the models (Section 6.2) developed in the previous chapters. We use the Lost City bolide as an example because of its well-documented trajectory. The size and the trajectory conditions are reported in Ceplecha and ReVelle [54], and we use those as boundary conditions in our simulation tools. Moreover, we consider that the Lost City bolide is an H5 chondrite ([36]). This bolide [170] has the advantage of having a low entry velocity and fragmentation occurring below 40 km. Thus, it is adequate to evaluate our model, which does not include fragmentation.

In the first section of the chapter, we present a methodology (Section 6.3) that includes accurate boundary conditions to simulate the evaporation of the meteoroid and coupled flow–radiation effects. From the detailed flow and radiative fields, we compute the heat-transfer coefficient and luminous efficiency for an H5 chondrite and an iron meteoroid (Section 6.3.2) that can be used in

Parts of this chapter have been published in

1. B. Dias, J.B. Scoggins, T. E. Magin, **Luminosity calculation of meteoroid entry based on detailed flow simulations in the continuum regime**, *Astronomy & Astrophysics* 635, A184 (2020).

the heuristic models. Finally, we compare the absolute magnitude of Lost City bolide with observations (Section 6.3.3) shown by Ceplecha and ReVelle [54].

In the Section 6.4, we couple the material and the flow solver (Section 6.4), where the latter includes flow–radiation effects described in the first part. The coupling between the flow and the material allows for a better description of the meteoroid ablation since it considers the removal of the molten layer by shear forces. We compare the mass loss obtained by this coupling with the dynamic mass derived from the observations by Ceplecha and ReVelle [54].

We focus on meteoroids that are within the continuum assumption; thus, their flow field can be solved using the Navier-Stokes equations. Moreover, no assumptions is made on the thermodynamic and chemical state of the flow. In contrast, we assume a non-fragmenting body with a perfectly spherical shape, and we only model the plasma flow around the main body. The study of the meteor trail is beyond the scope of this thesis. One original contribution of our work is to use high-fidelity models to compute the absolute light magnitude and to compare with observations without the complexity of multi-dimensional simulations. Moreover, the coupling of flow/radiation/material with such physico-chemical details is original, as well as its application to study meteoroid entry.

6.2. Coupling between solvers

The first and second parts of this chapter consider two levels of coupling. In this section, we describe the coupling procedure to study meteoroid entry, which involves three solvers described in the previous chapters.

Stagnation-line solver: The stagnation-line resolves Eq. (2.5) and the solution vector, fluxes and sources terms are described by Eqs. (2.6) to (2.12). We employ the Backward-Euler method to Eq. (2.5) for the temporal discretization, and the solution is obtained once the flow reaches a steady state. We compute the convective fluxes at the interface with the AUSM+-up2 scheme by Kitamura and Shima [133].

Regarding the boundary conditions, we use the Hertz-Knudsen model (Eq. (3.44)) to close the Surface Mass Balance (SMB) (Eq. (3.2)) and we assume the evaporation and condensation coefficient $\alpha_{\text{evap}} = \alpha_{\text{cond}} = 1$. The oxide composition of the H5 chondrite used as input in MAGMA is shown in Table (3.1) and the corresponding equilibrium vapor pressure in Fig. (3.4).

In the case of the methodology presented in the first part, i.e., just the flow solver, the surface temperature is computed by solving the Surface Energy Balance (SEB) (Eq. (3.6)) such that,

$$q^{\text{cond}} + \epsilon q_{\text{in}}^{\text{rad}} = \epsilon \sigma T_w^4 + \dot{m}_{\text{vap}} L_{\text{heat}}, \quad (6.1)$$

where the terms on the left side represent the incoming conductive heat flux and the radiative heat flux, which is a result of the radiative transfer equation (RTE) calculation (in this work we use $\epsilon=0.85$). On the right side, the leaving

Table 6.1.: Gaseous species used in this chapter. The evaporation products contain only the major species according to their saturated vapor pressure.

air species
e^- N NO N ₂ O O ₂ N ⁺ O ⁺ NO ⁺ N ₂ ⁺ O ₂ ⁺
H5 chondrite evaporation products
Mg Mg ⁺ MgO FeO Si SiO SiO ₂ Na Na ⁺ NaO K Fe Fe ⁺
iron meteoroid evaporation products
Fe Fe ⁺

fluxes are the re-radiation of the material and energy lost due to evaporation, where the material's latent heat of evaporation $L_{\text{heat}} = 6.0 \times 10^6 \text{J kg}^{-1}$ for the ordinary chondrite [265] and $L_{\text{heat}} = 6.1 \times 10^6 \text{J kg}^{-1}$ for iron meteorites. The open-source library MUTATION⁺⁺ provides the necessary thermodynamic, transport, and kinetic properties used in this chapter. The full set of species considered is listed in Table (6.1).

Radiation solver: The radiation solver (RTE-1D) solves the Radiative Transport Equation (RTE) (Eq. (5.24)) either using the tangent slab method, described in Section 5.2.3, or along a single line-of-sight. It includes all the mechanism shown in Table (C.1) – except the mechanism formed by the elements C and H. The radiative fluxes \mathbf{q}^{rad} , radiative powers \mathcal{P}^{rad} and $\mathcal{P}^{\text{rad,ve}}$, and the mass production rate due to photochemistry $\dot{\omega}^{\text{rad}}$ are described in Section 5.2.3. Chemical and energy source terms due to radiation are included in the Navier-Stokes equations in Eq. (2.12) by following the work of Soucasse et al. [238]. Moreover, we use the RTE-1D as standalone to derive luminosity by integrating the spectral intensity in a line-of-sight from the meteor to the ground, which we show on the first part of our analysis.

Material solver: We describe the material solver in Chapter 4, and it solves the material phase-change as well as the removal of the liquid layer by shear forces. The solver takes as boundary conditions \dot{m}_{vap} , q^{conv} , $\epsilon q_{\text{in}}^{\text{rad}}$, $\partial_x \tau_w$ and $\partial_{xx} P_w$ from the stagnation-line solver. The boundary condition at the surface is estimated via SEB, which in addition to Eq. (6.1), it includes the thermal conduction of the material such that,

$$q^{\text{cond}} + \epsilon q_{\text{in}}^{\text{rad}} = \epsilon \sigma T_w^4 + \dot{m}_{\text{vap}} L_{\text{heat}} + k_l \nabla T_w \cdot \mathbf{n}. \quad (6.2)$$

The high heat-flux at the surface and the low thermal diffusivity of the material induce large temperature gradients inside the material. Therefore, we modify Eq. (4.11) to consider a non-uniform mesh to have a better refinement close to the surface.

In the first part, we consider radiation/flow coupling illustrated in Fig. (6.1), which we call hereafter as “flow solver”. In this coupling, the stagnation-line solver provides the thermo-chemical state of the flow field to the radiation

solver, after a certain number of iterations. In turn, the RTE-1D solver returns the radiative and chemical source terms. At the first coupling iterations, the radiative source terms might introduce some instabilities to the governing equations. Hence, we apply the under-relaxation of the explicit radiative source term suggested by Chambers [59], such that,

$$\mathbf{S}^{\text{rad},\mathbf{p}^*+1} = r_{\text{fact}}\mathbf{S}^{\text{rad},\mathbf{p}} + (1 - r_{\text{fact}})\mathbf{S}^{\text{rad},\mathbf{p}+1}, \quad (6.3)$$

where the relaxation factor $r_{\text{fact}} = 0.5$ of the \mathbf{p} coupling iteration. We update the radiative source terms after $n = 150$ flow iterations within the stagnation-line solver. After a certain number of coupling iteration, when the flow field is reaching a steady solution, $\mathbf{S}^{\text{rad},\mathbf{p}}$ is equal to $\mathbf{S}^{\text{rad},\mathbf{p}+1}$.

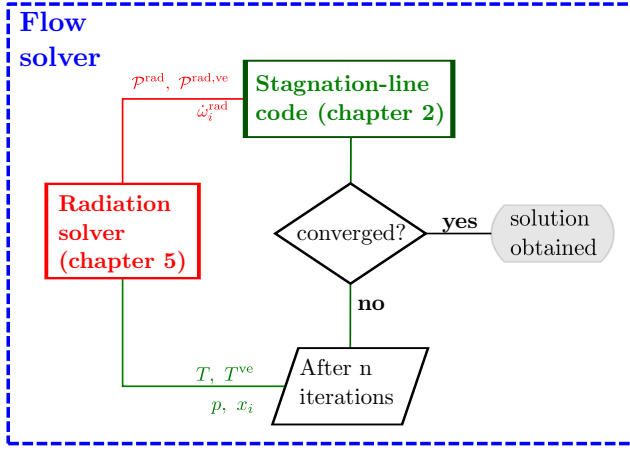


Figure 6.1.: Procedure of the radiation/flow coupling. This coupling will be mentioned hereafter as flow solver.

The second part considers the radiation/flow/material coupling illustrated by Fig. (6.2). For the present analysis, we follow the coupling strategy of Chen and Gökçen [63], Schrooyen et al. [226], referred to as implicit coupling. This type of coupling allows for time varying boundary conditions into the material solver from a time $t_i \rightarrow t_{i+1} = t_i + \Delta t$; and these boundary conditions are linearly interpolated within the transient solution. The algorithm is:

1. pass the initial solution of the flow \mathbf{F} and material \mathbf{M} properties to the material solver at t_i ;
2. solve the transient material field $t_i \rightarrow t_i + \Delta t$;
3. check if the surface temperature at $t_i + \Delta t$ is 10 K less than the previous coupling iteration;
4. if *step 3*:
 - i. is true end the coupling between $t_i \rightarrow t_{i+1}$; $\mathbf{F}^{t_{i+1}}$ and $\mathbf{M}^{t_i+\Delta t}$ serve as initial solution in *step 1* for $t_{i+1} \rightarrow t_{i+2}$;

- ii. is false go to *step 5*;
5. solve the flow field using $\mathbf{M}^{t_i+\Delta t}$ as boundary condition;
6. update the piecewise linear boundary conditions $\mathbf{F}^{t_i} \rightarrow \mathbf{F}^{t_{i+1}}$.

We repeat this procedure for the full trajectory where $t_i \rightarrow t_{i+1}$ represents the transient material solution from one trajectory point to another.

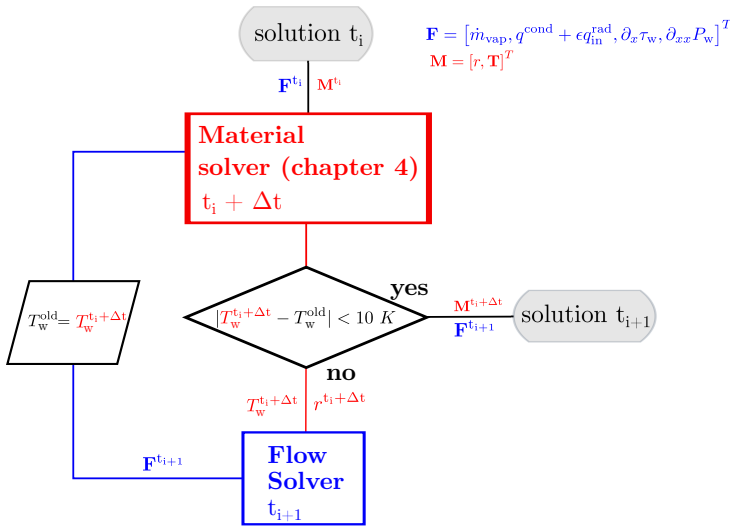


Figure 6.2.: Procedure of the radiation/flow/material coupling. The flow solver is described in Fig. (6.1).

6.3. Methodology to compute luminosity and heat transfer coefficient

6.3.1. Heat transfer coefficient and luminous efficiency

This section shows the methodology we develop to derive the heat-transfer coefficient and luminous efficiency from detailed simulations. The heat-transfer coefficient, C_h , indicates the amount of kinetic energy of the meteor that is translated to the surface of the body as heat. From the methodology presented in this chapter, we are able to directly estimate the stagnation point heat flux allowing us to define the heat-transfer coefficient as

$$C_h = \frac{q^{\text{conv}} + \epsilon q_{\text{in}}^{\text{rad}}}{\frac{1}{2} \rho_{\infty} v_{\infty}^3}. \quad (6.4)$$

The traditional luminosity equation for a non-decelerating body is given as

$$I_\alpha = \tau_\alpha \frac{v_\infty^2}{2} \frac{dm}{dt}, \quad \forall \alpha \in \{T, V, B, R\}, \quad (6.5)$$

where I_α represents the meteor luminosity and has the units of Watts, τ_α is the unitless luminous efficiency, v_∞ is the bolide velocity, and dm/dt is the mass loss in kg s^{-1} ($dm/dt = \int_A \dot{m}_{\text{vap}} dA$, where A is the surface area of the object). The index α in Eq. (6.5) concerns the luminosity in a specific band, i.e., T represents the total spectrum, V the visible band, B the blue band, and R the red band. The luminous efficiency represents the portion of kinetic energy transformed into radiation (the deceleration is not considered), and more specifically, Eq. (6.5) assumes that the radiation induced by the emission of the evaporation products and that the atmospheric radiative mechanism are negligible [42].

We write the original definition of the luminosity equation [55] to take into account the average quantities from the SNB method (in Section C.4 we show the derivation from the original equation):

$$I_\alpha = 4\pi r^2 \sum_{\Delta\sigma} \bar{\alpha}_\sigma^{\Delta\sigma} \bar{I}_\sigma^{\Delta\sigma} \Delta\sigma, \quad \forall \alpha \in \{T, V, B, R\}, \quad (6.6)$$

where $4\pi r^2$ represents the radiative spherical volume. In Eq. (6.6), $\bar{\alpha}_\sigma^{\Delta\sigma}$ is the UVBRI passband filter (taken from [22]) averaged over a narrow band; in the case of $\alpha = T$ we don't apply any filter since T is the total intensity, thus, $\bar{T}_\sigma^{\Delta\sigma} = 1$.

The luminosity recorded by any observation device corresponds to the radiative spectral flux from the meteor. Therefore, to represent this spectral flux, we solve the RTE on a line of sight from the meteoroid stagnation point to the ground. Moreover, since the surrounding environment can absorb the luminosity, we include the atmospheric conditions on the RTE integration. The spectral flux is,

$$\bar{F}_\sigma^{\Delta\sigma} = \pi \bar{I}_\sigma^{\Delta\sigma} \left(\frac{r}{R}\right)^2, \quad (6.7)$$

where the last term on the right-hand side represents the solid angle [179]. At $R = 60$ km altitude, the solid angle of a 1 m radiative volume is 3×10^{-7} sr, and therefore the RTE integration ($\bar{I}_\sigma^{\Delta\sigma}$) is done on a single ray.

The magnitude [0 mag] of the different bands is written from Eqs. (6.8) to (6.10). These equations compute the apparent and absolute magnitude. The difference between these two magnitudes is that the latter is computed by setting $R = 100$ km in Eq. (6.7). The constant after the integral is taken from Bessell [22], Bessell et al. [23] and Allen [5] based on Vega magnitude, denoted conventionally as

$$V = -2.5 \log \left(\sum_{\Delta\sigma} \bar{V}_\sigma^{\Delta\sigma} \cdot \bar{F}_\sigma^{\Delta\sigma} \Delta\sigma \right) - 13.72, \quad (6.8)$$

$$B = -2.5 \log \left(\sum_{\Delta\sigma} \overline{B}_\sigma^{\Delta\sigma} \cdot \overline{F}_\sigma^{\Delta\sigma} \Delta\sigma \right) - 13.22, \quad (6.9)$$

$$R = -2.5 \log \left(\sum_{\Delta\sigma} \overline{R}_\sigma^{\Delta\sigma} \cdot \overline{F}_\sigma^{\Delta\sigma} \Delta\sigma \right) - 13.76. \quad (6.10)$$

Ceplecha [52] provides the following equation to transform the UBVRI into the panchromatic system and to compute the photographic magnitude M_p of meteoroid entry

$$M_p = V + 0.62(B - V) - 0.52(V - R). \quad (6.11)$$

The photography and visual intensity in 0 mag units is expressed as,

$$I_\alpha^* = 10^{-0.4M_\alpha}, \quad \alpha = p, V, \quad (6.12)$$

[259], and the luminous efficiency with $\text{mag erg}^{-1} \text{ s}$ units,

$$\tau_\alpha^* = \frac{I_\alpha^*}{I_T} \tau_T, \quad \alpha = p, V, \quad (6.13)$$

where I_T is computed by Eq. (6.6) and τ_T by Eq. (6.5).

6.3.2. Application of the methodology

Based on detailed simulations — for which flow, ablation, and radiation are coupled — it is possible to derive the coefficients used in the single body theory and to gain more in-depth knowledge on the meteor phenomenon, as opposed to analysis of observations alone. The physics behind this phenomenon are sensitive to numerous parameters, such as the size, trajectory, and composition of the bolide. In this section, we explore some of these parameters, and we derive absolute magnitude, heat transfer, and luminous efficiency from detailed simulations. Moreover, we compute the spectra observed from ground spectrometers by solving the RTE on a line of sight from the stagnation point to the ground.

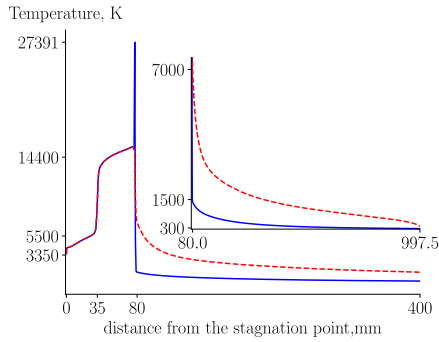
We divide the results section into two parts. In the first part, we present an application of the methodology to study iron and H5 chondrites of two different sizes (0.1 and 1 m radius) and at two different altitudes (60 and 50 km), with a velocity of 15 km s^{-1} . Within this study, we analyze the non-equilibrium effects in the flow due to radiation, and then we derive absolute magnitude, heat-transfer, and luminous efficiency. In the second part, we apply our methodology to study the entry of the Lost City bolide [170], at 70, 60, 50, and 40 km, and compare the derived absolute magnitude with the observations.

6.3.2.1. Flow field analysis

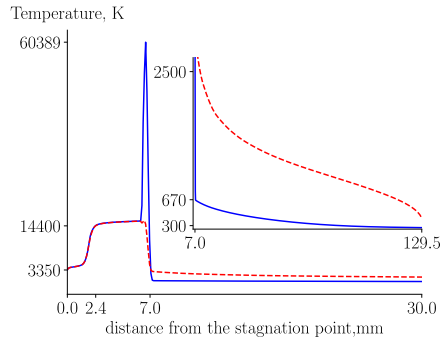
The magnitude of the light curves is correlated with the size of the incoming object, which means that the radiation effects are stronger for larger objects.

A strong radiative field induces non-equilibrium effects, especially in the free-stream where radiation can ionize and dissociate the flow. Moreover, at the typical regimes of meteoroid entry, the surface temperature highly depends on the incoming heat flux due to the radiative emission from the shock layer. Figures (6.3a) and (6.3b) show the temperature along the stagnation streamline for two H5 chondrites at 50 km altitude with different sizes (1.0 m on the left and 0.1 m on right). The surface temperature is approximately the same for both objects due to an energetic balance of incoming heat flux and mass removal, meaning that higher heat flux results in a higher evaporation rate (see Table (6.2)). The vapor layer in front of the surface is characterized by a small increase in temperature (around 2000 K for the 1.0 m radius) followed by a shock layer in thermal equilibrium, where the translational and internal temperatures reach more than 14000 K. The shock is located at 80 mm and 7 mm for the 1 and 0.1 m bodies, respectively. Upstream from the shock, a substantial departure from thermal equilibrium is observed with an increase of the internal temperature. The excitation of the internal modes is due to the radiated energy from the shock layer, resulting in a decrease of temperature at the shock layer and boundary layer. The sudden equilibrium of T and T^{ve} upstream in Figs. (6.3a) and (6.3b) are artifacts of the boundary condition, but due to the large computation domain the shock layer results are unaffected. Moreover, at the free-stream, the energy transfer between the internal and translational mode (via VT energy transfer) leads to an increase of the translational temperature. The emission of photons leads to photochemistry reactions forming ionized and dissociated species at the free-stream (see Figs. (6.3c) and (6.3d)). From the radiative heat flux at the wall (Table (6.2)) and the level of non-equilibrium in the free-stream, it is reasonable to conclude that the radiative emission is stronger for the 1 m object because of the size of the shock layer.

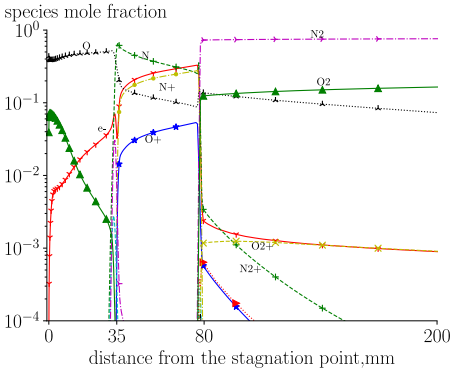
Under the conditions reported in this chapter, the increase of the surface temperature induces intensive evaporation of the meteoroid, forming a vapor layer in front of the surface. Figures (6.3e) and (6.3f) show the vapor layer composed mostly by evaporation products, which extends to 35 mm for the larger and 2.4 mm for the smaller bolide. Moreover, the low dissociation energy of the alkali metals leads to evaporation in the form of atoms or diatomic molecules, as in the case of Na and SiO. As the temperature increases in the vapor layer (Fig. (6.3a)), the SiO dissociates into Si and Na ionizes into Na^+ . Although K is a volatile, its low composition in the condensed phase results in a residual presence in the gas phase. The refractory elements such as Ca, Al, and Ti have low vapor pressure, and therefore they are not present in the gas phase. The vapor layer is formed due to the strong blowing of evaporation gases pushing the air upstream. Furthermore, this vapor layer blocks the convective heat flux at the surface (in Table (6.2) the convective heat flux is a small contribution to the total heat flux). As reported by [55], we identify the main spectrum as the radiative excitation of the atoms in the vapor layer (Figs. (6.3e) and (6.3f)) and the secondary spectrum corresponds to the radiative excitation of the atoms in the shock layer (Figs. (6.3c) and (6.3d)). This identification consists of the temperature results where the main spectrum contains elements



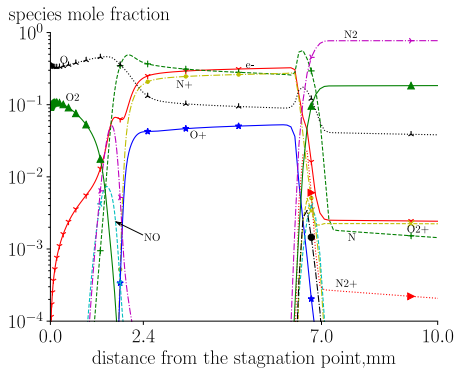
(a) Temperature profile of the 1.0 m radius at 50 km altitude: — T , - - - T^{ve} .



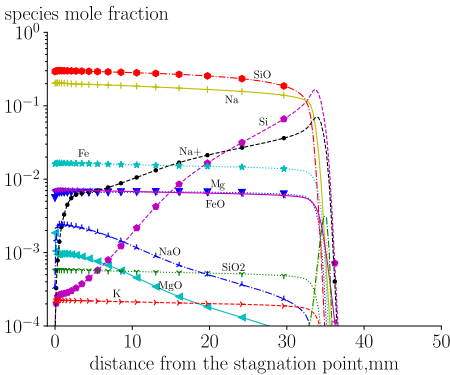
(b) Temperature profile of the 0.1 m radius at 50 km altitude: — T , - - - T^{ve} .



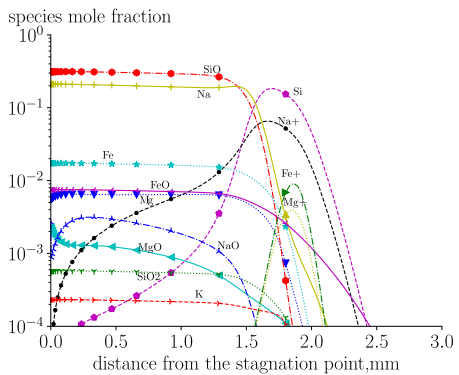
(c) Composition of the air species of the 1.0 m radius at 50 km altitude.



(d) Composition of the air species of the 0.1 m radius at 50 km altitude.



(e) Composition of the evaporation products of the 1.0 m radius at 50 km altitude.



(f) Composition of the evaporation products of the 0.1 m radius at 50 km altitude.

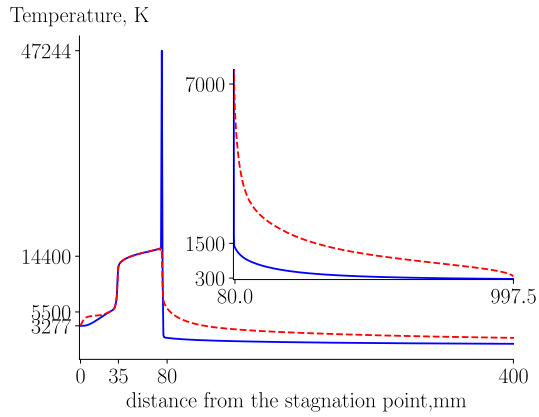
Figure 6.3.: Flow field results along the stagnation streamline of the H5 chondrite.

at a temperature of ≈ 3000 K, and the secondary spectrum contains elements of ≈ 14000 K as found by Borovička [30, 37].

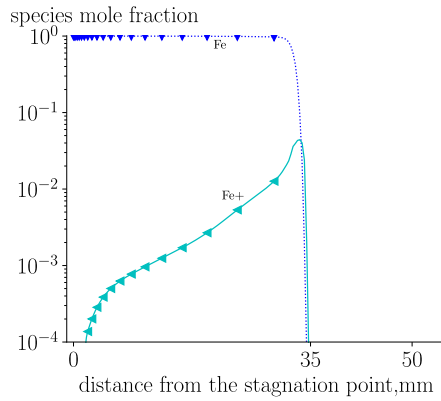
Table 6.2.: Parameters concerning the SEB and SMB on the H5 chondrite.

Alt.	Rad.	T_w	\dot{m}_{vap}	$\epsilon q_{in}^{\text{rad}}$	q^{cond}	$\epsilon \sigma T_w^4$	$\dot{m}_{\text{vap}} L_{\text{heat}}$
[km]	[m]	[K]	[kg s ⁻¹ m ⁻²]	[MW m ⁻²]	[MW m ⁻²]	[MW m ⁻²]	[MW m ⁻²]
50	0.1	3352.9	5.3	34.56	3.35	6.09	31.82
50	1.0	3354.6	8.7	56.19	1.92	6.1	52.01
60	0.1	3103.9	0.8	8.52	0.95	4.48	5.0
60	1.0	3110.1	2.3	17.36	0.78	4.51	13.64

Figure (6.4) shows the temperature profile (left figure) and the ablation composition (right figure) of a 1 m iron bolide at 50 km altitude with an entry velocity of 15 km s^{-1} . Figure (6.4b) shows that the vapor layer near the surface is composed of pure iron which partially ionizes further upstream. Compared to Fig. (6.3a), Fig. (6.4a) shows a similar temperature profile at the shock layer and the free-stream. This behavior suggests that the precursor effect is mainly sensitive to the entry conditions and the size of the object, and not to its composition. On the other hand, a thermal non-equilibrium is present in the vapor layer of the iron bolide (Fig. (6.4a)) due to energy transfer from electron-impact ionization reactions. Even though the mole fraction of the electron in the vapor layer is similar for both the H5 and iron, the energy transfer due to ionization reactions is higher for the iron bolide. This study (see Table (6.3)) reveals that the surface temperature is similar for bolides at the same altitude, and that the convective heat flux is negligible compared to the radiative heat flux, as for the H5 case. Also, in comparison with H5, the evaporation rate is higher for lower surface temperatures due to a higher equilibrium vapor pressure of pure iron for lower temperatures.



(a) Temperature profile of the 1.0 m radius at 50 km altitude: — T , - - - T^{ve} .



(b) Composition of the evaporation products of the 1.0 m radius at 50 km altitude.

Figure 6.4.: Flow field results along the stagnation streamline of the iron meteoroid.

Table 6.3.: Parameters concerning the SEB and SMB from the iron meteoroid.

Alt.	Rad.	T_w	\dot{m}_{vap}	$\epsilon q_{in}^{\text{rad}}$	q^{cond}	$\epsilon \sigma T_w^4$	$\dot{m}_{\text{vap}} L_{\text{heat}}$
[km]	[m]	[K]	[kg s ⁻¹ m ⁻²]	[MW m ⁻²]	[MW m ⁻²]	[MW m ⁻²]	[MW m ⁻²]
50	0.1	3265.3	6.0	40.9	0.11	5.48	36.77
50	1.0	3276.8	12.0	78.8	0.01	5.58	73.2
60	0.1	2985.8	1.1	9.63	0.78	3.83	6.41
60	1.0	3006.2	2.9	20.85	0.01	3.94	17.45

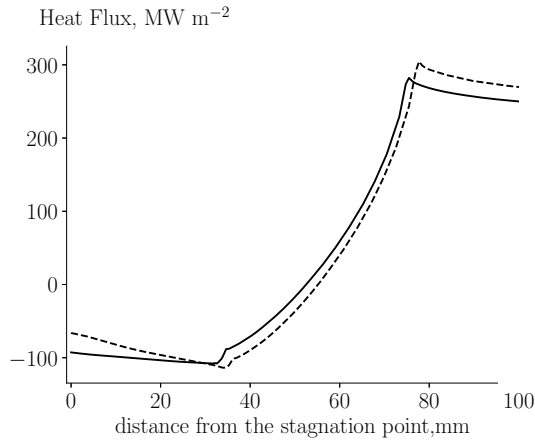


Figure 6.5.: Radiative heat flux along the stagnation streamline 1.0 m radius at 50 km: The solid line represents iron, and the dashed line represents H5 chondrite.

For the study presented here, the radiative heat flux is the major contribution to the total heat flux (see Tables (6.2) and (6.3)). The convective heat flux has a small contribution to the total heat flux due to the high ablation rate, leading to a temperature plateau where the vapor layer is located, and therefore the gradients of composition and temperature are small. For the iron case, the radiative heat flux into the wall is more significant due to a smaller radiative absorption in the boundary layer. Figure (6.5) shows the radiative heat flux vector $q^{\text{rad}}(r)$ along the stagnation streamline. A negative value represents a radiative heat flux towards the surface, and a negative slope corresponds to the absorption of the participating medium. In contrast, a positive slope of the radiative heat flux corresponds to emission. Close to the surface, the H5 chondrite shows a steeper negative slope, meaning that the absorption in the boundary layer is larger than the iron case. The small deviation of the radiative heat flux above 60 mm is due to the difference in the stand-off shock-distance between the H5 chondrite and the iron case. Since the pure iron gas density at the surface is higher than the H5 chondrite, the blowing velocity for both cases is similar, and this is why the stand-off shock-distance is comparable for both cases.

6.3.2.2. Meteor coefficient from the flow field

The detailed flow field allows us to retrieve the heat-transfer coefficient, the luminous efficiency, and the observed absolute photographic magnitude. We recall that the latter is modeled by integrating the RTE over a line of sight from the stagnation point to the ground. It is necessary to consider the atmospheric conditions along the line of sight because the atmospheric O₂ Schumann-Runge [184] absorbs part of the light. For the photographic magnitude in Eq. (6.11),

we use the UBVRI filters from Bessell [22] to compute the corresponding spectral intensity in the red, visible, and blue passband ranges. The difference between the photographic magnitude and the visual magnitude defines the color index CI , which quantifies the observed color of a meteor during entry.

Figure (6.6a) shows the red, visible, and blue spectral intensity for the case presented in Fig. (6.3a). The results shown in Table (6.4) concern the magnitude in the different ranges for the entire H5 study from which a $CI > 0$ is estimated, contradicting the observations of this type of bolide ([54, 121, 214]). The strong red and visible passband emission are due to the spectral intensity of Na (see Fig. (6.6c)) resulting from its composition in the vapor layer. Borovička and Betlem [32] attributes a $CI < 0$ to the emission of CaII lines in the blue passband. The models presented in this chapter are unable to predict the presence of Ca because the vapor pressure computed from MAGMA is $\mathcal{O}(4)$ lower than the volatile at these conditions (Na), and therefore the evaporation of this element is negligible. In conclusion, $CI > 0$ because of the absence of Ca and the low content of Fe and Mg combined with the strong presence of Na.

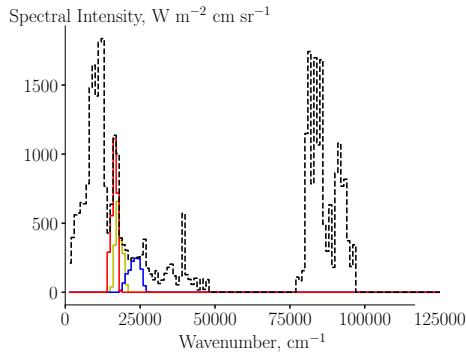
Figure (6.6c) shows the spectral intensity of each evaporated atom while Fig. (6.6b) shows the air species. In the visible range (between 12500 and 25000 cm^{-1}) the spectrum is dominated by O, N, and Na, while Si, Fe, and Na^+ are more intense in the UV region. In the near-infrared, the spectrum is mainly dominated by Na, N, and O and above 70000 cm^{-1} , only O, N, O^+ and N^+ are found.

Table 6.4.: Total intensity and absolute light magnitude obtained from the H5 chondrite.

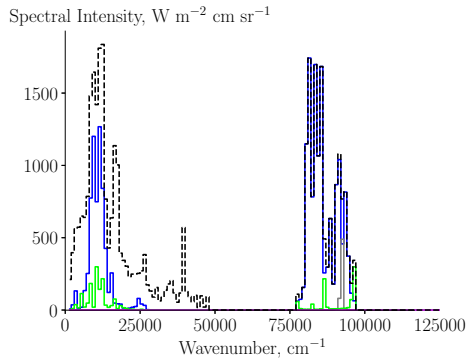
Alt.	Rad.	$I_T/10^{14}$	V	(B-V)	(V-R)	M_p
[km]	[m]	[erg s^{-1}]	[mag]	[mag]	[mag]	[mag]
50	0.1	3.88	-8.45	1.27	0.71	-8.03
50	1.0	90.1	-14.59	0.98	0.70	-14.24
60	0.1	1.22	-7.36	1.54	0.84	-6.85
60	1.0	21.0	-12.65	1.00	0.95	-12.52

Figure (6.7a) shows the spectral intensity through the different filters for the iron bolide case presented in Fig. (6.4). In this case, the blue passband is more intense than the H5 chondrite (see Table (6.5)) because of the spectral intensity of Fe in Fig. (6.7c). We recall that the vapor layer is mostly composed of pure Fe with a small trace of Fe^+ . The emission of Fe^+ is outside the range observed by the photographic cameras. As a consequence of the strong Fe emission, the CI turns negative for all the cases simulated on the iron bolide, as shown in Table (6.5).

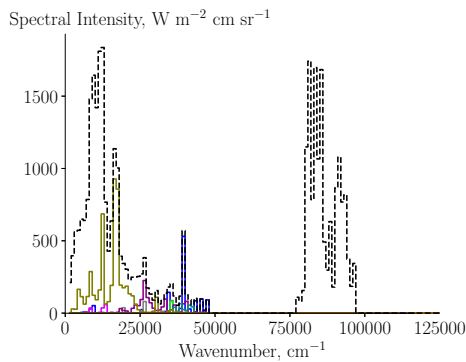
The total intensity in Eq. (6.6) is obtained by integrating the total spectral



(a) Comparison between the total spectral intensity (---) with the blue (—), visible (—) and red (—) passband.

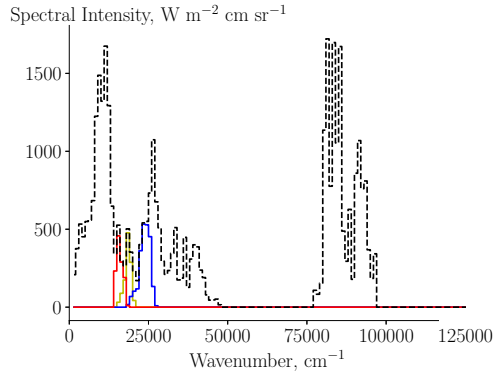


(b) Spectral intensity of the air atomic lines: — N, — N⁺, — O, — O⁺, --- total.

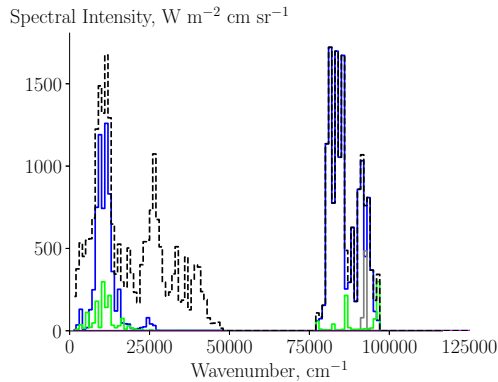


(c) Spectral intensity of the atomic lines concerning the most abundant evaporation products: — Si, — Mg, — Mg⁺, — K, — Fe, — Fe⁺, — Na, — Na⁺, --- total.

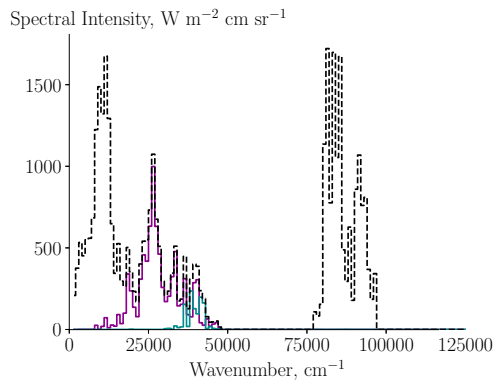
Figure 6.6.: Narrowband spectral intensity of the 1.0 m radius of the H5 chondrite at 50 km altitude.



(a) Comparison between the total spectral intensity (---) with the blue (—), visible (—) and red (—) passband.



(b) Spectral intensity of the air atomic lines: — N, — N^+ , — O, — O^+ , --- total.



(c) Spectral intensity of the evaporation atomic lines: — Fe, — Fe^+ , --- total.

Figure 6.7.: Narrowband spectral intensity of the 1.0 m radius of the iron meteoroid at 50 km altitude.

Table 6.5.: Total intensity and absolute light magnitude obtained from the iron meteoroid.

Alt.	Rad.	$I_T/10^{14}$	V	(B-V)	(V-R)	M_p
[km]	[m]	[erg s ⁻¹]	[mag]	[mag]	[mag]	[mag]
50	0.1	4.35	-8.44	-0.75	-0.20	-8.80
50	1.0	92.6	-14.09	-0.29	0.09	-14.32
60	0.1	1.37	-7.14	-0.77	-0.11	-7.56
60	1.0	22.3	-12.30	-0.43	0.06	-12.59

intensity shown in Figs. (6.6a) and (6.7a). We highlight the fact that term r in Eq. 22 corresponds to a distance whereby the radiative power is zero, which is approximately double the sphere radius. From the visual and photography magnitude (Tables (6.4) and (6.5)), one can estimate the corresponding intensity from Eq. (6.12) and the luminous efficiency from Eq. (6.13). Table (6.6) shows the different luminous efficiency (a negative CI corresponds to a $\log \tau_p - \log \tau_v > 0$ and vice-versa) and the heat-transfer coefficient (Eq. (6.4)) for all cases presented here. Our results allow us to conclude that the luminous efficiency does not depend only on the velocity, as is typically assumed, but on the size, composition, and altitude. Although our definition of C_h is different from that of [130], we estimate similar values for the H5 chondrite. Table (6.6) also shows that the heat-transfer coefficient for iron is higher than that for H5 chondrite due to a higher total heat flux entering the iron surface (Table (6.3)) compared to that entering H5 (Table (6.2)).

6.3.3. Luminosity of the Lost City bolide

We simulate the flow field of the bolide at four trajectory points (70, 60, 50 and 40 km). We consider a constant radius (~ 0.23 m) and velocity (~ 14.15 km s⁻¹) according to the results of Ceplecha and ReVelle [54]. The same methodology as in the previous section is used to compute the radiative intensity and the absolute magnitude from the flow field.

Figure (6.8) shows the comparison of the observed absolute magnitude with the numerical results; here the observation error is less than 0.5 mag ([54, 170]). The absolute magnitude M_p shows a small deviation from the observation. This deviation motivates a different approach to treat the evaporation boundary conditions, which disregard the evaporation of volatiles. In other words, the total vapor pressure is obtained from MAGMA, and the species vapor pressure is computed via Dalton's laws, forcing the composition of the alkali metals at the surface to be the same as in Table (3.1). This enforcement of the composition follows a more qualitative rather than a quantitative treatment of the boundary condition since it disregards the evaporation of volatiles. Nonetheless, when we

Table 6.6.: Luminous and heat transfer coefficient obtained from the H5 chondrite and the iron meteoroid.

Type	Alt.	Rad.	$\log \tau_v^*$	$\log \tau_p^*$	$C_h/10^{-2}$
	[km]	[m]	[mag erg ⁻¹ s]	[mag erg ⁻¹ s]	
H5	50	0.1	-11.42	-11.59	2.3
	50	1.0	-11.25	-11.35	3.52
	60	0.1	-11.08	-11.28	1.95
	60	1.0	-11.40	-11.45	3.73
Iron	50	0.1	-11.54	-11.39	2.56
	50	1.0	-11.59	-11.50	4.78
	60	0.1	-11.33	-11.16	2.09
	60	1.0	-11.67	-11.55	4.39

estimate the absolute magnitude ($M_{p,equil}$) using this modified boundary condition, we obtain better agreement with the observations. The standard and modified boundary conditions predict the evaporation of different species from the material which affects the flow field around the bolide. Figure (6.9) shows the flow field of Lost City bolide at 50 km; the left and right columns correspond to the simulation with the standard and the modified boundary conditions, respectively. The two top figures show the temperature along the stagnation line, where no significant differences are observed, and the two bottom figures show the composition of the evaporated species (see also Table (6.7)). In the left figure (standard boundary condition), the two major species in the flow are SiO and Na, followed by the presence of small amount of Fe and Mg. Molecules of SiO and Na dissociate and ionize further downstream creating Si and Na⁺. The volatile nature of Na leads to a substantial amount of this species being present in the flow, differently from the species formed by Ca. In the right figure, the modified boundary condition estimates SiO₂, MgO, and FeO as the major species. This figure also shows traces of Ca, which were not present in the previous example, and the composition of Na decreases significantly.

The difference of the absolute magnitude in Fig. (6.8) is a consequence of the species generated by both boundary conditions. The modification of the boundary condition impacts the flow field around the Lost City bolide and its spectra calculation. In the standard boundary condition case, the abundant presence of Na (Fig. (6.10c)) leads to a strong spectral intensity in the red and visible range (Fig. (6.10a)), meaning that the color index is positive. Moreover, the presence of a relatively small amount of Fe and Mg leads to a weak intensity in the blue region. The weak intensity of the blue region is also explained by the lack of Ca and Ca⁺, which are strong radiators in this range [32]. On the other

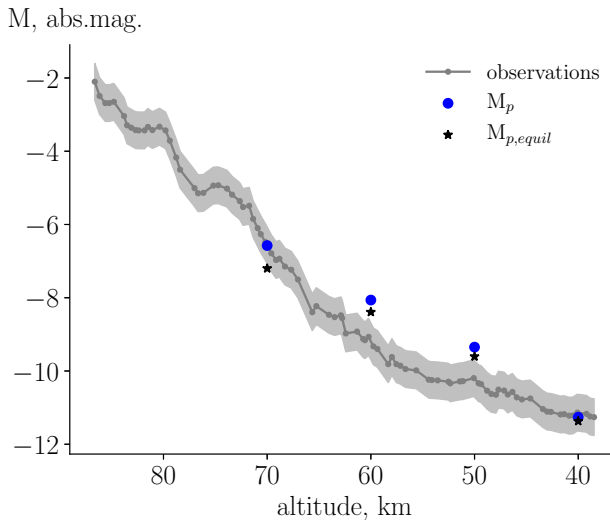
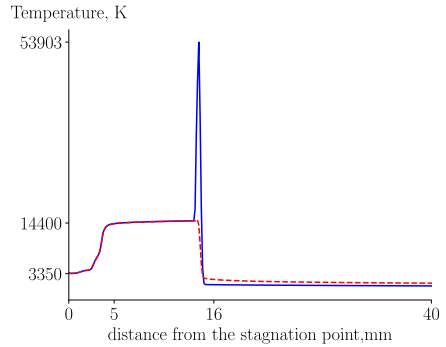
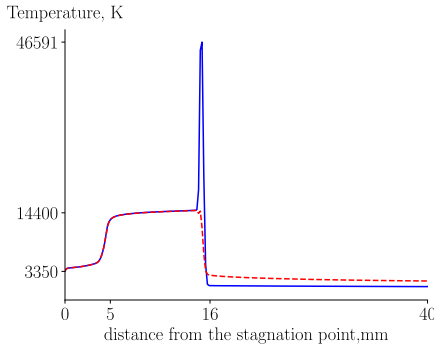


Figure 6.8.: Absolute magnitude luminosity of the Lost City bolide; comparison between the observations and the numerical results using standard (M_p) and modified boundary conditions ($M_{p,equil}$): (gray area) observations with uncertainty, \bullet M_p , \star $M_{p,equil}$.

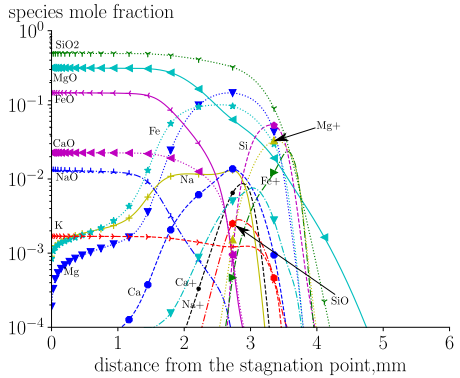
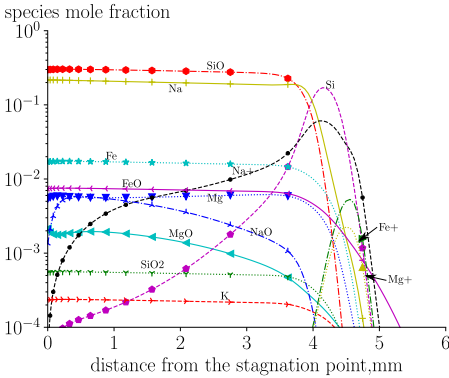
hand, when the modified boundary condition is used, the color index becomes negative which is due to a stronger emission in the blue region (Fig. (6.10b)) caused by the presence of Mg, Fe, Ca, and Ca^+ . Figure (6.10d) shows a strong emission of these atoms from 200000 to 300000 cm^{-1} . In this case, the presence of Ca and Ca^+ is clearly identified, confirming several spectroscopy observations from meteor observation [30, 32, 37]. Finally, the discrepancy between the observations and the numerical simulations might be attributable to the fact that we are not considering the wake. The work of Johnston and Stern [128] shows that the wake contributes significantly to the radiative flux observed from the ground for Tunguska-type bolides.

These results appear counterintuitive because, on one hand, we present a physical boundary condition (standard boundary condition) that overestimates the composition of Na and cannot predict the appearance of Ca, and on the other hand, we have a boundary condition (modified boundary condition) which does not distinguish the evaporation of volatile and refractory elements but provides a better qualitative agreement with the spectroscopic measurements. This contradiction could be explained by considering that the molten surface breaks up into small droplets which completely evaporate in the trail. The break up of the molten layer into small droplets was explored by Capek et al. [47], where the author was able to replicate the light curves of iron meteoroids by fitting the luminous efficiency. Nonetheless, spraying of the molten layer seems to be the most plausible explanation for the appearance of refractory elements in the spectra, as was also the conclusion of Borovička [37]. The



(a) Temperature profile at 50 km altitude with the standard boundary condition: — T , - - - T^{ve} .

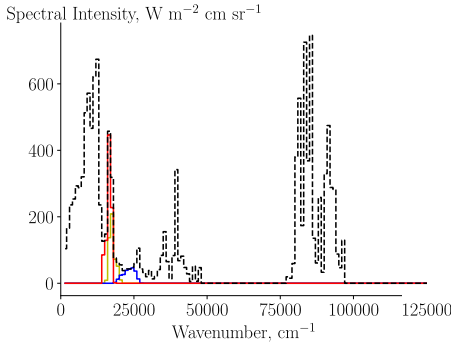
(b) Temperature profile at 50 km altitude with the modified boundary condition: — T , - - - T^{ve} .



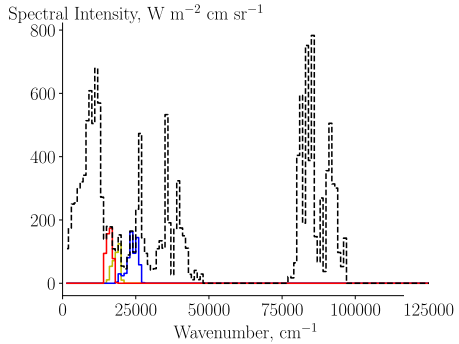
(c) Composition of the evaporation products at 50 km altitude with the standard boundary condition.

(d) Composition of the evaporation products at 50 km altitude with the modified boundary condition.

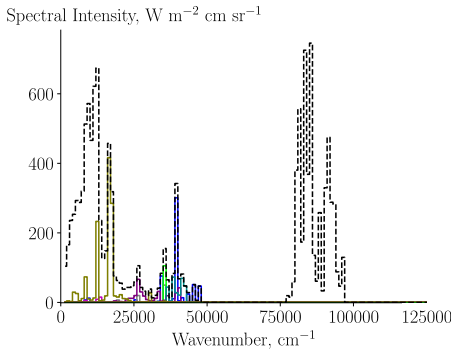
Figure 6.9.: Flow field results along the stagnation streamline of the Lost City; comparison of the standard and modified boundary conditions.



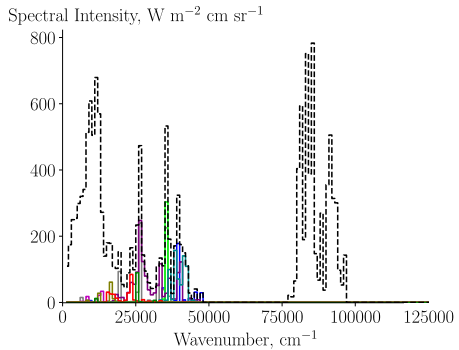
(a) Comparison between the total spectral intensity (---) with the blue (—), visible (—) and red (—) passband resulting the standard boundary condition.



(b) Comparison between the total spectral intensity (---) with the blue (—), visible (—) and red (—) passband resulting the modified boundary condition.



(c) Spectral intensity of the atomic lines concerning the most abundant evaporation products computed from the standard boundary condition: — Si, — Mg, — Mg⁺, — K, — Fe, — Fe⁺, — Na, — Na⁺, — Ca, — Ca⁺, --- total.



(d) Spectral intensity of the atomic lines concerning the most abundant evaporation products computed from the modified boundary condition: — Si, — Mg, — Mg⁺, — K, — Fe, — Fe⁺, — Na, — Na⁺, — Ca, — Ca⁺, --- total.

Figure 6.10.: Narrowband spectral intensity of the Lost City at 50 km altitude; comparison of the standard and modified boundary condition.

rationale proposed here can also be supported by the experimental spectra of [76], which does not consider the spraying of the molten thickness. From the high-resolution spectra, these latter authors observed an overestimation of Na with respect to Fe and Mg and a weak intensity of refractory Ca.

Table 6.7.: Parameters concerning the SEB and SMB on the Lost City.

Type	Alt.	Rad.	T_w	\dot{m}_{vap}	$\epsilon q_{in}^{\text{rad}}$	q^{cond}	$\epsilon \sigma T_w^4$	$\dot{m}_{\text{vap}} L_{\text{heat}}$
	[km]	[m]	[K]	[kg s ⁻¹ m ⁻²]	[MW m ⁻²]	[MW m ⁻²]	[MW m ⁻²]	[MW m ⁻²]
<i>Standart</i>	40	0.23	3616.9	19.7	119.7	8.81	8.25	120.34
	50	0.23	3353.8	6.1	40.63	2.79	6.1	37.37
	60	0.23	3105.4	1.0	9.47	0.8	4.48	5.8
	70	0.23	2748.0	0.06	1.5	1.63	2.75	0.38
<i>Equil</i>	40	0.23	3738.7	25.6	165.72	0.1	9.42	156.42
	50	0.23	3429.1	6.6	46.95	0.0	6.66	40.33
	60	0.23	3159.6	1.1	10.97	0.23	4.8	6.41
	70	0.23	2669.7	0.1	1.53	1.49	2.45	0.57

6.4. Lost City radiation/flow/material coupling

In this section, we apply the implicit coupling of radiation/flow/material to study the Lost City bolide trajectory. We focus on the trajectory between 60 km to 53 km – with an interval of 1 km from a point to another – with a constant velocity of 14.15 km s^{-1} [54]. We estimate the initial conditions at 60 km by iterating the implicit coupling until the surface temperature reaches a steady state. The density of the material is 3160 kg m^{-3} and the thermochemical properties are the same as Chapter 4.

Figure (6.11) compares the variation of mass along the trajectory with the dynamic mass derived from observations [54]. Both results agree well at the first trajectory points, and it slightly deviates below 57 km, where the numerical results underestimate the ablation. Both models estimate a low mass loss in this part of the trajectory. The observations suggest that most of the mass loss occurs below 40 km due to fragmentation.

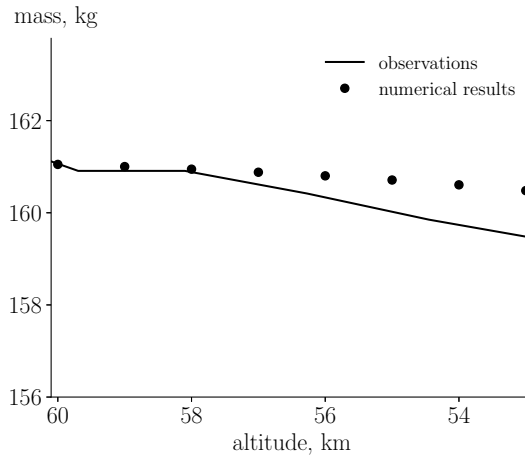


Figure 6.11.: Variation of the Lost City mass along the trajectory. Comparison between the numerical results and the dynamic mass derived from observations.

Figure (6.12) shows the different contributions of mass removal along the trajectory. The removal of mass due to shear forces is the primary source of ablation above 54 km, whereas the evaporation rate becomes dominant at 53 km. The evaporation rate increases at lower altitudes due to a surface temperature rise shown by Fig. (6.15a). The increase of the evaporation rate leads to a thinner molten layer shown by Fig. (6.14).

The rise of the surface temperature results from the increase of the radiative heat flux at the surface $\epsilon q_{\text{in}}^{\text{rad}}$, shown by Fig. (6.13a). The free-stream properties

considering an entry with an angle to the zenith of 52° [102] at this velocity, the $\Delta t=0.11 \text{ s}$ from a trajectory point to another (in Fig. (6.2))

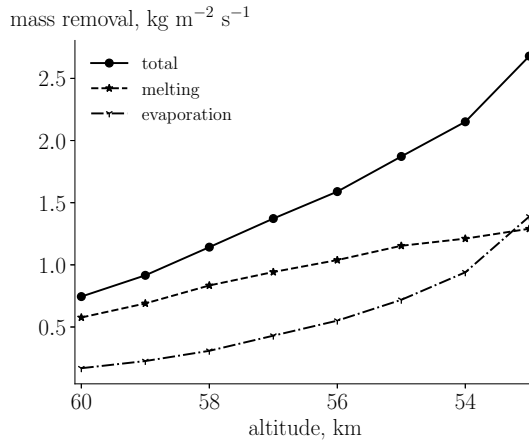


Figure 6.12.: Mass removal along the trajectory of the Lost City.

increase with the lowering of the altitude, leading to stronger shock jump conditions. This increases of physico-chemical properties in the shock layer lead to a more energetic radiative field, therefore explaining the increase of $\epsilon q_{\text{in}}^{\text{rad}}$. The conductive heat flux decreases due to the increase in the evaporation rate. The blowing of the evaporation gases leads to a vapor layer, decreasing the temperature gradient at the surface, as shown in Section 6.3.2.

Figure (6.13b) shows the average shear forces, which causes molten layer removal, increasing along the trajectory due to an increase of the free-stream pressure. Despite the increase of the aerodynamic forces, the melting mass removal tends to an asymptotic value. This effect is owed to a decrease of the molten thickness cause by a stronger evaporation rate, Fig. (6.14).

Figure (6.15b) shows the temperature inside the material, and each curve corresponds to a trajectory point. One observes a large temperature gradient close to the surface while the core remains unaltered (Fig. (6.15a)). This large temperature gradient at the surface is a combination of the low material thermal diffusivity and the large mass removal [65].

Interestingly, the surface temperature and, subsequently, the evaporation rate is lower than the results shown in Section 6.3.3, for the same conditions.

6.5. Conclusion

In this chapter, we have tackled the meteor phenomena by assembling all the models developed previously. As a case study, we have applied our models to the entry of the Lost City bolide. We have chosen this bolide because it suffered fragmentation below 40 km, meaning that we could test our models above this altitude up to the continuum limit.

An the beginning of the chapter, we have established a methodology to derive luminous efficiency and heat transfer coefficients used in heuristic models by

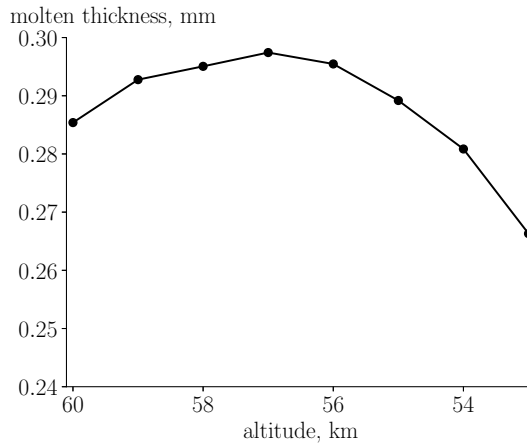
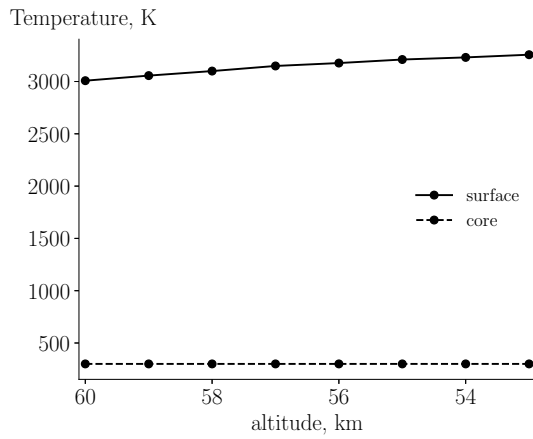


Figure 6.14.: Material molten thickness of the Lost City along the trajectory.

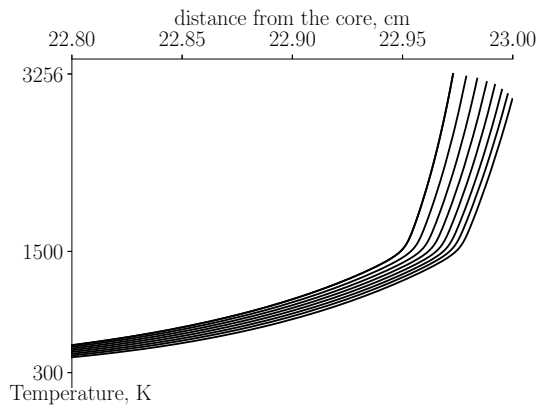
meteor astronomers. This method also allows one to simulate the corresponding spectrum observed by the ground spectrometers thanks to a detailed description of the flow field, which cannot be exploited by the single-body theory. We have noticed that the luminous efficiency depends on all of these parameters, and not only on the velocity as the classical theory typically assumes. The bolide size and altitude determine the shock layer radiative intensity and, consequently, the intensity of the luminosity. When we have applied this approach to the Lost City case, the results indicate a more prominent color index than the one inferred from observations. We believe that this discrepancy in the color index is due to the evaporation of droplets arising from the molten material.

At the end of the chapter, we couple the radiation/flow/material, and we analyze part of the Lost City trajectory. We have examined a much lower evaporation rate than the results shown in the first part for the same conditions, supporting the importance of material/flow coupling for this bolide. Moreover, the removal of the liquid layer is the dominant source of ablation for most of the trajectory. Additional processes might be missing from our analysis, such as the mass removal due to the inertial forces that might explain the small discrepancy between our findings and the observations. Nevertheless, these results support the conclusion made from the first part where we believe that the appearance of refractory elements is owed to the evaporation of droplets in the wake, also suggested by Borovička [37], Capek et al. [47], Girin [93]. It is essential to stress that for asteroid type bolides, the $\epsilon q_{\text{in}}^{\text{rad}}$ will be so large that the liquid layer might evaporate immediately without being removed. Although the vapor layer created in front of the surface shields the body from convective heating, the radiative heat flux drives the evaporation of the surface. The intense evaporation caused by radiative heating forms the vapor cloud observed during a fireball and bolide entry.

This chapter raises several questions and possible paths to better understand



(a) Surface and core temperature along the trajectory.



(b) Temperature profile along material for the different trajectory points.

Figure 6.15.: Material temperature of the Lost City.

the ablation of meteors. For instance, a multidimensional computational fluid dynamics (CFD) solver would be needed to study the effect of droplet evaporation on the wake. Nevertheless, the work developed in this chapter can be applied to deduce the composition and the bolide's size at a reasonable computational cost.

CHAPTER 7

Conclusions and Perspectives

The seeker after truth is not one who studies the writings of the ancients and, following his natural disposition, puts his trust in them, but rather the one who suspects his faith in them and questions what he gathers from them, the one who submits to argument and demonstration and not the sayings of human beings whose nature is fraught with all kinds of imperfection and deficiency. Thus the duty of the man who investigates the writings of scientists, if learning the truth is his goal, is to make himself an enemy of all that he reads, and, applying his mind to the core and margins of its content, attack it from every side. He should also suspect himself as he performs his critical examination of it, so that he may avoid falling into either prejudice or leniency.

— Ibn al-Haytham

For several decades, understanding the meteor phenomenon has been based on the correlation between observations and simplified models. However, these models lump most of the physics, disabling the detailed comprehension of the phenomenon. Interest in this problem has been growing substantially over the last ten years, especially after the Chelyabinsk event. This event raised awareness within the general population of the threat associated with asteroid entry. Since then, the scientific community is making an effort to improve the legacy models and to shift towards detailed simulations. It is a complex problem since it involves many of physical aspects, such as multi-phase and non-equilibrium flows. To date, the most detailed simulations either lack accurate physico-chemical models or do not address all the phenomena in meteoroid entry.

In this regard, we have identified two specific objectives at the beginning of the thesis. In the next section, we address the contributions to each objective and the limitations of the models developed. Afterward, we recommend some possible improvements to the models, as well as suggestions for future studies.

7.1. Contribution of this work

It is essential to recall that this work focus on a quasi-1D analysis of the flow. This analysis implies that the meteoroid has a perfectly spherical shape, and

it does not fragment. Moreover, we do not study the trail of the meteoroid. Finally, we only considered H5 chondrites and iron meteoroids, but in principle, our models can be extended to any other class of meteorites.

We recall that the meteor phenomenon involves a series of physical aspects. **Obj.1** is divided into sub-objectives, where we address the essential modeling features (evaporation, melting, and radiation). **Obj.2** is an overarching application of the models that can be used to interpret observations.

Development of the models to study the meteoroid thermal ablation in the continuum regime (Obj.1)

a) Derivation of evaporation & melting models to study the material ablation.

The accuracy of the ablation simulation (**evaporation & melting**) strongly relies on the gas-phase physico-chemical models. This aspect has been addressed in Chapter 2, where state-of-the-art thermodynamic, transport, kinetic, and energy transfer models for hypersonic flows have been presented. These models are implemented within the open-source MUTATION⁺⁺ library, and they are accessible to the community. As the main contribution of Chapter 2, we have integrated necessary data for metals such as Fe, Mg, Al, Na, Ca, K, Ti into the library. One contribution is the reduction of the atomic energy levels for metals, allowing for fast computation of the thermodynamic properties. It was essential to consider all levels in order to have an accurate evaluation of their thermodynamic properties. This reduction has proven to be useful since metallic species contain hundreds of electronic levels. Moreover, we have included collision integral data for the metallic species relevant to the calculation of transport properties. The review of the collision integral parameters was a complicated task due to the scarcity of data for the Lennard-Jones potential. The collected data in this thesis is an essential step for future meteor studies. This step will allow the community to build precise models based on high-fidelity data and algorithms relevant to hypersonic flows. Finally, in this chapter, we have presented a transfer of knowledge from well-established models developed for re-entry flows to meteor applications. Ultimately, these models have a substantial impact on the flow and ablation description of the meteor phenomenon.

The **evaporation models** have been addressed in Chapter 3. In this chapter, we have extended the chemical equilibrium models, typically utilized in the engineering community, to multiple evaporation elements. This is a significant improvement compared to the model developed by Milos and Chen [177], since they constrain the elemental evaporation hindering the volatilization. Although these models are widely used to design carbon-based ablators, they lose their purpose when applied to evaporation problems. Evaporation is intrinsically a non-equilibrium phenomenon. A significant contribution to this thesis is the development of chemical non-equilibrium evaporation models, which account for rarefied effects (translational non-equilibrium). This class of

models is more accurate than the equilibrium alternative since they evaluate the evaporation/condensation rate. We have shown that equilibrium models overestimate the evaporation rate substantially compared to non-equilibrium evaporation. Leveraging on the evaporation models established by the kinetic theory community, and starting from the work of Ytrehus and Østmo [279], we have built a kinetic-based model for multiple atomic species. This model considers the jump of thermodynamic properties across the Knudsen layer. We have compared the model outcome with a solution obtained by means of the Direct Simulation Monte Carlo (DSMC) method, an excellent agreement has been observed. Moreover, we have compared the developed model with the well-known Hertz-Knudsen theory – extensively used for evaporation problems – a significant deviation has been remarked. The kinetic-based model has shown a temperature jump to 30% between the surface and the edge of the Knudsen layer. This temperature jump might be significant for extreme meteoroid entry conditions where strong evaporation rates are expected. So far, this kinetic-based model is restricted to the evaporation of atoms. To extend this model to molecule evaporation, one would have to consider the departure from thermal equilibrium [85], i.e., a distinct Boltzmann distribution for each internal mode. This effect might lead to different internal temperatures at the edge of the Knudsen layer. Since the kinetic-based model is confined to atom evaporation, we have used the Hertz-Knudsen theory for the rest of the thesis. Finally, these evaporation models have been implemented into the MUTATION⁺⁺ library as an addition of the Gas-Surface Interaction (GSI) module designed by Bellas-Chatzigeorgis [19].

Chapter 4 focuses on the development of **melting models**. We have considered a single energy equation for both phases; i.e., the phase-transition is accounted for by regularizing the thermodynamic properties across the solid/liquid interface. This approach is called the enthalpy method, and it is widely employed in phase-transition problems. We have simulated the shear of the molten layer using Bethe and Adams [24] model as a starting point. The authors have only considered the shear ablation of glass, and we have extended it to the ablation at the stagnation point of any material type. Moreover, we have derived a shear ablation model able to describe the overall material degradation by averaging the aerodynamic forces along the surface. The underlying assumption behind this averaging procedure is due to the tumbling motion of the body, leading to uniform properties around the surface. We have developed this simplified model considering that it is quite challenging to study the material response for a full meteor trajectory with a 2-D Computational Fluid Dynamics (CFD) solver. This task becomes even more challenging if one considers coupled radiative transport. Nonetheless, we have made several assumptions on the model derivation that must be assessed by comparing it to a 2-D material melting analysis. The shear ablation model disregards the inertial terms in the momentum equation due to the low viscosity of the material. In the case of metals, the viscosity is several orders of magnitude higher than glass material; thus, neglecting the inertial terms might be a strong assumption. To assess this assumption, one would require a 2-D analysis where the momentum

equation is included. The main contribution of this chapter is the merging of the phase-transition and shear ablation model and its application to meteoroid ablation problems. The importance of devolving this model is twofold: i) recent ground experiments have shown the relevant material melting and removal of the molten layer ii) this phenomenon is poorly addressed in meteoroid ablation models. The meteorites collected from the ground show flow structures that derive from shear ablation. We have used this model to reproduce the Tamdakht H5 ordinary chondrite experiment carried out at NASA ARC [2]. In this simulation, we have used the evaporation model built in Chapter 3, and, we observed that its effect is negligible compared to the shear ablation process. It is worthwhile to mention that the developed melting model disregards any possible chemical reactions within the liquid phase. The reaction and diffusion of chemical species within this phase might lead to a different composition at the surface concerning the bulk material.

b) **Application of a radiation model which is computationally inexpensive and realistic for hypersonic flows.**

An accurate description of the radiative field is paramount for meteoroid entry modeling. At extreme entry conditions, the surface evaporation is mostly driven by radiative heating. Moreover, the luminosity observed during a meteor event is owed to the flow radiation. Simultaneously, coupling the flow field with thermal radiation is a complicated task due to the inherent high computation cost. Chapter 3 indicates the details on the **radiation model** utilized in this work. We leveraged the work by Soucasse et al. [238] and Scoggins [229] on flow/radiation/ablation coupling, applying the Hybrid Statistical Narrow-Band (HSNB) model to meteor applications. As the central development of this chapter, we have included the radiative properties of metallic atoms to the High Temperature Gas Radiation (HTGR) database. This model employs a hybrid spectral reduction, which allows for fast computation of the radiative flow field. The validity and accuracy of the HSNB model have been established in prior works such as Lamet et al. [140] and the previous references. In this chapter, we have used the model to assess the spectral features of flow simulation. This flow simulation had the objective to replicate the El Hammami H5 ordinary chondrite experiment, carried out at the von Karman Institute for fluid dynamics (VKI) Plasmatron. We have observed a good agreement between the numerical results and the experimental spectral data for the chondrite evaporation (**Obj.1a**) and the cork holder ablation. This result has given us confidence that the evaporation model is predictive to a certain extent. The poor spectral resolution combined with the strong emission of Na complicated the accurate description of this line intensity. The element Na is an essential chemical element in meteoroid ablation due to its intense radiation during flight. As a significant contribution, we have developed a consistent methodology to rebuild the high-enthalpy flow experiments with application to the Plasmatron facility. This methodology allowed us to compare the simulated spectral properties with the experimental data.

Design of a methodology to relate the models with meteor observations (Obj.2)

a) Comparison of the models with luminosity and dynamic mass observations.

In Chapter 6 we have employed the models developed in this thesis to analyze the Lost City bolide.

We have studied the **luminosity** of the bolide by coupling the flow, radiation (**Obj.1b**) and evaporation (**Obj.1a**). By just examining the flow around the object, we have obtained an excellent agreement with the observations carried out by McCrosky et al. [170] and presented in Ceplecha [53]. Within our simulations, we have considered photochemistry in the free stream due to precursor. For strong radiative fields at high altitudes, the precursor might lead to O_2 dissociation and ionization chemistry. This processes cause the departure between the translational-rotational and internal temperature. A contribution of the thesis was to devise a consistent energy source term due to the photodissociation process. This contribution has proven paramount for the modeling of the internal temperature at the free stream. To our best knowledge, the formulation of this source term is novel. We recall that our approach is limited to the simulation of the shock layer and ignores the wake modeling, which is an abundant luminosity source. According to our simulations, the boundary layer was mostly composed of SiO and Na, lacking the existence of refractory element Ca. However, in-depth spectral observations of different incidents [31, 37] have indicated the manifest presence of this element. On the other hand, ground experiments of Loehle et al. [151], Helber et al. [113], Agrawal et al. [2], and a detailed spectral analysis of Drouard et al. [76] have shown that the spectral intensity of Ca is orders of magnitude smaller than the volatile intensity, such as Na and K. We suspect that the measurement of Ca during the meteor event results from the evaporation of droplets sheared away from the main body.

This latter suggestion has driven the coupling between material and flow to quantify the mass loss due to shear ablation. We have correlated the overall mass loss, evaporation & shear ablation (**Obj.1a**), with **dynamic mass** observations. We recall that the typical meteoroid ablation model disregards the material degradation by shear ablation. This coupling is highly complex due to the rapid change of the flow conditions during flight. Therefore, we have focused on a small segment of the Lost City trajectory. We have obtained a fair comparison with the observations. Throughout our analysis, we have assumed that the body is tumbling, which leads to a uniform surface heat flux. Unfortunately, it is impossible to assess this hypothesis from the observations. If this latter inference is correct, then an additional mass loss term should be included, due to the inertial loads which we are not considering. Nevertheless, the outcome of our models has indicated that the shear ablation is prevalent for most of the trajectory studied. The evaporation rate has risen with lower altitude due to an increase in the radiative heating. These results also suggest that the evaporation is the dominant process for faster and more prominent objects, since the radiative heating is much larger, as shown in the work of

Johnston et al. [130] and Johnston and Stern [128].

b) **Derivation of the single-body theory coefficients from detailed simulations.**

Additionally, our models have enabled to **derive luminous efficiency and heat transfer coefficients** for H5 ordinary chondrites and iron meteoroids. We have computed similar heat transfer coefficients values similar to the ones reported by Johnston et al. [130] for the H5 ordinary chondrite. The fact that MUTATION⁺⁺ library centralizes algorithms and data allows studying the meteoroid entry with different compositions. Moreover, this library is flexible in the sense that it can be easily coupled to any CFD solver.

Finally, it is essential to mention that this coupling is novel in the community. Several attempts have been made in the past but never with such modeling detail. In this work, we could shift from the 0D correlations to predictive engineering models. Moreover, we paved the way for future studies, which might include fragmentation and spraying of the molten layer.

General remarks

In Table (1.3), we have highlighted some significant assumptions made throughout this thesis. These assumptions were necessary owing to the complexity of research milestones, mostly due to the multidisciplinary nature of the meteor phenomenon.

One of the difficulties encountered in this work was the lack of thermochemical data for the gas and material phases. Meteoroids are constituted of several chemical components that are not well characterized in the literature at these extreme conditions. One instance is the scarcity of chemical reaction rate coefficients at high temperatures, which can substantially affect the flow field. Another example is the absence of thermochemical properties for molten materials, which also impact the shear ablation process.

A proper multidimensional material solver would be ideal for studying the melting and the removal of the molten layer due to shear forces. Some efforts, not presented in the manuscript, were made to develop further the multiphase model in the high-order CFD platform Argo considering its capability to simulate the material and the flow in the same computational domain. The complexity to account for physical details such as species diffusion and real gas equation-of-state within the molten layer would require a dedicated thesis. This would allow for better understanding of differential ablation and improved insight into the elements depletion within the fusion crust.

In our multiphase model, we have assumed that the body is tumbling and rotating fast. This assumption is a necessary condition to have a uniform heat flux and molten layer, leading to the object's spherical recession. Although we enforce this condition, the mass loss due to the inertial forces and the molten layer's spraying has been ignored. These effects can be included in future research endeavors, in particular to understand the space-debris mitigation

process. One must also consider the potential consequences that the object rotation might have in the surrounding flow possibly affecting the surface forces.

Finally, the most consistent approach to validate the thermal ablation model is to have dedicated experiments for each physical aspect considered. For instance, one could study the evaporation of materials with a low sublimation point such as naphthalene or wax. To validate the melting model, one could test the melting and shear ablation of a flat plate made of low melting temperature material.

7.2. Future work and perspectives

The meteor phenomenon is an ideal candidate to develop basic research on the material response in a hypersonic flow. These natural flight experiments provide abundant observational data due to their frequent occurrence. Combining these data with the ground-experiments is an ideal validation tool for model improvement. The work established here benefits both from ground experiments carried out by engineers and observations obtained by astronomers. It gives a new perspective on the meteor phenomenon to both the meteor and aerospace community, opening a horizon of possible investigation paths in meteor physics and aerospace engineering.

Throughout the manuscript, we have highlighted the relevance of using accurate models to describe the meteor phenomenon, and have stressed the multi-physics inherent to this problem. We tackled the most important physical features, but we made several approximations due to the problem's complexity in this pursuit. In this work, we have studied different topics that can be broadened in the framework of doctoral work. We have focused on the continuum regime of the meteor entry, whereas the rarefied segment is another Ph.D. research conducted by Bariselli [16].

We propose a series of suggestions that can be employed in engineering applications and meteor physics. The material modeling of meteoroids is highly complex due to its composition. Meteoroids are formed by an oxide matrix and metallic bands of ferronickel and iron sulfide minerals. Recent microtomography analyses have shown the real-time decomposition of troilite (FeS) [107]. To analyze the material degradation with a dedicated material solver – such as Porous-material Analysis Toolbox based on OpenFOAM (PATO)[139], Argo [44, 116, 225] or ICARUS [227] – would allow the following: i) study the chemical reactions within the liquid layer; ii) understand the decomposition of metallic bands to infer on the differential ablation process.

An outcome of **Obj.2** was the plausible liquid fragmentation and spraying within the wake. The dynamics of liquid layers is a challenging problem to model. A possible path to tackle this problem is by solving both gas, liquid, and solid phases in a unified approach. Henneaux et al. [114] has shown some preliminary results towards that direction for space debris applications. This technique can be extended to study the shear ablation of meteoroids. Moreover, the spraying of particles in the combustion field is extensively studied using a

moment method of the Boltzmann equation [131]. This approach could also be utilized to analyze the liquid fragmentation within the meteor wake, which permits the refractory elements' comprehension.

Although the kinetic-based evaporation model developed in this thesis has shown promising outcomes, it only considers the evaporation of atomic species. Extending this model to molecules would allow us to understand the deviation of internal modes at the edge of the Knudsen layer. Some results have been obtained by Frezzotti [85] using the DSMC method, but this problem is still open regarding the moment method of the Boltzmann equation. This approach can also be broadened to study carbon-based ablatators, which is essential for Thermal Protection System (TPS) design.

The detailed models proposed in this section are not suitable to study meteoroid trajectories. Although they are rich in physics, their depth is a computational burden. Therefore, reduced models that retain high-fidelity physics and are computationally inexpensive should be sought. Lately, a significant focus has been given to Machine Learning (ML) and Uncertainty Quantification (UQ) methods to describe complex physical phenomena. Moreover, the models shown in this thesis rely on several uncertain parameters. UQ would allow us to do sensitivity analysis to understand the most critical parameters and perform Bayesian inference to deduce those parameters from observations.

This thesis's outcome can also be applied to study the space debris degradation in Earth's atmosphere. This topic has raised substantial awareness in the last decade. Future generations of satellites will have to follow strict design regulations to preserve the population on the ground. Moreover, we can employ the models developed in this thesis to detect the debris during their entry phase.

Outside the hypersonic space re-entry realm, the welding processes of the metallurgy industry could benefit from the models developed in this thesis. The melting and evaporation models could be applied to mitigate the defects, ensuring a longer material life. Another possible field is additive manufacturing, from which these models could be applied with the same purpose as the previous application. Additive manufacturing comprises different categories that focused on the manufacturing of metal components subjected to high heat fluxes, such as Powder Bed Fusion (PBF) and Directed Energy Deposition (DED).

Appendices

APPENDIX A

Physico-chemical properties

A.1. Chemical reactions

Table A.1.: Arrhenius parameters for the gas-phase chemical reactions, $k_r^f(T_r^f) = AT_f^\beta \exp(-\theta/T_r^f)$.

No.	Reaction	A m, s, mol	β	θ K	ref
<i>associative ionization</i> ($T_r^f = T, T_r^b = T^{\text{ve}}$)					
1.	$\text{N} + \text{O} \rightleftharpoons \text{NO}^+ + \text{e}^-$	5.30×10^6	0.00	31 900	1
2.	$\text{O} + \text{O} \rightleftharpoons \text{O}_2^+ + \text{e}^-$	7.10×10^{-4}	2.70	80 600	2
3.	$\text{N} + \text{N} \rightleftharpoons \text{N}_2^+ + \text{e}^-$	4.40×10^1	1.50	67 500	1
<i>charge exchange</i> ($T_r^f = T, T_r^b = T$)					
4.	$\text{NO}^+ + \text{O} \rightleftharpoons \text{N}^+ + \text{O}_2$	1.00×10^6	0.50	77 200	2
5.	$\text{N}^+ + \text{N}_2 \rightleftharpoons \text{N}_2^+ + \text{N}$	1.00×10^6	0.50	12 200	2
6.	$\text{O}_2^+ + \text{N} \rightleftharpoons \text{N}^+ + \text{O}_2$	8.70×10^7	0.14	28 600	2
7.	$\text{O}^+ + \text{NO} \rightleftharpoons \text{N}^+ + \text{O}_2$	1.40×10^{-1}	1.90	26 600	2
8.	$\text{O}_2^+ + \text{N}_2 \rightleftharpoons \text{N}_2^+ + \text{O}_2$	9.90×10^6	0.00	40 700	2
9.	$\text{O}_2^+ + \text{O} \rightleftharpoons \text{O}^+ + \text{O}_2$	4.00×10^6	0.09	18 000	2
10.	$\text{NO}^+ + \text{N} \rightleftharpoons \text{O}^+ + \text{N}_2$	3.40×10^7	-1.08	12 800	2
11.	$\text{NO}^+ + \text{O}_2 \rightleftharpoons \text{O}_2^+ + \text{NO}$	2.40×10^7	0.41	32 600	2
12.	$\text{NO}^+ + \text{O} \rightleftharpoons \text{O}_2^+ + \text{N}$	7.20×10^7	0.29	48 600	2
13.	$\text{O}^+ + \text{N}_2 \rightleftharpoons \text{N}_2^+ + \text{O}$	9.10×10^7	0.36	22 800	2
14.	$\text{NO}^+ + \text{N} \rightleftharpoons \text{N}_2^+ + \text{O}$	7.20×10^7	0.00	35 500	2
<i>electron impact dissociation</i> ($T_r^f = T^{\text{ve}}, T_r^b = T^{\text{ve}}$)					
15.	$\text{N}_2 + \text{e}^- \rightleftharpoons \text{N} + \text{N} + \text{e}^-$	3.00×10^{18}	-1.60	113 200	1
<i>heavy particle impact dissociation</i> ($T_r^f = \sqrt{TT^{\text{ve}}}, T_r^b = T$)					
16.	$\text{N}_2 + \text{M} \rightleftharpoons \text{N} + \text{N} + \text{M}$	7.00×10^{15}	-1.60	113 200	1
	M = N O	3.00×10^{16}			
17.	$\text{O}_2 + \text{M} \rightleftharpoons \text{O} + \text{O} + \text{M}$	2.00×10^{15}	-1.50	59 360	1
	M = N O	1.00×10^{16}			
18.	$\text{NO} + \text{M} \rightleftharpoons \text{N} + \text{O} + \text{M}$	5.00×10^9	0.00	75 500	1

Continued on next page

Table A.1 – *Continued from previous page*

No.	Reaction	A m, s, mol	β	θ K	ref
	M = N O NO	1.00×10^{11}			
19.	SiO + M \rightleftharpoons Si + O + M	4.00×10^8	0.00	95 600	3
20.	SiO ₂ + M \rightleftharpoons SiO + O + M	4.00×10^8	0.00	95 600	3
21.	CN + M \rightleftharpoons C + N + M	2.50×10^8	0.00	71 000	10
22.	CO ₂ + M \rightleftharpoons CO + O + M	6.90×10^{15}	-1.50	63 275	10
	M = C N O	1.40×10^{16}			
23.	CO + M \rightleftharpoons C + O + M	2.30×10^{14}	-1.00	129 000	10
	M = C N O	3.40×10^{14}			
	<i>exchange</i> ($T_r^f = T, T_r^b = T$)				
24.	NO + O \rightleftharpoons N + O ₂	8.40×10^6	0.00	19 400	1
25.	N ₂ + O \rightleftharpoons NO + N	5.70×10^6	0.42	42 938	1
26.	Si + NO \rightleftharpoons SiO + N	3.20×10^7	0.00	1775	4
27.	Si + O ₂ \rightleftharpoons SiO + O	2.10×10^9	-0.53	17	5
28.	Fe + O ₂ \rightleftharpoons FeO + O	1.3×10^8	0.0	10 200	6
29.	Mg + O ₂ \rightleftharpoons MgO + O	5.10×10^4	0.00	0	7
30.	NaO + O \rightleftharpoons Na + O ₂	2.20×10^8	0.00	0	8
31.	Ca + O ₂ \rightleftharpoons CaO + O	2.50×10^8	0.00	7250	9
32.	CO + C \rightleftharpoons C ₂ + O	2.00×10^{11}	-1.00	58 000	10
33.	CO + O \rightleftharpoons O ₂ + C	3.90×10^7	-0.18	69 200	10
34.	CO + N \rightleftharpoons CN + O	1.00×10^8	0.00	38 600	10
35.	N ₂ + C \rightleftharpoons CN + N	1.10×10^8	-0.11	23 200	10
36.	CN + O \rightleftharpoons NO + C	1.60×10^7	0.10	14 600	10
37.	CN + C \rightleftharpoons C ₂ + N	5.00×10^7	0.00	13 000	10
38.	CO ₂ + O \rightleftharpoons O ₂ + CO	2.10×10^7	0.00	27 800	10
	<i>electron impact ionization</i> ($T_r^f = T^{ve}, T_r^b = T^{ve}$)				
39.	O + e ⁻ \rightleftharpoons O ⁺ + e ⁻ + e ⁻	3.90×10^{27}	-3.78	158 500	1
40.	N + e ⁻ \rightleftharpoons N ⁺ + e ⁻ + e ⁻	2.50×10^{28}	-3.82	168 200	1
41.	Na + e ⁻ \rightleftharpoons Na ⁺ + e ⁻ + e ⁻	2.50×10^{13}	-0.82	59 600	3
42.	Fe + e ⁻ \rightleftharpoons Fe ⁺ + e ⁻ + e ⁻	2.50×10^{28}	-3.82	91 700	3
43.	Mg + e ⁻ \rightleftharpoons Mg ⁺ + e ⁻ + e ⁻	2.50×10^{28}	-3.82	88 700	3
44.	Ca + e ⁻ \rightleftharpoons Ca ⁺ + e ⁻ + e ⁻	2.50×10^{13}	-0.82	70 900	3
45.	Si + e ⁻ \rightleftharpoons Si ⁺ + e ⁻ + e ⁻	2.50×10^{28}	-3.82	94 600	3

References. (1) Park et al. [202]; (2) Park [197]; (3) Johnston and Stern [125]; (4) Mick et al. [174]; (5) Le Picard et al. [146] (6) Akhmadov et al. [3]; (7) Hodgson and Mackie [118]; (8) Plane and Husian [209]; (9) Kashireninov et al. [132]; (10) Olynyck et al. [187]

A.2. Transport properties

Table A.2.: Parameters of the Lennard-Jones potential for neutral-neutral interaction.

Species	Lennard-Jones			Polarizabilities	
	Parameters			α \AA^3	ref
	ε/k_b [K]	σ \AA	ref		
Fe	7556	2.467	1	8.40	5
FeO	150	4.436	1	9.17	6
Mg	1614	2.926	2	10.6	5
MgO	150	4.454	1	11.37	6
Si	3036	2.91	2	5.38	5
SiO	569	3.374	2	6.15	6
SiO ₂	2954	3.706	2	6.92	6
Na	1375	3.567	2	24.08	5
NaO	50	3.812	2	24.85	6
Ca	2954	4.517	1	22.8	5
CaO	100	4.650	1	23.57	6
K	850	4.250	1	43.4	5
N	119	2.98	3	1.10	7
N ₂	71.4	3.798	4	1.74	7
NO	91.0	3.599	4	1.70	7
O	70.0	2.660	3	0.80	7
O ₂	106.7	3.467	4	1.58	7

References. (1) McGee et al. [171]; (2) Svehla [245]; (3) Smith et al. [237]; (4) Park et al. [202]; (5) Lide [147]; (6) Lasaga and Cygan [144]; (7) Wright et al. [274]

A.3. Equilibrium vapor pressure

Table A.3.: Equilibrium vapor pressure fit, $p_{\text{vap},i}(T_w) = \exp(A - B/T_w)$.

No.	Reaction	A Pa	B Pa, K
<i>standard boundary condition</i>			
1.	$\text{MgO}(l) \rightleftharpoons \text{Mg}(g) + \text{O}(g)$	25.02	6.00×10^4
2.	$\text{MgO}(l) \rightleftharpoons \text{MgO}(g)$	28.28	7.38×10^4
3.	$\text{Na}_2\text{O}(l) \rightleftharpoons 2\text{Na}(g) + \text{O}(g)$	21.55	3.63×10^4
4.	$\text{SiO}_2(l) \rightleftharpoons \text{Si}(g) + 2\text{O}(g)$	31.17	1.06×10^5
5.	$\text{SiO}_2(l) \rightleftharpoons \text{SiO}(g) + \text{O}(g)$	31.21	6.72×10^4
6.	$\text{SiO}_2(l) \rightleftharpoons \text{SiO}_2(g)$	27.98	6.65×10^4
7.	$\text{FeO}(l) \rightleftharpoons \text{Fe}(g) + \text{O}(g)$	23.67	5.16×10^4
8.	$\text{FeO}(l) \rightleftharpoons \text{FeO}(g)$	22.8	5.15×10^4
9.	$\text{K}_2\text{O}(l) \rightleftharpoons 2\text{K}(g) + \text{O}(g)$	16.22	4.11×10^4
10.	$\text{CaO}(l) \rightleftharpoons \text{Ca}(g) + \text{O}(g)$	19.02	6.90×10^4
11.	$\text{CaO}(l) \rightleftharpoons \text{CaO}(g)$	22.71	8.18×10^4
<i>modified boundary condition</i>			
1.	$\text{MgO}(l) \rightleftharpoons \text{MgO}(g)$	26.28	5.23×10^4
2.	$\text{NaO}(l) \rightleftharpoons \text{NaO}(g)$ ¹	23.12	5.23×10^4
3.	$\text{SiO}_2(l) \rightleftharpoons \text{SiO}_2(g)$	26.74	5.23×10^4
4.	$\text{FeO}(l) \rightleftharpoons \text{FeO}(g)$	25.52	5.23×10^4
5.	$\text{KO}(l) \rightleftharpoons \text{KO}(g)$ ¹	21.05	5.23×10^4
6.	$\text{CaO}(l) \rightleftharpoons \text{CaO}(g)$	23.65	5.23×10^4

¹ For simplicity Na_2O and K_2O were replaced respectively by NaO and KO . This change has a small impact in the flow field because their concentration is much smaller than the other components (see Fig. (6.9d)).

A.4. Modified Steger-Warming scheme

The original Steger-Warming scheme is highly dissipative and gives a poor boundary layer resolution. Candler et al. [46] presents a less dissipative version of this scheme. The inviscid fluxes are approximated with the Modified Steger-Warming formulation,

$$\mathbf{F}_{i+\frac{1}{2}}^i = (\mathbf{R}\mathbf{\Lambda}^+\mathbf{L})_{i+\frac{1}{2}}\mathbf{U}_i + (\mathbf{R}\mathbf{\Lambda}^-\mathbf{L})_{i+\frac{1}{2}}\mathbf{U}_{i+1}. \quad (\text{A.1})$$

The main difference between the modified and the original Steger-Warming is that the former evaluates the eigenvalues and eigenvectors at the cell interface. Since $\mathbf{\Lambda}^\pm = 0.5(\mathbf{\Lambda} \pm |\mathbf{\Lambda}|)$ and $\mathbf{F} = \mathbf{A}\mathbf{U} = \mathbf{R}\mathbf{\Lambda}\mathbf{L}\mathbf{U}$, one can write Eq. (A.1) as

$$\mathbf{F}_{i+\frac{1}{2}}^i = \frac{1}{2} [\mathbf{F}^i(\mathbf{U}_{i+1}) + \mathbf{F}^i(\mathbf{U}_i)] - \frac{1}{2} |\mathbf{A}|(\mathbf{U})(\mathbf{U}_{i+1} - \mathbf{U}_i),$$

which is closely related to the Roe scheme in Eq. (2.52). The main difference is the how the properties are averaged at the interface. The Modified Steger-Warming suffers from the same issue as Roe for strong shock waves. One approach to resolve this issue is to switch into a more dissipative scheme at the shock location [46], i.e., to the standard Steger-Warming scheme. Therefore, we can write Eq. (A.1) as,

$$\mathbf{F}_{i+\frac{1}{2}}^i = (\mathbf{R}\mathbf{\Lambda}^+\mathbf{L})_+\mathbf{U}_i + (\mathbf{R}\mathbf{\Lambda}^-\mathbf{L})_-\mathbf{U}_{i+1},$$

where the conservative vector to evaluate the Jacobians is,

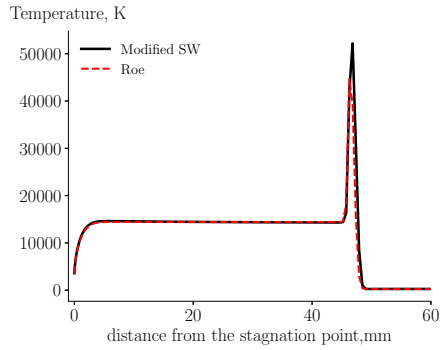
$$\begin{aligned} \mathbf{U}_+ &= \omega_{i+\frac{1}{2}}\mathbf{U}_i + (1 - \omega_{i+\frac{1}{2}})\mathbf{U}_{i+1}, \\ \mathbf{U}_- &= (1 - \omega_{i+\frac{1}{2}})\mathbf{U}_i + \omega_{i+\frac{1}{2}}\mathbf{U}_{i+1}. \end{aligned}$$

The weighting function $\omega_{i+\frac{1}{2}}$ adjusts the dissipation of the scheme based on the pressure gradient,

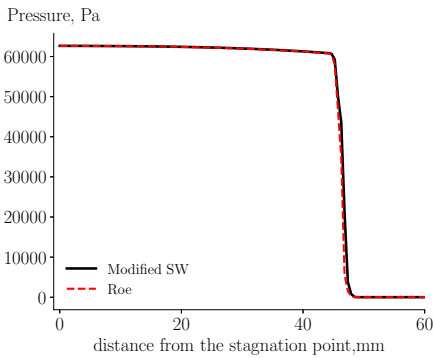
$$\omega_{i+\frac{1}{2}} = 1 - \frac{1}{2} \left(\frac{1}{(g\delta p)^2 + 1} \right), \text{ and } \delta p = \frac{p_{i+1} - p_i}{\min p_i, p_{i+1}}$$

where $0.5 \leq g \leq 5$ controls the sensitivity of the weighting function.

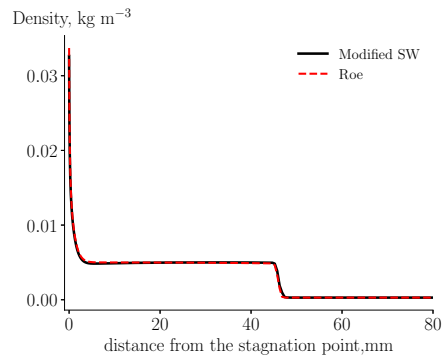
Figure (A.1) shows the comparison between the Modified Steger-Warming and Roe scheme, for the same test case in Section 2.5. We observe a difference at the shock location, which might be attributed to the extra dissipation added by the weighting function. Furthermore, a small difference in the boundary layer is observed, as shown in the boundary layer density, Fig. (A.1c). This difference results in a relative error $\delta \approx 17\%$ of the surface heat flux.



(a) Temperature profile along the stagnation streamline.



(b) Pressure profile along the stagnation streamline.



(c) Density profile along the stagnation streamline.

Figure A.1.: Comparison of the thermodynamic properties between Roe and Modified Steger-Warming scheme.

APPENDIX B

Melting properties

B.1. Verification of the material solver

We select two test cases to verify the material solver with known analytic solutions derived in cartesian coordinates. Although Section 4.2.1 can be solved either in spherical or cartesian coordinates, we are mostly interested in spherical bodies. Hence, we compare the numerical solution in spherical coordinates with the analytical by transforming $T_i^{\text{cart}} = r_i T_i^{\text{sph}}$, where the superscripts cart and sph represent the solution in cartesian and spherical coordinates, respectively. For simplicity, we drop the superscript since the following verification is made in cartesian coordinates; $\alpha = k/(\rho c_p)$ is the thermal diffusivity, T_s and T_0 are the surface and initial temperature, respectively.

The first case concerns the mesh movement due to surface recession. For a single phase, the analytical solution given by Bianchi [25], Turchi [254] is

$$\frac{(T - T_0)}{(T_s - T_0)} = \exp\left(\frac{-\dot{s}x}{\alpha}\right) \quad (\text{B.1})$$

where \dot{s} is the recession velocity and x_w coordinate is tied to the surface. As mentioned in Section 4.2.3, Bianchi [25], Chen and Milos [64] include a convective term in the heat equation to consider the conservation of energy in a moving reference frame. In our case, in between time-steps, the numerical domain is reduced, according to \dot{s} , and the numerical solution is mapped into the new domain. Figure (B.1) compares the analytical solution from Eq. (B.1) and the numerical solution obtained with the material solver. We obtain an excellent match between both solutions which gives us confidence that our approach is similar to Bianchi [25], Chen and Milos [64].

The analytical solution of the Stefan problem [51, 157], or the phase-change of a material, is given by,

$$T(x, t) = \begin{cases} T_{\text{solid}} = T_s - \frac{T_s - T_m}{\text{erf}(\lambda)} \text{erf}\left(\frac{x}{2\sqrt{\alpha_{\text{liquid}}t}}\right), & x < x^*(t), \\ T_{\text{liquid}} = T_0 + \frac{T_m - T_0}{\text{erfc}(\lambda\sqrt{\alpha_{\text{liquid}}/\alpha_{\text{solid}}})} \text{erfc}\left(\frac{x}{2\sqrt{\alpha_{\text{solid}}t}}\right), & x > x^*(t), \end{cases}$$

where x^* is the solid/liquid interface position, , and T_{solid} and T_{liquid} are the temperature field of the solid and liquid phase, respectively.

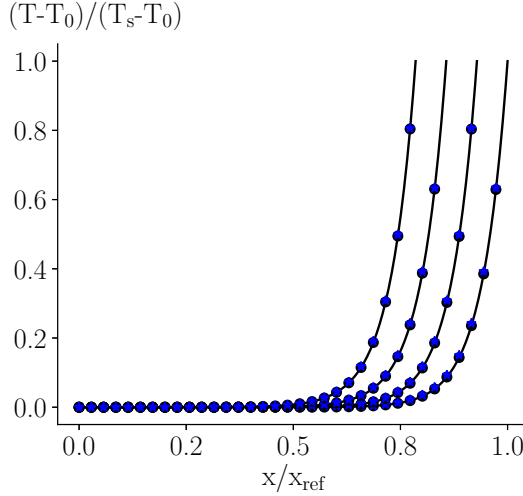


Figure B.1.: Comparison of the analytical (\bullet) and numerical ($-$) solution for the mesh movement due to surface recession.

Before solving the previous equation, one must estimate the location of the solid/liquid interface by solving the following non-linear equation,

$$\frac{\exp(-\lambda^2)}{\operatorname{erf}(\lambda)} - \frac{k_{\text{solid}}}{k_{\text{liquid}}} \sqrt{\frac{\alpha_{\text{liquid}}}{\alpha_{\text{solid}}}} \frac{(T_m - T_0)}{(T_s - T_m)} \frac{\exp(-\lambda^2 \alpha_{\text{liquid}}/\alpha_{\text{solid}})}{\operatorname{erfc}\left(\lambda \sqrt{\alpha_{\text{liquid}}/\alpha_{\text{solid}}}\right)} = \frac{\lambda L_m \sqrt{\pi}}{c_{p,\text{liquid}}(T_s - T_m)}$$

where $x^*(t) = 2\lambda\sqrt{\alpha_{\text{liquid}}t}$. Figure (B.2) compares the analytical and the numerical solution, where a good agreement is observed.

B.2. Stagnation-point formulation

This formulation concerns the recession only valid on the stagnation point. We choose a (x, y) reference frame based on the curvilinear coordinates for bodies of revolution which is related to the spherical coordinates (r, θ) by the transformation,

$$\begin{cases} y &= r - R, \\ x &= r\theta, \end{cases}$$

where the radius of revolution is equal to $r^* = r \sin \theta$.

At steady-state, the incompressible mass and momentum equations for axisymmetric bodies reads as,

$$\frac{\partial(r^* u_x)}{\partial x} + \frac{\partial(r^* u_y)}{\partial y} = 0. \quad (\text{B.2})$$

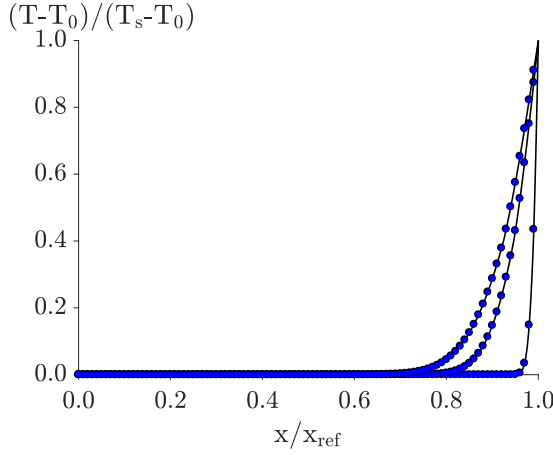


Figure B.2.: Comparison of the analytical (•) and numerical (-•) solution for the Stefan problem.

$$\rho u_x \frac{\partial u_x}{\partial x} + \rho u_y \frac{\partial u_x}{\partial y} = \frac{\partial}{\partial y} \left[\mu \frac{\partial u_x}{\partial y} \right] - \frac{\partial P}{\partial x}, \quad (\text{B.3})$$

and the boundary conditions are the following,

$$\begin{aligned} \text{at } y = 0: \quad & \mu \frac{\partial u_x}{\partial y} = \tau_w, \\ \text{at } y = -R: \quad & u_x = 0; \quad u_y = 0. \end{aligned}$$

Starting from Eq. (B.3),

$$\mu \frac{\partial u_x}{\partial y} = \frac{\partial P}{\partial x} \int_{-R}^y d\eta + C_1 \Leftrightarrow \mu \frac{\partial u_x}{\partial y} = \frac{\partial P}{\partial x} [\eta - (-R)] + C_1,$$

at $y = 0$,

$$\tau_w = -\frac{\partial P}{\partial x}(-R) + C_1,$$

hence,

$$\mu \frac{\partial u_x}{\partial y} = \frac{\partial P}{\partial x} y + \tau_w,$$

integrating once more,

$$u_x(x, y) = \tau_w(x) \int_{-R}^y \frac{d\eta}{\mu} + \frac{\partial P}{\partial x}(x) \int_{-R}^y \frac{\eta}{\mu} d\eta + C_2, \quad (\text{B.4})$$

since $u_x = 0$ at $y = -R$ then $C_2 = 0$.

From the Newtonian theory and the Reynolds analogy, quantities $\partial P/\partial x$ and

τ_w depend linearly on the x coordinate, thus we can write,

$$\begin{aligned}\tau_w &= \partial_x \tau_w x, \\ \left. \frac{\partial P}{\partial x} \right|_w &= \partial_{xx} P|_w x.\end{aligned}$$

Following the approach of [24], we neglected the inertial terms due to the viscosity of the liquid melt and integrating twice Eq. (B.3) from the center $-R$ to y we obtain Eq. (4.5),

$$u_x(x, y) = \left[\partial_x \tau_w \int_{-R}^y \frac{1}{\mu} d\eta + \partial_{xx} P|_w \int_{-R}^y \frac{\eta}{\mu} d\eta \right] x,$$

which is Eq. (4.5).

From Eq. (B.2),

$$u_y(x, y) = -\frac{1}{r^*} \int_{-R}^y \frac{\partial r^* u_x}{\partial x} dy, \quad (\text{B.5})$$

and considering that near the stagnation point the radius $r^* \rightarrow x$,

$$\begin{aligned}u_y(0, 0) &= \lim_{x \rightarrow 0} \left(-\frac{1}{x} \int_{-R}^0 \frac{\partial(x^2 \partial_x u_x)}{\partial x} dy \right) \\ &= -2 \int_{-R}^0 \partial_x u_x(y) dy.\end{aligned}$$

B.3. Average surface formulation

This appendix regards the derivation of the uniform recession along the entire surface based on average quantities. We recall our assumption of constant molten layer thickness around the surface, making viscosity only dependent on y , and this layer is removed at the shoulder of the sphere where $\theta = \pi/2$. Equation (4.5) can be averaged, over a length $\Delta x = \pi R/2$ using the following definition,

$$\overline{(\cdot)} \equiv \frac{1}{\Delta x} \int_0^{\Delta x} (\cdot) dx, \quad (\text{B.6})$$

and it becomes,

$$\overline{u_x(y)} = \overline{\tau_w} \int_{-R}^y \frac{1}{\mu} d\eta + \left. \frac{\partial \overline{P}}{\partial x} \right|_w \int_{-R}^y \frac{\eta}{\mu} d\eta. \quad (\text{B.7})$$

The conservation of fluxes in spherical coordinates writes as,

$$\rho_l \int_0^{2\pi} \int_0^R u_\theta|_{\theta=\frac{\pi}{2}} r \sin \frac{\pi}{2} dr d\phi = \rho_l \int_0^{2\pi} \int_0^{\frac{\pi}{2}} u_r|_{r=R} R^2 \sin \theta d\theta d\phi,$$

$$2\pi\rho_l \int_0^R u_\theta|_{\theta=\frac{\pi}{2}} r \, dr = 2\pi\rho_l \int_0^{\frac{\pi}{2}} u_r|_{r=R} R^2 \sin\theta \, d\theta. \quad (\text{B.8})$$

Since Eq. (B.7) is written in a different coordinate system the transformation $(x, y) \mapsto (r, \theta)$ is needed, giving to the following Jacobian of the transformation,

$$\mathbf{G} = \frac{\partial(x, y)}{\partial(r, \theta)} = \begin{pmatrix} \theta & r \\ 1 & 0 \end{pmatrix}, \quad \mathbf{G}^{-1} = \begin{pmatrix} 0 & 1 \\ 1/r & -\theta/r \end{pmatrix} \quad (\text{B.9})$$

which leads to the following transformation,

$$\begin{aligned} u_x &= r\omega_\theta + \theta u_r, \\ u_y &= u_r, \end{aligned}$$

note that $r\omega_\theta = u_\theta$ in $[\text{m s}^{-1}]$. This transformation of coordinates together with Eq. (B.2) retrieves exactly the mass equation in spherical coordinates. By inserting the velocity transformation in Eq. (B.8) one retrieves,

$$\int_{-R}^0 \left(u_x|_{\theta=\frac{\pi}{2}} - \frac{\pi}{2} u_r|_{\theta=\frac{\pi}{2}} \right) (y + R) \, dy = \int_0^{\frac{\pi}{2}} u_r|_{r=R} R^2 \sin\theta \, d\theta, \quad (\text{B.10})$$

Finally, one assumes that the radial velocity u_r is constant over the radius and one substitutes u_r and u_x by their average value,

$$\int_{-R}^0 \overline{u_x} (y + R) \, dy = \overline{u_r} \left(R^2 \int_0^{\frac{\pi}{2}} \sin\theta \, d\theta + \frac{\pi}{2} \int_{-R}^0 (y + R) \, dy \right). \quad (\text{B.11})$$

APPENDIX C

Radiation Properties

C.1. HTGR database

Table C.1.: A summary of the radiative mechanisms included in the High Temperature Gas Radiation (HTGR) database and used in this work. The first reference corresponds to the spectroscopic data while the second reference corresponds to the SNB parameters (when applicable). This table has been adapted from Scoggins [229].

Species	Process / Band System	Upper - Lower Electronic States	Spectral Range [1000 cm ⁻¹]	Ref.
C	Lines			(1)
	Bremsstrahlung		1 - 200	(1), (2)
	Photoionization		1 - 200	(1), (2)
C ⁺	Lines			(1)
	Bremsstrahlung		1 - 200	(1), (2)
	Photoionization		1 - 200	(1)
C ⁻	Photodetachment		1 - 200	(1), (2)
C ₂	Balik-Ramsay	$b^3\Sigma_g^- - a^3\Pi_u$	1 - 48	(1), (2)
	Deslandres-d'Azambuja	$C^1\Sigma_g - A^1\Pi_u$	1 - 42	(1), (2)
	Fox-Herzberg	$e^3\Sigma_g - a^3\Pi_u$	5 - 51	(1), (2)
	Mulliken	$D^1\Sigma_u^+ - X^1\Sigma_g^+$	28 - 77	(1), (2)
	Phillips	$A^1\Sigma_g - X^1\Sigma_g^+$	1 - 49	(1), (2)
	Swan	$d^3\Sigma_g - a^3\Pi_u$	1 - 43	(1), (2)
	Photoionization		1 - 200	(1), (2)
C ₃	Swings	$A^1\Pi_u - X^1\Sigma_g^+$	20 - 35	(3), (14)
	UV	$^1\Sigma_u^+ - X^1\Sigma_g^+$	30 - 74	(4), (14)
CH	AX	$A^2\Delta - X^2\Pi$	1 - 37	(5), (5)
	BX	$B^2\Sigma^- - X^2\Pi$	1 - 27	(5), (5)
	CX	$C^2\Sigma^+ - X^2\Pi$	1 - 40	(5), (5)
	Infrared	$X^2\Pi - X^2\Pi$	1 - 27	(5), (5)
	Photoionization		85 - 193	(6), (14)
CN	LeBlanc	$B^2\Sigma^+ - A^2\Pi_i$	1 - 54	(1), (2)
	Red	$A^2\Pi_i - X^2\Sigma^+$	1 - 58	(1), (2)
	Violet	$B^2\Sigma^+ - X^2\Sigma^+$	4 - 62	(1), (2)
	Photoionization		1 - 200	(1), (2)

Continued on next page

Table C.1 – *Continued from previous page*

Species	Process / Band System	Upper - Lower Electronic States	Spectral Range [1000 cm ⁻¹]	Ref.	
CO	Third positive	$b^3\Sigma_g^+ - a^3\Pi$	13 - 43	(1), (2)	
	Fourth positive	$A^1\Pi - X^1\Sigma^+$	11 - 90	(1), (2)	
	Hopfield-Birge	$B^1\Sigma^+ - X^1\Sigma^+$	14 - 91	(1), (2)	
	Infrared Photoionization	$X^1\Sigma^+ - X^1\Sigma^+$	1 - 77 1 - 200	(1), (2) (1), (2)	
CO ⁺	Baldet-Johnson	$B^2\Sigma^+ - A^2\Pi_i$		(1), (2)	
	Comet-tail	$A^2\Pi_i - X^2\Sigma^+$		(1), (2)	
	First negative	$B^2\Sigma^+ - X^2\Sigma^+$		(1), (2)	
CO ₂	Infrared	$X^1\Sigma_g^+ - X^1\Sigma_g^+$	0.25 - 8.3	(7), (8)	
H	Lines			(14)	
	Photoionization			(14)	
H ₂	Lyman	$B^1\Sigma - X^1\Sigma$	60 - 120	(9), (14)	
	Werner	$C^1\Pi - X^1\Sigma$	60 - 120	(9), (14)	
	Photoionization			(10), (14)	
N	Lines		1 - 200	(11)	
	Photoionization		1 - 200	(11), (12)	
	Bremsstrahlung		1 - 200	(11), (12)	
N ⁺	Lines		1 - 200	(11)	
	Bremsstrahlung		1 - 200	(11), (12)	
N ⁻	Photodetachment		1 - 200	(11), (12)	
N ₂	First positive	$B^3\Pi_g - A^3\Sigma_u^+$	1 - 42	(13), (12)	
	Second positive	$C^3\Pi_u - B^3\Pi_g$	1 - 40	(13), (12)	
	Birge-Hopfield 1	$b^1\Pi_u - X^1\Sigma_g^+$	55 - 117	(13), (12)	
	Birge-Hopfield 2	$b'^1\Sigma_u^+ - X^1\Sigma_g^+$	36 - 124	(13), (12)	
	Caroll-Yoshino	$c'_4^1\Sigma_u^+ - X^1\Sigma_g^+$	54 - 123	(13), (12)	
	Worley	$o_3^1\Pi_u - X^1\Sigma_g^+$	71 - 121	(13), (12)	
	Worley-Jenkins	$c_3^1\Pi_u - X^1\Sigma_g^+$	67 - 116	(13), (12)	
	Photoionization		1 - 200	(11), (12)	
	Bremsstrahlung		1 - 200	(11), (12)	
N ₂ ⁺	First negative	$B^2\Sigma_u^+ - X^2\Sigma_g^+$	1 - 42	(13), (12)	
	Second negative	$C^2\Sigma_u^+ - X^2\Sigma_g^+$	26 - 77	(13), (12)	
	Meinel	$A^2\Pi_u - X^2\Sigma_g^+$	1 - 49	(13), (12)	
NO	11 000 Å	$D^2\Sigma^+ - A^2\Sigma^+$	1 - 22	(13), (12)	
	β	$B^2\Pi_r - X^2\Pi_r$	7 - 74	(13), (12)	
	β'	$B'^2\Delta - X^2\Pi_r$	22 - 69	(13), (12)	
	δ	$C^2\Pi_r - X^2\Pi_r$	15 - 75	(13), (12)	
	ϵ	$D^2\Sigma^+ - X^2\Pi_r$	16 - 68	(13), (12)	
	γ	$A^2\Sigma^+ - X^2\Pi_r$	7 - 66	(13), (12)	
	γ'	$E^2\Sigma^+ - X^2\Pi_r$	23 - 73	(13), (12)	
	Infrared	$X^2\Pi_r - X^2\Pi_r$	1 - 37	(13), (12)	
	Photoionization		1 - 200	(11), (12)	
	O	Lines		1 - 200	(11)
		Photoionization		1 - 200	(11), (12)
Bremsstrahlung			1 - 200	(11), (12)	
O ⁺	Lines		1 - 200	(11)	
	Bremsstrahlung		1 - 200	(11), (12)	

Continued on next page

Table C.1 – *Continued from previous page*

Species	Process / Band System	Upper - Lower Electronic States	Spectral Range [1000 cm ⁻¹]	Ref.
O ⁻	Photodetachment		1 - 200	(11), (12)
O ₂	Schumann-Runge Photoionization Photodissociation (Schumann-Runge) Bremsstrahlung	$B^3\Sigma_u^- - X^3\Sigma_g^-$	14 - 60 1 - 200 1 - 200 1 - 200	(13), (12) (11), (12) (11), (12) (11), (12)
Na, Na ⁺ Fe, Fe ⁺ Si, Si ⁺ Mg, Mg ⁺ Ca, Ca ⁺ Al, Al ⁺ K, K ⁺ Cu, Cu ⁺ Ti, Ti ⁺	Lines		1 - 200	here
Na, Na ⁺ Si Mg Al	Photoionization		1 - 200	here

References. (1) Babou et al. [9]; (2) Depraz et al. [70]; (3) Cooper and Jones [66]; (4) Shinn [234]; (5) Soufiani et al. [240]; (6) Walker and Kelly [266]; (7) Tashkun and Perevalov [248]; (8) Rivière et al. [217]; (9) Prasanna et al. [213]; (10) Yan et al. [275]; (11) Chauveau et al. [62]; (12) Lamet et al. [140]; (13) Chauveau et al. [61]; (14) Scoggins [229]

C.2. Line broadening mechanisms

For atomic lines we have considered contributions from both Doppler and Lorentz broadening mechanisms.

C.2.1. Doppler broadening

Radiating atoms are assumed to have a Maxwellian velocity distribution, such that the Doppler line profile is Gaussian,

$$f_D(\sigma - \sigma_{ul}) = \sqrt{\frac{\ln 2}{\pi}} \frac{1}{\gamma_{ul}^D} \exp \left[- \ln 2 \left(\frac{\sigma - \sigma_{ul}}{\gamma_{ul}^D} \right)^2 \right], \quad (\text{C.1})$$

where the half width at half maximum (HWHM) γ_{ul}^D is expressed as

$$\gamma_{ul}^D = \sigma_{ul} \sqrt{\frac{2kT_r \ln 2}{m_r c^2}}, \quad (\text{C.2})$$

and T_r is the translational temperature of the radiator, and m_r its mass.

C.2.2. Collision broadening

Under the impact approximation, collisional broadening results in a Lorentzian distribution,

$$f_L(\sigma - \sigma_{ul}) = \frac{\gamma_{ul}^L}{\pi} \frac{1}{(\gamma_{ul}^L)^2 + (\sigma - \sigma_{ul})^2}, \quad (\text{C.3})$$

where the HWHM γ_{ul}^L is expressed as the sum of van der Waals, resonance, Stark broadening contributions,

$$\gamma_{ul}^L = \gamma_{ul}^{\text{vdw}} + \gamma_{ul}^{\text{res}} + \gamma_{ul}^{\text{stark}}. \quad (\text{C.4})$$

Each of these contributions are detailed in the following sections. All HWHM's are presented here in wavenumber units of cm^{-1} .

C.2.2.1. van der Waals broadening

Griem [99] provides the following expression for van der Waals broadening,

$$\gamma_{ul}^{\text{vdw}} = \frac{1}{2c} \sum_p N_p \langle v^{\frac{3}{5}} \rangle \left(\frac{9\pi\hbar^5 |\Delta\bar{r}^2|}{16m_e^3 E_p^2} \right)^{\frac{2}{5}}, \quad (\text{C.5})$$

where N_p is the number density of the neutral perturber p , E_p is the energy of the first excited state of the perturber which mainly determines its polarizability. $\Delta\bar{r}^2 = \bar{r}_u^2 - \bar{r}_l^2$ is the difference between the mean square radii of the radiating particle in the upper and lower transition levels, if the radiator and perturber are of different types. For identical particles, only the term \bar{r}^2 associated with the level u or l of the same parity as the radiator ground level is included in the above difference. In this case, the other level will contribute to the resonance broadening in the next section. The mean square radius of the radiator in a given state j is computed using the Bates-Dammgard approximation, such that

$$\bar{r}_j^2 = \frac{n_j^{*2}}{2} (5n_j^{*2} + 1 - 3l_j(l_j + 1)) \left[\frac{a_0}{1 + q_r/q_e} \right]^2, \quad (\text{C.6})$$

where n_j^* is the effective quantum number of the radiator in state j and l_j is the orbital electronic angular momentum quantum number relative to an outer electron for the j configuration. The effective quantum number is written as

$$n_j^{*2} = (Z + 1)^2 \frac{I_H}{E_{\text{ion}} - E_j}, \quad (\text{C.7})$$

where E_{ion} is the ionization energy of the radiator, E_j is the energy of the level j , and I_H is the Rydberg constant. The orbital angular momentum quantum number is pragmatically taken as

$$l_j = \min(L_j, \text{int}(n_j^*) + 1), \quad (\text{C.8})$$

where L_j is the electronic angular momentum quantum number relative to level j .

Finally, the bracket $\langle \cdot \rangle$ denotes the average of the quantity inside the brackets, weighted by the relative velocity distribution $f(v)$ of the perturbing species to the radiator. For a Maxwellian distribution at the translational temperature of the perturbing species T_p and mass m_p , an analytical solution is readily provided,

$$\langle v^n \rangle = \int_0^\infty v^n f(v) dv = \frac{(n+2)!}{2^{n+1} \{(\frac{1}{2}(n+2))!\}} \left(\frac{2kT_p}{m_p} \right)^{\frac{1}{2}n} \quad \forall n > -3. \quad (\text{C.9})$$

Prasanna [239] used a different formulation which may be written as

$$\gamma_{ul}^{\text{vdw}} = \frac{8.16}{4\pi c} \left(\frac{q_e^2 |\Delta r^2|}{2h\epsilon_0} \right)^{0.4} \left(\frac{8R_u}{\pi} \right)^{0.3} \sum_p N_p \alpha_p^{0.4} \left(\frac{T}{\mu_{ip}} \right)^{0.3}, \quad (\text{C.10})$$

where α_p is the polarizability of the neutral perturber p and μ_{ip} is the reduced molecular weight of the radiator and perturber. This formula has been used in this work in order to remain consistent with the work of Prasanna [239].

C.2.2.2. Resonance broadening

The usual expression of Griem [99] has been used to compute the resonance contribution to the half width, such that

$$\gamma_{ul}^{\text{res}} = \frac{3q_e^2}{16\pi^2 \epsilon_0 m_e c^2} \sum_j N_j \left(\sqrt{\frac{g_j}{g_u}} \left| \frac{f_{ju}}{\sigma_{uj}} \right| + \sqrt{\frac{g_j}{g_l}} \left| \frac{f_{jl}}{\sigma_{lj}} \right| \right), \quad (\text{C.11})$$

where the summation is over energy levels j of the radiator. Note that for a given level j , only one of the two terms inside the summation are non-zero, since the parities of states u and l differ.

C.2.2.3. Stark broadening

Since the mass of free electrons is substantially smaller than that of the radiating species considered, the impact approximation may be used, which assumes that radiator-electron collisions occur instantaneously, relative to the time between collisions. For collisions with ions, this theory may not be used. Instead, we have considered the quasi-static approximation. Thus, Stark contribution to the line broadening is divided into two components,

$$\gamma_{ul}^{\text{stark}} = \gamma_{ul}^{\text{stark,e}} + \gamma_{ul}^{\text{stark,ion}}, \quad (\text{C.12})$$

where $\gamma_{ul}^{\text{stark,e}}$ represents the contribution due collisions with electrons using the impact approximation and $\gamma_{ul}^{\text{stark,ion}}$ is the contribution from collisions with ions following the quasi-static approximation. Each contribution is described in the following sections.

Electron impact Stark broadening: Electron impact Stark broadening is computed following the impact approximation. For neutral radiators, the semi-empirical approach of Dimitrijević and Kršljanin [75] has been retained, where the HWHM is written as

$$\gamma_{ul}^{\text{stark,e}} = \frac{N_e}{4\pi c} \left(\frac{32}{27} \right)^{\frac{1}{2}} \left(\frac{ha_0}{m_e} \right) \left(\frac{I_H}{kT_e} \right)^{\frac{1}{2}} \left\{ \sum_j \overline{r_{uj}^2} f \left(\frac{|\Delta E_{uj}|}{3kT_e} \overline{r_{uj}} \right) + \sum_j \overline{r_{jl}^2} f \left(\frac{|\Delta E_{jl}|}{3kT_e} \overline{r_{jl}} \right) \right\}, \quad (\text{C.13})$$

where f is

$$f(x) = \exp(-1.33x) \ln \left(1 + \frac{2.27}{x} \right) + \frac{0.487x}{0.153 + x^{5/3}} + \frac{x}{7.93 + x^3}, \quad (\text{C.14})$$

and $\overline{r_{ij}^2}$ is

$$\overline{r_{ij}^2} = \frac{3I_H}{|\Delta E_{ij}|} \frac{g_j}{g_i} |f_{ij}|. \quad (\text{C.15})$$

For ion radiators, the semi-empirical method of Popovic has been used, where the HWHM is written as

$$\gamma_{ul}^{\text{stark,e}} = \frac{N_e h^2}{6\pi c m_e^2} \left(\frac{2m_e}{3\pi kT_e} \right)^{\frac{1}{2}} \left\{ \sum_j \overline{r_{uj}^2} g \left(\frac{3kT_e}{2\Delta E_{uj}} \right) + \sum_j \overline{r_{jl}^2} g \left(\frac{3kT_e}{2\Delta E_{lj}} \right) \right\}, \quad (\text{C.16})$$

where g is a gaunt factor.

Ion impact Stark broadening: The quasi-static approximation of Rivière [215] has been used to compute ion Stark broadening corrections, where the HWHM's for neutral radiators are given as

$$\gamma_{ul}^{\text{stark,ion}} = 1.75A(1 - 0.75r)\gamma_{ul}^{\text{stark,e}}, \quad (\text{C.17})$$

and for ion radiators as

$$\gamma_{ul}^{\text{stark,ion}} = 1.75A(1 - 1.2r)\gamma_{ul}^{\text{stark,e}}, \quad (\text{C.18})$$

where $\gamma_{ul}^{\text{stark,e}}$ is expressed in wavenumber, and

$$A = \left(\frac{|C_q| F_0^2}{hc\gamma_{ul}^{\text{stark,e}}} \right)^{\frac{3}{4}}, \quad (\text{C.19})$$

$$r = \frac{1}{b_D} \left(\frac{4\pi}{3} N_e \right)^{-\frac{1}{3}}, \quad (\text{C.20})$$

$$2C_q = 16\pi\epsilon_0 a_0^3 \left[\sum_j f_{uj} \left(\frac{I_H}{\Delta E_{uj}} \right)^2 - \sum_j f_{lj} \left(\frac{I_H}{\Delta E_{lj}} \right)^2 \right], \quad (\text{C.21})$$

$$F_0 = \left(\frac{4\pi}{3}\right)^{\frac{4}{3}} \frac{q_e}{4\pi\epsilon_0} N_e^{\frac{2}{3}}, \tag{C.22}$$

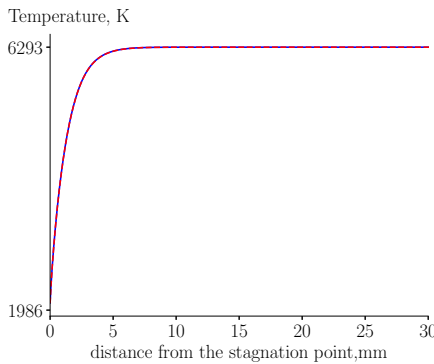
and b_D is the Debye radius, taken as

$$b_D = \sqrt{\frac{\epsilon_0 k T}{q_e^2 (N_e + \sum_j z_j^2 N_j)}}, \tag{C.23}$$

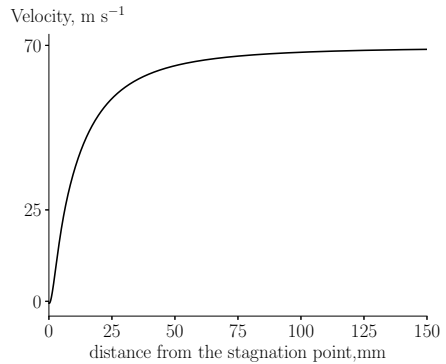
where z_j is the degree of ionization of heavy species j .

C.3. Comparison with Plasmatron for higher nitridation and oxidation probability

C.3.1. Flow field

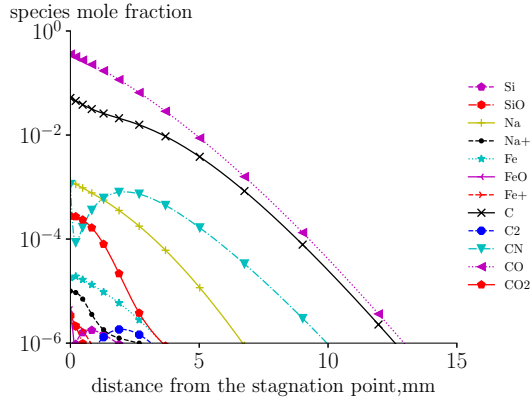


(a) Temperature profile: — T , - - - T^{ve} .

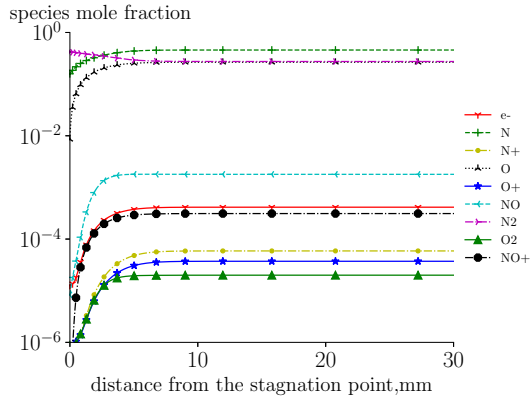


(b) Velocity profile.

C.3.2. Radiative field



(c) Species composition regarding the evaporation of the H5 sample and the ablation of the cork.



(d) Air species composition.

Figure C.1.: Flow field properties along the stagnation streamline at 6 s. The γ_N^{CN} and γ_O^{CO} are defined in Eq. (5.64) and Eq. (5.65), respectively.

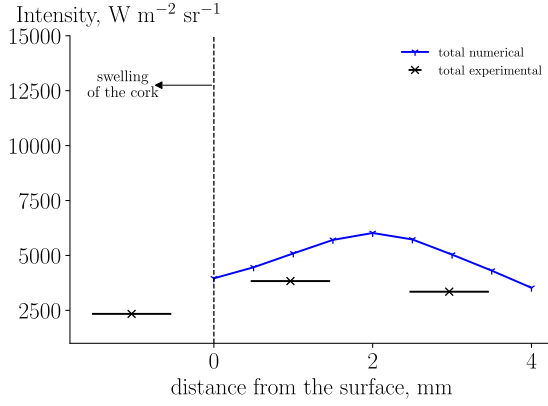
C.4. Filter

The luminosity equations:

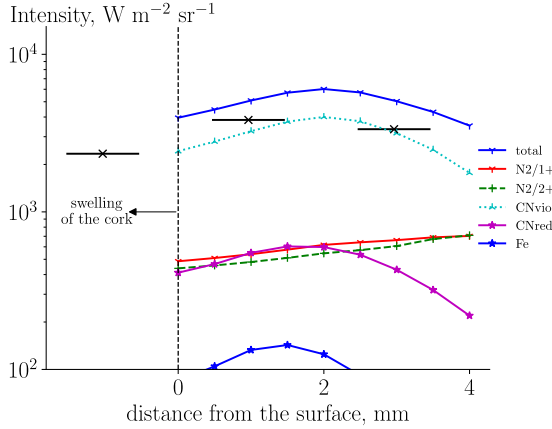
$$I_\alpha = 4\pi r^2 \int_0^\infty \alpha_\sigma \cdot I_\sigma d\sigma, \quad \alpha = T, V, B, R, \quad (C.24)$$

from which α_σ corresponds to the specific passband filter.

The term inside the integral of Eq. (C.26) can be written as a narrow-band



(a) Intensity based on the sum of all mechanism



(b) Intensity of the individual mechanism

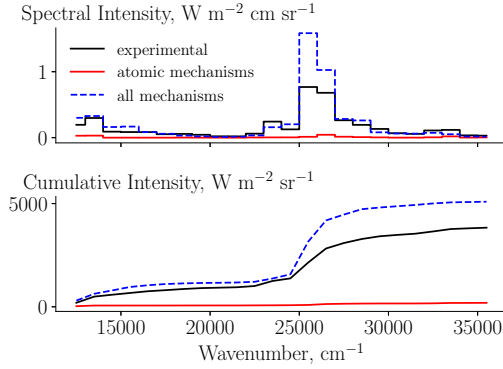
Figure C.2.: Comparison of the integrated intensity at different locations with the data recorded by the three spectrometers. The spectrometer data is represented by \times and the horizontal bar represents the error due to its location. The cork swelling is linearly interpolated from Fig. (5.17).

average following the definition:

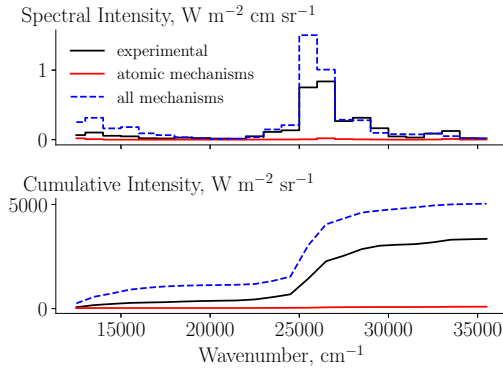
$$\overline{X}^{\Delta\sigma} \equiv \frac{1}{\Delta\sigma} \int_{\sigma_1}^{\sigma_2} X \Delta\sigma, \quad (\text{C.25})$$

such that Eq. (C.26) becomes

$$I_\alpha = 4\pi r^2 \sum_{\Delta\sigma} \overline{\alpha_\sigma I_\sigma}^{\Delta\sigma} \Delta\sigma, \quad \alpha = T, V, B, R. \quad (\text{C.26})$$



(a) Comparison of the intensity simulated at 1 mm from the surface with the middle spectrometer: (top) spectral and (bottom) cumulative intensity.



(b) Comparison of the intensity simulated at 3 mm from the surface with the furthest spectrometer: (top) spectral and (bottom) cumulative intensity.

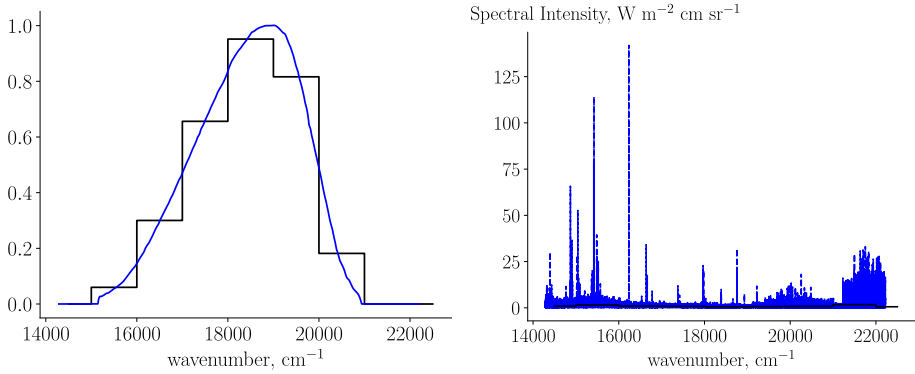
Figure C.3.: Comparison of the simulated intensity with the spectrometer data at a certain location.

In order to use the RTE solution from the SNB method, the following expression has to be verified:

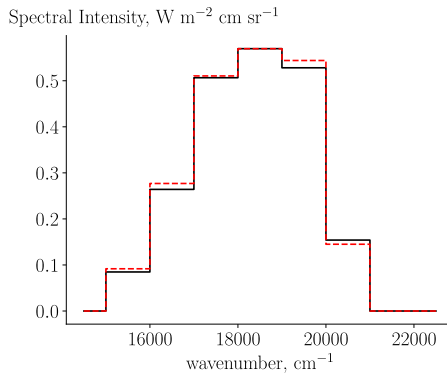
$$\overline{\alpha_\sigma I_\sigma}^{\Delta\sigma} \approx \overline{\alpha_\sigma}^{\Delta\sigma} \cdot \overline{I_\sigma}^{\Delta\sigma} \quad (\text{C.27})$$

and this separation is possible if the filter function α_σ is uncorrelated from the spectral intensity I_σ . To this end, we use the Specair library Laux [145] to generate a high-resolution spectrum with which to test Eq. (C.27). Figure (C.4a) shows the visible passband filter (taken from Bessell [22]) averaged

over a narrow band while Fig. (C.4b) shows the high-resolution spectral intensity and the corresponding narrow-band spectral intensity. Finally, Fig. (C.4c) shows both sides of Eq. (C.27).



(a) Filter function in the visible range (b) Spectral intensity for air computed taken from Bessell [22] and the corresponding narrowband average: — $\overline{V_\sigma}^{\Delta\sigma}$, narrowband average: — $\overline{I_\sigma}^{\Delta\sigma}$, - - - I_σ .
— V_σ .



(c) Narrowband spectral intensity in the visible range; comparison of both sides in Eq. (C.27): — $\overline{V_\sigma}^{\Delta\sigma} \cdot \overline{I_\sigma}^{\Delta\sigma}$, - - - $\overline{V_\sigma}^{\Delta\sigma} \cdot \overline{I_\sigma}^{\Delta\sigma}$.

Figure C.4.: Verification of the narrowband properties of the filtered spectral intensity.

The relative error between the two curves is approximately 1.5%, which leads us to conclude that the Eq. (C.27) conserves the luminosity equation. This verification is also applicable to the Eqs. (6.8) to (6.10).

Bibliography

- [1] M. C. Adams, W. Powers, and S. Georgiev. An experimental and theoretical study of quartz ablation at the stagnation point. *Journal of the Aerospace Sciences*, 27(7):535–543, 1960. doi:10.2514/8.8624. 86, 106
- [2] P. Agrawal, P. M. Jenniskens, E. Stern, J. Arnold, and Y.-K. Chen. Arcjet Ablation of Stony and Iron Meteorites. In *2018 Aerodynamic Measurement Technology and Ground Testing Conference*. Atlanta, Georgia, 2018. doi:10.2514/6.2018-4284. AIAA 2018-4284. 12, 13, 85, 86, 87, 93, 96, 98, 108, 192, 193
- [3] U. Akhmadov, I. Zaslanko, and V. Smirnov. Mechanism and kinetics of interaction of Fe, Cr, Mo, and Mn atoms with molecular oxygen. *Kinet. Catal. (Engl. Transl.); (United States)*, 29:2, 9 1988. 200
- [4] C. M. O. Alexander. Exploration of quantitative kinetic models for the evaporation of silicate melts in vacuum and in hydrogen. *Meteoritics & Planetary Science*, 36(2):255–283, 2001. doi:10.1111/j.1945-5100.2001.tb01870.x. 58, 143
- [5] C. Allen. *Allen's Astrophysical Quantities*. Springer New York, 2002. doi:10.1007/978-1-4612-1186-0. 162
- [6] T. Allison. JANAF Thermochemical Tables, NIST Standard Reference Database 13, 1996. 28
- [7] J. D. Anderson Jr. *Hypersonic and High-Temperature Gas Dynamics*. American Institute of Aeronautics and Astronautics, Inc., second edition, Jan. 2006. doi:10.2514/4.861956. 19, 140
- [8] E. Aursand and T. Ytrehus. Comparison of kinetic theory evaporation models for liquid thin-films. *International Journal of Multiphase Flow*, 116:67–79, jul 2019. doi:10.1016/j.ijmultiphaseflow.2019.04.007. 52, 71
- [9] Y. Babou, P. Rivière, M.-Y. Perrin, and A. Soufiani. Spectroscopic data for the prediction of radiative transfer in CO₂-N₂ plasmas. *Journal of Quantitative Spectroscopy and Radiative Transfer*, 110(1-2):89–108, jan 2009. doi:10.1016/j.jqsrt.2008.09.007. 118, 213
- [10] B. Baldwin and Y. Sheaffer. Ablation and breakup of large meteoroids during atmospheric entry. *Journal of Geophysical Research*, 76(19):4653–4668, 1971. doi:10.1029/JA076i019p04653. 9

- [11] B. S. Baldwin and H. J. Allen. A method for computing luminous efficiencies from meteor data. NASA-TN-D-4808, NASA Ames Research Center, Moffett Field, California, 1968. 90
- [12] P. Barbante. *Accurate and Efficient Modelling of High Temperature Nonequilibrium Air Flows*. PhD thesis, von Karman Institute for Fluid Dynamics & Université Libre de Bruxelles, 1997. 44, 70
- [13] P. Barbante and O. Chazot. Flight extrapolation of plasma wind tunnel stagnation region flowfield. *Journal of Thermophysics and Heat Transfer*, 20(3):493–499, Nov. 2006. doi:10.2514/1.17185. 139
- [14] P. Barbante, G. Degrez, and G. Sarma. Computation of nonequilibrium high temperature axisymmetric boundary-layer flows. *J. Thermophys. Heat Transfer*, 16(4):490–497, 2002. doi:10.2514/2.6723. 139
- [15] P. F. Barbante and T. E. Magin. Fundamentals of hypersonic flight - Properties of hightemperature gases. In *RTO AVT Course on Critical Technologies for Hypersonic Vehicle Development*, RTO-EN-AVT-116, pages 5–1 –5–50, Rhode-Saint-Genèse, Belgium, May 2004. 19
- [16] F. Bariselli. *Development of an Ablation Model for Rarefied Flows with Application to Meteoroid Entry*. PhD thesis, von Karman Institute for Fluid Dynamics & Vrije Universiteit Brussel, 2020. 11, 195
- [17] F. Bariselli, A. Frezzotti, A. Hubin, and T. E. Magin. Aerothermodynamic modelling of meteor entry flows. *Monthly Notices of the Royal Astronomical Society*, 492(2):2308–2325, dec 2019. doi:10.1093/mnras/stz3559. 11, 143
- [18] Belgian Institute for Space Aeronomy. BRAMS (Belgian RAdio Meteor Stations). <http://brams.aeronomie.be/pages/home>. 5
- [19] G. Bellas-Chatzigeorgis. *Development of advanced gas-surface interaction models for chemically reacting flows for re-entry conditions*. PhD thesis, von Karman Institute for Fluid Dynamics & Politecnico di Milano, 2018. 41, 144, 191
- [20] G. Bellas-Chatzigeorgis, P. F. Barbante, and T. E. Magin. Development of Detailed Chemistry Models for Boundary Layer Catalytic Recombination. In *Proceedings of 8th European Symposium on Aerothermodynamics for Space Vehicles*, Lisbon, Portugal, 2015.
- [21] G. Bellas-Chatzigeorgis, P. F. Barbante, and T. E. Magin. Energy accommodation coefficient calculation methodology using state-to-state catalysis applied to hypersonic flows. *AIAA Journal*, 58(1):278–290, jan 2020. doi:10.2514/1.J058543. 41, 54, 70
- [22] M. S. Bessell. UVBRI passbands. *Publications of the Astronomical Society of the Pacific*, 102:1181, oct 1990. doi:10.1086/132749. 162, 172, 220, 221

- [23] M. S. Bessell, F. Castelli, and B. Plez. Model atmospheres broad-band colors, bolometric corrections and temperature calibrations for O - M stars. *Astronomy & Astrophysics*, 333:231–250, May 1998. 162
- [24] H. Bethe and M. C. Adams. A Theory for the Ablation of Glassy Materials. *Journal of the Aerospace Sciences*, 26(6):321–328, 1959. doi:10.2514/8.8080. 86, 89, 96, 191, 208
- [25] D. Bianchi. *Modeling of Ablation Phenomena in Space Applications*. PhD thesis, Università degli Studi di Roma “La Sapienza”, 2007. 51, 55, 58, 60, 205
- [26] G. A. Bird. *Molecular gas dynamics and the direct simulation of gas flows*. Oxford, 1995. 70
- [27] J. Blazek. *Computational Fluid Dynamics: Principles and Applications*. Elsevier, 2015. ISBN 978-0-08-099995-1. doi:10.1016/c2013-0-19038-1. 44
- [28] M. Bond and H. Struchtrup. Mean evaporation and condensation coefficients based on energy dependent condensation probability. *Physical Review E*, 70(6), dec 2004. doi:10.1103/PhysRevE.70.061605. 52, 143
- [29] D. L. Bones, J. C. Gómez Martín, C. J. Empson, J. D. Carrillo Sánchez, A. D. James, T. P. Conroy, and J. M. C. Plane. A novel instrument to measure differential ablation of meteorite samples and proxies: The Meteoric Ablation Simulator (MASI). *Review of Scientific Instruments*, 87(9):094504, 2016. doi:10.1063/1.4962751. 13
- [30] J. Borovička. Line identifications in a fireball spectrum. *Astronomy & Astrophysics*, 103:83–96, 1994. 166, 177
- [31] J. Borovička and A. Berezhnoy. Radiation of molecules in Benešov bolide spectra. *Icarus*, 278:248–265, nov 2016. doi:10.1016/j.icarus.2016.06.022. 10, 193
- [32] J. Borovička and H. Betlem. Spectral analysis of two perseid meteors. *Planetary and Space Science*, 45(5):563 – 575, 1997. doi:10.1016/S0032-0633(97)00024-X. 10, 172, 176, 177
- [33] J. Borovička and P. Spurný. Radiation study of two very bright terrestrial bolides and an application to the comet s-19 collision with jupiter. *Icarus*, 121(2):484 – 510, 1996. doi:10.1006/icar.1996.0104. 141
- [34] J. Borovička, R. Stork, and J. Bocek. First results from video spectroscopy of 1998 leonid meteors. *Meteoritics & Planetary Science*, 34(6): 987–994, 1999. doi:10.1111/j.1945-5100.1999.tb01418.x. 4, 9
- [35] J. Borovička, P. Spurný, P. Brown, P. Wiegert, P. Kalenda, D. Clark, and L. Shrubený. The trajectory, structure and origin of the chelyabinsk asteroidal impactor. *Nature*, 503:235–237, 11 2013. doi:10.1038/nature12671. 4, 141

- [36] J. Borovička, P. Spurný, and P. Brown. Small near-earth asteroids as a source of meteorites. In *Asteroids IV*. University of Arizona Press, 2015. doi:10.2458/azu_uapress_9780816532131-ch014. 157
- [37] J. Borovička. A fireball spectrum analysis. *Astronomy & Astrophysics*, 279:627–645, Nov. 1993. 10, 166, 177, 185, 193
- [38] B. Bottin, O. Chazot, M. Carbonaro, V. van der Haegen, and S. Paris. The VKI Plasmatron Characteristics and Performance. In *RTO AVT Course on Measurement Techniques for High Enthalpy and Plasma Flows*, RTO EN-8, pages 6–01 – 6–26, Rhode-Saint-Genèse, Belgium, October 1999. 112, 131
- [39] K. J. Bowles and L. Rosenblum. Vapor pressure of sodium from 0.5 to 120 atmospheres. NASA-TN-D-2849, Lewis Research Center, Cleveland, Ohio, 1965. 56
- [40] I. Boyd. Computation of Atmospheric Entry Flow About a Leonid Meteoroid. *Earth, Moon and Planets*, 82-83(0):93–108, 2000. doi:10.2514/6.2000-583. 11
- [41] I. D. Boyd and T. E. Schwartzenruber. *Nonequilibrium Gas Dynamics and Molecular Simulation*. Cambridge Aerospace Series. Cambridge University Press, Cambridge, Apr. 2017. ISBN 9781139683494. doi:10.1017/9781139683494. 67, 71
- [42] V. A. Bronshten. *Physics of Meteoric Phenomena*. D. Reidel Pub. Co., 1983. 12, 86, 90, 91, 108, 162
- [43] P. G. Brown, J. D. Assink, L. Astiz, R. Blaauw, M. B. Boslough, J. Borovička, N. Brachet, D. Brown, M. Campbell-Brown, L. Ceranna, W. Cooke, C. de Groot-Hedlin, D. P. Drob, W. Edwards, L. G. Evers, M. Garces, J. Gill, M. Hedlin, A. Kingery, G. Laske, A. Le Pichon, P. Mialle, D. E. Moser, A. Saffer, E. Silber, P. Smets, R. E. Spalding, P. Spurný, E. Tagliaferri, D. Uren, R. J. Weryk, R. Whitaker, and Z. Krzeminski. A 500-kiloton airburst over Chelyabinsk and an enhanced hazard from small impactors. *Nature*, 503:238 EP –, 11 2013. doi:10.1038/nature12741. 4
- [44] J. S. Cagnone, K. Hillewaert, and N. Poletz. A discontinuous galerkin method for multiphysics welding simulations. In *Material Forming ESAFORM 2014*, volume 611 of *Key Engineering Materials*, pages 1319–1326. Trans Tech Publications Ltd, 7 2014. doi:10.4028/www.scientific.net/KEM.611-612.1319. 53, 86, 87, 195
- [45] M. Campbell-Brown, D. Koschny, J. Zender, and O. Witasse. Model of the Ablation of Faint Meteors. *Astronomy & Astrophysics*, 418(2): 751–758, 2004. doi:10.1051/0004-6361:20041001-1. 9, 85, 92

- [46] G. V. Candler, P. K. Subbareddy, and I. Nompelis. CFD Methods for Hypersonic Flows and Aerothermodynamics. In *Hypersonic Nonequilibrium Flows: Fundamentals and Recent Advances*, pages 203–237. American Institute of Aeronautics and Astronautics, Inc., jan 2015. doi:[10.2514/5.9781624103292.0203.0238](https://doi.org/10.2514/5.9781624103292.0203.0238). 203
- [47] D. Capek, P. Koteň, J. Borovička, V. Vojáček, P. Spurný, and R. Stork. Small iron meteoroids - observation and modeling of meteor light curves. *Astronomy & Astrophysics*, 625:A106, 2019. doi:[10.1051/0004-6361/201935203](https://doi.org/10.1051/0004-6361/201935203). 86, 110, 177, 185
- [48] M. Capitelli, C. Gorse, S. Longo, and D. Giordano. Collision Integrals of High-Temperature Air Species. *Journal of Thermophysics and Heat Transfer*, 14(2):259–268, 2000. doi:[10.2514/2.6517](https://doi.org/10.2514/2.6517). 32, 33
- [49] M. Capitelli, G. Colonna, and A. D’Angola. *Fundamental Aspects of Plasma Chemical Physics: Thermodynamics*. Springer Series on Atomic, Optical, and Plasma Physics 66. Springer-Verlag New York, 1 edition, 2012. ISBN 978-1-4419-8181-3,978-1-4419-8182-0. doi:[10.1007/978-1-4419-8182-0](https://doi.org/10.1007/978-1-4419-8182-0). 27
- [50] M. Capitelli, D. Bruno, and A. Laricchiuta. *Fundamental Aspects of Plasma Chemical Physics: Transport*, volume 74. Springer New York, 1 edition, 2013. ISBN 978-1-4419-8172-1. doi:[10.1007/978-1-4419-8172-1](https://doi.org/10.1007/978-1-4419-8172-1). 33
- [51] H. S. Carslaw and J. C. Jaeger. *Conduction of Heat in Solids*. Oxford Science Publications, 1959. 205
- [52] Z. Ceplecha. Geometric, dynamic, orbital and photometric data on meteoroids from photographic fireball networks. *Bulletin of the Astronomical Institutes of Czechoslovakia*, 38:222–234, July 1987. 163
- [53] Z. Ceplecha. Luminous efficiency based on photographic observations of the Lost City fireball and implications for the influx of interplanetary bodies onto Earth. *Astronomy & Astrophysics*, 311:329–332, July 1996. 10, 193
- [54] Z. Ceplecha and D. O. ReVelle. Fragmentation model of meteoroid motion, mass loss, and radiation in the atmosphere. *Meteoritics & Planetary Science*, 40(1):35–54, 2005. doi:[10.1111/j.1945-5100.2005.tb00363.x](https://doi.org/10.1111/j.1945-5100.2005.tb00363.x). 10, 157, 158, 172, 175, 182
- [55] Z. Ceplecha, J. Borovička, W. G. Elford, D. O. ReVelle, R. L. Hawkes, V. Porubčan, and M. Šimek. Meteor phenomena and bodies. *Space Science Reviews*, 84(3):327–471, Sep 1998. doi:[10.1023/A:1005069928850](https://doi.org/10.1023/A:1005069928850). 162, 164

- [56] Z. Ceplecha, J. Borovička, and P. Spurný. Dynamical behavior of meteoroids in the atmosphere derived from very precise photographic records. *Astronomy & Astrophysics*, 357:1115–1122, May 2000. 10
- [57] C. Cercignani. *Rarefied Gas Dynamics*. Cambridge Texts in Applied Mathematics, 2000. 51, 68
- [58] A. B. Chamberlain. <https://cneos.jpl.nasa.gov/fireballs/>, 2020. 5
- [59] L. H. Chambers. Predicting Radiative Heat Transfer in Thermochemical Nonequilibrium Flow Fields. NASA STI/Recon Technical Report N, Sept. 1994. 160
- [60] M. W. Chase, N. I. of Standards, and T. U. editors. *NIST-JANAF thermochemical tables*. American Chemical Society: American Institute of Physics for the National Institute of Standards and Technology, 4th edition, 1998. ISBN 1563968312. 28
- [61] S. Chauveau, M.-Y. Perrin, P. Rivière, and A. Soufiani. Contributions of diatomic molecular electronic systems to heated air radiation. *Journal of Quantitative Spectroscopy and Radiative Transfer*, 72(4):503–530, feb 2002. doi:10.1016/S0022-4073(01)00141-8. 118, 213
- [62] S. Chauveau, C. Deron, M.-Y. Perrin, P. Rivière, and A. Soufiani. Radiative transfer in LTE air plasmas for temperatures up to. *Journal of Quantitative Spectroscopy and Radiative Transfer*, 77(2):113–130, mar 2003. doi:10.1016/S0022-4073(02)00080-8. 118, 213
- [63] Y.-K. Chen and T. Gökçen. Implicit coupling approach for simulation of charring carbon ablaters. *Journal of Spacecraft and Rockets*, 51(3):779–788, may 2014. doi:<https://arc.aiaa.org/doi/10.2514/1.A32753>. 160
- [64] Y.-K. Chen and F. S. Milos. Two-dimensional implicit thermal response and ablation program for charring materials. *Journal of Spacecraft and Rockets*, 38(4):473–481, 2001. doi:10.2514/2.3724. 92, 205
- [65] Y.-K. Chen, E. C. Stern, and P. Agrawal. Thermal ablation simulations of quartz materials. *Journal of Spacecraft and Rockets*, 56(3):865–874, 2019. doi:10.2514/1.A34303. 51, 58, 86, 183
- [66] D. Cooper and J. Jones. An experimental determination of the cross section of the swings band system of C3. *Journal of Quantitative Spectroscopy and Radiative Transfer*, 22(2):201–208, aug 1979. doi:10.1016/0022-4073(79)90042-6. 213
- [67] W. Cunto, C. Mendoza, F. Ochsenbein, and C. J. Zeippen. Topbases at the cds. *Astronomy & Astrophysics*, 275, 1993. 127

- [68] G. Degrez, D. P. Vanden Abeele, P. F. Barbante, and B. Bottin. Numerical simulation of inductively coupled plasma flows under chemical non-equilibrium. *Int. J. Numer. Meth. Heat. Fluid Flow*, 14(4):538–558, 2004. doi:10.1108/09615530410532286. 139
- [69] W. Demtröder. *Atoms, Molecules and Photons – An Introduction to Atomic, Molecular and Quantum Physics*. Springer Berlin Heidelberg, 2010. ISBN 978-3-642-10298-1. doi:10.1007/978-3-642-10298-1. 25, 113, 114
- [70] S. Depraz, P. Rivière, M.-Y. Perrin, and A. Soufiani. Band Models for Radiative Transfer in Non-LTE Diatomic Molecules of CO₂-N₂ Plasmas. jan 2010. doi:10.1115/IHTC14-22301. 213
- [71] B. Dias, A. Turchi, and T. Magin. Stagnation-Line Simulations of Meteor Ablation. In *45th AIAA Thermophysics Conference*. Dallas, TX, 22-26 June 2015. doi:10.2514/6.2015-2349. AIAA 2015-2349. 41
- [72] B. Dias, F. Bariselli, A. Turchi, A. Frezzotti, P. Chatelain, and T. Magin. Development of a melting model for meteors. *AIP Conference Proceedings*, 1786(1):160004, 2016. doi:10.1063/1.4967661. 41, 55
- [73] B. Dias, J. B. Scoggins, and T. Magin. Shock layer radiation of an evaporating meteor. In *European Planetary Science Congress*, pages EPSC2018–495, Sept. 2018. 41
- [74] B. Dias, J. Scoggins, and T. E. Magin. Luminosity calculation of meteor entry based on detailed flow simulations in the continuum regime. *Astronomy & Astrophysics*, feb 2020. doi:10.1051/0004-6361/202037498. 41, 55
- [75] M. S. Dimitrijević and V. Kršljanin. Electron-impact shifts of ion lines: modified semiempirical approach. *Astronomy & Astrophysics*, 165:269–274, Sept. 1986. 216
- [76] A. Drouard, P. Vernazza, S. Loehle, J. Gattacceca, J. Vaubaillon, B. Zanda, M. Birlan, S. Bouley, F. Colas, M. Eberhart, T. Hermann, L. Jorda, C. Marmo, A. Meindl, R. Oefele, F. Zamkotsian, and F. Zander. Probing the use of spectroscopy to determine the meteoritic analogues of meteors. *Astronomy & Astrophysics*, 613:A54, may 2018. doi:10.1051/0004-6361/201732225. 180, 193
- [77] G. Duffa. *Ablative Thermal Protection Systems Modeling*. AIAA Education Series. AIAA (American Institute of Aeronautics & Ast), 2013. ISBN 1624101712,9781624101717. 60, 91
- [78] T. M. Erickson, C. L. Kirkland, N. E. Timms, A. J. Cavosie, and T. M. Davison. Precise radiometric age establishes Yarrabubba, Western Australia, as Earths oldest recognised meteorite impact structure. *Nature Communications*, 11(1), jan 2020. doi:10.1038/s41467-019-13985-7.

- [79] A. Faghri and Y. Zhang. Melting and Solidification. In *Transport Phenomena in Multiphase Systems*, pages 421 – 530. Elsevier Academic Press, 2006. ISBN 978-0-12-370610-2. 53, 88
- [80] B. Fegley and A. Cameron. A vaporization model for iron/silicate fractionation in the mercury protoplanet. *Earth and Planetary Science Letters*, 82(3):207 – 222, 1987. doi:10.1016/0012-821X(87)90196-8. 57
- [81] M. Ferus, J. Koukal, L. Lenža, J. Srba, P. Kubelík, V. Laitl, E. M. Zanozina, P. Vána, T. Kaiserová, A. Knížek, P. Rimmer, E. Chatzitheodoridis, and Civiš, S. Calibration-free quantitative elemental analysis of meteor plasma using reference laser-induced breakdown spectroscopy of meteorite samples. *Astronomy & Astrophysics*, 610:A73, 2018. doi:10.1051/0004-6361/201629950. 13
- [82] J. H. Ferziger and H. G. Kaper. *Mathematical Theory of Transport Processes in Gases*. North-Holland Publishing Company, 1972. 31
- [83] G. J. Flynn. *Extraterrestrial Dust in the Near-Earth Environment*, page 77. 2002. 1
- [84] A. Frezzotti. Kinetic Theory Description of the Evaporation of Multi-Component Substances. In *Rarefied Gas Dynamics: Proceedings of the 20th International Symposium*, 1996. 52, 70, 73, 83
- [85] A. Frezzotti. A numerical investigation of the steady evaporation of a polyatomic gas. *European Journal of Mechanics - B/Fluids*, 26(1):93–104, jan 2007. doi:doi:10.1016/j.euromechflu.2006.03.007. 52, 84, 191, 196
- [86] A. Frezzotti. Boundary conditions at the vapor-liquid interface. *Physics of Fluids*, 23(3):030609, mar 2011. doi:10.1063/1.3567001. 52
- [87] A. Frezzotti and P. Barbante. Kinetic theory aspects of non-equilibrium liquid-vapor flows. *Mechanical Engineering Reviews*, 4(2), 2017. doi:10.1299/mer.16-00540. 52, 59, 86
- [88] A. Frezzotti, L. Gibelli, and S. Lorenzani. Mean field kinetic theory description of evaporation of a fluid into vacuum. *Physics of Fluids*, 17(1):012102, 2005. doi:10.1063/1.1824111. 52, 71
- [89] A. Frezzotti, L. Gibelli, D. A. Lockerby, and J. E. Sprittles. Mean-field kinetic theory approach to evaporation of a binary liquid into vacuum. *Physical Review Fluids*, 3(5), may 2018. doi:10.1103/PhysRevFluids.3.054001. 52, 59, 65
- [90] FRIPON . Fireball Recovery and Planetary InterPlanetary Observation Network. <https://www.fripon.org/>. 5

- [91] Y. Furukawa, Y. Chikaraishi, N. Ohkouchi, N. O. Ogawa, D. P. Glavin, J. P. Dworkin, C. Abe, and T. Nakamura. Extraterrestrial ribose and other sugars in primitive meteorites. *Proceedings of the National Academy of Sciences*, 116(49):24440–24445, nov 2019. doi:[10.1073/pnas.1907169116](https://doi.org/10.1073/pnas.1907169116). 7
- [92] D. Giordano, J. K. Russell, and D. B. Dingwell. Viscosity of magmatic liquids: A model. *Earth and Planetary Science Letters*, 271(1):123 – 134, 2008. doi:[10.1016/j.epsl.2008.03.038](https://doi.org/10.1016/j.epsl.2008.03.038). 90
- [93] O. G. Girin. A hydrodynamic mechanism of meteor ablation - the melt-spraying model. *Astronomy & Astrophysics*, 606:A63, 2017. doi:[10.1051/0004-6361/201629560](https://doi.org/10.1051/0004-6361/201629560). 86, 110, 185
- [94] P. Gnoffo, R. Gupta, and J. Shinn. Conservation equations and physical models for hypersonic air flows in thermal and chemical nonequilibrium. Technical Paper 2867, NASA, 1989. 10, 21, 22, 30, 39
- [95] R. H. Goddard. Report Concerning Further Developments. Technical report, Smithsonian Institution Archives, Mar. 1920. 2, 4
- [96] A. P. Golub, I. B. Kosarev, I. V. Nemchinov, and V. V. Shuvalov. Emission and Ablation of a Large Meteoroid in the Course of Its Motion through the Earth’s Atmosphere. *Solar System Research*, 30:183, 1996. 11, 157
- [97] R. M. Goody and Y. L. Yung. *Atmospheric Radiation: Theoretical Basis*. Oxford Univ.Press, New York, 2nd edition edition, 1995. 115, 119, 120, 123
- [98] B. Graille, T. E. Magin, and M. Massot. Kinetic Theory of Plasmas: Translational Energy. *Mathematical Models and Methods in Applied Sciences*, 19(04):527–599, apr 2009. doi:[10.1142/S021820250900353X](https://doi.org/10.1142/S021820250900353X). 41
- [99] H. R. Griem. *Plasma spectroscopy*. Cambridge Monographs on Plasma Physics. McGraw-Hill Book Company, New York, 1964. doi:[10.1017/CB09780511524578](https://doi.org/10.1017/CB09780511524578). 214, 215
- [100] M. Gritsevich. Determination of parameters of meteor bodies based on flight observational data. *Advances in Space Research*, 44(3):323–334, aug 2009. doi:[10.1016/j.asr.2009.03.030](https://doi.org/10.1016/j.asr.2009.03.030). 9
- [101] M. Gritsevich and D. Koschny. Constraining the luminous efficiency of meteors. *Icarus*, 212(2):877 – 884, 2011. doi:[10.1016/j.icarus.2011.01.033](https://doi.org/10.1016/j.icarus.2011.01.033). 9
- [102] M. Gritsevich, V. Dmitriev, V. Vinnikov, D. Kuznetsova, V. Lupovka, J. Peltoniemi, S. Mönkölä, J. Brower, and Y. Popyrev. Constraining the Pre-atmospheric Parameters of Large Meteoroids: Košice, a Case Study. In J. M. Trigo-Rodríguez, M. Gritsevich, and H. Palme, editors,

- Assessment and Mitigation of Asteroid Impact Hazards*, pages 153–183, Cham, 2017. Springer International Publishing. ISBN 978-3-319-46179-3. 9, 182
- [103] M. I. Gritsevich. The Pribram, Lost City, Innisfree, and Neuschwanstein falls: An analysis of the atmospheric trajectories. *Solar System Research*, 42(5):372–390, sep 2008. doi:10.1134/s003809460805002x. 9
- [104] L. V. Gurvich, I. V. Veits, and C. B. Alcock. *Thermodynamics properties of individual substances. Volume 1 - Elements O, H/D, T/, F, Cl, Br, I, He, Ne, Ar, Kr, Xe, Rn, S, N, P, and their compounds. Part 1 - Methods and computation. Part 2 - Tables (4th revised and enlarged edition)*. 1989. 28
- [105] L. C. Hartung, R. A. Mitcheltree, and P. A. Gnoffo. Stagnation point nonequilibrium radiative heating and the influence of energy exchange models. *Journal of Thermophysics and Heat Transfer*, 6(3):412–418, 1992. doi:10.2514/3.376. 40
- [106] A. Hashimoto. Evaporation metamorphism in the early solar nebula. evaporation experiments on the melt FeO-MgO-SiO₂-CaO-al₂o₃ and chemical fractionations of primitive materials. *GEOCHEMICAL JOURNAL*, 17(3):111–145, 1983. doi:10.2343/geochemj.17.111. 143
- [107] J. B. Haskins, H. S. Barnard, B. Bessire, E. C. Stern, and F. Panerai. Micro-tomography and Modeling Based Reconstruction of the High Temperature Behavior of Meteoritic Material in Air: Implications for Entry. In *11th Ablation Workshop*. University of Minnesota, Sept. 2019. 195
- [108] J. B. Haskins, E. C. Stern, C. W. Bauschlicher, and J. W. Lawson. Thermodynamic and transport properties of meteor melt constituents from ab initio simulations: Mgsio 3, sio 2, and mgo. *Journal of Applied Physics*, 125(23):235102, 2019. doi:10.1063/1.5079418. 89, 110
- [109] J. Hastie and D. Bonnell. A predictive phase equilibrium model for multicomponent oxide mixtures, II. Oxides of Na-K-Ca-Mg-Al-Si. *High Temperature Science*, 19:275–306, 1985. doi:10.1016/0022-3093(86)90772-6. 57
- [110] B. Helber, C. O. Asma, Y. Babou, A. Hubin, O. Chazot, and T. E. Magin. Material response characterization of a low-density carbon composite ablator in high-enthalpy plasma flows. *J. Mater. Sci.*, 49(13):4530 – 4543, 2014. doi:10.1007/s10853-014-8153-z. 132
- [111] B. Helber, O. Chazot, A. Hubin, and T. Magin. Microstructure and gas-surface interaction studies of a low-density carbon-bonded carbon fiber composite in atmospheric entry plasmas. *Composites: Part A*, 72:96–107, 2015. doi:10.1016/j.compositesa.2015.02.004. 139

- [112] B. Helber, O. Chazot, A. Hubin, and T. E. Magin. Emission Spectroscopic Boundary Layer Investigation during Ablative Material Testing in Plasmatron. *J. Vis. Exp.*, 112(e53742), 2016. doi:10.3791/53742. 132
- [113] B. Helber, B. Dias, F. Bariselli, L. F. Zavalan, L. Pittarello, S. Goderis, B. Soens, S. J. McKibbin, P. Claeys, and T. E. Magin. Analysis of meteoroid ablation based on plasma wind-tunnel experiments, surface characterization, and numerical simulations. *The Astrophysical Journal*, 876(2):120, may 2019. doi:10.3847/1538-4357/ab16f0. 12, 13, 85, 131, 193
- [114] D. Henneaux, P. Schrooyen, B. Dias, A. Turchi, P. Chatelain, and T. Magin. Towards a High-Fidelity Multiphase Solver with Application to Space Debris Aerothermal Ablation Modeling. In *AIAA Aviation 2019 Forum*. American Institute of Aeronautics and Astronautics, jun 2019. doi:10.2514/6.2019-2876. 195
- [115] H. Hertz. Ueber die Verdunstung der Flüssigkeiten, insbesondere des Quecksilbers, im luftleeren Raume. *Annalen der Physik*, 253(10):177–193, 1882. doi:10.1002/andp.18822531002. 51, 68
- [116] K. Hillewaert. *Development of the discontinuous Galerkin method for high-resolution, large scale CFD and acoustics in industrial geometries*. PhD thesis, Université catholique de Louvain, 2013. 195
- [117] C. Hirsch. *Numerical Computation of Internal and External Flows: The Fundamental of Computational Fluid Dynamic*. Elsevier Science, 2007. 41
- [118] A. Hodgson and J. Mackie. A shock-tube study of the kinetics of evaporation and oxidation of magnesium. *Combustion and Flame*, 35:323 – 334, 1979. doi:10.1016/0010-2180(79)90037-3. 200
- [119] R. M. Howie, J. Paxman, P. A. Bland, M. C. Towner, M. Cupak, E. K. Sansom, and H. A. R. Devillepoix. How to build a continental scale fireball camera network. *Experimental Astronomy*, 43(3):237–266, Jun 2017. doi:10.1007/s10686-017-9532-7. 4, 9
- [120] P. M. Hull, A. Bornemann, D. E. Penman, M. J. Henehan, R. D. Norris, P. A. Wilson, P. Blum, L. Alegret, S. J. Batenburg, P. R. Bown, T. J. Bralower, C. Cournede, A. Deutsch, B. Donner, O. Friedrich, S. Jehle, H. Kim, D. Kroon, P. C. Lippert, D. Loroch, I. Moebius, K. Moriya, D. J. Peppe, G. E. Ravizza, U. Röhl, J. D. Schueth, J. Sepúlveda, P. F. Sexton, E. C. Sibert, K. K. Śliwińska, R. E. Summons, E. Thomas, T. Westerhold, J. H. Whiteside, T. Yamaguchi, and J. C. Zachos. On impact and volcanism across the Cretaceous-Paleogene boundary. *Science*, 367(6475): 266–272, jan 2020. doi:10.1126/science.aay5055. 14

- [121] L. G. Jacchia and F. L. Whipple. Precision Orbits of 413 Photographic Meteors. *Smithsonian Contributions to Astrophysics*, 4:97–129, Sept. 1961. doi:10.5479/si.00810231.4-4.97. 141, 172
- [122] E. Jarosewich. Chemical analyses of meteorites: A compilation of stony and iron meteorite analyses. *Meteoritics*, 25(4):323–337, 1990. doi:10.1111/j.1945-5100.1990.tb00717.x. 57, 133, 135
- [123] P. Jenniskens. Meteor induced chemistry, ablation products, and dust in the middle and upper atmosphere from optical spectroscopy of meteors. *Advances in Space Research*, 33(9):1444 – 1454, 2004. doi:10.1016/j.asr.2003.05.001. The Impact of Minor Bodies of Our Solar System on Planets and Their Middle and Upper Atmosphere. 11
- [124] P. Jenniskens. *Meteor Showers and their Parent Comets*. Cambridge University Press, 2006. doi:10.1017/cbo9781316257104. 1, 2
- [125] C. Johnston and E. Stern. Influence of Coupled Radiation and Ablation on Meteor Entries. In *47th AIAA Thermophysics Conference*,. Denver, Colorado, 2017. doi:10.2514/6.2017-4533. AIAA 2017-4533. 106, 200
- [126] C. O. Johnston. *Nonequilibrium Shock-Layer Radiative Heating for Earth and Titan Entry*. PhD thesis, Virginia Polytechnic Institute and State University, 2006. 127
- [127] C. O. Johnston. Improved Exponential Integral Approximation for Tangent-Slab Radiation Transport. *Journal of Thermophysics and Heat Transfer*, 24(3):659–661, jul 2010. doi:10.2514/1.46197. 129
- [128] C. O. Johnston and E. C. Stern. A model for thermal radiation from the tunguska airburst. *Icarus*, 327:48–59, jul 2019. doi:10.1016/j.icarus.2019.01.028. 157, 177, 194
- [129] C. O. Johnston, B. R. Hollis, and K. Sutton. Spectrum Modeling for Air Shock-Layer Radiation at Lunar-Return Conditions. *Journal of Spacecraft and Rockets*, 45(5):865–878, sep 2008. doi:10.2514/1.33004. 120
- [130] C. O. Johnston, E. C. Stern, and L. F. Wheeler. Radiative heating of large meteoroids during atmospheric entry. *Icarus*, 309:25 – 44, 2018. doi:10.1016/j.icarus.2018.02.026. 11, 51, 58, 85, 129, 157, 175, 194
- [131] D. Kah, F. Laurent, M. Massot, and S. Jay. A high order moment method simulating evaporation and advection of a polydisperse liquid spray. *Journal of Computational Physics*, 231(2):394–422, jan 2012. doi:10.1016/j.jcp.2011.08.032. 196
- [132] O. Kashireninov, V. Kuznetsov, and G. Manelis. Kinetics of alkaline-earth atoms reactions with molecular oxygen. *AIAA Journal*, 15(7):1035–1037, 1977. doi:10.2514/3.60746. 200

- [133] K. Kitamura and E. Shima. Towards shock-stable and accurate hypersonic heating computations: A new pressure flux for ausm-family schemes. *Journal of Computational Physics*, 245:62 – 83, 2013. doi:[10.1016/j.jcp.2013.02.046](https://doi.org/10.1016/j.jcp.2013.02.046). 44, 45, 158
- [134] A. Klomfass and S. Muller. A Quasi-One Dimensional Approach for Hypersonic Stagnation-Point Flows. Technical report, RWTH Aachen, 2000. 21
- [135] M. Knudsen. *Die maximale Verdampfungsgeschwindigkeit des Quecksilbers*, volume 352. Wiley, 1915. doi:[10.1002/andp.19153521306](https://doi.org/10.1002/andp.19153521306). 51, 68
- [136] A. F. Kolesnikov. Conditions of Simulation of Stagnation Point Heat Transfer from a High-enthalpy Flow. *Fluid Dyn.*, 28(1):131–137, 1993. doi:[10.1007/BF01055676](https://doi.org/10.1007/BF01055676). 139
- [137] M. Kon, K. Kobayashi, and M. Watanabe. Molecular simulation of evaporation mass flux during net evaporation/condensation. 2016. doi:[doi:10.1063/1.4967621](https://doi.org/10.1063/1.4967621). 52, 143
- [138] A. Kramida and Y. Ralchenko. NIST Atomic Spectra Database, NIST Standard Reference Database 78, <https://www.nist.gov/pml/atomic-spectra-database>, 1999. 27, 28, 29, 128
- [139] J. Lachaud and N. N. Mansour. Porous-material analysis toolbox based on OpenFOAM and applications. *Journal of Thermophysics and Heat Transfer*, 28(2):191–202, apr 2014. doi:[10.2514/1.T4262](https://doi.org/10.2514/1.T4262). 61, 195
- [140] J. Lamet, P. Rivière, M. Perrin, and A. Soufiani. Narrow-band model for nonequilibrium air plasma radiation. *Journal of Quantitative Spectroscopy and Radiative Transfer*, 111(1):87–104, 2010. doi:[10.1016/j.jqsrt.2009.07.010](https://doi.org/10.1016/j.jqsrt.2009.07.010). 112, 120, 121, 123, 125, 127, 192, 213
- [141] J.-M. Lamet. *Transferts radiatifs dans les écoulements hypersoniques de rentrée atmosphérique terrestre*. PhD thesis, Ecole Centrale Paris, 2009. 123, 125
- [142] J.-M. Lamet, Y. Babou, P. Rivière, M.-Y. Perrin, and A. Soufiani. Radiative transfer in gases under thermal and chemical nonequilibrium conditions: Application to earth atmospheric re-entry. *Journal of Quantitative Spectroscopy and Radiative Transfer*, 109(2):235–244, jan 2008. doi:[10.1016/j.jqsrt.2007.08.026](https://doi.org/10.1016/j.jqsrt.2007.08.026). 116
- [143] H. Lamy, S. Ranvier, J. Keyser, E. Gamby, and S. Calders. BRAMS: The Belgian RADio Meteor Stations. *Meteoroids Conference Proceedings*, NASA/CP–2011–216469:351–356, 2011. doi:[10.1109/URSIGASS.2011.6050925](https://doi.org/10.1109/URSIGASS.2011.6050925). 9

- [144] A. C. Lasaga and R. T. Cygan. Electronic and ionic polarizabilities of silicate minerals. *American Mineralogist*, 67(3-4):328–334, 04 1982. 201
- [145] C. Laux. Radiation and Nonequilibrium Collisional-Radiative Models. In Fletcher, D., Charbonnier, J.M., Sarma, G.S.R., and Magin, T., editor, *Physico-Chemical Modeling of High Enthalpy and Plasma Flows*, VKI LS 2002-07, Rhode-Saint-Genèse, Belgium, 2002. von Karman Institute for Fluid Dynamics. 220, 221
- [146] S. D. Le Picard, A. Canosa, D. Reignier, and T. Stoecklin. A comparative study of the reactivity of the silicon atom si(3p) towards o₂ and no molecules at very low temperature. *Phys. Chem. Chem. Phys.*, 4:3659–3664, 2002. doi:10.1039/B201374F. 200
- [147] D. R. Lide, editor. *CRC Handbook of Chemistry and Physics*. CRC Press LLC Boca Raton., 84th edition, 2004. ISBN 0-8493-0484-9. 201
- [148] M.-S. Liou. A sequel to AUSM, part II: AUSM⁺-up for all speeds. *Journal of Computational Physics*, 214(1):137–170, may 2006. doi:10.1016/j.jcp.2005.09.020. 44
- [149] M.-S. Liou and B. van Leer. Choice of implicit and explicit operators for the upwind differencing method. jan 1988. doi:10.2514/6.1988-624. 42
- [150] S. Loehle, P. Jenniskens, H. Böhrk, T. Bauer, H. Elsäßer, D. W. Sears, M. E. Zolensky, and M. H. Shaddad. Thermophysical properties of almahata sitta meteorites (asteroid 2008 TC3) for high-fidelity entry modeling. *Meteoritics & Planetary Science*, 52(2):197–205, nov 2016. doi:doi:10.1111/maps.12788. 100
- [151] S. Loehle, F. Zander, T. Hermann, M. Eberhart, A. Meindl, R. Oefele, J. Vaubaillon, F. Colas, P. Vernazza, A. Drouard, and J. Gattacceca. Experimental simulation of meteorite ablation during earth entry using a plasma wind tunnel. *The Astrophysical Journal*, 837(2):112, mar 2017. doi:10.3847/1538-4357/aa5cb5. 12, 13, 85, 133, 137, 155, 193
- [152] G. M. Longo and S. Longo. Theoretical analysis of the atmospheric entry of sub-mm meteoroids of Mg x Ca_{1-x}CO₃ composition. *Icarus*, 310:194–202, aug 2018. doi:10.1016/j.icarus.2017.12.001. 2
- [153] G. M. Longo, V. Laporta, and S. Longo. New insights on prebiotic chemistry from plasma kinetics. *arXiv:1912.00647 [physics.plasm-ph]*, 2019. URL <https://arxiv.org/abs/1912.00647>. 2
- [154] B. Lopez, M. Perrin, Ph. Rivière, and A. Soufiani. Coupled nonequilibrium flowfield-radiative transfer calculation behind a shock wave. *Journal of Thermophysics and Heat Transfer*, 27(3):404–413, 2013. doi:10.2514/1.T3972. 129

- [155] S. G. Love and D. E. Brownlee. A direct measurement of the terrestrial mass accretion rate of cosmic dust. *Science*, 262(5113):550–553, 1993. doi:[10.1126/science.262.5133.550](https://doi.org/10.1126/science.262.5133.550). 140
- [156] C. B. Ludwig, W. Malkmus, J. E. Reardon, J. A. L. Thomson, and R. Goulard. *Handbook of Infrared Radiation from Combustion Gases*. NASA SP-3080, volume 3080. 1973. 123
- [157] V. Lunardini. *Heat transfer with freezing and thawing*. Elsevier Distributors for the United States, Elsevier Science Pub. Co, Amsterdam New York New York, NY, U.S.A, 1991. ISBN 9780444599575. 205
- [158] J. M. Madiedo, J. M. Trigo-Rodríguez, N. Konovalova, J. L. Ortiz, A. J. Castro-Tirado, J. Alonso-Azcárate, J. Lacruz, and J. Cabrera-Caño. Orbit, emission spectrum, and photometric analysis of two flickering sporadic fireballs. *Astronomy & Astrophysics*, 555:A149, jul 2013. doi:[10.1051/0004-6361/201321751](https://doi.org/10.1051/0004-6361/201321751). 10
- [159] J. M. Madiedo, J. M. Trigo-Rodríguez, J. L. Ortiz, A. J. Castro-Tirado, S. Pastor, J. A. de los Reyes, and J. Cabrera-Caño. Spectroscopy and orbital analysis of bright bolides observed over the Iberian Peninsula from 2010 to 2012. *Monthly Notices of the Royal Astronomical Society*, 435(3):2023–2032, 09 2013. doi:[10.1093/mnras/stt1418](https://doi.org/10.1093/mnras/stt1418). 10
- [160] T. E. Magin. *A Model for Inductive Plasma Wind Tunnels*. PhD thesis, von Karman Institute for Fluid Dynamics & Université Libre de Bruxelles, 2004. 23, 31, 32, 33, 34, 36, 139
- [161] T. E. Magin and G. Degrez. Transport algorithms for partially ionized and unmagnetized plasmas. *Journal of Computational Physics*, 198:424–449, 2004. doi:[10.1016/j.jcp.2004.01.012](https://doi.org/10.1016/j.jcp.2004.01.012). 31, 34, 37
- [162] T. E. Magin and G. Degrez. Transport properties of partially ionized and unmagnetized plasmas. *Physical Review E*, 70(4), oct 2004. doi:[10.1103/physreve.70.046412](https://doi.org/10.1103/physreve.70.046412). 31, 34
- [163] T. E. Magin, M. Panesi, A. Bourdon, R. L. Jaffe, and D. W. Schwenke. Coarse-grain model for internal energy excitation and dissociation of molecular nitrogen. *Chemical Physics*, 398:90–95, apr 2012. doi:[10.1016/j.chemphys.2011.10.009](https://doi.org/10.1016/j.chemphys.2011.10.009). 28, 113
- [164] N. Mansour. Private Communication, 2019. 62
- [165] R. Marek and J. Straub. Analysis of the evaporation coefficient and the condensation coefficient of water. *International Journal of Heat and Mass Transfer*, 44(1):39 – 53, 2001. doi:[10.1016/S0017-9310\(00\)00086-7](https://doi.org/10.1016/S0017-9310(00)00086-7). 142
- [166] A. Martínez Picar, C. Marqué, C. Verbeeck, S. Calders, S. Ranvier, E. Gamby, M. Anciaux, C. Tetard, and H. Lamy. Numerical simulation

- of the BRAMS interferometer in Humain. In *Proceedings of the International Meteor Conference, Egmond, the Netherlands, 2-5 June 2016*, 2016. 5
- [167] J. C. G. Martín, D. L. Bones, J. D. Carrillo-Sánchez, A. D. James, J. M. Trigo-Rodríguez, B. F. Jr., and J. M. C. Plane. Novel Experimental Simulations of the Atmospheric Injection of Meteoric Metals. *The Astrophysical Journal*, 836(2):212, 2017. doi:[10.3847/1538-4357/aa5c8f](https://doi.org/10.3847/1538-4357/aa5c8f). 13
- [168] B. J. McBride, S. Gordon, and M. A. Reno. Thermodynamic Data for Fifty Reference Elements. NASA TP-3287-REV1, Glenn Research Center, Cleveland, Ohio, February 2001. 29, 95
- [169] R. E. McCrosky and Z. Ceplecha. Fireballs and the physical theory of meteors. *Bulletin of the Astronomical Institutes of Czechoslovakia*, 21: 271, Jan 1970. 9
- [170] R. E. McCrosky, A. Posen, G. Schwartz, and C.-Y. Shao. Lost city meteorite—its recovery and a comparison with other fireballs. *Journal of Geophysical Research (1896-1977)*, 76(17):4090–4108, 1971. doi:[10.1029/JB076i017p04090](https://doi.org/10.1029/JB076i017p04090). 10, 157, 163, 175, 193
- [171] B. C. McGee, M. L. Hobbs, and M. R. Baer. Exponential 6 Parameterization for the JCZ3-EOS. SAND98-1191, Sandia National Laboratories, 1998. 201
- [172] R. Meland, A. Frezzotti, T. Ytrehus, and B. Hafskjold. Nonequilibrium molecular-dynamics simulation of net evaporation and net condensation, and evaluation of the gas-kinetic boundary condition at the interphase. *Physics of Fluids*, 16(2):223–243, feb 2004. doi:[10.1063/1.1630797](https://doi.org/10.1063/1.1630797). 52, 65, 143
- [173] J. B. Meurisse, J. Lachaud, F. Panerai, C. Tang, and N. N. Mansour. Multidimensional material response simulations of a full-scale tiled ablative heatshield. *Aerospace Science and Technology*, 76:497–511, may 2018. doi:[10.1016/j.ast.2018.01.013](https://doi.org/10.1016/j.ast.2018.01.013). 61
- [174] H.-J. Mick, M. Burmeister, and P. Roth. Atomic resonance absorption spectroscopy measurements on high-temperature co dissociation kinetics. *AIAA Journal*, 31(4):671–676, 1993. doi:[10.2514/3.11602](https://doi.org/10.2514/3.11602). 200
- [175] E. P. Milley, R. L. Hawkes, and J. M. Ehrman. Meteor luminosity simulation through laser ablation of meteorites. *Monthly Notices of the Royal Astronomical Society: Letters*, 382(1):L67–L71, 2007. doi:[10.1111/j.1745-3933.2007.00390.x](https://doi.org/10.1111/j.1745-3933.2007.00390.x). 13
- [176] R. C. Millikan and D. R. White. Systematics of Vibrational Relaxation. *The Journal of Chemical Physics*, 39(12):3209–3213, 1963. doi:[10.1063/1.1734182](https://doi.org/10.1063/1.1734182). 39

- [177] F. S. Milos and Y.-K. Chen. Comprehensive model for multicomponent ablation thermochemistry. In *AIAA, Aerospace Sciences Meeting & Exhibit, 35th.*, Reno, NV, 1997. doi:10.2514/6.1997-141. AIAA 97-0141. 51, 61, 190
- [178] F. S. Milos and D. J. Rasky. Review of numerical procedures for computational surface thermochemistry. *Journal of Thermophysics and Heat Transfer*, 8(1):24–34, jan 1994. doi:10.2514/3.497. 51, 61
- [179] M. F. Modest. *Radiative Heat Transfer*. Academic Press, 2 edition, 2003. ISBN 9780125031639,0125031637. 114, 115, 123, 125, 131, 162
- [180] L. Monchick and E. A. Mason. Transport Properties of Polar Gases. *The Journal of Chemical Physics*, 35(5):1676–1697, nov 1961. doi:10.1063/1.1732130. 32
- [181] A. Munafò. *Multi-Scale Models and Computational Methods for Aerothermodynamics*. PhD thesis, von Karman Institute for Fluid Dynamics & Ecole Central Paris, 2014. 41, 42
- [182] A. Munafò and T. E. Magin. Modeling of stagnation-line nonequilibrium flows by means of quantum based collisional models. *Physics of Fluids*, 26(9):097102, 2014. doi:10.1063/1.4894842. 41
- [183] G. Nagayama and T. Tsuruta. A general expression for the condensation coefficient based on transition state theory and molecular dynamics simulation. *The Journal of Chemical Physics*, 118(3):1392–1399, jan 2003. doi:10.1063/1.1528192. 143
- [184] M. Nicolet and W. Peetermans. Atmospheric absorption in the o₂ schumann-runge band spectral range and photodissociation rates in the stratosphere and mesosphere. *Planetary and Space Science*, 28(1):85 – 103, 1980. doi:10.1016/0032-0633(80)90106-3. 171
- [185] O. R. Norton and L. Chitwood. *Field Guide to Meteors and Meteorites*. Springer Science & Business Media, 2008. 3
- [186] Y. Ogasawara, T. S. Hadi, and M. Maeda. Rates of evaporation in a vacuum in liquid ni-ti alloys. *ISIJ International*, 38(8):789–793, 1998. doi:10.2355/isijinternational.38.789. 143
- [187] D. Olynick, Y.-K. Chen, and M. E. Tauber. Aerothermodynamics of the stardust sample return capsule. *Journal of Spacecraft and Rockets*, 36(3): 442–462, 1999. doi:10.2514/2.3466. 200
- [188] C. P. Opeil, G. J. Consolmagno, D. J. Safarik, and D. T. Britt. Stony meteorite thermal properties and their relationship with meteorite chemical and physical states. *Meteoritics & Planetary Science*, 47(3):319–329, 2012. doi:10.1111/j.1945-5100.2012.01331.x. 100

- [189] M. Panesi. *Physical Models for Nonequilibrium Plasma Flow Simulations at High Speed Re-Entry Conditions*. PhD thesis, von Karman Institute for Fluid Dynamics & Universita degli Studi di Pisa, 2009. 25, 39, 40, 113
- [190] M. Panesi, R. L. Jaffe, D. W. Schwenke, and T. E. Magin. Rovibrational internal energy transfer and dissociation of $N_2(1\Sigma g^+)$ - $N(4Su)$ system in hypersonic flows. *The Journal of Chemical Physics*, 138(4):044312, 2013. doi:[10.1063/1.4774412](https://doi.org/10.1063/1.4774412). 21
- [191] M. Panesi, A. Munafò, T. E. Magin, and R. L. Jaffe. Nonequilibrium shock-heated nitrogen flows using a rovibrational state-to-state method. *Physical Review E*, 90(1), jul 2014. doi:[10.1103/PhysRevE.90.013009](https://doi.org/10.1103/PhysRevE.90.013009). 113
- [192] C. Park. Effects of atomic oxygen on graphite ablation. *AIAA Journal*, 14(11):1640–1642, nov 1976. doi:[10.2514/3.7267](https://doi.org/10.2514/3.7267). 143
- [193] C. Park. Assessment of a two-temperature kinetic model for dissociating and weakly ionizing nitrogen. *Journal of Thermophysics and Heat Transfer*, 2(1):8–16, 1988. doi:[10.2514/3.55](https://doi.org/10.2514/3.55). 19, 21, 38
- [194] C. Park. Assessment of two-temperature kinetic model for ionizing air. *Journal of Thermophysics and Heat Transfer*, 3(3):233–244, 1989. doi:[10.2514/3.28771](https://doi.org/10.2514/3.28771). 19, 21, 38
- [195] C. Park. *Nonequilibrium Hypersonic Aerothermodynamics*. Wiley, NewYork, 1990. 21, 39, 41
- [196] C. Park. Modeling of hypersonic reacting flows. In *Advances in Hypersonics*, pages 104–127. Birkhäuser Boston, 1992. doi:[10.1007/978-1-4612-0371-1_4](https://doi.org/10.1007/978-1-4612-0371-1_4). 39
- [197] C. Park. Review of chemical-kinetic problems of future nasa missions. i - earth entries. *Journal of Thermophysics and Heat Transfer*, 7(3):385–398, 1993. doi:[10.2514/3.431](https://doi.org/10.2514/3.431). 200
- [198] C. Park. The limits of two-temperature kinetic model in air. *AIAA* 2010-911, jan 2010. doi:[10.2514/6.2010-911](https://doi.org/10.2514/6.2010-911). 21
- [199] C. Park. Rosseland mean opacities of air and h-chondrite vapor in meteor entry problems. *Journal of Quantitative Spectroscopy and Radiative Transfer*, 127:158 – 164, 2013. doi:[10.1016/j.jqsrt.2013.05.011](https://doi.org/10.1016/j.jqsrt.2013.05.011). 11, 120
- [200] C. Park. Stagnation region radiative ablation of asteroidal meteoroids in the rosseland approximation. *Journal of Thermophysics and Heat Transfer*, 28(4):598–607, 2014. doi:[10.2514/1.T4384](https://doi.org/10.2514/1.T4384). 11, 120

- [201] C. Park. Rosseland mean opacities for the flow around cometary meteoroids. *Journal of Quantitative Spectroscopy and Radiative Transfer*, 154:44 – 54, 2015. doi:[10.1016/j.jqsrt.2014.10.024](https://doi.org/10.1016/j.jqsrt.2014.10.024). 11, 120
- [202] C. Park, R. Jaffe, and H. Partridge. Chemical-kinetic parameters of hyperbolic earth entry. *Journal of Thermophysics and Heat Transfer*, 15(1):76–90, 2001. doi:[10.2514/2.6517](https://doi.org/10.2514/2.6517). 55, 70, 200, 201
- [203] C. Patterson. Age of meteorites and the earth. *Geochimica et Cosmochimica Acta*, 10(4):230–237, oct 1956. doi:[10.1016/0016-7037\(56\)90036-9](https://doi.org/10.1016/0016-7037(56)90036-9). 1
- [204] A. H. Persad and C. A. Ward. Expressions for the Evaporation and Condensation Coefficients in the Hertz-Knudsen Relation. *Chemical Reviews*, 116(14):7727–7767, jun 2016. doi:[10.1021/acs.chemrev.5b00511](https://doi.org/10.1021/acs.chemrev.5b00511). 69, 142
- [205] F. Pirani, S. Brizi, L. F. Roncaratti, P. Casavecchia, D. Cappelletti, and F. Vecchiocattivi. Beyond the lennard-jones model: a simple and accurate potential function probed by high resolution scattering data useful for molecular dynamics simulations. *Physical Chemistry Chemical Physics*, 10(36):5489, 2008. doi:[10.1039/b808524b](https://doi.org/10.1039/b808524b). 49
- [206] L. Pittarello, S. Goderis, B. Soens, S. J. McKibbin, G. Giuli, F. Bariselli, B. Dias, B. Helber, G. O. Lepore, F. Vanhaecke, C. Koeberl, T. E. Magin, and P. Claeys. Meteoroid atmospheric entry investigated with plasma flow experiments: Petrography and geochemistry of the recovered material. *Icarus*, 331:170–178, oct 2019. doi:[10.1016/j.icarus.2019.04.033](https://doi.org/10.1016/j.icarus.2019.04.033). 12, 62, 85, 133, 134, 139
- [207] L. Pittarello, A. Yamaguchi, J. Roszjar, V. Debaille, C. Koeberl, and P. Claeys. To be or not to be oxidized: A case study of olivine behavior in the fusion crust of ureilite a 09368 and h chondrites a 09004 and a 09502. *Meteoritics & Planetary Science*, 54(7):1563–1578, 2019. doi:[10.1111/maps.13284](https://doi.org/10.1111/maps.13284). 85
- [208] J. M. C. Plane. A time-resolved model of the mesospheric na layer: constraints on the meteor input function. *Atmospheric Chemistry and Physics*, 4(3):627–638, 2004. doi:[10.5194/acp-4-627-2004](https://doi.org/10.5194/acp-4-627-2004). 96
- [209] J. M. C. Plane and D. Husian. Determination of the absolute rate constant for the reaction $O + NaO \rightarrow Na + O_2$ by time-resolved atomic chemiluminescence at $\lambda = 589 \text{ nm}$ [$Na(3\ 2P) \rightarrow Na(3\ 2S_{1/2}) + h\nu$]. *J. Chem. Soc., Faraday Trans. 2*, 82:2047–2052, 1986. doi:[10.1039/F29868202047](https://doi.org/10.1039/F29868202047). 200
- [210] S. B. Pope. Gibbs function continuation for the stable computation of chemical equilibrium. *Combustion and Flame*, 139(3):222–226, nov 2004. doi:[10.1016/j.combustflame.2004.07.008](https://doi.org/10.1016/j.combustflame.2004.07.008). 59

- [211] D. K. Prabhu, P. Agrawal, J. Allen, Gary A., J. Bauschlicher, Charles W., A. M. Brandis, Y.-K. Chen, R. L. Jaffe, G. E. Palmer, D. A. Saunders, and E. C. Stern. Physics-based modeling of meteor entry and breakup. In *4th 2015 IAA Planetary Defense Conference; 13-17 Apr. 2015; Frascati; Italy*, 2015. 4
- [212] R. K. Prabhu. An approximate Riemann solver for thermal and chemical nonequilibrium flows. NASA STI/Recon Technical Report N, Oct. 1994. 44
- [213] S. Prasanna, P. Rivière, and A. Soufiani. Modelling radiative properties of participating species in a microwave plasma reactor for diamond deposition. *Journal of Physics: Conference Series*, 550:012050, nov 2014. doi:[10.1088/1742-6596/550/1/012050](https://doi.org/10.1088/1742-6596/550/1/012050). 213
- [214] D. O. ReVelle and R. S. Rajan. On the luminous efficiency of meteoritic fireballs. *Journal of Geophysical Research: Solid Earth*, 84(B11):6255–6262, 1979. doi:[10.1029/JB084iB11p06255](https://doi.org/10.1029/JB084iB11p06255). 10, 172
- [215] P. Rivière. Systematic semi-classical calculations of Stark broadening parameters of NI, OI, NII, OII multiplets for modelling the radiative transfer in atmospheric air mixture plasmas. *Journal of Quantitative Spectroscopy and Radiative Transfer*, 73(1):91–110, apr 2002. doi:[10.1016/S0022-4073\(01\)00173-X](https://doi.org/10.1016/S0022-4073(01)00173-X). 216
- [216] P. Rivière and A. Soufiani. Generalized malkmus line intensity distribution for CO2 infrared radiation in doppler broadening regime. *Journal of Quantitative Spectroscopy and Radiative Transfer*, 112(3):475–485, feb 2011. doi:[10.1016/j.jqsrt.2010.09.010](https://doi.org/10.1016/j.jqsrt.2010.09.010). 125
- [217] P. Rivière, M.-Y. Perrin, and A. Soufiani. New Developments for CO2 IR Radiation: Comparison Between Experiments and Spectroscopic Database Predictions, and Updated Band Model Parameters. In *ESA Special Publication*, volume 714 of *ESA Special Publication*, page 39, Dec. 2012. 213
- [218] P. Roe. Approximate riemann solvers, parameter vectors, and difference schemes. *Journal of Computational Physics*, 43(2):357–372, oct 1981. doi:[10.1016/0021-9991\(81\)90128-5](https://doi.org/10.1016/0021-9991(81)90128-5). 44
- [219] J. Safarian and T. A. Engh. Vacuum evaporation of pure metals. *Metallurgical and Materials Transactions A*, 44(2):747–753, oct 2012. doi:[10.1007/s11661-012-1464-2](https://doi.org/10.1007/s11661-012-1464-2). 143
- [220] E. K. Sansom, P. Bland, J. Paxman, and M. Towner. A novel approach to fireball modeling: The observable and the calculated. *Meteoritics & Planetary Science*, 50(8):1423–1435, jul 2015. doi:[10.1111/maps.12478](https://doi.org/10.1111/maps.12478).

- [221] E. K. Sansom, P. A. Bland, M. G. Rutten, J. Paxman, and M. C. Towner. Filtering meteoroid flights using multiple Unscented Kalman Filters. *The Astronomical Journal*, 152(5):148, oct 2016. doi:[10.3847/0004-6256/152/5/148](https://doi.org/10.3847/0004-6256/152/5/148). 9
- [222] E. K. Sansom, M. Gritsevich, H. A. R. Devillepoix, T. Jansen-Sturgeon, P. Shober, P. A. Bland, M. C. Towner, M. Cupák, R. M. Howie, and B. A. D. Hartig. Determining Fireball Fates Using the α - β Criterion. *The Astrophysical Journal*, 885(2):115, nov 2019. doi:[10.3847/1538-4357/ab4516](https://doi.org/10.3847/1538-4357/ab4516). 9
- [223] L. Schaefer and B. Fegley. A thermodynamic model of high temperature lava vaporization on io. *Icarus*, 169:216–241, May 2004. doi:[10.1016/j.icarus.2003.08.023](https://doi.org/10.1016/j.icarus.2003.08.023). 57
- [224] R. W. Schrage. *A theoretical study of interphase mass transfer*. Columbia University Pres, New York, Mar. 1953. ISBN 978-0-231-87736-7. 52, 69
- [225] P. Schrooyen. *Numerical simulation of aerothermal flows through ablative thermal protection systems*. PhD thesis, von Karman Institute for Fluid Dynamics & Université catholique de Louvain, 2016. 195
- [226] P. Schrooyen, A. Turchi, K. Hillewaert, P. Chatelain, and T. E. Magin. Two-way coupled simulations of stagnation-point ablation with transient material response. *International Journal of Thermal Sciences*, 134:639 – 652, 2018. doi:[10.1016/j.ijthermalsci.2018.08.014](https://doi.org/10.1016/j.ijthermalsci.2018.08.014). 41, 100, 160
- [227] J. C. Schulz, E. Stern, S. Muppidi, G. Palmer, O. Schroeder, and A. Martin. Development of a three-dimensional, unstructured material response design tool. In *55th AIAA Aerospace Sciences Meeting*. American Institute of Aeronautics and Astronautics, jan 2017. doi:[10.2514/6.2017-0667](https://doi.org/10.2514/6.2017-0667). 195
- [228] J. Scoggins, L. Soucasse, P. Rivière, S. Soufiani, and T. Magin. Coupled Flow, Radiation, and Ablation Simulations of Atmospheric Entry Vehicles using the Hybrid Statistical Narrow Band Model. In *45th AIAA Thermophysics Conference*. Dallas, Texas, 2015. doi:[10.2514/6.2015-3112](https://doi.org/10.2514/6.2015-3112). AIAA 2015–3112. 41
- [229] J. B. Scoggins. *Development of numerical methods and study of coupled flow, radiation, and ablation phenomena for atmospheric entry*. PhD thesis, von Karman Institute for Fluid Dynamics & CentraleSupélec, 2017. 33, 36, 40, 42, 112, 114, 120, 122, 123, 124, 125, 128, 130, 192, 211, 213
- [230] J. B. Scoggins and T. E. Magin. Development of Mutation++: Multi-component Thermodynamic and Transport Properties for Ionized Plasmas written in C++. In *11th AIAA/ASME Joint Thermophysics and Heat Transfer Conference*. Atlanta,GA, 2014. ISBN 978-1-62410-281-3. doi:[10.2514/6.2014-2966](https://doi.org/10.2514/6.2014-2966). AIAA 2014-2966. 24

- [231] J. B. Scoggins and T. E. Magin. The Gibbs Function Continuation Method for Linearly Constrained Multiphase Equilibria. *Combustion and Flame*, 162(12):4514–4522, 2015. doi:[10.1016/j.combustflame.2015.08.027](https://doi.org/10.1016/j.combustflame.2015.08.027). 30, 59
- [232] J. B. Scoggins, V. Leroy, G. Bellas-Chatzigeorgis, B. Dias, and T. E. Magin. Mutation++: MUlticomponent Thermodynamic And Transport properties for IONized gases in C++. *SoftwareX*, 12:100575, 2020. doi:[10.1016/j.softx.2020.100575](https://doi.org/10.1016/j.softx.2020.100575). 24
- [233] C. E. Shepard, H. A. Stine, J. W. Vorreiter, and W. Winovich. A study of artificial meteors as ablaters. NASA-TN-D-4808, NASA Ames Research Center, Moffett Field, California, 1967. 12, 141
- [234] J. Shinn. Optical absorption of carbon and hydrocarbon species from shock heated acetylene and methane in the 135-220 nm wavelength range. jun 1981. doi:[10.2514/6.1981-1189](https://doi.org/10.2514/6.1981-1189). 213
- [235] V. Shuvalov and N. Artemieva. Numerical modeling of tunguska-like impacts. *Planetary and Space Science*, 50(2):181 – 192, 2002. doi:[10.1016/S0032-0633\(01\)00079-4](https://doi.org/10.1016/S0032-0633(01)00079-4). 11, 157
- [236] E. A. Silber, W. K. Hocking, M. L. Niculescu, M. Gritsevich, and R. E. Silber. On shock waves and the role of hyperthermal chemistry in the early diffusion of overdense meteor trains. *Monthly Notices of the Royal Astronomical Society*, 469(2):1869–1882, 04 2017. doi:[10.1093/mnras/stx923](https://doi.org/10.1093/mnras/stx923). 11
- [237] G. P. Smith, D. M. Golden, M. Frenklach, N. W. Moriarty, B. Eiteneer, M. Goldenberg, C. Thomas, R. K. Hanson, S. Song, W. C. G. Jr., V. V. Lissianski, and Z. Qin. Gri-mech 3.0. http://www.me.berkeley.edu/gri_mech/. 201
- [238] L. Soucasse, J. Scoggins, P. Rivière, T. Magin, and A. Soufiani. Flow-radiation coupling for atmospheric entries using a hybrid statistical narrow band model. *Journal of Quantitative Spectroscopy and Radiative Transfer*, 180:55–69, 2016. doi:[10.1016/j.jqsrt.2016.04.008](https://doi.org/10.1016/j.jqsrt.2016.04.008). 20, 22, 41, 120, 121, 123, 125, 159, 192
- [239] A. Soufiani and P. Rivière. Private Communication, 2018. 215
- [240] A. Soufiani, P. Rivière, and M.-Y. Perrin. High temperature gas radiation (HTGR) database and models. In *Von Karman Institute Lecture Series*, number STO-EN-AVT-218, 2013. 118, 213
- [241] S.R. Drayson. Rapid computation of the Voigt profile. *Journal of Quantitative Spectroscopy and Radiative Transfer*, 16(7):611–614, jul 1976. doi:[10.1016/0022-4073\(76\)90029-7](https://doi.org/10.1016/0022-4073(76)90029-7). 114

- [242] J. Stallcop, H. Partridge, and E. Levin. Analytical Fits for the Determination of the Transport Properties of Air. *Journal of Thermophysics and Heat Transfer*, 10(4):697–699, 1996. doi:10.2514/3.847. 32
- [243] D. Subasinghe and M. Campbell-Brown. Luminous efficiency estimates of meteors. II. application to canadian automated meteor observatory meteor events. *The Astronomical Journal*, 155(2):88, jan 2018. doi:10.3847/1538-3881/aaa3e0. 10
- [244] T. Suzuki, K. Fujita, K. Ando, and T. Sakai. Experimental study of graphite ablation in nitrogen flow. *Journal of Thermophysics and Heat Transfer*, 22(3):382–389, jul 2008. doi:10.2514/1.35082. 143
- [245] R. A. Svehla. Estimated Viscosities and Thermal Conductivities of Gases at High Temperatures. NASA TR R-132, Lewis Research Center, Cleveland, Ohio, 1962. 201
- [246] V. V. Svetsov, V. V. Shuvalov, and O. P. Popova. Radiation from a superbolide. *Solar System Research*, 52(3):195–205, May 2018. doi:10.1134/S0038094618020065. 11, 157
- [247] J. Taine and A. Soufiani. Gas IR radiative properties: From spectroscopic data to approximate models. pages 295–414, 1999. doi:10.1016/S0065-2717(08)70306-X. 113, 118, 120, 121, 123
- [248] S. Tashkun and V. Perevalov. CDSD-4000: High-resolution, high-temperature carbon dioxide spectroscopic databank. *Journal of Quantitative Spectroscopy and Radiative Transfer*, 112(9):1403–1410, jun 2011. doi:10.1016/j.jqsrt.2011.03.005. 213
- [249] M. G. G. T. Taylor, N. Altobelli, B. J. Buratti, and M. Choukroun. The rosetta mission orbiter science overview: the comet phase. *Philosophical Transactions of the Royal Society of London A: Mathematical, Physical and Engineering Sciences*, 375(2097), 2017. doi:10.1098/rsta.2016.0262. 2
- [250] C. Tien. Thermal Radiation Properties of Gases. pages 253–324, 1969. doi:10.1016/S0065-2717(08)70131-X. 114, 119, 120
- [251] F. Torres-Herrador, J. B. E. Meurisse, F. Panerai, J. Blondeau, J. Lachaud, B. K. Bessire, T. E. Magin, and N. N. Mansour. A high heating rate pyrolysis model for the Phenolic Impregnated Carbon Ablator (PICA) based on mass spectroscopy experiments. *Journal of Analytical and Applied Pyrolysis*, May 2019. doi:10/gf27n7. 143
- [252] F. Torres-Herrador, J. Coheur, F. Panerai, T. E. Magin, M. Arnst, N. N. Mansour, and J. Blondeau. Competitive kinetic model for the pyrolysis of the Phenolic Impregnated Carbon Ablator. *Aerospace Science and Technology*, 100:105784, May 2020. doi:10/ggm55f. 143

- [253] J. M. Trigo-Rodríguez and I. P. Williams. Dynamic Sources of Contemporary Hazard from Meteoroids and Small Asteroids. In *Astrophysics and Space Science Proceedings*, pages 11–32. Springer International Publishing, dec 2016. doi:[10.1007/978-3-319-46179-3_2](https://doi.org/10.1007/978-3-319-46179-3_2). 2
- [254] A. Turchi. *A Gas-Surface Interaction Model for the Numerical Study of Rocket nozzle flows over pyrolyzing ablative materials*. PhD thesis, Università degli Studi di Roma “La Sapienza”, 2013. 55, 70, 205
- [255] A. Turchi, J. J. Matesanz Saiz, T. Magin, and O. Chazot. On the flight extrapolation of stagnation-point ablative material plasma wind tunnel tests. In *Proceedings of 8th European Symposium on Aerothermodynamics for Space Vehicles*, Lisbon, Portugal, 2015. 41
- [256] B. van Leer. Towards the ultimate conservative difference scheme. v. a second-order sequel to godunov's method. *Journal of Computational Physics*, 32(1):101–136, jul 1979. doi:[10.1016/0021-9991\(79\)90145-1](https://doi.org/10.1016/0021-9991(79)90145-1). 43
- [257] D. Vanden Abeele and G. Degrez. Efficient computational model for inductive plasmas flows. *AIAA J.*, 38(2):234–242, 2000. doi:[10.2514/2.977](https://doi.org/10.2514/2.977). 139
- [258] J. Vaubaillon, L. Neslušan, A. Sekhar, R. Rudawska, and G. O. Ryabova. *Meteoroids: Sources of Meteors on Earth and Beyond*, chapter From Parent Body to Meteor Shower: The Dynamics of Meteoroid Streams, pages 161–186. Cambridge, UK: Cambridge University Press, 2019. 2
- [259] F. Verniani. On the luminous efficiency of meteors. *Smithsonian Contributions to Astrophysics.*, 8(5):141–171, 1965. doi:[10.5479/si.00810231.8-5.141](https://doi.org/10.5479/si.00810231.8-5.141). 10, 163
- [260] A. N. F. Versypt and R. D. Braatz. Analysis of finite difference discretization schemes for diffusion in spheres with variable diffusivity. *Computers & Chemical Engineering*, 71:241 – 252, 2014. doi:[10.1016/j.compchemeng.2014.05.022](https://doi.org/10.1016/j.compchemeng.2014.05.022). 92
- [261] F. Vilas. Spectral Characteristics of Hayabusa 2 Near-Earth Asteroid Targets 162173 1999 JU3 and 2001 QC34. *The Astronomical Journal*, 135(4):1101, 2008. doi:[10.1088/0004-6256/135/4/1101](https://doi.org/10.1088/0004-6256/135/4/1101). 2
- [262] W. G. Vincenti and C. H. Kruger. *Introduction to Physical Gas Dynamics.*, volume 70. Cambridge University Press (CUP), jul 1965. doi:[10.1017/s0001924000057304](https://doi.org/10.1017/s0001924000057304). 24, 25, 31
- [263] V. Vojáček, J. Borovička, P. Koten, P. Spurný, and R. Štork. Catalogue of representative meteor spectra. *Astronomy & Astrophysics*, 580:A67, aug 2015. doi:[10.1051/0004-6361/201425047](https://doi.org/10.1051/0004-6361/201425047). 10

- [264] V. Vojáček, J. Borovička, P. Spurný, and D. Čapek. The properties of cm-sized iron meteoroids. *Planetary and Space Science*, 184:104882, may 2020. doi:10.1016/j.pss.2020.104882. 111
- [265] T. Vondrak, J. M. Plane, S. Broadley, and D. Janches. A Chemical Model of Meteoric Ablation. *Atmospheric Chemistry and Physics*, 8(23):7015–7031, 2008. doi:10.5194/acp-8-7015-2008. 6, 62, 85, 108, 159
- [266] T. Walker and H. Kelly. The photoionization cross section for diatomic CH. *Chemical Physics Letters*, 16(3):511–514, oct 1972. doi:10.1016/0009-2614(72)80412-3. 213
- [267] G.-X. Wang and V. Prasad. Microscale heat and mass transfer and non-equilibrium phase change in rapid solidification. *Materials Science and Engineering: A*, 292(2):142–148, nov 2000. doi:10.1016/s0921-5093(00)01003-0. 89
- [268] M. K. Weisberg, C. Smith, G. Benedix, L. Folco, K. Righter, J. Zipfel, A. Yamaguchi, and H. C. Aoudjehane. The meteoritical bulletin, no. 95. *Meteoritics & Planetary Science*, 44(3):429–462, 2009. doi:10.1111/j.1945-5100.2009.tb00742.x. 93
- [269] R. Weryk, M. Campbell-Brown, P. Wiegert, P. Brown, Z. Krzeminski, and R. Musci. The canadian automated meteor observatory (camo): System overview. *Icarus*, 225(1):614 – 622, 2013. doi:10.1016/j.icarus.2013.04.025. 4, 9
- [270] L. F. Wheeler and D. L. Mathias. Probabilistic assessment of tunguska-scale asteroid impacts. *Icarus*, 327:83 – 96, 2019. doi:10.1016/j.icarus.2018.12.017. Tunguska. 9
- [271] L. F. Wheeler, P. J. Register, and D. L. Mathias. A fragment-cloud model for asteroid breakup and atmospheric energy deposition. *Icarus*, 295:149 – 169, 2017. doi:10.1016/j.icarus.2017.02.011. 9
- [272] S. M. White and E. Stern. Laser Ablation Experiments on the Tamdakht H5 Chondrite. In *80th Annual Meeting of The Meteoritical Society; 23-28 Jul. 2017; Santa Fe, NM; United States*, 2017. 13
- [273] M. J. Wright, G. V. Candler, and D. Bose. Data-parallel line relaxation method for the navier-stokes equations. *AIAA Journal*, 36(9):1603–1609, 1998. doi:10.2514/2.586. 30, 93
- [274] M. J. Wright, H. H. Hwang, and D. W. Schwenke. Recommended collision integrals for transport property computations part ii: Mars and venus entries. *AIAA Journal*, 45(1):281–288, 2007. doi:10.2514/1.24523. 201
- [275] M. Yan, H. R. Sadeghpour, and A. Dalgarno. Photoionization cross sections of he and h2. *The Astrophysical Journal*, 496(2):1044–1050, apr 1998. doi:10.1086/305420. 213

- [276] S. Yasuda, S. Takata, and K. Aoki. Evaporation and condensation of a binary mixture of vapors on a plane condensed phase: Numerical analysis of the linearized boltzmann equation. *Physics of Fluids*, 17(4):047105, apr 2005. doi:10.1063/1.1882252. 52
- [277] K. Yomogida and T. Matsui. Physical properties of ordinary chondrites. *Journal of Geophysical Research*, 88(B11):9513–9533, 1983. doi:10.1029/JB088iB11p09513. 133
- [278] T. Ytrehus. *Theoretical and Experimental Study of a Kinetic Boundary Layer Produced by Molecular Effusion from a Perforated Wall*. PhD thesis, von Karman Institute for Fluid Dynamics & Vrije Universiteit Brussel, 1975. 52, 68
- [279] T. Ytrehus and S. Østmo. Kinetic theory approach to interphase processes. *International Journal of Multiphase Flow*, 22(1):133–155, feb 1996. doi:10.1016/0301-9322(95)00056-9. 52, 65, 67, 68, 69, 70, 73, 75, 77, 81, 82, 83, 191
- [280] E. J. Öpik. *Physics of meteor flight in the atmosphere*. 1958. 9